ABSTRACT

Title of dissertation: EXPERIMENTS WITH STRONGLY-INTERACTING RYDBERG ATOMS

Dalia Patricia Ornelas Huerta,
Doctor of Philosophy, 2020

Dissertation directed by: Professor Steven Rolston
Dr. Trey Porto
Joint Quantum Institute,
National Institute of Standards and Technology and
University of Maryland College Park

Interacting Rydberg excitations in cold atomic ensembles can exhibit large quantum nonlinearities that enable engineering of strong interactions between individual photons. Consequently, Rydberg ensembles are a promising platform for quantum information applications and the study of more fundamental physics of few- and many-body phenomena with interacting photons. This thesis presents a series of experiments that study and exploit different regimes of Rydberg-mediated interactions.

We report the realization of an efficient on-demand single-photon source. The strong long-range Rydberg interactions allow the excitation of only a single collective Rydberg state within the entire atomic medium. The collective excitation can be subsequently retrieved as a single-photon. We use this scheme to generate highly pure and highly indistinguishable photons, which are suitable for scalable quantum information applications. These photons can be compatible with other atomic systems due to their narrow bandwidth, which makes building

practical hybrid quantum systems feasible. Here, we demonstrate high visibility two-photon quantum interference between our Rydberg-produced photons, and photons emitted by a remote single-trapped ion.

We also study Rydberg atoms under electromagnetically induced transparency conditions, where coherent superpostions of photons and Rydberg excitations propagate through the atomic medium as lossless dark-state polaritons. In the experiment, we use the external control fields to tune the interactions to a many-body regime where we can observe resonant scattering of dark-state polaritons to lossy channels. We show that the enhanced scattering process arises as a pure three-body effect.

EXPERIMENTS WITH STRONGLY-INTERACTING RYDBERG ATOMS

by

Dalia Patricia Ornelas Huerta

Dissertation submitted to the Faculty of the Graduate School of the
University of Maryland, College Park in partial fulfillment
of the requirements for the degree of
Doctor of Philosophy
2020

Advisory Committee:
Professor Steven L. Rolston, Chair/Advisor
Professor Trey V. Porto, Co-Advisor
Professor Thomas E. Murphy
Professor Gretchen K. Campbell
Professor Alicia J. Kollár

Dedication

A David, a mis padres, a mi hermana, a mi Yuki y a mi Sora que siempre alegran mis días

Acknowledgments

I feel very happy and fortunate to have had the unique opportunity to work at JQI. I met really kind, smart, hardworking people doing very exciting and cutting edge research in AMO. I owe this opportunity to Luis Orozco, *mi padrino*. He has always been willing to answer my questions, discuss physics, and teach me about beauty, nature, science, and art. His mentorship, guidance, and friendship have been a significant source of support throughout grad school that has helped me to grow as a scientist and as a person, and I will always be grateful to him.

I am very fortunate to have worked with the most knowledgeable AMO physicists, as well as the most supportive and kindest advisers Trey Porto and Steve Rolston. They accepted me to join their research group and build a lab despite not having a previous background in AMO. This experience has been a great opportunity to learn so many different things. Whenever they wouldn't be in a faculty meeting or hiding to write a grant, their door would always be open to any of their students to answer questions, teach and discuss physics, but also just having amusing non-physics related conversations. Besides being my mentors, they have been my strongest advocates and helped me stand up against some of the grad school adversities I have experienced. I can not thank them enough for everything.

Elizabeth Goldschmidt has been another mentor that I look up to and have had the pleasure of collaborating many times. Her knowledge about quantum optics is only matched by her great sense of humor and kind spirit.

Building a lab was a fun ride (most of the times) that I shared with Mary Lyon and Sandy Craddock. Mary was, without a doubt, the most skill-full and knowledgeable person of us, and I valued all her teachings and patience for the

time she stayed in the lab. Sandy's technical skills, programming knowledge, and hands-on approach were crucial for moving things forward during the construction of the apparatus and experiments. Even in his short time in the lab, Andrew "AJ" Hachtel showed he is the most hardworking and kindest grad student, I really appreciate the time we worked together. I am lucky to have co-mentored Nathan Friedman, he was a smart and friendly undergraduate student that also made important contributions to the experiment. Now, Patrick Banner and Deniz Kurdak are taking over the lab; they are motivated, diligent, and smart students. I am sure more exciting results will be coming in the near future.

The results in this thesis are a product from different collaborations with other people. Along with John Hannegan and James Siverns from Qudsia Quraishi's research group, we accomplished to interconnect two completely different experiments. I enjoyed our discussions about ion-trapping and frequency conversion, and had good laughs from our Slack and in-person conversations.

I was fortunate to work with Michael Gullans, Przemek Bienias, and Alexey Gorshkov. All of them brilliant scientists, I definitely learned a lot from all the discussions, notes, and lengthy email chains. Alexey's summary emails after every meeting were always constructive and very much appreciated! I also had fruitful discussions and collaborations with Yidan Wang, Marcin Kalinowsky, and Jeremy Young, all brilliant and friendly theory grad students.

Special thanks to Alessandro Restelli, who always was so patient to teach electronics to us physicists. His knowledge and skills, as well as his charismatic and gentle personality, are valuable assets for the JQI community!

There are other senior grad students and postdocs that significantly con-

tributed to my learning experience: Creston Herold, Varun Vadya, Dan Barker, Ben Reschovsky, Jon Hoffman, Jeff Grover, Matt Reed, Zach Smith, Xiao Li, Dimitri Trypogiorgos, Qiyu Liang, Jiraphat Tiamsuphat and Dan Campbell. I enjoyed the many interactions during lunch and group meetings with my fellow grad students Peter Elgee, Ananya Sitaram, Mónica Gutierrez and Neal Pisenti. I also appreciated the physics discussions with Madison Anderson, Eric Magnan, James Maslek, Swarnav Banik, Tsz-Chun Tsui, and Sarthak Subhankar.

I had really fun times with Burkley Patterson, Marcell Gall, Pierre Dussarat, Daniel Ohl de Melo, and Joao Braz. They were visiting students that (unfortunately) had a brief stay at JQI.

Shot-out to the staff members at JQI and the physics Department that make all this possible: Cindy Dooley, Ahn La, Melissa Britton, Lorraine de Salvo, Paulina Alejandro, Pauline Rikssopa, Josiland Chambers. Thank you for all your work and dedication; each interaction I had with them always ended with a smile. I should also recognize the hard work of Samantha Suplee, Kelly Hickman, Jessica Crosby, Donna Hammer, Taylor Prendergast, Judi Cohn, and Nancy Boone.

Outside the physics world, I would meet with my friends Sarah Surcayan, Karen David, Praneeth Boda, Brandon Ives, Yidan Wang, Jori Breslawski, Zachi Tamo, and Antonis Kyprianidis for endless and needed hours of laughs and salsa dancing. I am surely going to miss our time together.

I was lucky to meet my dearest friend Holly Tinkey during my first year of grad school, which was more amusing and less painful thanks to her sense of humor and kindness! Dina Genkina is such a fun person to be around and always willing to help you. Steve Moses another dear friend I met at JQI, thanks for all

our adventures camping in the wild and beautiful nature.

It was an honor to be accepted as a member of the IHOP (International House of Physicists founded in ∼2008). When I started grad school Kanu, Ana, Marko, Juraj, Yigit, and Jupe made me feel like I found a second home in the livable community of College Park. I have fond memories of the pig farming dinners, movie nights, JR shuttle rides, IHOP operations, BBQs, and parties. Other notable and historical members that are part of the IHOP society: Dinko, Zrinka, Prateek, Paco, Shannon, Wrick, Mosab, Dimitri, Seyit, and Cem, thanks to everyone for all the happy years that we shared as roommates!

I can say so many wonderful things about Kanu. Her kind, fun, witty and unique personality, along with her resilience and passion for science, were sources of support and inspiration at all times. Ana and I started this journey together. It has been so special and fun to share all these experiences. Her friendship made grad school so much better!

La banda Latina fue como una segunda familia durante mi estancia en Maryland: Ale, Pablo, Ana, Paco, Kris, Israel (Reverendo y master chef), Andrés, Andrea, Alex, Carlos, Carla, Mónica, Maggie, Héctor y Alex. Me hará mucha falta su calidez y cariño, gracias a todos por su amistad y haber hecho mi tiempo en College Park más divertido.

No importa cuánto tiempo pase, cada vez que regreso a México, mis amigos siempre me hacen sentir como si nunca me hubiera ido, gracias a Andrés (Botchito), Paulina (Bicha), Tete, Xareni, Pau, Fátima, Carlitos y Ernesto, por todos los años de amistad y los que vienen.

Claudia y Arturo los considero como mi familia, gracias también a todos

mis tíos y tíos, espcialmente a Guillermo Huerta, los hermanos Ornelas: José, Cuca, María, Javier, Pedro, Raquel, Carmen, Angelina and Alicia. Siempre estaré agradecida por el apoyo y cariño que me ofrecieron al crecer.

David, eres mi persona favorita, mi mejor amigo, mi compañero, mi refugio y mi cielo. Gracias por todo tu amor, apoyo, comprensión, por hacerme sonreír cuando más me hacía falta y por inspirarme a ser mejor. Es difícil imaginar que estos años fueran tan felices sin estar a tu lado y me siento afortunada de seguir compartiendo mi vida contigo.

A mi familia, no hay suficienties palabras para agradecerles todo el amor y apoyo incondicional que me han brindado, no estaría aquí sin ustedes. Papá no me queda duda alguna que eres el padre más dedicado y amoroso. Mamá eres la mujer más fuerte, amorosa y a la que más admiro. Claudia, hermanita linda, tu empatía y fortaleza son una constante fuente de inspiración. Me siento tan afortunuda y feliz de haber crecido a su lado y aprendido de ustedes.

Table of Contents

List of Tables

List of Figures

List of Abbreviations

AOM	Acousto-optic modulator
AR	Anti-reflection
AWG	American Wire Gauge
BS	Beamsplitter
CCD	Charge-coupled device
CMOT	Compressed magneto-optical trap
CF	Conflat
DAC	Digital to analog converter
DC	Direct current
DDS	Direct digital synthesizer
DFG	Difference frequency conversion
DSP	Dark-state polariton
ECDL	External cavity diode laser
EIT	Electromagnetically-induced transparency
EOM	Electro-optical modulator
HBT	Hanbury Brown and Twiss
HOM	Hong-Ou-Mandel
HWP	Half-wave plate
JQI	Joint Quantum Institute
LPD	Long-pass dichroic mirror
MCP	Multi-channel plate detector
MHV	Miniature high-voltage
MMF	Multi-mode fiber
MOT	Magneto-optical trap
NA	Numerical aperture
OD	Optical depth
PBS	Polarizing beamsplitter
PDH	Pound-Drever-Hall
PEEK	Polyether ether ketone
PID	Proportional, integral, derivative
PLL	Phase locked loop
PMF	Polarization maintaining fiber
POVM	Positive-Operator-Valued Measure
PNR	Photon-number resolving
QWP	Quarter-wave plate
RF	Radio frequency
RMS	Root mean square
SHG	Second harmonic generation
SMF	Single-mode fiber
SPAD	Single-photon avalanche detector
SPD	Short-pass dichroic mirror
ss	Stainless steel
TA	Tapered amplifier
TTL	Transistor-transistor logic
UHV	Ultra-high vacuum
ULE	Ultra-low expansion
VBG	Volume Bragg grating
WKB	Wentzel-Kramers-Brillouin

Chapter 1: Introduction

Photons are ideal carriers to encode and transmit information in their quantum states as qubits, due to their weak interaction with the environment. This property allows preserving the fidelity of the stored information over long propagation distances while traveling at the speed of light. Additionally, their degrees of freedom, such as frequency, bandwidth, polarization, and spatial mode, can be manipulated with great control [1]. On the other hand, processing the information requires interactions among photons [2]. Interacting photons would enable the development of different applications for quantum information [3, 4], quantum communication [5], quantum metrology [6], and exploring many-body physics in correlated states of light [7, 8].

Photon-photon interactions can be mediated through light-matter interactions. An ideal light-matter interface would exhibit a strong nonlinear response at the single-photon level with controlled dissipation. In other words, the response of a nonlinear quantum medium would significantly depend on the photon number of the propagating light pulse. At the same time, the ability to control dissipative processes is important to suppress unwanted decoherence effects, or filter determined quantum states.

The optical response of a medium is characterized by the complex susceptibility χ, where the real part describes dispersive properties such as phase shifts

or propagation velocities, while the imaginary part characterizes the absorption of the light as it propagates through the medium. The light-matter nonlinear response can be expanded as a power series of the incoming electromagnetic field E [9]:

$$\chi = \chi^{(1)} + \chi^{(2)}E + \chi^{(3)}E^2 + \cdots . \tag{1.1}$$

Here, the power of the field modifies the optical response of χ. However, typical nonlinear effects are very weak in conventional media, so they pose a challenge at the single photon level. Nonetheless, Chuang and Yamamoto proposed to use Kerr-nonlinearities $\chi^{(3)}$ for quantum computation [10], where cross-modulation with a pair of photons produces a conditional phase gate. Later theoretical work demonstrated that the noninstantaneous response of a medium with entirely local nonlinearities imposes hard limits for these protocols, in which phase noise impedes high-fidelity operations [11]. It is possible to increase the Kerr nonlinearities of a medium, for example, using electromagnetically induced transparency (EIT) in ultra-cold atomic ensembles [12]. In this configuration, $\chi^{(3)}$ can take values of $\sim 10^{-7}$ $\mathrm{m}^2/\mathrm{V}^2$ [13], which is 15 orders of magnitude larger than fused silica. However, the limitations due to the local nature of the nonlinearities remain.

There are many challenges to realize quantum nonlinearities. First, let us consider a single two-level atom in free space, which has a highly nonlinear response (see Fig. 1.1). Suppose it has a ground state $|g\rangle$, and an excited state $|e\rangle$, with decay rate Γ, and a transition frequency $\omega_a = 2\pi c/\lambda$. If the atom is initially in $|g\rangle$, a photon with frequency ω_a can excite the atom to $|e\rangle$. Then, if a second photon arrives, it cannot be absorbed. Although the response of a single atom can be saturated with a single photon, there are two problems with this simple system.

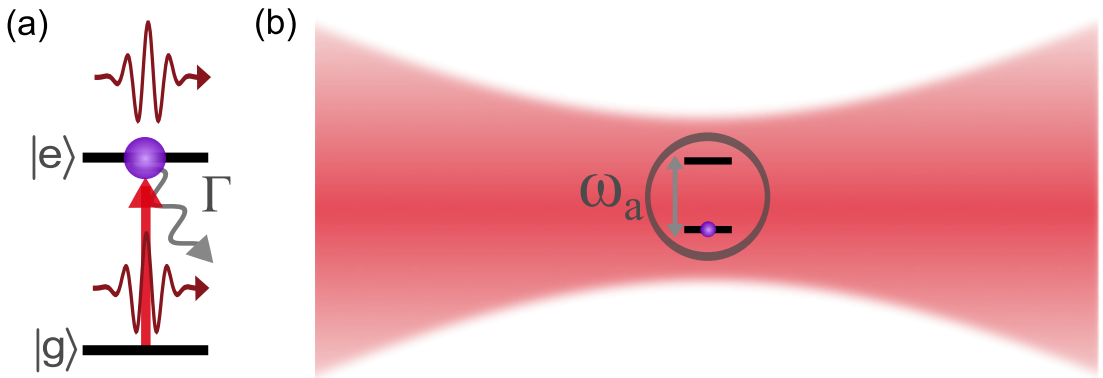

Figure 1.1: **Two-level single atom in free space.** (a) Two-level atom with a ground state $|g\rangle$ and an excited state $|e\rangle$ with a lifetime $1/\Gamma$. Once an atom absorbs a photon at resonant frequency transition ω_a, it can not absorb a second photon. (b) The beam waist size of the driving light is limited by diffraction resulting in a low interaction probability with the atom.

First, the nonlinearity coherence time is fundamentally limited by the lifetime $1/\Gamma$ of the excited state. However, by coupling to a third long-lived atomic state, the coherence time can potentially be increased. The second major problem is that the photon-atom coupling in free-space is very weak. The probability of interaction is proportional to the ratio of the resonant atomic cross-section $\sigma_a = 3\lambda^2/2\pi$, and the area of the photon beam $A = \pi w^2 \geq \lambda^2$, where diffraction prevents that the beam waist w to be smaller than λ. Given that the interaction probability $p = \sigma_a/A \ll 1$, $N \approx 1/p$ photons are required to saturate an atom, or conversely, N atoms are needed to observe single-photon nonlinearities [2]. Despite such limitations, there have been important demonstrations using a single atom in free-space, including single-photon generation [14], Bell-test experiments [15], high-fidelity quantum gates [16], or high-fidelity remote entanglement [17, 18].

Over the years, many different approaches have been developed to increase light-matter interaction. Here, we will consider atomic-based systems in the optical domain: cavities, atomic ensembles, and interacting Rydberg atoms; the latter is the focus of this thesis.

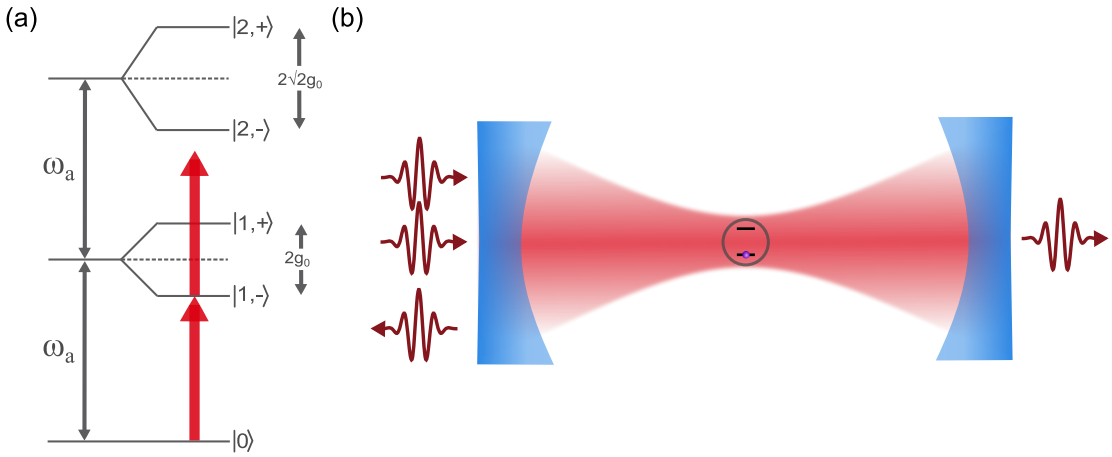

Figure 1.2: **Two-level system coupled to n photons in a cavity.** (a) Dressed atomic states of the Jaynes-Cummings ladder. The doublets are separated by $2\sqrt{n}g_0$, where g_0 is the single-photon Rabi frequency. The bare resonant frequency is ω_a. (b) The coupling to the cavity shifts the doubly photon excited state off-resonance, so only one photon can be transmitted at a time.

An emitter confined in a high-finesse optical cavity enhances the light-matter interaction by increasing the number of times a photon interacts with the emitter (in general, it can be a single atom, an atomic ensemble or a solid-state "artificial atom"). A high finesse F ensures that the photon repeatedly bounces back and forth between the cavity mirrors before it finally leaks. Moreover, if the mode volume of the light is small, the electric field per photon can increase as well. The cooperativity $\eta \propto F\lambda^2/w^2$ measures the strength of the interaction, if $\eta \gg 1$, then the interaction probability $p \to 1$ [2]. The cavity field dresses the atomic levels (see Fig. 1.2(a)). When the laser field is tuned to the first excited state resonance (corresponding to the manifold of a single-photon excitation), a second photon is not resonant with the doubly-excited state and is reflected from the cavity, so only one photon is transmitted at a time [19]. This results in a strong quantum nonlinearity, as shown in Fig. 1.2(b). This description can be extended to a three-level system in which the transitions are driven between two ground-states, allowing an increase in the coherence time, as opposed to being limited by the excited

state lifetime. There have been numerous realizations for quantum information applications using cavities, to mention a few: efficient single-photon sources [20], quantum gates [21], two-node quantum networks [22], as well as the study of many-body physics [23, 24]. A recent platform consists of interfacing atoms with tightly

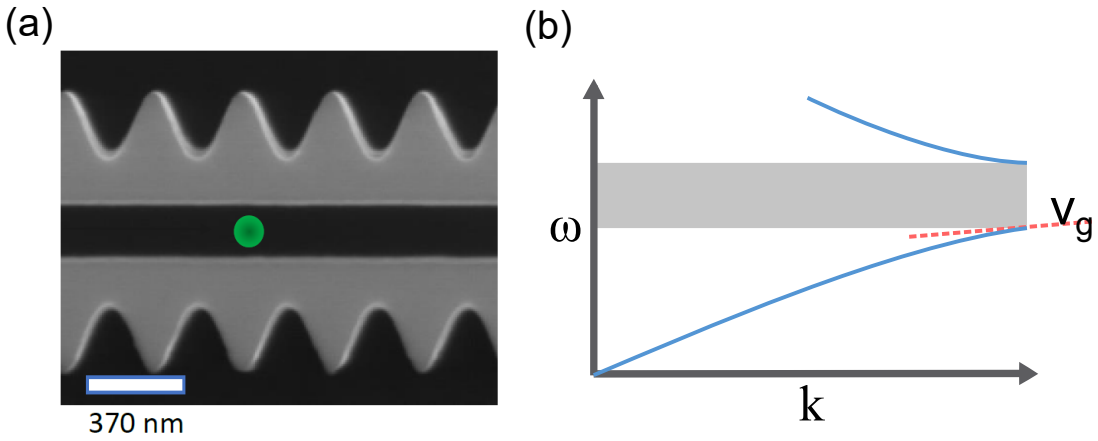

Figure 1.3: **Nanophotonic waveguides.** (a) Atom coupled to an "alligator" waveguide with sub-wavelength structure. Image taken from Ref. [25]. (b) Propagating dispersion mode relation indicated by the blue lines from the waveguide in (a). The gray rectangle indicates the frequency bandgap, the red-dashed line is the derivative near the bandgap edge, the group velocity $v_g = \frac{\mathrm{d}\omega}{\mathrm{d}k}$

confined light in nano-photonic structures, like sub-wavelength nanofibers [26, 27] or photonic crystal waveguides [28] (Fig. 1.3(a)). Nano-structure devices can be engineered to make the photon mode area smaller than the atomic cross-section $A < \sigma_a$. Moreover, the mode dispersion relation in waveguides can have bandgaps, where specific frequencies destructively interfere and do not propagate. If the light frequency is near the edge of the bandgap it will experience a reduced group velocity approaching zero (see Fig. 1.3(b)). When the bandgap edge is near the atomic resonant frequency, it increases the interaction time and the interaction strength [29]. The development of these systems is a promising approach to build scalable integrated quantum devices.

A different approach to enhance light-matter interactions involves using more

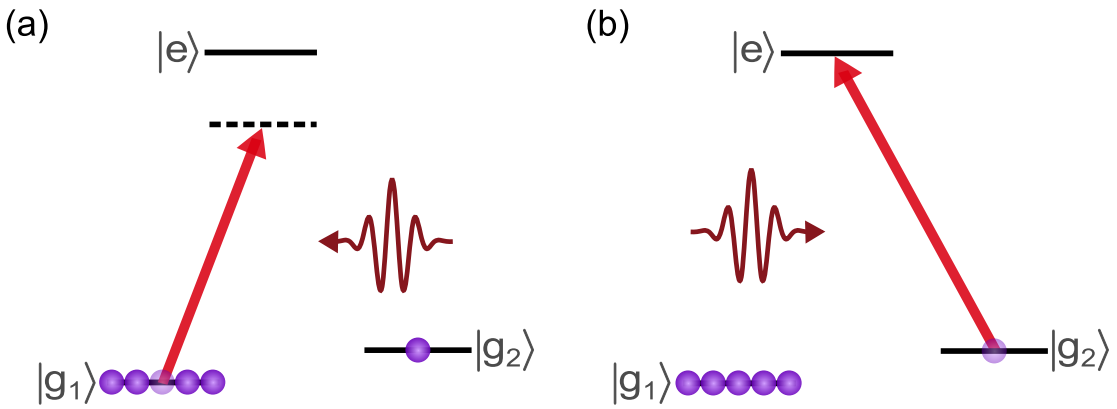

Figure 1.4: **Write-read pulse sequence for DLCZ.** (a) All atoms in the ensemble are prepared in the $|g_1\rangle$ state. The write pulse detuned from the excited state induces an spontaneous emitted Stokes photon and results in a spin wave $N-1$ atoms in $|g_1\rangle$ and a single atom in $|g_2\rangle$. (b) The read pulse retrieves the spin wave as a anti-Stokes photon.

atoms while remaining in the single-photon and single excitation regime. One of the pioneer ideas to use atomic ensembles as a light-matter interface with an enhanced coupling originated with the proposal of Duan, Lukin, Cirac and Zoller, the DLCZ protocol [30]. Figure 1.4 illustrates the protocol sequence. Let us consider a medium composed N three-level atoms, with two non-degenerate ground-states $|g_1\rangle$, $|g_2\rangle$, and an excited state $|e\rangle$, where all the atoms are prepared in $|g_1\rangle$. A "write" pulse on the $|g_1\rangle \rightarrow |e\rangle$ generates an emitted Stokes photon from $|e\rangle \rightarrow |g_2\rangle$ with some probability. Detection of the Stokes photon in a particular direction, heralds the creation of a N-atomic spin wave that is a coherent superposition of all the possible combinations where one atom is in $|g_2\rangle$ and $N-1$ atoms are in $|g_1\rangle$. The spin wave is phase-matched to the write-Stokes process and can be retrieved as an emitted Anti-Stokes photon by a "read" pulse. The read pulse drives $|g_2\rangle \rightarrow |e\rangle$ with an $\sqrt{N}$-enhanced coupling arising from the coherent superposition. The emitted photon has a well-defined propagation mode as a result of collective, constructive interference, as long as the phase coherence is preserved

during the write-read process [31]. This protocol is useful to realize quantum networks with distributed entanglement [32]. Modifications of this approach with other schemes like EIT [33] and photon-echo have been used to realize quantum memories [34]. However, there is a trade-off between the fidelity of heralding a single-Stokes photon and a high repetition rate arising from the finite multi-photon emission probability. Due to the Poissonian statistics of laser light, the incoming write pulse must have, on average, much less than a photon at a time, resulting in a very low emission probability of a Stokes photon [31]. Despite the enhanced coupling, the system exhibits a linear behavior at the few-photon level. An alternative to observe quantum nonlinearities is by embedding the ensemble into a cavity [35–37].

Another scheme to achieve quantum nonlinearities that does not require a cavity consists of exploiting long-range interactions of Rydberg atoms, which is the focus of this thesis. Rydberg atoms are in highly-excited states, in which the valence electron is far from the core [38]. A very large dipole moment arises from the large orbital radius, which results in strong long-range dipole-dipole interactions (see Fig. 1.5(a)). One manifestation of these interactions is the blockade effect, where only a single atom can be excited to the Rydberg state within a blockaded volume. This effect arises from the dipole-dipole interaction, which induces an energy shift for multiply excited-Rydberg states, meaning that the shifted resonance can no longer be excited [39], Fig. 1.5(b) depicts this effect. The quantum nonlinearities are significant since the response of the medium to the single-photon level, changes in the presence of a single excitation within the blockaded volume. For sufficient high principal quantum number n, the blockade radius can be up to

tens of microns.

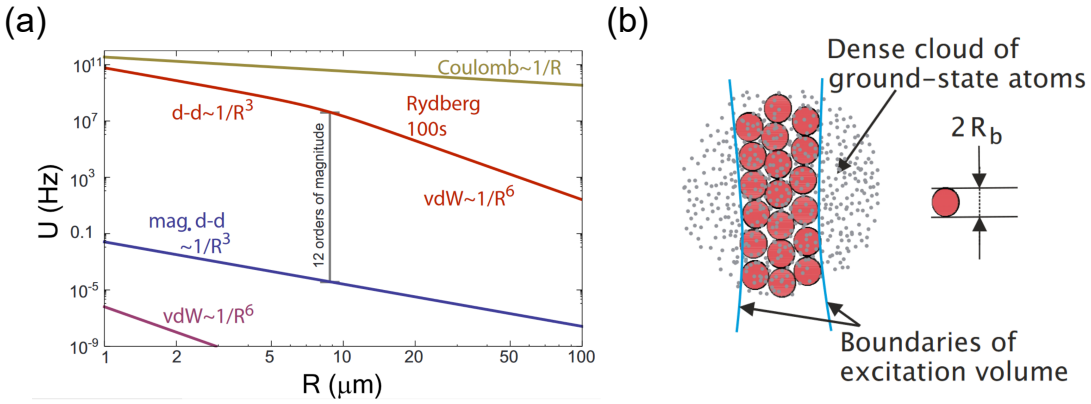

Figure 1.5: **Rydberg atoms long-range interactions.** (a) Two-body interaction strength as a function of their separation R. The purple line indicates van der Waals interaction, and the blue line represents magnetic dipole-dipole interactions for Rb ground-state atoms. The red line indicates van der Waals interactions for Rb $100S_{1/2}$ Rydberg state. The yellow line is the Coulomb interaction of charged ions. (b) Schematic of the Rydberg blockade effect. In each blockade volume with radius r_b (orange) contains a single Rydberg excitation and many ground-state atoms. Images taken from Ref. [39].

Rydberg atoms embedded in atomic ensembles present several advantages as a light-matter interface. It exhibits the coupling enhancement from the collective excitation, as well as the strong-quantum nonlinearities arising from the dipole interactions. Rydberg states also posses long lifetimes allowing for long coherence times. Moreover, current cooling and excitation techniques enable to manipulate the optical and atomic properties of trapped atoms with great control, making this system very versatile to engineer interactions among optical photons.

Lukin et. al [40] in 2001 theoretically investigated using the blockade effect for quantum information storage and processing by creating a single-collective excitation in an atomic ensemble. Another pioneering work from Friedler et al. [41] in 2005, considered combining Rydberg interactions with the nonlinearities of EIT to realize a π-photon phase shift. The first experimental observation of the coherent coupling of Rydberg states in an EIT-atomic medium was done by Mohapatra et al.

in 2007 [42]. Gorshkov et al. [43] in 2011, proposed to use Rydberg-EIT to map the strong atomic interaction into photon-photon interactions to generate non-classical states of light, quantum gates and studying strongly-correlated states of light. A year later, ground-breaking experimental works demonstrated these ideas by observing single-photon quantum nonlinearities [44–46]. Since then, there have been numerous theoretical studies and experimental realizations of quantum information applications, to mention a few: a single-photon switch [47], a single-photon transistor [48–50], atomic phase gates [51–53] and photonic phase gates [54], as well as strongly-correlated states of light [55–57].

1.1 Thesis Outline

This dissertation describes a series of experiments using Rydberg states in atomic ensembles to engineer effective interactions among photons. It is organized as follows:

- Chapter 2 reviews some of the properties of Rydberg atoms, detailing the calculation of dipole matrix elements to estimate the magnitude and behavior of the Rydberg atom's properties and interactions. The resulting long-range van der Waals interactions give rise to the Rydberg blockade effect.

- Chapter 3 outlines the theoretical framework for Electromagnetically Induced Transparency with Rydberg atoms, where the tunable Rydberg interactions can be coherently mapped to a quantum electromagnetic field.

- Chapter 4 describes the schemes used to characterize our single-photon source based on a Rydberg ensemble. It also introduces new metrics to

benchmark the performance of single-photon sources, which are used in quantum information protocols that require single photons in a well-defined fully-single-mode. We describe them in this Reference [58]. The formulation of these metrics was done in collaboration with Elizabeth Goldschmidt.

- Chapter 5 details the design and construction of the experimental apparatus to make cold atomic ensembles and perform controllable, coherent excitations of Rydberg atoms.

- Chapter 6 presents the characterization of our Rydberg-based single-photon source producing highly pure and indistinguishable single photons, with generation efficiencies of up to 0.4 after the atomic cloud. It also includes the study of contaminant states limiting the efficiency of the source under certain conditions. The calculations used to estimate the retrieval probability of our system were carried out by Yidan Wang. This chapter is based on the following publication [58]:

  Ornelas-Huerta, D.P., Craddock, A.N., Goldschmidt, E.A., Hachtel, A.J., Wang Y., Bienias P., Gorshkov A.V., Rolston, S.L. and Porto, J.V., 2020. On-demand indistinguishable single photons from an efficient and pure source based on a Rydberg ensemble. Optica 7, p. 813-819.

- Chapter 7 reports the experimental realization of high-visibility in a time-resolved two-photon quantum interference between our photons and photons produced from a remote single-trapped ion. This chapter is based on the following publication [59]:

  Craddock, A.N., Hannegan, J., Ornelas-Huerta, D.P., Siverns, J.D., Hachtel,

A.J., Goldschmidt, E.A., Porto, J.V., Quraishi, Q. and Rolston, S.L., 2019. Quantum interference between photons from an atomic ensemble and a remote atomic ion. Physical review letters, 123(21), p.213601.

- Chapter 8 discusses the theoretical analysis of resonant three-body scattering process in Rydberg polaritons, as well as the experimental probing of this phenomenon through the measurement of two- and three-photon correlation functions. This work is still in progress.

- Finally, Chapter 9 summarizes the relevant results in this thesis, describes some current and possible experimental upgrades, and discusses future research work.

1.1.1 Contributions to the experimental work and results

All the results presented here are a product of the collective effort and participation of several people. During grad school, I was in charge of designing the overall vacuum system configuration, including the in-vacuum elements for the Rydberg states fine control. I designed, built, and initially aligned the main optical systems around the science chamber (probe, control, dipole, optical pumping, and imaging systems). I also built various hardware and electronic components. Along with Mary Lyon and Sandy Craddock, we assembled together the vacuum system, set up the laser systems, and developed the overall construction and maintenance of the experimental apparatus.

With this setup, I optimized our Rydberg system to generate single photons with the highest fidelity reported to date compared to other atomic-based single-photon sources. I extensively analyzed and processed all the data. I rectified the

theoretical predictions of the writing efficiency and contaminant creation model that Sandy originally initiated.

In collaboration with John Hannegan and James Siverns from the group of Qudsia Quraishi at the Army Research Laboratory, we demonstrated high-visibility quantum interference between our high-fidelity photons and photons generated by a single ion. This hybrid quantum interference experiment was led by Sandy and John, where I contributed to collect data and performed some preliminary data analysis.

Finally, we reported the observation of three-body scattering in Rydberg-polaritons, where I collected and analyzed the data, and performed various numerical simulations. Michael Gullans wrote the numerical code, and I helped to debug and modify the code for our purposes. Przemyslaw Bienias and Michael Gullans developed the theoretical framework to understand the experimental observations.

Chapter 2: Rydberg Atoms

Rydberg atoms have one electron excited to a state with a high principal quantum number, n. In this state, the electron is weakly bound since it lies far from the atomic core, where the distance to the atomic core increases with n^2 [38]. For example, the average orbital radius of an electron in the state $n = 139S_{1/2}$ is 1.5 μm, which is about 5,000 times larger than the orbital radius of the ground state[1].

The average orbital size sets many properties as it gives rise to a large induced dipole moment. For instance, Rydberg atoms exhibit exaggerated polarizabilities, since external electric fields can easily perturb the electron's weakly bound state; or long radiative lifetimes due to the small overlap between the excited and ground-state wavefunction. This thesis focuses on the study of the long-range interactions resulting from the large dipole moment. One consequence of these interactions is the blockade effect, where multiple Rydberg excitations within a volume of radius, r_b, called the blockade radius, are suppressed. This suppression is due to the Van der Waals dipole-dipole interaction shifting the excitation of neighboring Rydberg atoms out of resonance within the blockade radius [40, 61]. The length scale of this interaction is typically longer than the interatomic distance and can reach up to tens of microns.

[1]These numbers and the following in this chapter are explicitly quoted for ^{87}Rb atom, where the average orbital radius of the ground state is $5.63a_0$ [60].

Such long-range interactions give rise to some interesting behavior. For example, the observation of quantum non-linear effects to the single-photon level [43,44], or the emergence of collective effects where many individual absorbers behave as a single two-level atom, referred as a superatom [62]. Platforms using Rydberg excitations have become common for different quantum information applications demonstrations, as well as in the study of fundamental physics like few-body systems or quantum electrodynamics.

This chapter describes the quantum defect theory and the Schrödinger equation for an electron in a Rydberg state to find its energy and wavefunction. The wavefunction allows us to calculate the dipole matrix elements, which determine the properties of Rydberg atoms and their interactions.

2.1 Rydberg Atom properties

2.1.1 Quantum Defect Theory

Since Rubidium is an alkali metal, we focus on describing the properties of Rydberg atoms for this group of elements. Alkali atoms in their ground state have all their inner orbitals fully occupied with a single outermost electron in a S-orbital. The electronic configuration of alkali atoms with a single valence electron and a positively charged core resembles a hydrogen atom. We can describe the alkali spectral properties the same way as a hydrogenic system, adding some corrections that take into account the more complex alkali core structure.

The Rydberg formula is an empirical equation for the energy of the state n, and is used to determine the spectral lines for hydrogen-like atoms. As originally

stated by Johannes Rydberg, the binding energy spectrum is well described by,

$$E_n = -\frac{R_{\rm y}}{n^2}, \tag{2.1}$$

this formula was later supported by the Bohr model and from the Schrödinger equation of a simplified Hydrogen atom (with an infinitely heavy nucleus, and no relativistic corrections, spin interaction or angular momentum coupling). In Eq. (2.1) n is the principal quantum number, and, $R_{\rm y}$ is the Rydberg constant; in terms of fundamental constants, $R_{\rm y}$ is given by,

$$R_{\rm y} = \frac{m_e e^4}{8\epsilon_0^2 h^2} = 13.605 \text{ eV}. \tag{2.2}$$

Taking into account that the mass of the nucleus is not infinite compared to the mass of the electron m_e, the Rydberg constant for an atomic mass M is modified to,

$$R_{\rm M} = R_{\rm y}\left(1 - \frac{m_e}{M}\right)^{-1}. \tag{2.3}$$

The outer electron of the alkali atom interacts with an effective positively charged core, due to the screening of the electrons of the inner filled orbitals. Moreover, the elliptical orbits for valence electrons with angular momentum $l \leq 3$, can penetrate the closed electron shells interacting with the unscreened nuclear charge. The proximity to the ionic core can also polarize the electrons of the inner shells [63]. These two interactions deviate from a pure Coulomb potential between the positively charged core and the valence electron, which effectively increase the binding energy compared to the hydrogen atomic states. This deviation is de-

scribed by including a term $\delta_{n,l,j}$, known as a quantum defect [38]. Equation (2.1) is modified as follows,

$$E_{n,l,j} = -\frac{R_{\mathrm{M}}}{(n-\delta_{n,l,j})^2} = -\frac{R_{\mathrm{M}}}{n^{*2}}, \tag{2.4}$$

here, $n^* = n - \delta_{n,l,j}$, is the effective quantum principal number, which is no longer an integer. The quantum defect, $\delta_{n,l,j}$, depends on the principal quantum number, n, the orbital angular momentum, l, and, the total orbital angular momentum, j. It is obtained using the Rydberg-Ritz formula,

$$\delta_{n,l,j} = \delta_0(l,j) + \frac{\delta_2(l,j)}{(n-\delta_0(l,j))^2} - \frac{\delta_4(l,j)}{(n-\delta_0(l,j))^4} + ... \tag{2.5}$$

where the coefficients δ_i depend on the angular momentum state of the valance electron, as shown in Table 2.1. For low angular momentum states, the quantum defects strongly depend on l, and to a minor extent on j; however, they are negligibly small for states with $l > 3$. Quantum defects have been determined from different spectroscopic measurements [64–66]. They have also been calculated theoretically using the WKB approximation [67] and variational methods [68].

Many properties of Rydberg atoms are well described by scaling laws of the effective quantum number, n^*, for example, recalling that the binding energy scales as, $(n^*)^{-2}$, the energy difference between consecutive Rydberg states is, $(E_n - E_{n-1}) \propto (n^*)^{-3}$.

Similarly, the fine structure arising from the interaction of the electron spin and the orbital angular momentum, $\Delta_{nP} = E_{nP_{3/2}} - E_{nP_{1/2}}$, $\Delta_{nD} = E_{nD_{5/2}} - E_{nD_{3/2}}$ and, $\Delta_{nF} = E_{nF_{7/2}} - E_{nF_{5/2}}$ scale as $(n^*)^{-3}$ for large n^*.

State		Value	Ref.
$ns_{1/2}$	δ_0	3.131 180 4(10)	[64]
	δ_2	0.1784(6)	
$np_{1/2}$	δ_0	2.654889(10)	[64]
	δ_2	0.2900(6)	
$np_{3/2}$	δ_0	2.6416737(10)	[64]
	δ_2	0.2950(7)	
$nd_{3/2}$	δ_0	1.34809171(40)	[64]
	δ_2	-0.60283(26)	
$nd_{5/2}$	δ_0	1.34646572(30)	[64]
	δ_2	-0.59600(18)	
$nf_{5/2}$	δ_0	0.0165192(9)	[65]
	δ_2	-0.085(9)	
$nf_{7/2}$	δ_0	0.0165437(7)	[65]
	δ_2	-0.086(7)	

Table 2.1: **Quantum defects values for ^{87}Rb..**

The hyperfine splitting coming from the magnetic interaction of the total angular momentum and the nuclear spin also scales as $(n^*)^{-3}$. However, this splitting is typically negligible compared to relevant energy scales, particularly as n^* increases since the interaction becomes weaker as the electron is further away from the nucleus. For this reason, the quantum numbers J and m_J are used as an appropriate basis to compute the electron wavefunction.

2.1.2 Rydberg atom wavefunction

The valence electron wavefunction is obtained by solving the Schrödinger equation with the Hamiltonian $\hat{H}_0 = \hat{T} + \hat{V}$:

$$\left[-\frac{\hbar^2}{2\mu}\nabla^2 + V(r)\right]\psi_{n,l,m}(r,\theta,\phi) = E_{n,l,m}\psi_{n,l,m}(r,\theta,\phi), \tag{2.6}$$

where $V(r)$ is the interaction potential between the core and the electron, assuming the potential has no dependence on the θ and ϕ coordinates. The radial part

$R_{n,l,m}(r)$ of the wavefunction can be written as,

$$\left[-\frac{1}{2\mu}\left(\frac{\mathrm{d}^2}{\mathrm{d}r^2}+\frac{2}{r}\frac{\mathrm{d}}{\mathrm{d}r}\right)+\frac{l(l+1)}{2\mu r^2}+V(r)\right]R_{n,l,m}(r)=E_{n,l,m}R_{n,l,m}. \tag{2.7}$$

It is necessary to make a proper choice for the potential $V(r)$ to accurately describe the electron wavefunction. The model potential proposed by Marinescu *et al.* [69], adds some modifications to the Coulomb potential,

$$\begin{aligned} V_C(r) &= -\frac{Z_{nl}(r)}{r}-\frac{\alpha_c}{2r^4}\left(1-e^{-\left(\frac{r}{r_c}\right)^6}\right), \\ Z_{nl}(r) &= 1+(Z-1)e^{-a_1 r}-r(a_3+a_4)e^{-a_2 r}. \end{aligned} \tag{2.8}$$

Z_{nl} accounts for the $l-$orbit of the electron penetrating the core, where each coefficient a_i, r_c has a different value for each $l \leq 3$. The detailed definition of these values is given in Ref. [69]. The second part of the equation accounts for the core polarization, and its strength is given by the core polarizability α_c.

The spin-orbit coupling that causes the fine-structure splitting and adds the relativistic description to ensure the correct behavior closer to the core, can also be included [67, 70],

$$V_{SO}(r)=\frac{1}{1-\alpha^2 V_C}\left[\frac{\alpha^2}{2r}\frac{\partial V_C}{\partial r}\frac{j(j+1)-l(l+1)-\frac{3}{4}}{2}\right]. \tag{2.9}$$

The total radial potential is,

$$V(r)=V_C(r)+V_{SO}(r). \tag{2.10}$$

With the proper choice of the potential, $V(r)$ and knowing the eigenenergies

using quantum defect theory[2], the radial differential equation can be solved numerically using, for example, the Numerov method, described by Zimmerman *et al.* [72]. We need to make a change of variables to transform Eq. (2.7) into the standard Numerov form,

$$\frac{\mathrm{d}^2X}{\mathrm{d}x^2} = g(x)X(x). \tag{2.11}$$

It is known that the solution to a differential equation with $V(r) = 1/r$ is an oscillating function, where the frequency of the oscillation increases closer to the origin. Therefore, the number of grid points per period should remain fairly constant to correctly solve the differential equation (2.11). Bhatti *et al.* [73] proposed a square root scaling, $x = \sqrt{r}$ as a change of variable to achieve this. In addition, changing the radial wavefunction to $X(x) = R_{n,l,m}r^{3/4}$, transforms Eq. (2.7) to:

$$\frac{\mathrm{d}^2X}{\mathrm{d}x^2} = -\left[8\mu x^2(E_{n,l,m} - V(x)) - \frac{(2l+3/2)(2l+1/2)}{x^2}\right]X(x), \tag{2.12}$$

Following the method described in [72,73] [3], the equation is integrated inwards to minimize numerical errors, since the boundary condition $X(x \to \infty) = 0$, must be satisfied. Starting at an outer point $r_{\mathrm{max}} = 2n(n+15)a_0$ and finalizing the integration at $r_{\mathrm{min}} = 5 \times 10^{-3}a_0$.

The importance of knowing the radial wavefunctions lies in the need to compute the dipole matrix elements. These are necessary to calculate the main properties of the Rydberg states that govern their properties, and interactions with external

[2]We found that quantum defect theory is not accurate to predict the energies for states, nP, with $n \leq 10$, in order to get more accurate results calculations for the dipole matrix elements calculations, the energies for these states were taken from [71].

[3]Zimmerman *et al.* used a logarithmic scaling $x = \log(r)$, $X(x) = R_{n,l,m}\sqrt{r}$, Pritchard [63] found that the square root scaling leads to a smaller numerical error for large n states.

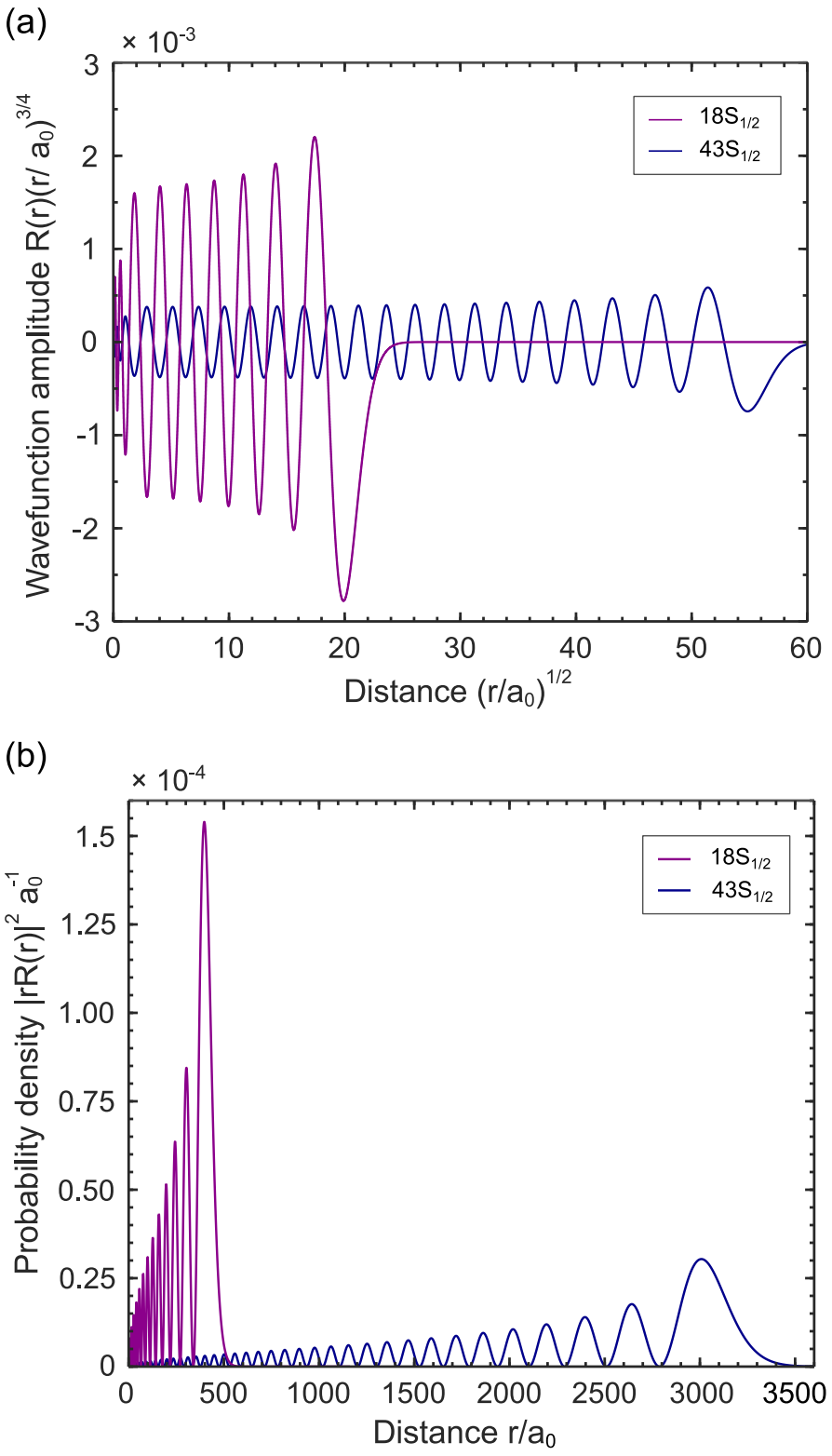

Figure 2.1: **Numerical results for the radial wavefunction and the probability density of $18S_{1/2}$ and $43S_{1/2}$ Rydberg states.** (a) Radial wavefunction amplitude for $18S_{1/2}$ and $43S_{1/2}$. (b) Probability density for $18S_{1/2}$ and $43S_{1/2}$. Note that $\langle r \rangle$ is $331a_0$ and $2384a_0$ for $18S_{1/2}$ and $43S_{1/2}$, respectively.

fields and other atoms, such as, lifetimes, polarizabilities, and Van der Waals coefficients.

Since the hyperfine splitting is negligible, we choose the fine basis, n, l, j, m_j to compute the dipole matrix elements $\langle n', l', j', m'_j | \hat{d}^1_q | n, l, j, m_j \rangle$. Here the dipole operator $\hat{d}_q = e\hat{r}^1_q$ is a tensor operator of rank 1, and it is defined in the spherical basis [74], where $q \in \{-1, 0, 1\}$:

$$\begin{aligned} \hat{d}^1_{-1} &= \sqrt{\frac{4\pi}{3}} \hat{d} Y^1_{-1}(\theta, \phi) = \frac{1}{\sqrt{2}} (\hat{d}_x - i\hat{d}_y) \\ \hat{d}^1_0 &= \sqrt{\frac{4\pi}{3}} \hat{d} Y^1_0(\theta, \phi) = \hat{d}_z, \\ \hat{d}^1_1 &= \sqrt{\frac{4\pi}{3}} \hat{d} Y^1_1(\theta, \phi) = -\frac{1}{\sqrt{2}} (\hat{d}_x + i\hat{d}_y), \end{aligned} \tag{2.13}$$

The Wigner Eckart theorem allows us to break down the dipole matrix elements as a product of two components: the first one contains information about the geometry of the system imposed by the rotational symmetries; and the second one is the reduced matrix element $\langle n', l', j' || \hat{d} || n, l, j \rangle$,

$$\langle n', l', j', m'_j | \hat{d}^1_q | n, l, j, m_j \rangle = (-1)^{j' - m'_j} \begin{pmatrix} j' & 1 & j \\ -m'_j & q & m_j \end{pmatrix} \langle n', l', j' || \hat{d} || n, l, j \rangle \,, \tag{2.14}$$

where the parentheses indicate the Wigner-3j symbol. This symbol vanishes unless the selection rules are satisfied, $j' - j = 0, \pm 1$ and $q = mj' - m_j$. Meanwhile, the reduced matrix element is independent of the projection of the angular momentum

and is given by [74],

$$\langle n', l', j' || \hat{d} || n, l, j \rangle = (-1)^{j+3/2+l_>} \sqrt{l_>(2j'+1)(2j+1)} \times \begin{Bmatrix} l' & 1 & l \\ j & 1/2 & j' \end{Bmatrix} \langle n', l', j' | \hat{d} | n, l, j \rangle \,, \tag{2.15}$$

where $l_>$ is the larger of l' and l, and the braces indicate the Wigner-6j symbol that obeys the selection rules $j'-j = 0, \pm 1$, and $l'-l = \pm 1$, . Here, $\langle n, l, j | \hat{d} | n', l', j' \rangle$ is the expectation value of the radial scalar part of the dipole operator, and depends only on the radial wavefunctions of the two states:

$$\langle n', l', j' | \hat{d} | n, l, j \rangle = \int_0^\infty r^2 \, \mathrm{d}r R^*_{n',l',j'}(r) \hat{d} R_{n,l,j}(r) \tag{2.16}$$

The following sections describe some of the relevant properties of Rydberg atoms and show the calculated values for some nS-Rydberg states. These values are obtained from the dipole matrix elements after solving numerically Eq. (2.12).

2.1.3 Rydberg states lifetimes

Any atom in an excited state experiences a decay to other energy states. For Rydberg states, n, l, j, this decay depends on two different processes: spontaneous emission and induced transitions due to black-body radiation.

The process of spontaneous emission originates from the coupling to vacuum fluctuations, which leads an excited state to decay to lower energetic states. The radiative transition rate between two states, $|i\rangle$, and, $|f\rangle$, is determined by Fermi's golden rule,

$$\Gamma_{i\to f} = \frac{3\alpha\omega_{if}^3}{4c^2} \left|\langle f| \hat{r} |i\rangle\right|^2, \tag{2.17}$$

where, $\frac{3\alpha\omega^3}{4c^2}$ is the radiation field density of states in free-space, $\langle f| \hat{r} |i\rangle$ is the dipole matrix element, and $\hbar\omega = (E_f - E_i)$ is the energy difference between the final and initial state. Using the Wigner Ekart theorem and applying the normalization of $3j$-symbols [74], each transition rate in the fine structure basis is given by,

$$\Gamma_{n'l'j'\to nlj} = \frac{3\alpha\omega_{if}^3}{4c^2} \frac{\left|\langle n', l', j'||\hat{d}||n, l, j\rangle\right|^2}{2J'+1}. \tag{2.18}$$

Here, the factor $2J'+1$ takes into account the degeneracy of the final state. The total spontaneous decay is obtained by carrying the sum over all dipole allowed transitions,

$$\Gamma_{\text{SPD}} = \sum_{n'l'j', n'\leq n} \Gamma_{nlj\to n'l'j'}, \tag{2.19}$$

As a result of the close spacing of nearby Rydberg eigenenergies, the interaction with black-body radiation at room temperature is not negligible. The black body radiation at temperature T induce transitions to lower (higher) neighboring states due to stimulated emission (absorption). The contribution to the black-body decay rate depends on the number of black body photons $N(\omega)$ per mode at T,

$$\Gamma_{\text{BBR}} = \sum_{n'l'j'} \frac{\Gamma_{nlj\to n'l'j'}}{e^{\hbar\omega k_B T} - 1}. \tag{2.20}$$

Following the derivation from Ref. [38], Eq. (2.20) can be approximated as:

$$\Gamma_{\text{BBR}} = \frac{4\alpha^3 k_B T}{3\hbar n^{*2}}. \tag{2.21}$$

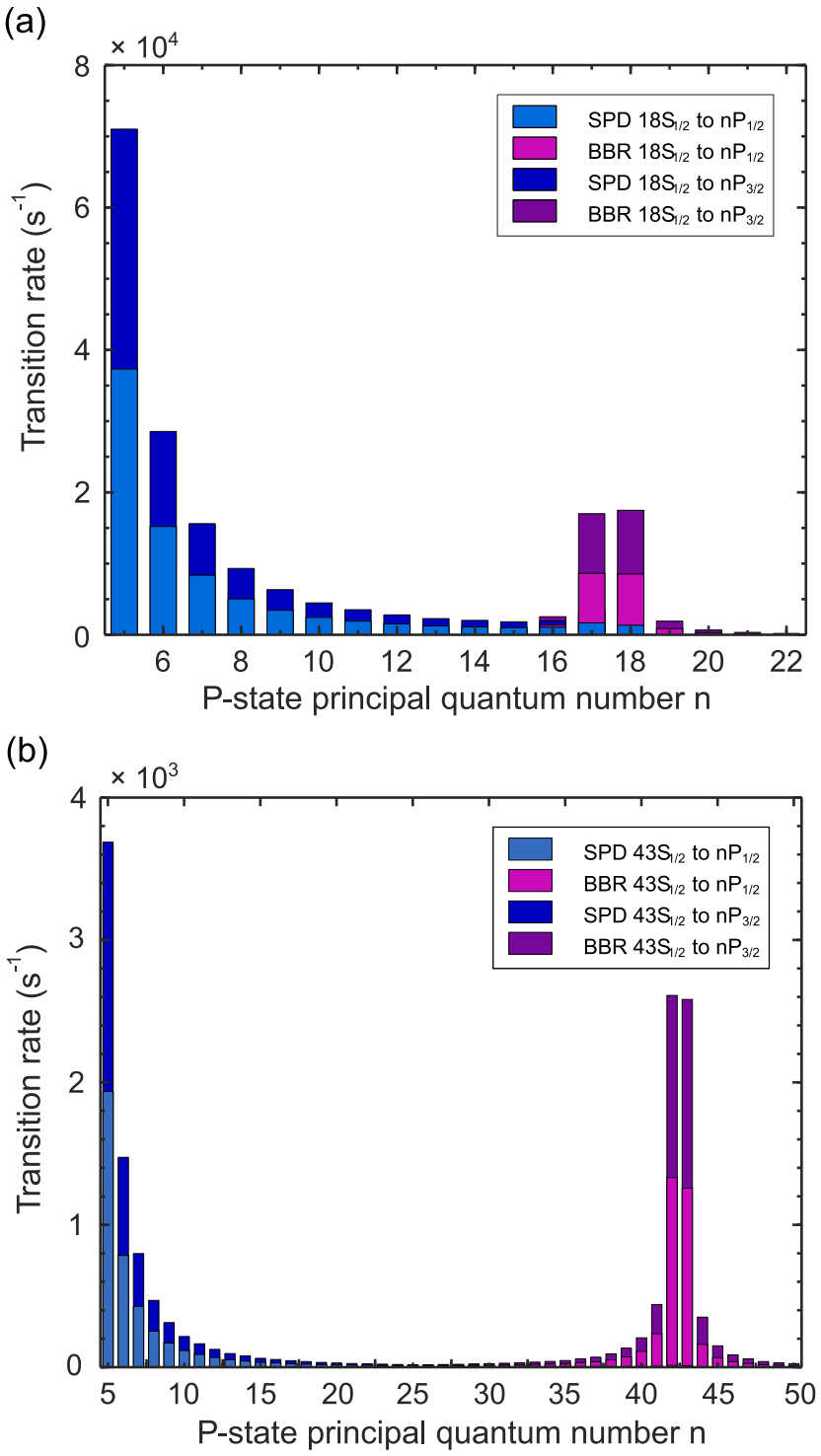

Figure 2.2: **Histogram of decay channels transition rates for Rydberg states $18S_{1/2}$ and $43S_{1/2}$.** The blue bars correspond to transitions due to spontaneous decay, whereas the magenta bars correspond to black-body induced transitions. (a) Decay rates for $18S_{1/2}$ with a calculated linewidth of 48.5 kHz and a lifetime of $\tau = 3.28\mu s$ at $T = 300K$, where black body radiation accounts for about 20% of the decay rate. (b) Decay rates for $43S_{1/2}$ with a calculated linewidth of 3.75 kHz and a lifetime $\tau = 42.48\mu s$ at $T = 300K$, where black body radiation accounts for about 48% of the decay rate.

The total lifetime for a given Rydberg state, including the contributions for both spontaneous emission and black-body radiation (BBR) is,

$$\tau = \tau_{\text{SPD}} + \tau_{\text{BBR}} = \frac{1}{\Gamma_{\text{SPD}}} + \frac{1}{\Gamma_{\text{BBR}}}. \tag{2.22}$$

Figure 2.2 shows that the spontaneous emission rate is dominated by transitions with the highest energy difference, in particular from the nS Rydberg states to the $5P$ states. From Eq. (2.18) these contributions scale as $\sim (n^*)^{-3}$, since the dipole matrix element $\langle 5P||\hat{d}||nS\rangle$ goes as $(n^*)^{-1.5}$. In contrast, spontaneous emission to nearby states has a minor contribution as it scales as $(n^*)^{-5}$, this scaling arises from the energy of neighboring states $\omega \propto (n^*)^{-3}$, while the dipole matrix elements $\propto (n^*)^2$. It is also evident that as n^* increases, the black-body transitions to neighboring states increase as well, due to the large coupling strengths and the thermal distribution of the BBR.

2.1.4 Static Polarizability

The atom eigenenergies get split and shifted in the presence of an external electric field, an effect known as the Stark effect. First, let us consider an applied field E oriented along the z-axis, the total Hamiltonian can be written as:

$$\hat{H} = \hat{H}_0 - E\hat{d}_z. \tag{2.23}$$

For the case that the field is small, such that the Stark shift is smaller than the bare eigenenergies separations, the energy shift ΔE can be calculated by means of perturbation theory. Due to the odd-parity operator $\hat{z}$, the first-order correc-

tion vanishes. Using the spherical basis defined in Eq. (2.13), the second-order correction is

$$\begin{aligned}\Delta E &= \sum_{n',l',j',mj'} \frac{\left|\left\langle n',l',j',m'_j\right|\hat{d}^1_0\left|n,l,j,m_j\right\rangle\right|^2}{E_{n',l',j',mj'} - E_{n,l,j,m_j}} E^2 \\ &= -\frac{1}{2}\alpha E^2,\end{aligned} \tag{2.24}$$

where α is the polarizability of the state $|n,l,j,m_j\rangle$, and the sum is over all dipole allowed transitions. The largest contributions to the polarizability come from the nearby states since the energy difference is the smallest, and the overlap of the wavefunctions is the largest. Thus, the scaling for the static polarizability to a good approximation goes as $(n^*)^7$. Rydberg states with large principal quantum number are very sensitive to electric fields. Table 2.2 shows the polarizability values for some $nS_{1/2}$ Rydberg states.

State	Calculated	Quoted value	Ref.
$43S_{1/2}$	17.3	17.7	[75]
$60S_{1/2}$	172.9	171.1	[76]
$80S_{1/2}$	1306	1340	[76]

Table 2.2: **Polarizabilty values for different Rydberg states.** Calculated polarizability values compared to the ones found in the literature. Units for polarizability are MHz/(V/cm)^2.

Second-order perturbation theory, as used in Eq. (2.24), is suitable to calculate the polarizability. However, if the field cannot be treated in a perturbative manner, it is necessary to diagonalize the full Hamiltonian $\hat{H}_0 + E\hat{z}$ to find the new eigenenergies and eigenstates.

2.1.5 Summary of Rydberg properties scaling

Table 2.3 provides a summary of the scaling of Rydberg state properties with the effective quantum number n^*. It also shows a comparison between the ground state $5S_{1/2}$ properties [75], and the calculated values of $43S_{1/2}$ used with the Numerov method.

Property	Scaling	Rb $5S_{1/2}$	Rb $43S_{1/2}$
Binding energy E_{n^*}	$(n^*)^{-2}$	4.18 eV	8.56 meV
Level spacing $E_{n^*} - E_{n^*-1}$	$(n^*)^{-3}$	6.05×10^5 GHz (5S-6S)	100.07 GHz (43S-44S)
Orbit radius $\langle r \rangle$	$(n^*)^2$	5.632 a_0	2384 a_0
Polarizability α	$(n^*)^7$	79.4 mHz/(V/cm)^2	17.3 MHz/(V/cm)^2
Lifetime τ	$(n^*)^3$	$5P_{3/2} - 5S_{1/2}$: 26.2 ns	42.5 μs at 300 K
Dipole moment $\langle 5P_{3/2}\vert\, \hat{d}\, \vert nS_{1/2}\rangle$	$(n^*)^{-3/2}$	4.227 ea_0	0.0101 ea_0
Van der Waals coefficient C_6	$(n^*)^{11}$	6.76×10^{-7} Hzμm^6	2.02×10^9 Hzμm^6

Table 2.3: **Summary of Rydberg properties scaling.** Comparison of the $5S_{1/2}$ ground state and the $43S_{1/2}$ Rydberg state.

2.2 Rydberg interactions

Due to their large dipole moment $\propto n^{*2}a_0$, Rydberg atoms interact strongly by the dipole-dipole interaction. Assuming that two atoms labeled by A and B with dipoles $\hat{\mathbf{d}}_A$, $\hat{\mathbf{d}}_B$, are far enough so their wavefunction does not overlap, the interaction potential is

$$\hat{V}_{dd} = \frac{1}{4\pi\epsilon_0}\frac{\hat{\mathbf{d}}_A \cdot \hat{\mathbf{d}}_B - 3(\hat{\mathbf{d}}_A \cdot \hat{\mathbf{R}})(\hat{\mathbf{d}}_B \cdot \hat{\mathbf{R}})}{R^3}. \tag{2.25}$$

Let us consider that both dipoles are aligned along the quantization axis z, then Eq. (2.25) simplifies to:

$$\hat{V}_{dd} = \frac{1}{4\pi\epsilon_0}\frac{\hat{d}_{A,x}\hat{d}_{B,x} + \hat{d}_{A,y}\hat{d}_{B,y} - 2\hat{d}_{A,z}\hat{d}_{B,z}}{R^3}. \tag{2.26}$$

Changing Eq. (2.26) into the spherical basis defined in Eq. (2.13):

$$\hat{V}_{dd} = -\frac{1}{4\pi\epsilon_0}\frac{\hat{d}_{A,1}\hat{d}_{B,-1} + \hat{d}_{A,-1}\hat{d}_{B,1} + 2\hat{d}_{A,0}\hat{d}_{B,0}}{R^3}, \tag{2.27}$$

Since we are interested in the long-range interactions, we make the case that the dipoles are far enough that the interaction is smaller than the eigenenergies of the states A and B. Under this circumstance, the shift ΔE_{dd} of the bare atomic pair state can be calculated with perturbation theory. Otherwise, at short distances, the dipole-dipole interaction mixes the eigenstates, and the total Hamiltonian, $H = \hat{H}_0 + \hat{V}_{dd}$ needs to be diagonalized.

The second-order correction to the energy shift using perturbation theory [77] is given by,

$$\begin{aligned}
\Delta E_{dd} &= \sum_{ij} \frac{\left|\langle\psi_A\psi_B|\,\hat{V}_{dd}\,|\psi_i\psi_j\rangle\right|^2}{E_A + E_B - E_i - E_j} \\
&= \frac{1}{9\epsilon_0^2 R^6}\sum_{i,j}\frac{\left|\langle\psi_A\psi_B|\,\hat{d}^2\,|\psi_i\psi_j\rangle\right|^2}{\delta_{ABij}} D_{(i,j)}(\theta,\phi) \\
&= \frac{1}{R^6}\sum_{\nu=(i,j)} C_6^\nu D_\nu(\theta,\phi) \\
&= \frac{1}{R^6} C_6(\theta,\phi),
\end{aligned} \tag{2.28}$$

where, E_i are the unperturbed eigenenergies, $\delta_{ABij} = E_A + E_B - E_i - E_j$ is called the Förster defect, and $D_\nu(\theta,\phi)$ consists of the angular couplings that follow the selection rules, while C_6^ν contains the radial integrals between the coupled states and is independent of the angular projections m_j. Here, the pair state of $\psi_A = |n,l,j,m_j\rangle_A$ and $\psi_B\,|n,l,j,m_j\rangle_B$, is coupled to a set of virtual intermediate states $\psi_i = \left|n',l',j',m_j'\right\rangle$ and $\psi_j = \left|n'',l'',j'',m_j''\right\rangle$, these interaction channels

are indicated by ν. The Van der Waals coefficient $C_6(\theta, \phi)$ is the sum of the interactions from all the possible channels with $|\psi_A \psi_B\rangle$.

In particular for a $nS_{1/2}nS_{1/2}$ pair state, the possible interaction channels are: $nS_{1/2}nS_{1/2} \rightarrow n'P_{1/2}n''P_{1/2}$, $nS_{1/2}nS_{1/2} \rightarrow n'P_{1/2}n''P_{3/2}$ and $nS_{1/2}nS_{1/2} \rightarrow n'P_{3/2}n''P_{3/2}$. Furthermore for $nS_{1/2}$-pair states the dipole-dipole interaction is nearly isotropic and the angular dependence can be neglected [63], thus we can write the van der Waals shift as,

$$\Delta E_{dd} = \frac{C_6}{R^6} \tag{2.29}$$

The Van der Waals coefficient is a measure of the strength of the interaction, and it increases dramatically with n^*. From Eq. (2.28) the numerator scales as $(n^*)^8$, while the energy difference in the numerator goes as $(n^*)^{-3}$, which yields $C_6 \propto (n^*)^{11}$. Table 2.4 shows the C_6 coefficients for some $nS_{1/2}$ states, where is evident the rapid growth with the principal quantum number.

State	Calculated	Quoted value	Ref.
$43s_{1/2}$	2.53	2.44	[75]
$60s_{1/2}$	139.3	137.5	[78]
$70s_{1/2}$	853.7	815	[79]
$100s_{1/2}$	5334	5600	[80]

Table 2.4: **Van der Waals coefficient values for different $nS_{1/2}$.** Calculated values using Eq. (2.28) are compared to the ones found in the literature. Units are GHz μm^6.

2.2.1 Dipole Blockade Effect

This section focuses on the effects arising from the long-range dipole-dipole interactions. The energy shift for a pair state depends on their relative distance

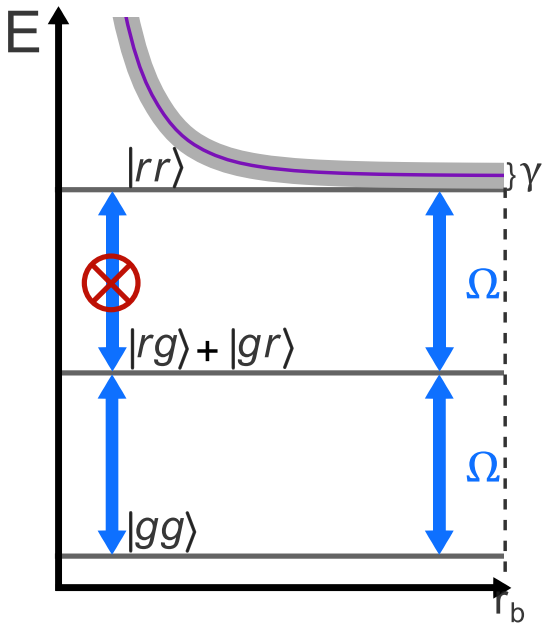

Figure 2.3: **Dipole-induced shift as a function of the relative distance between two atoms.** In the case R is large such that $\Delta E_{dd} \approx 0$, the two atoms can be excited $|gg\rangle \rightarrow |rr\rangle$. If the distance is shorter than the blockade radius (indicated with the gray dashed line), the interaction energy tunes out of resonance the doubly-excited state $|rr\rangle$.

R, as demonstrated in Eqs. (2.29). If the atoms are far away from each other, such that $\Delta E_{dd} \rightarrow 0$, the atom-pair is resonantly excited from the ground state $|gg\rangle$ to the doubly-excited state $|rr\rangle$ with a coupling strength Ω. However, as the atoms get closer together this shift increases and tunes the double excitation out of resonance [40,61]. This effect is known as the dipole blockade and is illustrated in Figure 2.3 for a pair state. The characteristic length of the interaction is determined by the Rydberg blockade radius r_b, and it depends on the energy scale of the system (See next chapter for details). In particular, for the weakly excited limit where the coupling strength Ω is less than the linewidth of the excitation process γ, the blockade radius is

$$r_b = \left(\frac{2|C_6|}{\gamma}\right)^{1/6}. \tag{2.30}$$

The blockade radius scales as $\propto (n^*)^{11/6}$ for a fixed excitation linewidth. The blockade radius for high principal quantum numbers can reach up to tens of microns with typical alkali atom linewidths.

2.2.2 Superatom: Rydberg blockade and collective excitation

The pair-excitation blockade effect [81–83], can be extended to an ensemble of N-atoms where only one excitation is allowed within the blockaded volume [44–46, 84–86]. Assuming all the ground-state atoms can be coupled equally to the Rydberg state, the single excitation shared among the N atoms inside the blockaded volume can be written as a symmetric Dicke state [62],

$$|S\rangle = \frac{1}{\sqrt{N}} \sum_{j=1}^{N} e^{ik_c x_j} \, |g_1, g_2 \ldots g_{j-1}, r_j, g_{j+1} \ldots g_{N-1}, g_N\rangle \,, \tag{2.31}$$

where k_c is the wavevector of the coupling field and x_j is the position of the j-th atom. The quantum state in Eq. (2.31) is a superposition of all collective states $|g_1, \ldots r_j, \ldots, g_N\rangle$, where the j-th atom is in the Rydberg state while the others are in the ground state.

Because of the blockade effect, the N atoms can be described as a two-level super atom, with a ground state $|G\rangle = |g_1, \ldots g_N\rangle$ and excited state $|S\rangle$. Moreover, the coupling between these two levels exhibits a $\sqrt{N}$ enhancement:

$$\begin{aligned} \langle G|\hat{d}|S\rangle &= \frac{1}{\sqrt{N}} \sum_{j=1}^{N} \langle g_j|\hat{d}|r_j\rangle \, \langle g_1, \ldots g_{j-1}, g_{j+1}, \ldots g_n|g_1, \ldots g_{j-1}, g_{j+1}, \ldots g_n\rangle \\ &= \sqrt{N} \, \langle g|\hat{d}|r\rangle \,. \end{aligned}$$

The strong long-range interaction of Rydberg states and the collective nature of the superatom provide a system where nonlinearities at the single-photon level are strong. Here, due to the blockade effect, a single photon can saturate the absorption of the atomic medium, while the shared collective excitation enhances the coupling to the field by $\sqrt{N}$.

These qualities make the superatom a powerful tool for different quantum applications, and it constitutes one of the main pillars of this thesis. For instance, this coupling can be used to realize a single-photon source [45, 62], which we discuss extensively in Chapter 6 and in Ref. [58]. Other relevant applications are single-photon transistors [48–50], collective qubits [51, 87, 88], quantum phase gates [49,51], and is thus a promising platform for quantum networking [59,89–92].

2.2.2.1 Single-photon retrieval

Figure 2.4(a) shows the creation of a super atom using a two-photon excitation to the Rydberg state. Here, the phase matching condition is crucial to retrieve the super atom spin wave into a single photon in a well-defined mode. For writing the spin wave where a photon is stored as a collective excitation in the state $|S, 0\rangle$, the initial phase imprinted by the two-excitation lasers is:

$$|S,0\rangle = \frac{1}{\sqrt{N}} \sum_{j=1}^{N} e^{i(\vec{k}_1+\vec{k}_w)\cdot\vec{x}_j} \left|g_1, g_2 \ldots g_{j-1}, r_j, g_{j+1} \ldots g_{N-1}, g_N\right\rangle \otimes |0\rangle \,, \qquad (2.32)$$

where $\vec{k}_1$, $\vec{k}_w$ are the wave vectors of the excitation lasers, then the spin wave vector is given by $\vec{k}_s = \vec{k}_1 + \vec{k}_w$. To retrieve the spin wave as a single photon, we drive the Rydberg state to the intermediate state with a field having a wave

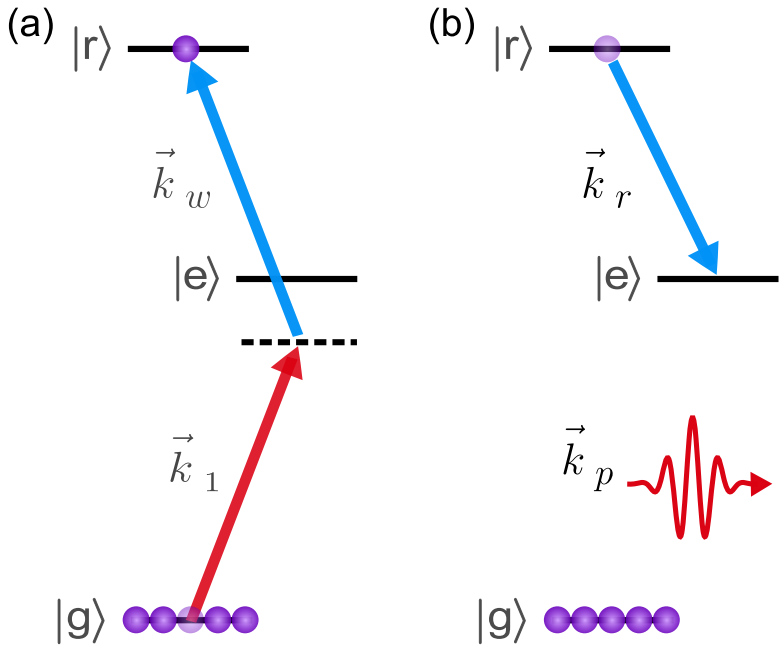

Figure 2.4: **Retrieving a super atom spin wave as a single photon..** (a) Writing the spin wave with two excitation fields having wave vectors $\vec{k}_1$ and $\vec{k}_w$. After a *pi*-pulse the blockade effect allows for a single spin wave excitation in the Rydberg state. (b) A retrieving field with wave vector $\vec{k}_r$ maps the stored excitation into a single photon.

vector $\vec{k}_r$ (Fig. 2.4(b)), which results in the state

$$|G, \mathcal{E}\rangle = \frac{1}{\sqrt{N}} \sum_{j=1}^{N} e^{i(\vec{k}_s - \vec{k}_r)\cdot\vec{x}_j} |g_1, g_2 \ldots g_{j-1}, g_j, g_{j+1} \ldots g_{N-1}, g_N\rangle \otimes |1\rangle \,. \tag{2.33}$$

The probability of emitting a photon $|1\rangle$ with a wave vector $\vec{k}_p$ is proportional to

$$P_1 \propto \frac{1}{N} \Big| \sum_{j=1}^{N} e^{i(\vec{k}_s - \vec{k}_r - \vec{k}_p)\cdot\vec{x}_j} \Big|^2, \tag{2.34}$$

this probability is maximized when the phase matching condition is satisfied:

$$\vec{k}_s - \vec{k}_r - \vec{k}_p = \vec{k}_1 + \vec{k}_w - \vec{k}_r - \vec{k}_p = 0, \tag{2.35}$$

thus, all the terms in Eq. (2.33) interfere constructively. For the case where $\vec{k}_w = \vec{k}_r$, then $\vec{k}_1 = \vec{k}_p$, the retrieved photon is in the same forward propagating mode as the input excitation laser. Although, backward retrieval where the photon propagates in the opposite direction as the input field (by setting the proper propagation direction of $\vec{k}_w$ and $\vec{k}_r$), can lead to a higher directional emission probability due to decreased re-absorption from the atoms [93].

Another important consideration is the number of atoms participating in the collective excitation. The addition of the phase terms in Eq. (2.33) during the constructive interference into a well-defined mode is more effectively enhanced with a larger number of atoms [93].

There are factors that can reduce the photon retrieval like dephasing mechanisms, for example, atomic motion, atom loss, decay of the Rydberg state into other state, or that the ground state and Rydberg state acquire different phase shifts due to light shifts from the trapping light.

Chapter 3: Rydberg-EIT Polaritons

Electromagnetically induced transparency (EIT) is a an interference phenomena that occurs in atomic physics when different transitions pathways in a multilevel system interfere with each other [12]. This effect can drastically change the dispersive and dissipative optical properties of a medium. For instance, the interference results in a transparency window combined with a steep dispersion around the resonance frequency of a transition.

First, we discuss EIT for a classical and a quantized electromagnetic fields in an atomic ensemble. For both cases, the input field can experience an absorption-free propagation with a reduced group velocity through the medium. For the quantum field, quasi-particles, called dark-state polaritons arise as the field couples with a collective spin-excitation [94]. The analysis and derivation for a classical and a quantum field presented in this Chapter are based on the References [12, 94, 95].

Later, we analyze Rydberg atoms and their interactions in the presence of EIT, where Rydberg-dark-state polaritons are described as bosonic fields that are a coherent superposition of a quantum photonic field and a collective Rydberg-state excitation. By changing different parameters of the system, we are able to control and tailor the dissipative or coherent attributes of Rydberg-polariton interactions.

The goal of this chapter is to introduce the theoretical framework needed to

describe the scattering processes that arise due to the few-body Rydberg-EIT interactions derived in Reference [96].

3.1 EIT features

Let us consider an ensemble of three-level atoms in a ladder configuration, where $|g\rangle$ is the ground state, $|e\rangle$, is a state with decay rate, Γ, and, $|r\rangle$, is a long-lived state with decay rate, γ, as shown in Figure 3.1. Suppose the atom is driven by two monochromatic electromagnetic fields a weak probe field and a control field. The probe is a weak field tuned close to resonance of, $|g\rangle \rightarrow |e\rangle$ with a frequency ω_p, a detuning Δ_p, and a Rabi frequency Ω_p; while the control field couples the states, $|e\rangle \rightarrow |r\rangle$, with a frequency ω_c, a detuning Δ_c, and Rabi frequency Ω_c.

The Hamiltonian of the bare atom (without the kinetic energy term) and the dipole interaction under the rotating wave approximation is given by,

$$H = \frac{\hbar}{2} \begin{pmatrix} 0 & \Omega_p^* & 0 \\ \Omega_p & -2\Delta_p & \Omega_c^* \\ 0 & \Omega_c & -2\delta \end{pmatrix} \tag{3.1}$$

where $\delta = \Delta_p + \Delta_c$ is the two-photon detuning. For the case of single- and two-

photon resonance $\Delta_p = 0, \delta = 0$, the Hamiltonian (3.1) has the eigenstates [12]:

$$|D\rangle = \cos\theta\,|g\rangle - \sin\theta\,|r\rangle\,, \tag{3.2}$$

$$|+\rangle = \frac{1}{\sqrt{2}}\left(\sin\theta\,|g\rangle + |e\rangle + \cos\theta\,|r\rangle\right), \tag{3.3}$$

$$|-\rangle = \frac{1}{\sqrt{2}}\left(\sin\theta\,|g\rangle - |e\rangle + \cos\theta\,|r\rangle\right), \tag{3.4}$$

with eigenenergies:

$$\begin{aligned} \hbar\omega_D &= 0, \\ \hbar\omega_\pm &= \pm\frac{\hbar}{2}\sqrt{\Omega_c^2 + \Omega_p^2}, \end{aligned} \tag{3.5}$$

where θ is the mixing angle,

$$\cos\theta = \frac{\Omega_c}{\sqrt{\Omega_c^2 + \Omega_p^2}}, \quad \sin\theta = \frac{\Omega_p}{\sqrt{\Omega_c^2 + \Omega_p^2}}.$$

The first eigenstate has no contribution from the short-lived state $|e\rangle$ and has a zero eigenenergy. Since this state is a superposition of the ground and the long-lived state only, it can not absorb or scatter light from the probe field, $|D\rangle$ is known as a dark state. On the other hand, the other two states $|\pm\rangle$ have an $|e\rangle$ component and are called bright states.

This dressed-state basis provides another picture to explain the EIT effect. In the case $\Delta_p = 0$ and $\Omega_p \ll \Omega_c$, the dark state is approximately the ground state $|D\rangle \approx |g\rangle$; the bright states $|\pm\rangle = (|r\rangle \pm |e\rangle)/\sqrt{2}$ have an equal energy shift but with opposite sign, and acquire a π-phase shift with respect to each other. The phase shift causes destructive interference between these two decay

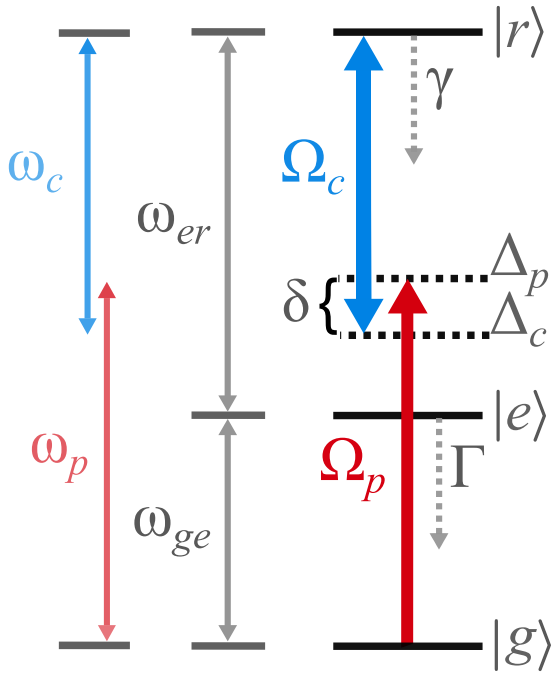

Figure 3.1: **Three level ladder system for EIT.** Relevant states are the ground state $|g\rangle$, excited state $|e\rangle$ with decay rate Γ, and the metastable state $|r\rangle$ with decay rate γ. The resonant frequency transition for $|g\rangle \rightarrow |e\rangle$ is denoted by ω_{ge} and the frequency transition for $|e\rangle \rightarrow |r\rangle$ is denoted by ω_{er}. The weak probe field with frequency, ω_p, couples $|g\rangle \rightarrow |e\rangle$ with a detuning $\Delta_p = \omega_p - \omega_{ge}$. A strong control field with frequency, ω_c, drives the atomic states, $|e\rangle \rightarrow |r\rangle$ with a detuning $\Delta_c = \omega_c - \omega_{er}$.

channels preventing the absorption of the probe light, making the atomic system transparent.

It is convenient to use the density matrix ρ, for a comprehensive and general description that takes into account the effects of dissipation and decoherence processes. We use the master equation formalism to compute the non-unitary dynamics of the system:

$$\dot{\rho} = -\frac{i}{\hbar}[\hat{H}, \rho] + \mathcal{L}[\rho], \tag{3.6}$$

where $\mathcal{L}$ is the Lindbland operator:

$$\mathcal{L} = \sum_n \left(C_n \rho C_n^\dagger - \frac{1}{2}\{\rho, C_n^\dagger C_n\} \right). \tag{3.7}$$

Here the sum is carried out for all possible decay channels. For a particular decay channel from $|i\rangle$ to $|j\rangle$, the jump operator is given by, $C = \sqrt{\gamma_{ij}}\,|j\rangle\langle i|$. Using Eqs. (3.6)-(3.7), we get the coupled differential equations for the density matrix elements:

$$\dot{\rho}_{gg} = \Gamma\rho_{ee} + \frac{i}{2}\left(\Omega_p\rho_{eg} - \Omega_p^*\rho_{ge}\right), \tag{3.8}$$

$$\dot{\rho}_{ee} = -\Gamma\rho_{ee} + \gamma\rho_{rr} + \frac{i}{2}\left(\Omega_p^*\rho_{eg} - \Omega_p\rho_{ge} + \Omega_c\rho_{re} - \Omega_c^*\rho_{er}\right), \tag{3.9}$$

$$\dot{\rho}_{rr} = -\gamma\rho_{rr} + \frac{i}{2}\left(\Omega_c^*\rho_{re} - \Omega_c\rho_{er}\right), \tag{3.10}$$

$$\dot{\rho}_{ge} = -\frac{1}{2}\left(\Gamma + 2i\Delta_p\right)\rho_{ge} + \frac{i}{2}\left[\Omega_p^*\left(\rho_{gg} - \rho_{ee}\right) + \Omega_c\rho_{gr}\right], \tag{3.11}$$

$$\dot{\rho}_{gr} = -\frac{1}{2}\left(\gamma + 2i\delta\right)\rho_{gr} + \frac{i}{2}\left(\Omega_c^*\rho_{ge} - \Omega_p^*\rho_{er}\right), \tag{3.12}$$

$$\dot{\rho}_{er} = -\frac{1}{2}\left[\Gamma + \gamma + 2i\Delta_c\right]\rho_{er} + \frac{i}{2}\left[\Omega_c^*\left(\rho_{rr} - \rho_{ee}\right) - \Omega_p\rho_{gr}\right]. \tag{3.13}$$

Solving Eqs. (3.11)-(3.13) in the weak probe limit $\Omega_p \ll \Omega_c$, and asssuming that most of the atomic population is in the ground state $\rho_{gg} \approx 1$, we obtain the steady-state solution to the excited state and ground state coherence,

$$\rho_{eg} = -\frac{i\Omega_p\left(\gamma - 2i\delta\right)}{(\Gamma - 2i\Delta_p)(\gamma - 2i\delta) + |\Omega_c|^2}.$$

The coherence element ρ_{eg} along with the dipole moment $d_{eg} = \langle e|d|g\rangle$ are related to the linear susceptibility of the medium at the probe frequency $\chi(\omega_p)$,

$$\chi(\omega_p) = \frac{2\varrho d_{eg}^2\rho_{eg}}{\hbar\epsilon_0\Omega_p}, \tag{3.14}$$

$$= \frac{\varrho\sigma_0}{k_p}\frac{i\Gamma\left(\gamma - 2i\delta\right)}{(\Gamma - 2i\Delta_p)(\gamma - 2i\delta) + |\Omega_c|^2}, \tag{3.15}$$

where ϱ is the atomic density of the sample, $k_p = 2\pi/\lambda_p$ is the probe angular wavenumber, and $\sigma_0 = \frac{2|d_{eg}|^2}{\hbar\epsilon_0\Gamma\lambda_p}$ is the absorption cross section for the transition $|g\rangle \rightarrow |e\rangle$. The susceptibility is related to the refractive index n, which determines the optical properties of the medium. This relation is given by $n = \sqrt{1+\chi} \approx 1 + \chi/2$, where this approximation is valid for $|\chi| \ll 1$.

After propagating through an atomic ensemble of length L assuming a constant density for simplicity, the relation between the output probe field and the input field is determined by n as,

$$\begin{aligned} \frac{E_{\text{out}}}{E_{\text{in}}} &= e^{ink_pL} \\ &= e^{-\text{Im}\{\chi\}k_pL/2} e^{i(1+\text{Re}\{\chi\}/2)k_pL}. \end{aligned} \tag{3.16}$$

The first term, which contains the imaginary part of χ, describes the attenuation from the absorption of the input field. The second term with the real part of χ takes into account the dispersion manifesting as a phase shift in the output field with respect to the input field. Figure 3.2 shows the transmission and phase shift in the presence and absence of the control field, illustrating the drastic changes in the optical properties arising from EIT.

Let us first analyze the case for a resonant-control field ($\Delta_c = 0$). The transmission at $\delta = 0$ changes from exponentially decreasing as a function of the optical depth OD$= \varrho\sigma_0 L$, with $T = e^{-\text{OD}}$ to (first-order in γ):

$$T = e^{-\frac{\text{OD}}{1+\Omega_c^2/\Gamma\gamma}}. \tag{3.17}$$

The medium becomes transparent for $\Omega_c^2/\Gamma\gamma \gg$ OD. Furthermore, the transmis-

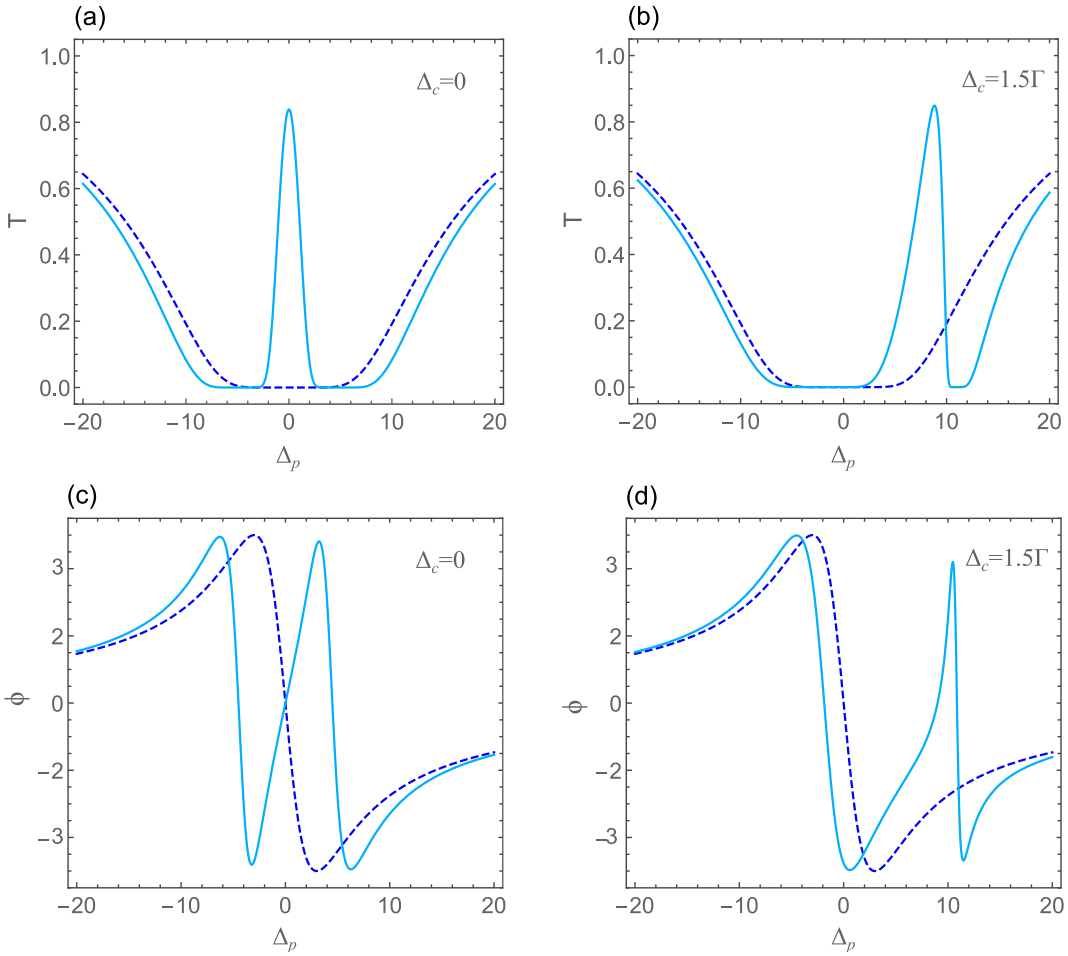

Figure 3.2: **Probe transmission and phase shift after propagating through medium of length L.** (a)-(b) Probe transmission spectra where $T = I_{\text{out}}/I_{\text{in}} = e^{-\text{Im}\{\chi\}k_p L}$ for $\Delta_c = 0$ and $\Delta_c = -1.5\Gamma$. (c)-(d) Acquired phase shift $\phi = \text{Re}\{\chi\}k_p L/2$ for $\Delta_c = 0$ and $\Delta_c = -1.5\Gamma$. The dark-blue dashed line corresponds to a two level atom susceptibility, ie, without control field; light-blue solid line shows when the control field is present. The parameters used are: $\Omega_c = 1.5\Gamma$, $\gamma = 0.02\Gamma$, and $OD = 20$.

sion window width $\Delta\omega$ as shown in Fig. 3.2a can be approximated as,

$$\Delta\omega = \frac{\Omega_c^2}{\sqrt{8\text{OD}\Gamma}}, \tag{3.18}$$

this width sets an upper-bound on the bandwidth of the input pulses. Pulses with $\Delta\tau \gg \Delta\omega^{-1}$ can propagate without absorption through the sample.

Another consequence arising from EIT is the change in the dispersion of the medium, as shown in Fig. 3.2c-(d). Around resonance $\Delta_p = 0, \delta = 0$, there is

a steep slope with opposite sign respect to the refractive index of the two-level system. The propagation velocity of the pulse inside the ensemble is related to the derivative of n as,

$$v_g = \frac{c}{1 + \omega_p \frac{dn}{d\omega}}. \tag{3.19}$$

If the derivative is large and positive, then the group velocity v_g is drastically reduced compared to the speed of light c. This effect is known as slow light. If $\gamma \ll \Gamma$, the group velocity in an EIT-medium is approximately,

$$v_g \approx \frac{L\Omega_c^2}{\mathrm{OD}\Gamma}. \tag{3.20}$$

The time that takes for the pulse to emerge from the sample corresponds to the time delay given by $\tau_d = L/v_g = \mathrm{OD}\Gamma/\Omega_c^2$.

The spatial extent of a pulse inside the medium is compressed by a factor of v_g/c. This compression arises because the front end of the pulse is traveling much slower than the back end that has not entered the sample. During this process, the atomic system takes most of the input pulse energy, with a fraction of v_g/c remaining as electromagnetic energy. This mechanism imposes another constraint for a loss-free propagation: the time delay needs to be much longer than the pulse width $\Delta\tau$

$$\frac{\tau_d}{\Delta\tau} \ll \sqrt{\mathrm{OD}}. \tag{3.21}$$

The more optically thick the sample is, the better the input pulse bandwidth fits into the finite EIT bandwidth, while at the same time compressing the pulse into

the medium. However, for a non-negligible γ, the loss is not minimized for an unbounded OD.

Similarly, for a control field detuned off-resonance with $\Delta_c > \Gamma$, the transmission and phase shift are different than the two-level case as shown in Fig. 3.2(b) and (d). The transmission reaches a maximum on two-photon resonance $\delta = 0$, followed by a narrow absorption dip at the two-photon Raman resonance with $\delta \approx \Omega_c^2/4\Delta_c$. As for the dispersion, the group velocity is also reduced with a steep phase difference around $\delta = 0$.

3.2 Dark-State Polaritons

We review in this section the EIT problem with a quantized probe field in an ensemble of atoms and generalize the concept of a dressed-dark state to a dark-state polariton (DSP). This polariton can be described as a form-stable quasi-particle composed of a coherent superposition of an electromagnetic field and an atomic excitation. For the mathematical description of the polariton picture, we use the methods in [94–96].

Let us start by describing the quantized probe field as a continuous-mode operator. In the paraxial approximation[1], a beam propagating along the z-axis with polarization $\mathbf{x}$ is given by,

$$\hat{\mathbf{E}}_p(z) = \mathbf{x}\sqrt{\frac{\hbar\omega_p}{4\pi c\epsilon_0 A}}e^{-i\omega_p(t-z/c)}\int \mathrm{d}\omega \hat{a}_\omega e^{i\omega z/c} + \text{c.c.}, \tag{3.22}$$

here, c.c stands for complex conjugate, A is the transversal area of the beam; $\hat{a}_\omega$ is the bosonic operator for modes of different frequencies around ω_p. This operator

[1] $|\mathbf{k}| \approx \mathbf{k_z} \approx \omega_\mathbf{p}/\mathbf{c}$ in the paraxial approximation

follows the commutation relation $[\hat{a}_\omega, \hat{a}^\dagger_{\omega'}] = \delta(\omega - \omega')$.

Additionally, we can define the control field (coupling $|e\rangle \to |r\rangle$) as a classical plane wave:

$$\mathbf{E}_c(z,t) = \mathbf{x}\mathcal{E}_c(t - z/c)\left(e^{-i\omega_c(t-z/c)} + e^{i\omega_c(t-z/c)}\right), \tag{3.23}$$

where $\mathcal{E}_c(t-z/c)$ is the real and slowly varying amplitude, and ω_c is its frequency.

The bare Hamiltonian $\hat{H}_0$ is

$$\begin{aligned}\hat{H}_0 =& \hat{H}_l + \hat{H}_a \\ =& \hbar\left[\int \mathrm{d}\omega\omega\hat{a}^\dagger_\omega\hat{a}_\omega + \sum_{j=1}^{N}\left(\omega_{ge}\hat{\sigma}^j_{ee} + \omega_{er}\hat{\sigma}^j_{rr}\right)\right],\end{aligned} \tag{3.24}$$

where N is the number of atoms in the ensemble, ω_{ge} is the transition frequency $|g\rangle \to |e\rangle$, ω_{er} is the transition frequency $|e\rangle \to |r\rangle$, and $\sigma^j_{mn} = |m\rangle\langle n|$ is the internal state operator between states $|m\rangle$ and $|n\rangle$ for the jth atom.

Using the dipole and the rotating-wave approximations, the interaction Hamiltonian,

$$\begin{aligned}\hat{V} =& -\sum_{j=1}^{N}\hat{\mathbf{d}}_i\cdot\left[\hat{\mathbf{E}}_p + \mathbf{E}_c\right], \\ =& -\frac{\hbar}{2}\sum_{j=1}^{N}\Big[g\sqrt{\frac{L}{2\pi c}}e^{-i\omega_p(t-z_j/c)}\int \mathrm{d}\omega\hat{a}_\omega e^{i\omega z_j/c}\hat{\sigma}^j_{eg} \\ &+ \Omega_c(t - z_i/c)e^{-i\omega_c(t-z_j/c)}\hat{\sigma}^j_{er} + \text{c.c.}\Big].\end{aligned} \tag{3.25}$$

Here, $\hat{\mathbf{d}}$ is the dipole operator, $\Omega_c = \langle e|\hat{\mathbf{d}}\cdot\mathbf{x}|r\rangle\,\mathcal{E}_c/\hbar$, and $g_0 = \langle e|\hat{\mathbf{d}}\cdot\mathbf{x}|g\rangle\sqrt{\frac{2\omega_p}{\hbar\epsilon_0 AL}}$ is the coupling constant between the atoms and the probe. We have assumed that the coupling is the same for all atoms and choose the length of the quantized volume to be the length of the sample.

We redefine the slowly varying atomic operators averaged in a cross section with thickness δz containing $N_z \gg 1$ atoms (to take into account the position dependence of the atoms along L), while being driven by the probe and control fields,

$$\begin{aligned}
\hat{\sigma}_{ii}(z,t) &= \frac{1}{N_z}\sum_{j=1}^{N_z}\sigma_{ii}^{j}(t), \\
\hat{\sigma}_{eg}(z,t) &= \frac{1}{N_z}\sum_{j=1}^{N_z}\sigma_{eg}^{j}(t)e^{-i\omega_p(t-z_j/c)}, \\
\hat{\sigma}_{er}(z,t) &= \frac{1}{N_z}\sum_{j=1}^{N_z}\sigma_{er}^{j}(t)e^{-i\omega_c(t-z_j/c)}, \\
\hat{\sigma}_{rg}(z,t) &= \frac{1}{N_z}\sum_{j=1}^{N_z}\sigma_{rg}^{j}(t)e^{-i(\omega_p-\omega_c)(t-z_j/c)}.
\end{aligned}$$

These atomic operators satisfy the commutation relations:

$$[\hat{\sigma}_{jk}(z,t),\hat{\sigma}_{lm}(z',t)] = \frac{1}{N_z}\left[\delta_{kl}\hat{\sigma}_{jm}(z,t) - \delta_{mj}\hat{\sigma}_{lk}(z,t)\right]\delta(z-z'). \tag{3.26}$$

Similarly, it is more convenient to redefine the probe field as the slowly varying operator,

$$\hat{\mathcal{E}}(z,t) = \sqrt{\frac{L}{2\pi c}}\int \hat{a}_{\omega}(t)e^{i\omega z/c}\mathrm{d}\omega, \tag{3.27}$$

which follows the commutation relations:

$$\left[\hat{\mathcal{E}}(z,t),\hat{\mathcal{E}}^{\dagger}(z',t)\right] = L\delta(z-z'), \qquad \left[\hat{\mathcal{E}}(z,t),\hat{\mathcal{E}}^{\dagger}(z,t')\right] = \frac{L}{c}\delta(z-z'). \tag{3.28}$$

We can rewrite the atom and interacting Hamiltonian,

$$\begin{aligned}\hat{H}_a &= -\hbar \int_0^L \mathrm{d}z n(z) \left[\Delta_p \hat{\sigma}_{ee}(z,t) + \delta \hat{\sigma}_{rr}(z,t)\right], \\ \hat{V} &= \frac{\hbar}{2} \int_0^L \mathrm{d}z n(z) \left[g_0 \hat{\mathcal{E}}(z,t)\hat{\sigma}_{eg}(z,t) + \Omega_c(t - z/c)\hat{\sigma}_{er}(z,t) + \text{c.c.}\right],\end{aligned} \tag{3.29}$$

where $n(z)$ is the linear atomic density distribution along z, $\Delta_p = \omega_p - \omega_{ge}$ is the single-photon detuning, and $\delta = \omega_p + \omega_c - (\omega_{ge} + \omega_{er})$ is the two-photon detuning.

We use Eqs. (3.29) and (3.6) to determine the dynamics of the polarization operator $\hat{P} = \sqrt{N}\hat{\sigma}_{ge}(z,t)$, and the spin wave operator $\hat{S} = \sqrt{N}\hat{\sigma}_{gr}(z,t)$ (with a decay rate $\gamma_s = \gamma_r$). The operators $\hat{P}$ and $\hat{S}$ describe collective excitations shared among N atoms in the medium. Assuming that most of the atoms remain in the ground state, the equations of motion are,

$$\partial_t \hat{P} = -\frac{1}{2}\left(\Gamma - 2i\Delta_p\right)\hat{P} + \frac{i}{2}\left(\sqrt{N} g_0 \hat{\mathcal{E}} + \Omega_c \hat{S}\right), \tag{3.30}$$

$$\partial_t \hat{S} = -\frac{1}{2}\left(\gamma_s - 2i\delta\right)\hat{S} + \frac{i}{2}\Omega_c \hat{P}. \tag{3.31}$$

Note that there is a collective enhancement of the coupling constant g_0 by a factor $\sqrt{N}$.

Similarly, we can calculate the time evolution of the operator $\hat{\mathcal{E}}(z,t)$ using the commutators defined in Eq. (3.28),

$$\begin{aligned}\partial_t \hat{\mathcal{E}} &= -\frac{i}{\hbar}\left[\hat{\mathcal{E}}, \hat{H}_l + \hat{V}\right], \\ &= i\left(\frac{g_0 n(z) L}{2}\hat{\sigma}_{ge} - \sqrt{\frac{L}{2\pi c}}\int \omega e^{i\omega z/c}\hat{a}_\omega \mathrm{d}\omega\right).\end{aligned} \tag{3.32}$$

Since $\hat{\mathcal{E}}$ is defined with the paraxial approximation, we only include the spatial

derivative $\partial_z \hat{\mathcal{E}}$. The equation of motion reads,

$$\left(\partial_t + c\partial_z\right)\hat{\mathcal{E}} = i\frac{g_0 n(z) L}{2\sqrt{N}}\hat{P}$$

Defining $g = g_0\sqrt{N}$ as the collective coupling and assuming an uniform medium $N = nL$, the equations of motion read:

$$\partial_t \hat{P} = -\frac{1}{2}\left(\Gamma - 2i\Delta_p\right)\hat{P} + \frac{i}{2}\left(g\hat{\mathcal{E}} + \Omega_c \hat{S}\right), \tag{3.33}$$

$$\partial_t \hat{S} = -\frac{1}{2}\left(\gamma_s - 2i\delta\right)\hat{S} + \frac{i}{2}\Omega_c \hat{P}, \tag{3.34}$$

$$\left(\partial_t + c\partial_z\right)\hat{\mathcal{E}} = \frac{i}{2} g\hat{P}. \tag{3.35}$$

This set of equations generally describes the propagation and dynamics of the electromagnetic quantum field with the collective excitations in the medium. We use Eqs. (3.33)-(3.35) to determine the evolution of a dark-state polariton, as well as the quantum retrieval efficiency of a stored spin wave in a medium (see Chapter 6).

We can further simplify the Eqs. (3.33)-(3.35) by assuming that $\gamma_s \approx 0$, and that both the probe and control fields are on resonance $\Delta_p = \delta = 0$. By rearranging (3.33) and (3.34) considering that $\Omega_c(t)$ has only time dependence and is slowly varying [94], we find:

$$\hat{P} = -\frac{2i}{\Omega_c}\partial_t \hat{S}, \tag{3.36}$$

$$\hat{S} = -\frac{g}{\Omega_c}\hat{\mathcal{E}}, \tag{3.37}$$

$$\left(\partial_t + c\partial_z\right)\hat{\mathcal{E}} = \frac{g}{\Omega_c}\partial_t \hat{S}. \tag{3.38}$$

We introduce the quantum field operator $\hat{\Psi}(z,t)$ in terms of the mixing angle θ:

$$\hat{\Psi}(z,t) = \cos\theta(t)\hat{\mathcal{E}}(z,t) - \sin\theta(t)\hat{S}(z,t), \tag{3.39}$$

where,

$$\cos\theta = \frac{\Omega_c(t)}{\sqrt{\Omega_c^2(t)+g^2}}, \qquad \sin\theta = \frac{g}{\sqrt{\Omega_c^2(t)+g^2}}. \tag{3.40}$$

Note that these definitions are similar to the dark eigenstate in Eq. (3.2), with $\hat{\Psi}$ accounting for the collective coupling enhancement and quantum nature of the probe field.

Using the definitions in Eq. (3.39) and Eq. (3.40) in (3.37) and (3.38), the quantum field $\hat{\Psi}$ follows the wave equation:

$$\left(\partial_t + c\cos^2\theta\partial_z\right)\hat{\Psi}(z,t) = 0,$$

where the DSP propagates through the medium loss-free with a velocity $v_g = c\cos^2\theta$. Thus, we can treat the DSP as a quasi-particle consisting of a coherent superposition of an electromagnetic field and a collective spin excitation with a controlled propagation. The admixture and propagation are mediated by the mixing angle θ, which depends on the atomic density and the strength of the control field. For example, if $\theta \to 0$, the DSP is almost purely electromagnetic and propagates close to the speed of light. The opposite limit happens when $\theta \to \pi/2$, where the DSP is mostly composed of the atomic excitation and propagates much slower than c. If the control field is adiabatically turned off such that $v_g \to 0$, the quantum field can be mapped to a stationary atomic excitation. It then can

be converted back to a photon by turning on the control field. Note that the collective enhancement of g is critical to get into the $\theta \to \pi/2$, where $g \gg \Omega_c/$.

Nevertheless, when adding corrections for the non-adiabticity of $\Omega_c(t)$, it is found that there is a spectral narrowing for the quantum field in the DSP due to the finite bandwidth of the EIT-transparency window (in a similar fashion as the classical problem). Thus, for negligible losses in the propagation of a quantum field with pulse width $\Delta\tau$, the following condition should be satisfied [94]:

$$\frac{g^2\Delta\tau}{\Gamma} \gg 1 \tag{3.41}$$

Let us study a more general case with $\Delta_p \neq 0$ and $\delta \neq 0$, but with the assumptions that the control field is changing adiabatically $\dot{\Omega}_c \approx 0$, and $\gamma_s \approx 0$. Changing to the dark- and bright-polariton, and polarization basis $\{\hat{\Psi}, \hat{\Phi}, \hat{P}\}$, where the bright polariton is given by,

$$\hat{\Phi} = \sin\theta\hat{\mathcal{E}} + \cos\theta\hat{S},$$

the equations of motion (3.33), (3.34) and (3.35) become,

$$\begin{aligned}
\partial_t\hat{\Psi} &= (i\delta\sin^2\theta - c\partial_z\cos^2\theta)\hat{\Psi} - (i\delta + c\partial_z)\cos\theta\sin\theta\hat{\Phi}, \\
\partial_t\hat{\Phi} &= (i\delta\cos^2\theta - c\partial_z\sin^2\theta)\hat{\Phi} - (i\delta + c\partial_z)\cos\theta\sin\theta\hat{\Psi} + \frac{i}{2}\Omega_e\hat{P}, \\
\partial_t\hat{P} &= -\frac{1}{2}\left(\Gamma - 2i\Delta_p\right)\hat{P} + \frac{i}{2}\Omega_e\hat{\Phi},
\end{aligned}$$

here, $\Omega_e = \sqrt{\Omega_c^2 + g^2}$ is the effective Rabi frequency. Since $\hat{P}$ and $\hat{\Phi}$ are weakly coupled, we can adiabatically eliminate these states by assuming $\dot{\hat{P}} \approx 0$ and $\dot{\hat{\Phi}} \approx 0$.

The time evolution of the DSP is determined by the equation:

$$\partial_t \hat{\Psi} = \left(i\delta \sin^2\theta - c\partial_z \cos^2\theta + \frac{\cos^2\theta \sin^2\theta (i\delta + c\partial_z)^2}{c\partial_z \sin^2\theta - i\delta\cos^2\theta + \frac{\Omega_e^2/2}{\Gamma + 2i\Delta_p}} \right) \hat{\Psi}.$$

In the regime of a slowly-varying polariton along z (low momentum), and small two-photon detuning, we can expand the third term and obtain:

$$\begin{aligned} \partial_t \hat{\Psi} =& i\delta \sin^2\theta \left(1 + 4\frac{v_g}{c}\frac{\delta\tilde{\Delta}}{\Omega_e^2} \right) \hat{\Psi} \\ & - iv_g k \left(1 + 8\sin^2\theta \frac{\delta\tilde{\Delta}}{\Omega_e^2} \right) \hat{\Psi} + 4ik^2 c v_g \sin^2\theta \frac{\tilde{\Delta}}{\Omega_e^2} \hat{\Psi}, \end{aligned} \tag{3.42}$$

where $\tilde{\Delta} = \Delta_p + i\Gamma/2$, and $\partial_z = ik$ in momentum space. The first term arises from an energy shift due to a finite δ, the second term describes the propagation of the polariton with group velocity $v_g = c\cos^2\theta$, and the third term is a second-order correction accounting for deviations from the slow-light propagation. In the regime where $\delta \ll \Omega_c,\ \Delta_p,\ g$ then Eq. (3.42) becomes,

$$\partial_t \hat{\Psi} = -i \left(v_g k + \frac{\hbar k^2}{2m} \right) \hat{\Psi}, \tag{3.43}$$

here, the mass term is given by,

$$m = -\hbar \frac{\Omega_c^2(\Omega_c^2 + g^2)}{8\tilde{\Delta} v_g^2 g^2}. \tag{3.44}$$

We can write the dispersion relation of the polariton as,

$$\hbar\omega(k) = \hbar v_g k + \frac{\hbar^2 k^2}{2m}. \tag{3.45}$$

For low momentum k, the group velocity is proportional to the first-order derivative of the energy dispersion, while the mass dictates the curvature through the second-order derivative around $k = 0$.

3.3 Rydberg polaritons in EIT media

Figure 3.3 shows the configuration for Rydberg-EIT. Note the change in nomenclature of the atomic levels and detunings from the previous sections to make it consistent with the nomenclature used in Reference [96] and Chapter 8. Here, the weak probe field with collective coupling g, couples the ground state $|G\rangle$ with an intermediate state $|P\rangle$, and a strong-classical control field with Rabi frequency Ω_c couples $|P\rangle$ with the Rydberg state $|S\rangle$. For simplicity, we reduce the dimensionality of the system to the field propagation axis where the paraxial approximation is a good approximation.

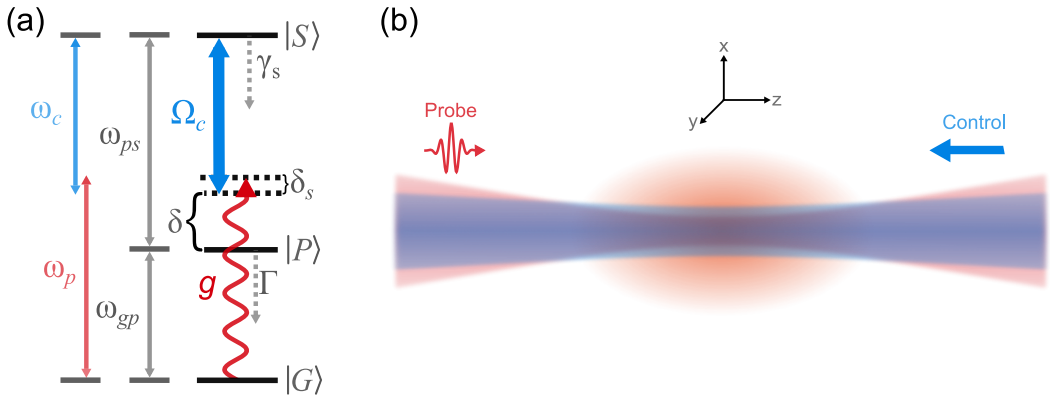

Figure 3.3: **Atomic levels and physical setup for Rydberg-EIT.** (a) The relevant states are the ground state $|G\rangle$, excited state $|P\rangle$ with decay rate Γ, and the Rydberg state $|S\rangle$ with decay rate γ_s. The resonant frequency transition for $|G\rangle \to |P\rangle$ is ω_{gp} and the frequency transition for $|P\rangle \to |S\rangle$ is by ω_{ps}. The weak probe field with frequency ω_p, couples $|G\rangle \to |P\rangle$ with a detuning $\delta + \delta_s = \omega_p - \omega_{gp}$. A classical control field with frequency ω_c, drives the atomic states, $|P\rangle \to |S\rangle$ with a detuning $\delta = \omega_{ps} - \omega_c$, and strength Ω_c. (b) The probe photons propagate along the z-axis through a cloud of optical density OD and length L. The collective coupling strength of the probe is $g = \sqrt{\frac{OD\Gamma c}{L}}$.

Let us introduce the bosonic field operators $\hat{\psi}_e^\dagger, \hat{\psi}_p^\dagger$ and $\hat{\psi}_s^\dagger$. The bosonic operator of the incoming electromagnetic quantum field $\hat{\psi}_e^\dagger(z)$ is given by Eq. (3.22), and the atomic operators $\hat{\psi}_p^\dagger(z)$ and $\hat{\psi}_s^\dagger(z)$ are associated with the creation of a spin-excitation of P and S at position z, respectively. The Hamiltonian of the system is,

$$H = \int \mathrm{d}z \begin{pmatrix} \hat{\psi}_e^\dagger \\ \hat{\psi}_p^\dagger \\ \hat{\psi}_s^\dagger \end{pmatrix} \begin{pmatrix} -ic\partial_z & g/2 & 0 \\ g/2 & -\delta - \delta_s & \Omega_c/2 \\ 0 & \Omega_c/2 & -\delta_s \end{pmatrix} \begin{pmatrix} \psi_e \\ \psi_p \\ \psi_s \end{pmatrix}, \tag{3.46}$$

where $\delta + \delta_s$ is the probe field single-photon detuning and δ_s is the two-photon detuning.

It is also of importance to consider the effect of decoherence using the density matrix operator ρ with the master equation in (3.6)-(3.7). However, the dynamics evolution is simplified in the limit where the probability of $N+1$ excitations is much lower than the probability of N excitations (either atomic or photonic). This condition is satisfied when the number of excitations is limited by the few-photon input field. Discarding the correlations between N and $N+1$ by truncating the Hilbert space to N excitations, and introducing the non-Hermitian Hamiltonian H_0:

$$H_0 = \begin{pmatrix} -ic\partial_z & g/2 & 0 \\ g/2 & -\delta - \delta_s - i\Gamma/2 & \Omega_c/2 \\ 0 & \Omega_c/2 & -\delta_s - i\gamma_s/2 \end{pmatrix}, \tag{3.47}$$

we find that the time evolution from the Schrödinger equation using H_0 is equivalent to the dynamics described by Eq. (3.6) [96]. The non-Hermitian part of the

effective Hamiltonian (3.47), includes Γ the decay rate of $|P\rangle$, and γ_s the decay rate for $|S\rangle$. Nevertheless, the use of this effective Hamiltonian is inappropriate when considering dephasing (from mechanisms that decrease the coherence elements of ρ, but without decreasing the populations), and needs the full rigorous approach using the Master equation. We assume that dephasing can be neglected for the rest of this section.

It is convenient to rewrite Eq. (3.47) in momentum-space to calculate the energy-dispersion relations of the eigenstates of H_0, where the momentum $k \equiv -i\partial_z$. For simplicity, we also make the approximation $\gamma_s = 0$ (this is a valid approximation since the typical time scales of the system are much shorter than γ_s^{-1}). The new eigenstates of the system consist of three branches of polaritons, which are composed of the electromagnetic quantum field and atomic-spin excitations. There are two bright polaritons indicated by the subscript $\mu = \pm 1$, and a dark state polariton (DSP) with $\mu = 0$, the latter does not have contributions from the lossy P-state and hence is called dark. These new field operators are

$$\tilde{\psi}_\mu(k) = \sum_{i=\{e,P,S\}} U^i_\mu(k)\psi_i(k)$$

where U is the matrix that diagonalizes H_0. Similarly the creation operators are written as $\tilde{\psi}^\dagger_\mu(k) = \sum_i \bar{U}^i_\mu(k)\hat{\psi}^\dagger_i(k)$, here $\bar{U} = U^{-1}$.

The diagonalized Hamiltonian takes the form:

$$H_0 = \sum_{\mu=0,\pm1} \epsilon_\mu(k)\tilde{\psi}^\dagger_\mu(k)\tilde{\psi}_\mu(k) \tag{3.48}$$

where ϵ_μ denotes the energy spectrum of each of the polaritons branches. Fig-

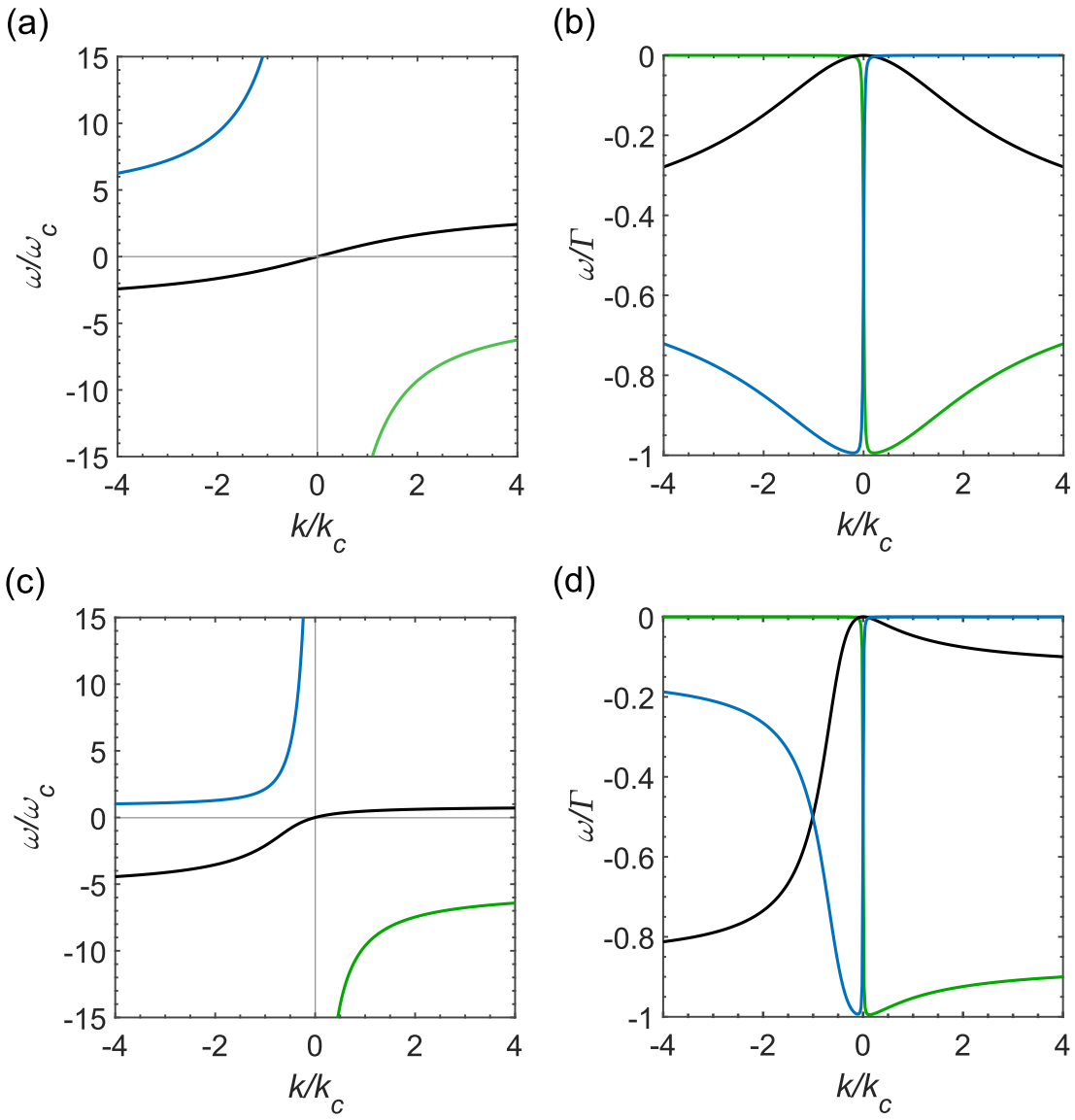

Figure 3.4: **Real and imaginary parts of the dispersion relation for the three polariton branches with no interactions.** Upper bright state (blue), lower bright state (green) and dark-sate polariton (black). (a) Real and (b) imaginary components of the eigenenergies for the parameters ($g \sim 10^4\Gamma, \Omega = 3.9\Gamma, \delta = 0, \delta_r = 0$) with single- and two-photon resonance. (c) Real and (d) imaginary components of the eigenergies for ($g \sim 10^4\Gamma, \Omega = 3.9\Gamma, \delta = 4.1\Gamma, \delta_r = 0$). Around $k \approx 0$, the DSP consists mainly of the S-spin-wave excitation with the real and imaginary part of the energy $\epsilon_0 \to 0$. For larger momentum, the DSP photonic part starts to dominate and experiences losses as it gets further away from the resonant-EIT condition.

ure 3.4 shows the energy spectrum for different set of parameters. Of particular interest is the dispersion relation of the dark-state energy, for low momentum

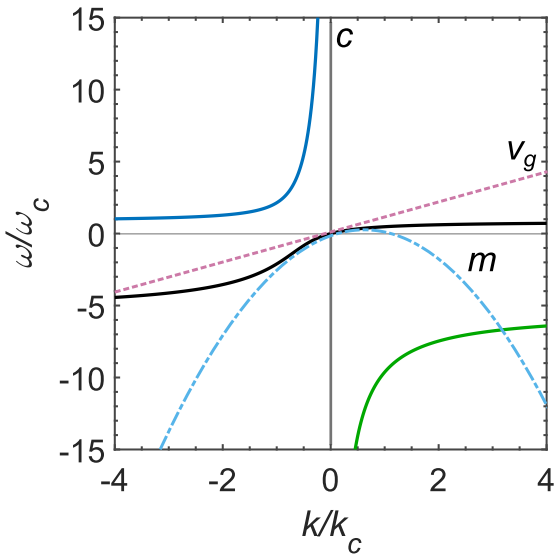

Figure 3.5: **DSP polariton dispersion behavior for $k \approx 0$.** The speed of light in vacuum is indicated by the dark-grey vertical line. For low momenta $k \approx 0$, the velocity at which the DSP propagates trough the medium is given by $v_g = \partial\omega/\partial k$ (pink dashed line), and it is proportional to the slope of the dispersion. Additionally, the dispersion has a quadratic contribution from the real component of the mass m (dotted-dashed light-blue line), which determines the curvature. The curvature will be negative (positive) for $\delta > 0$ ($\delta < 0$).

(near the EIT-two-photon resonance) is given by,

$$\epsilon_0(k) = \hbar v_g k + \frac{\hbar^2 k^2}{2m}. \tag{3.49}$$

The behavior of this dispertion relation for low-momenta DSPs is illustrated in Fig. 3.5, where v_g has a linear contribution, and the mass has a quadratic contribution. As we found in the previous section, v_g the group velocity, and m the effective mass are defined as,

$$v_g = \frac{\Omega_c^2}{g^2 + \Omega_c^2} c \qquad m = -\hbar\Omega_c^2 \frac{\Omega_c^2 + g^2}{8\Delta g^2 v_g^2}, \tag{3.50}$$

where, $\Delta = \delta + i\Gamma/2$ is the complex detuning. More generally, by evaluating the determinant $\mathrm{Det}[I\omega - H_0]$, we can also obtain the dispersion relation for the

momentum as a function of the energy:

$$ck(\omega) = \omega\left(1 + \frac{g^2(1+\Delta_s/\omega)}{4(\Delta+\delta_s+\omega)(\omega+\Delta_s)-\Omega_c^2}\right). \tag{3.51}$$

where $\Delta_s = \delta_s + i\gamma_s/2$ is the two-photon complex detuning. From this relation, we can obtain the general expressions for the group velocity and effective mass for $\delta_s \neq 0$ and $\gamma_s \neq 0$ are [97],

$$v_g(\omega) = c\left(\frac{\partial k}{\partial \omega}\right)^{-1} = \frac{\left[4(\omega+\Delta_s)(\omega+\Delta+\delta_s)-\Omega^2\right]^2}{g^2(4(\omega+\Delta_s)^2+\Omega_c^2)}c \tag{3.52}$$

$$\begin{aligned}\frac{1}{m(\omega)} = -c^2\frac{\partial^2 k}{\partial\omega^2}\left(\frac{\partial k}{\partial\omega}\right)^{-3} &= -\frac{8v_g^2}{4(\omega+\Delta_s)^2+\Omega_c^2} \\ &\times \frac{4(\omega+\Delta_s)^3+(\Delta+\delta_s+2\Delta_s+3\omega)\Omega_c^2}{4(\omega+\Delta_s)(\omega+\Delta+\delta_s)-\Omega^2}\end{aligned} \tag{3.53}$$

Finally, we define the characteristic energy scale of the system $\omega_c = \min(|\Delta|, \Omega_c^2/|4\Delta|)$ and the characteristic momentum $k_c = \omega_c/v_g$. These units are used to define the energy and momentum scale of Fig. 3.4.

3.4 Interacting Polaritons

The interaction between two Rydberg atoms has the following quartic form in the one-dimensional limit,

$$H_{\text{int}} = \frac{1}{2}\int \mathrm{d}z \int \mathrm{d}z' \psi_s^\dagger(z)\hat{\psi}_s^\dagger(z')V(z-z')\psi_s(z')\psi_s(z), \tag{3.54}$$

here, $\psi_s^\dagger(z)$ is the bosonic field operator that creates a s-excitation at position z, and $V(z) = C_6/z^6$ is the interaction potential, where the van der Waals coefficient C_6 determines the strength of the interaction.

The scattering process due to the interaction in Eq. (3.54), where the total energy $\hbar\omega$, and center of mass momentum $\hbar K$ are conserved, can be described by the T-matrix formalism. The only non-vanishing matrix elements of the T-matrix correspond to the ones describing the interaction between Rydberg states. The T-matrix of the Rydberg states, $T_{kk'}(K,\omega)$ of two incoming polaritons with relative momentum $\hbar k$ to two outgoing polaritons with relative momentum $\hbar k'$ is given by the recursive integral equation [96, 98],

$$T_{kk'}(K,\omega) = \tilde{V}(k-k') + \int \frac{\mathrm{d}q}{2\pi} T_{kq}(K,\omega)\chi_q(K,\omega)\tilde{V}(q-k'), \tag{3.55}$$

where $\tilde{V}$ is the Fourier transform of the potential, and $\chi_q(K,\omega)$ is the Green's propagator of the two polaritons:

$$\chi_q(K,\omega) = \sum_{\mu,\beta\in\{0,\pm1\}} \frac{S_\mu^p S_\beta^{p'}}{\hbar\omega - \epsilon_\mu(p) - \epsilon_\beta(p') + i\eta} \tag{3.56}$$

$S_\mu^p = \bar{U}_s^\mu(p)U_\mu^s(p)$ is the overlap of the μ-branch polariton with the Rydberg state at momentum p, with $p = K/2 + q$ and $p' = K/2 - q$. The full propagator in Eq. (3.56) consists of terms with poles due to the propagation and scattering of the polariton pair, and a term that accounts for the polariton saturation at large momentum for $q \to \pm\infty$,

$$\bar{\chi}(\omega) = \frac{4\Delta^2 + 6\Delta\omega + 2\omega^2 - \Omega^2}{2(\Delta+\omega)(\omega(2\Delta+\omega) - \Omega_c^2)}, \tag{3.57}$$

for a finite two photon detuning $\delta_s \neq 0$ and/or Rydberg decay rate $\gamma_s \neq 0$, then $\omega \to \omega + 2\Delta_s$. This saturation term renormalizes the van der Waals interaction

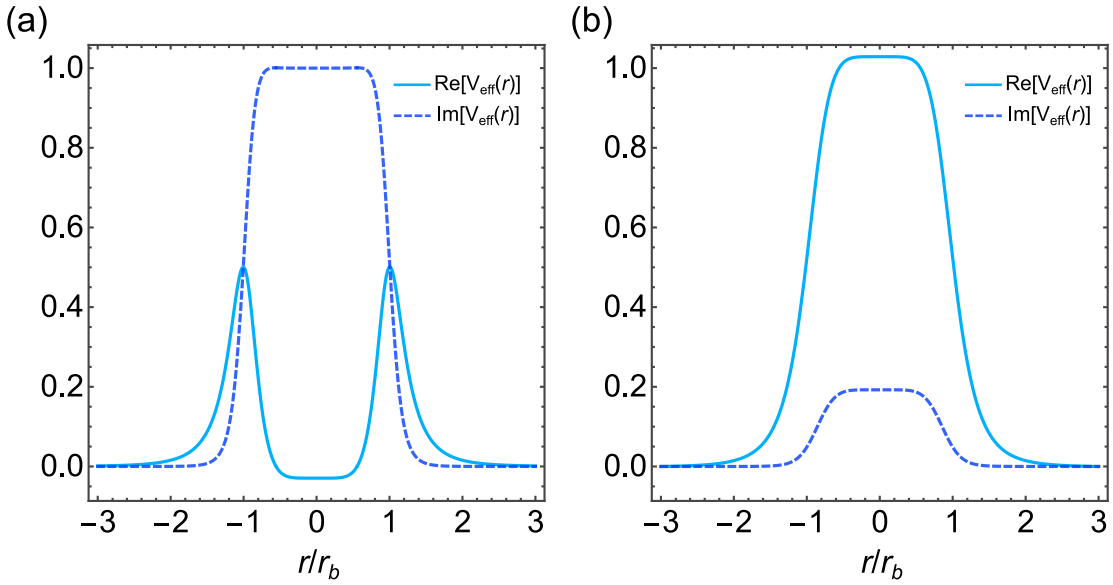

Figure 3.6: **Real and imaginary parts of the effective potential $V_{\text{eff}}(r)$.** (a) Real and imaginary components of the effective potential in the dissipative regime for the parameters ($C_6 \sim 10^6\Gamma, \Omega = 3.9\Gamma, \delta = 0, \delta_r = 0$) with single- and two-photon resonance. The real part shows the blockade effect with a potential barrier around $r = r_b$, and a large imaginary component inside the barrier. In addition, the effective mass is purely imaginary on-resonance. (b) Real and imaginary components of the effective potential in the dispersive regime for the parameters ($C_6 \sim 10^6\Gamma, \Omega = 3.9\Gamma, \delta = 4.1\Gamma, \delta_r = 0$). Here, the mass is negative and the effective interactions between polaritons are attractive. Note that the height of the imaginary component of the potential is lower, and therefore, less lossy than in the dissipative case.

potential to an effective potential,

$$V_{\text{eff}}(r) = \frac{V(r)}{1 - \bar{\chi}(\omega)V(r)}, \tag{3.58}$$

$V_{\text{eff}}(r)$ converges to $-1/\bar{\chi}(\omega)$ as the relative coordinate $r = z - z' \ll r_b$, where r_b is the blockade radius and is defined by the saturation term of the propagator as,

$$V(r_b) = \frac{C_6}{r_b^6} = \frac{1}{|\bar{\chi}(\omega)|}, \tag{3.59}$$

here, $1/\bar{\chi}(\omega)$ sets the relevant energy scale for r_b. If the relative coordinate $r > r_b$, the effective potential exhibits a long-range van der Waals tail. Note that $\bar{\chi}(\omega)$

modifies the attributes of the polaritons interaction for $r < r_b$. Thus, by changing the macroscopic parameters Ω, δ, δ_s, we can adjust the potential along with the sign of the mass, so the interactions are repulsive or attractive, as well as the dispersive and dissipative properties (see Fig. 3.6). Using the effective potential reduces Eq. (3.55) for the T-matrix to:

$$T_{kk'} = \tilde{V}_{\text{eff}}(k - k') + \int \frac{\mathrm{d}q}{2\pi} \bar{\chi}_q(\omega, K) \tilde{V}_{\text{eff}}(k - q) T_{qk'}, \tag{3.60}$$

where $\bar{\chi}_q$ is the part of the propagator that contains the pole structure and its analytical expression is in Ref. [98].

The two-Rydberg excitation wavefunction can be written in terms of the T-matrix as,

$$\varphi_{ss}(r) V(r) = \int \frac{\mathrm{d}k'}{2\pi} e^{ik'r} T_{kk'}. \tag{3.61}$$

The full propagator and T-matrix allow us to calculate other properties from the scattering process such as the scattering length [97–99], or the transition rate β from the incoming to the outgoing states. The latter can be calculated using Fermi's Golden Rule as,

$$\beta = \frac{2\pi}{\hbar} |\mathcal{M}|^2 \rho(E), \tag{3.62}$$

where $\rho(E)$ is the density of final states, and $\mathcal{M}$ is the transition amplitude between the incoming states and the outgoing states. As we show in Chapter 8, we use β to quantify the three-body scattering rate in a regime where weak interactions and energy and momentum conservation allow for an enhancement of resonant three-body loss.

Chapter 4: Characterizing single-photon sources

Single photons are promising for encoding and communicating quantum information as qubits, where the information can be stored in the quantum state of the photon. There are many reasons why a single photon is an ideal candidate for different quantum information applications: its degrees of freedom can be easily manipulated with high control; it can travel over long distances while interacting weakly with the environment (reducing noise and loss of the information); and in free-space, it travels at the maximal speed allowed by physical laws [1].

The realization of many quantum information protocols with photonic qubits requires high quality single-photon sources. An ideal source would produce photons on-demand with 100% efficiency at a high repetition rate, emitting one, and only one photon at a time, and with all produced photons identical to each other. Despite the numerous platforms used to build a single-photon source, an ideal source is still lacking, and any imperfections hinder the fidelity and practicality for scaling quantum information protocols. In this context, it is crucial to characterize the properties of a single-photon source: efficiency, repetition rate, multi-photon suppression, and indistinguishability.

Single-photon detectors are the basis for nearly all photon-based quantum measurement schemes. However, since single-photon detectors display non-ideal properties such as dark counts, after-pulsing, dead time, non-linearities, and limited

single-photon detection efficiency, one has to take into account these features to obtain an accurate measurement of the single-photon source efficiency and generation rate [1, 100]. Since most quantum information applications require single photons in a single mode, in this thesis, we consider the fibered brightness [101] or fibered efficiency as the relevant measurement to characterize the probability of obtaining a photon in a single transversal spatial mode with a single polarization mode.

The multi-photon emission is described by the photon-number distribution of the source. A photon-number-resolving detector can measure the photon-number distribution, but this kind of detector is not widely commercially available. By far the most common measurement for multi-photon emission probability is done by characterizing the second-order autocorrelation function $g^{(2)}$ of the produced light using click/no-click detectors, which yield the same result for one or more photons.

The fidelity or purity of the quantum state of a photon can be reconstructed from the Wigner function for a single-photon Fock state [102]; however, this procedure is involved and susceptible to losses. The indistinguishability characterizes if the photon is in a statistical mixture or in a pure state with a single spectro-temporal, spatial and polarization mode. The most prevalent scheme to quantify the indistinguishability is by measuring the visibility of the Hong-Ou-Mandel (HOM) interference[1]. In the particular case of time-resolved HOM-interference, it also provides a measure of the temporal coherence or coalescence of the interfering photons [104, 105].

[1] A recent work [103] proposes a scheme where the efficiency, the multi-photon component and the indistinguishability of a single photon source are determined by using two photon-number resolving detectors in a single measurement.

In this Chapter, we review the most commonly used schemes to characterize a single-photon source. First, we discuss the measurement outcome when using click/no-click detectors. Next, we examine the definition and properties of the second-order correlation function. Then, we analyze the quantum mechanical description of a beamsplitter with single-photons to derive $g^{(2)}$ and HOM-interference. The discussion of this material is based mainly on References [100, 106–108].

Finally, we conclude by introducing metrics to describe the probability, rate, and fidelity of producing a single photon in a fully single mode (spectral, temporal, spatial, and polarization). The purpose of these metrics is to benchmark the performance of on-demand single-photon sources for quantum information protocols that require single photons in a fully single mode. They are defined in terms of the fibered efficiency, repetition rate, multi-photon emission suppression, and indistinguishability.

4.1 Source Efficiency, Generation Rate, and Detection

The source efficiency P is defined as the joint probability that the source generates one or more photons P_g, along with the probability P_t that these photons are transmitted to the detection system at any given time:

$$P = P_g P_t. \tag{4.1}$$

where P_t includes the optical losses such as absorption/reflection from optical collection elements and/or fiber coupling (but not detection losses), since any

component that filters the photon (either in frequency or spatially) is considered part of the source. In particular for pulsed sources, P is the photon probability within a pulse; here the effective source rate R_{eff} in terms of the pulse rate R_p is:

$$R_{\text{eff}} = PR_p. \tag{4.2}$$

A careful analysis is required, to take into account the properties of the detection system while characterizing the source efficiency. Let us start by representing the photon states generated from a light source with the density matrix operator in the basis of the number states (Fock states) [100]:

$$\hat{\rho} = \sum_n P_n \left|n\right\rangle\!\left\langle n\right| \tag{4.3}$$

where P_n is the probability that the field is in the number state $|n\rangle$, and is given by,

$$P_n = \text{Tr}\{\hat{\rho}\left|n\right\rangle\!\left\langle n\right|\} = \left\langle n|\hat{\rho}|n\right\rangle. \tag{4.4}$$

The probabilities P_n are in the diagonal elements of ρ in this basis, which satisfy the condition,

$$\sum_{n=0}^{\infty} \text{Tr}\{\hat{\rho}\} = 1. \tag{4.5}$$

The mean photon number of the source is found by taking the trace:

$$\bar{n} = \text{Tr}\{\hat{\rho}\hat{n}\} = \sum_{n=0}^{\infty} nP_n. \tag{4.6}$$

For a good single-photon source, the probability that the output field occupies a

single photon number-state should be much greater than the probability of the field occupying higher-number states $P_1 \gg P_{n>1}$.

The measurement of the diagonal elements of $\hat{\rho}$ depends on the type and detection efficiency of the photon-counting device. The outcome of the measurement will be different if it is done with a photon-number resolving (PNR) detector or a click/no-click detector. In the absence of losses, dark-counts, or afterpulsing, a PNR detector can identify the photon number state, whereas a click/no-click detector can only discriminate between zero and non-zero photon number states. For the rest of the discussion, we assume that the detector has not dark-counts or after pulsing, but has a single-photon detection efficiency less than one.

We use the POVM (Positive-Operator-Valued Measure) operator to describe the measurement of $\hat{\rho}$ with a particular detection system. The POVM $\hat{\pi}_m$ in the number-state basis is defined as [100],

$$\hat{\pi}_m = \sum_{n=m}^{\infty} P(m|n) \, |n\rangle\langle n| \, , \tag{4.7}$$

where $P(m|n)$ is the conditional probability of detecting m photons given that the input state has n photons. We trace $\hat{\pi}_m$ to obtain the measured probability of detecting m photons:

$$P_{\text{meas}} = \text{Tr}\{\hat{\rho}\hat{\pi}_m\} = \sum_{n=m}^{\infty} P(m|n) P_n. \tag{4.8}$$

For a click/no-click photon counting device with detection efficiency η_{det}, the

POVM for a "no-click" or null event outcome is [109],

$$\hat{\pi}_0 = \sum_{n=0}^{\infty} (1-\eta_{\rm det})^n \left|n\right\rangle\!\left\langle n\right| , \tag{4.9}$$

and the POVM for a click detection event is:

$$\hat{\pi}_1 = \sum_{n=1}^{\infty} \left[1-(1-\eta_{\rm det})^n\right] \left|n\right\rangle\!\left\langle n\right| , \tag{4.10}$$

where the conditional probabilities are $P(\text{no-click}|n) = (1-\eta_{\rm det})^n$ and $P(\text{click}|n) = [1-(1-\eta_{\rm det})^n]$. The definition of the POVM for a PNR detector is in Refs. [100, 109].

Tracing Eq. (4.10) we get that the measured probability of detecting the output of a light source is given by,

$$P_{\rm meas} = \eta_{\rm det} \left[P_1 + (2-\eta_{\rm det})P_2 + (3+\eta_{\rm det}(\eta_{\rm det}-3))P_3 + \cdots\right] . \tag{4.11}$$

When $\eta_{\rm det} \to 1$, the measured probability is the source efficiency. If $\eta_{\rm det} < 1$, we can not simply extract the single-photon source efficiency as $P_1 = P_{\rm meas}/\eta_{\rm det}$, except when the probability of multi-photon states are negligibly small $P_1 \gg P_{n>1}$.

4.2 Correlation functions

Correlation functions give a measure of the coherence and fluctuations of an electromagnetic field, yielding important bounds about the properties and statistics of both classical and quantum light sources. The theory of optical coherence was originally developed in the fifties and sixties by Wolf and Glauber [110, 111].

The n-th normalized auto-correlation function characterizes the degree of temporal coherence of an electric field up to $2n$ time positions [108],

$$g^{(n)}(t_1, \cdots, t_n; t'_1, \cdots, t'_n) = \frac{\langle E^*(t_1) \dots E^*(t_n) E(t'_n) \dots E(t'_1) \rangle}{\prod_{i=1}^{n} \langle E^*(t_i) E(t_i) \rangle}, \tag{4.12}$$

where $E_i^*(t)$ is the complex conjugate of $E_i(t)$ at a given time t, and the braces $\langle\rangle$ indicate a time average. The most general form of Eq. (4.12) can also depend on spatial coordinates and measure the correlation between n different fields. However, we will focus only in the time variable and auto-correlation function for the rest of the discussion.

The first-order auto correlation function, $n = 1$ is related to the change in the visibility obtained from interfering the field at two different points in time t_1 and t'_1, where $\tau = t'_1 - t_1$:

$$g^{(1)}(\tau) = \frac{\langle E^*(t) E(t+\tau) \rangle}{\langle E^*(t) E(t) \rangle}, \tag{4.13}$$

since $g^{(1)}(\tau)$ characterizes the temporal coherence and fluctuations of the field itself, it requires an interferometer (such a Mach-Zehnder) where it is possible to get a time delay that generates a relative phase change in the electric fields.

Higher-order correlation functions involve intensity and not field measurements. An array of $n-1$ beamspitters (BS) that splits the light equally among n detectors as shown in Fig. 4.1, can be used to characterize the n-th correlation function in a generalized Hanbury Brown and Twiss (HBT) interferometer.

The second-order correlation function is a conditional measurement, which gives the conditional probability of a detection event at a time $t + \tau$ given a detection event at t. However, this correlation function evaluated at zero time delay

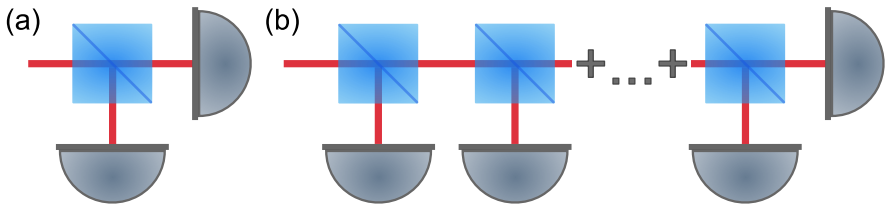

Figure 4.1: **Interferometer configuration to measure the n-th correlation function $g^{(n)}$.** (a) Standard HBT interferometer used to measure $g^{(2)}(0)$. (b) The light is split equally with $n-1$ BS among n detectors in a generalized HBT interferometer.

$\tau = 0$ is of particular interest, since it characterizes the statistical properties of an electromagnetic field by measuring its intensity fluctuations. These fluctuations are dictated by the variance, so we can infer the classical or quantum nature of a light source by identifying its statistics: super-Poissonian (classical), Poissonian (coherent), or sub-Poissonian (quantum).

It also provides a measure of the multiphoton-emission probability for a single-photon source when measuring with click/no-click detectors. Due to the operational mode of these detectors, every instance there is photodetection event, there is a finite time where the detector cannot respond to subsequent photons [1], this time is know as "dead time". As a result, click/no-click detectors are unable to discriminate between one or multiple photon events occurring in a time interval shorter than the dead time, so two or more detectors are needed to characterize the multiphoton-emission probability with $g^{(2)}(0)$.

Finally, in the context of Rydberg-EIT, the n-correlation function can provide information about the dynamics and the nature of the interactions for n-polaritons in the atomic medium, as discussed in Chapter 8.

4.2.1 Classical fields

The second-order correlation function for a stationary classical field is given by,

$$g^{(2)}(\tau) = \frac{\langle I(t)I(t+\tau)\rangle}{\bar{I}^2}, \tag{4.14}$$

where the intensity $I(t) = E^*(t)E(t)$, and $\bar{I} = \langle I(t)\rangle$ is the time-average intensity. Note that $g^{(2)}(\tau)$ is even since the intensity is real and positive:

$$g^{(2)}(\tau) = g^{(2)}(-\tau).$$

The correlation function typically converges to one for long enough delays, since the field is not correlated with itself at long delay times. The time scale where $g^{(2)}(\tau_c) \to 1$ determines the coherence time of the light.

Since $g^{(2)}(0)$ provides the relevant information to characterize a light source by its statistical properties [108], let us rewrite Eq. (4.14) at $\tau = 0$, in terms of the intensity fluctuations $\delta(t) = I(t) - \bar{I}$,

$$g^{(2)}(0) = 1 + \frac{\langle \delta(t)^2\rangle}{\bar{I}^2}, \tag{4.15}$$

where the average fluctuations $\langle \delta(t)\rangle = 0$. Necessarily the quantity $\langle \delta(t)^2\rangle \geq 0$, and

$$g^{(2)}(0) \geq 1. \tag{4.16}$$

This equation is equivalent to the Cauchy-Schwarz inequality:

$$\langle AB \rangle^2 \leq \left\langle A^2 \right\rangle \left\langle B^2 \right\rangle, \tag{4.17}$$

which we can expand for $\tau \neq 0$

$$\langle I(t)I(t+\tau) \rangle^2 \leq \left\langle I(t)^2 \right\rangle \left\langle I(t+\tau)^2 \right\rangle,$$

for stationary systems $\langle I(t)^2 \rangle = \langle I(t+\tau)^2 \rangle$. The inequality becomes $\langle I(t)I(t+\tau) \rangle \leq \langle I(t)^2 \rangle$ [107], yielding to

$$g^{(2)}(\tau) \leq g^{(2)}(0). \tag{4.18}$$

The inequalities in Eqs. (4.16) and (4.18) are always satisfied for classical light sources such as thermal light and coherent light, with $g^{(2)}(0) = 2$ and $g^{(2)}(0) = 1$, respectively.

4.2.2 Quantized fields

We use the bosonic creation and annihilation operators to describe the quantized electromagnetic field. Without loss of generality, let us assume that the electric field operator is well defined in a single mode of frequency ω:

$$\hat{E}^\dagger = \hat{a}^\dagger e^{-i\omega t} \qquad \hat{E}(t) = \hat{a} e^{i\omega t}. \tag{4.19}$$

The second order correlation function in terms of the creation and annihilation operators is given by,

$$g^{(2)}(\tau) = \frac{\left\langle \hat{a}^\dagger(t)\hat{a}^\dagger(t+\tau)\hat{a}(t+\tau)\hat{a}(t)\right\rangle}{\langle \hat{a}^\dagger(t)\hat{a}(t)\rangle \left\langle \hat{a}^\dagger(t+\tau)\hat{a}(t+\tau)\right\rangle}, \tag{4.20}$$

where it is written in the normal and time ordering of the operators. Using the number operator $\hat{n} = \hat{a}^\dagger\hat{a}$, and the commutation relation

$$\left[\hat{a}, \hat{a}^\dagger\right] = 1, \tag{4.21}$$

it is possible to define $g^{(2)}(\tau = 0)$ as a function of the number operator[2],

$$g^{(2)}(0) = \frac{\langle \hat{n}(t)(\hat{n}(t) - 1)\rangle}{\langle \hat{n}(t)\rangle^2}. \tag{4.22}$$

Rewriting the correlation function in terms of the variance $\sigma_n^2 = \langle n^2\rangle - \bar{n}^2$, where $\bar{n}$ is the mean photon number, Eq. (4.22) becomes,

$$g^{(2)}(0) = 1 + \frac{\sigma_n^2 - \bar{n}}{\bar{n}^2}. \tag{4.23}$$

It is possible to get $g^{(2)}(0) < 1$ for fields with a distribution where the mean photon number is greater than the variance $\bar{n} > \sigma_n^2$. Non-classical light can violate the Cauchy-Schwartz inequality in (4.16) defined for classical fields. Note that $g^{(2)}(\tau \to \infty) = 1$ is true for any stationary fields. For quantum fields, the inequality (4.18) can also be violated.

[2]This definition is only satisfied at $\tau = 0$, because $\hat{a}, \hat{a}^\dagger$ do not commute with each other, we cannot rewrite the numerator of Eq. (4.20) as $\langle \hat{n}(t)\hat{n}(t+\tau)\rangle$

For example, number states are the eigenstates of the operator $\hat{n}$, and constitute a complete set for a single mode field [106]. Since there is no uncertainty in the photon number, the variance vanishes $\sigma_n^2 = 0$, the second-order correlation function for number states takes the form,

$$g^{(2)}(0) = 1 - \frac{1}{n}, \tag{4.24}$$

which exhibits anti-bunching with $g^{(2)}(0) < 1$ and a $g^{(2)}(\tau) > g^{(2)}(0)$, which is in complete contradiction with Eq. (4.16) and (4.18).

In particular, for a single-photon state in a pure state where $\bar{n} = 1$, we find $g^{(2)}(0) = 0$, which is a lower bound on $g^{(2)}(0)$ for non-classical light. At zero time delay, the second-order correlation function is also a measure of the multi-photon nature of a light source. For this reason, $g^{(2)}(\tau = 0)$ is an important metric that determines the quality of a single-photon source.

Note that Eq. (4.23) is not limited to the description of non-classical states. Table 4.1 shows the statistical properties and $g^{(2)}$ for thermal (classical), coherent (semi-classical) and number states (quantum).

States	Statistics	$P(n)$	σ_n^2	$g^{(2)}(0)$
Thermal	Super-Poissonian	$\frac{1}{\bar{n}+1}\left(\frac{\bar{n}}{\bar{n}+1}\right)^n$	$\bar{n} + \bar{n}^2$	2
Coherent	Poissonian	$\frac{\bar{n}}{n!}e^{-\bar{n}}$	$\bar{n}$	1
Number ($n = 1$)	Sub-Poissonian	1	0	0

Table 4.1: **Probability distribution $P(n)$, variance σ_n^2 and $g^{(2)}$ for different classical and non-classical states of light.**

We can relate the photon-number probabilities P_n to $g^{(2)}(0)$, by using the

density matrix operator defined in (4.3), and the equations (4.22) and (4.6) as,

$$g^{(2)}(0) = \frac{\mathrm{Tr}\{\hat{\rho}\hat{n}(\hat{n}-1)\}}{\mathrm{Tr}\{\hat{\rho}\hat{n}\}^2} \tag{4.25}$$

$$= \frac{\sum_{n=0}^{\infty} n(n-1)P_n}{\bar{n}^2}. \tag{4.26}$$

For a photon source where $P_1 \gg P_2 \gg P_{n>2}$, Eq. (4.26) becomes,

$$g^{(2)}(0) \approx \frac{2P_2}{P_1^2}, \tag{4.27}$$

$g^{(2)}(0)$ provides a direct measure of the multi-photon probability for single-photon sources.

4.3 A photon and a beamsplitter

Figure 4.2 shows a basic setup with two click/no-click detectors after the output ports of a beamsplitter to characterize $g^{(2)}(0)$ and the indistinguishability. Both characterizations require to measure the conditional probability of one detector registering an event given that the other detector registers another event simultaneously.

The relation between the inputs and outputs of a beamsplitter is given by the scattering matrix S as [112],

$$S = \begin{pmatrix} t_1 & r_2 e^{i\phi_2} \\ r_1 e^{i\phi_1} & t_2 \end{pmatrix}, \tag{4.28}$$

where r_1 (r_2), t_1 (t_2), without loss of generality are the real reflection and trans-

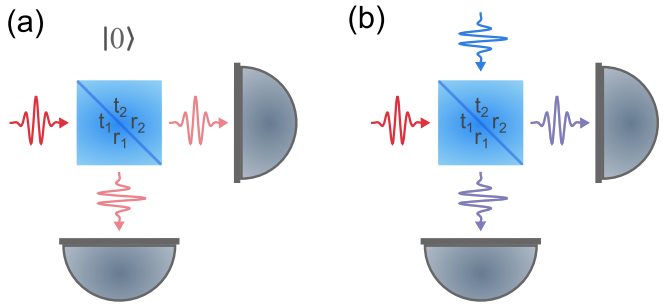

Figure 4.2: **Setup schematic to characterize $g^{(2)}(0)$ and HOM-visibility.** (a) Standard HBT interferometer, if a single photon is incident at port one, and the vacuum state is in port 2. The single photon can only exit one output path at a time. (b) HOM-interferometer, two photons are incident at each BS port. If both photons are indistinguishable, both photons will exit the same port.

mission amplitudes with a relative phase ϕ_1 (ϕ_2) for port 1 (2) as shown in Fig. 4.2.

In terms of the creation and annihilation bosonic operators, and ignoring any frequency dependence of the reflection/transmission amplitudes, the input-output (BS) relation is:

$$\begin{pmatrix} \hat{a}_3 \\ \hat{a}_4 \end{pmatrix} = \begin{pmatrix} t_1 & r_2 e^{i\phi_2} \\ r_1 e^{i\phi_1} & t_2 \end{pmatrix} \begin{pmatrix} \hat{a}_1 \\ \hat{a}_2 \end{pmatrix}, \tag{4.29}$$

here $\hat{a}_i^\dagger(\hat{a}_i)$ creates (annihilates) a photon in the i-port of the BS. In the most general case, the scattering matrix, S, is not symmetric and/or unitary. The non-unitarity is characteristic of a lossy BS, where the total energy of the output fields is lower than the energy of the input fields, and the following inequality holds:

$$\sqrt{T_1 R_2 + R_1 T_2 + 2t_1 r_1 t_2 r_2 \cos\alpha} \leq \sqrt{(1 - T_1 - R_1)(1 - T_2 - R_2)}, \tag{4.30}$$

where $T_i = t_i^2$, $R_i = r_i^2$ are the transmission and reflection coefficients, and $\alpha = \phi_1 + \phi_2$ is constrained by energy conservation. The phase α can have an important effect on two-photon interference by setting an upper-bound on the visibility if $\alpha \neq \pi$ (assuming $g^{(2)}$ is negligibly small) [112]. For the following discussion we

assume $\alpha = \pi$.

Using Eq. (4.29), we can write the BS input-output relations in terms of the number operators as,

$$\hat{n}_3 = T_1\hat{n}_1 + r_1t_2(e^{i\phi_2}\hat{a}_1\hat{a}_2^\dagger + e^{-i\phi_2}\hat{a}_1\hat{a}_2^\dagger) + R_2\hat{n}_2, \tag{4.31}$$

$$\hat{n}_4 = R_1\hat{n}_1 + t_1r_2(e^{i\phi_1}\hat{a}_1\hat{a}_2^\dagger + e^{-i\phi_1}\hat{a}_1\hat{a}_2^\dagger) + T_2\hat{n}_2, . \tag{4.32}$$

In the case for a lossless BS the photon number is conserved $\hat{n}_3+\hat{n}_4 = \hat{n}_1+\hat{n}_2$, this is equivalent as energy conservation for classical fields. The cross term is $\hat{n}_3\hat{n}_4$:

$$\begin{aligned}\hat{n}_3\hat{n}_4 &= T_1R_1\hat{n}_1\left(\hat{n}_1 - \frac{t_2r_2}{t_1r_1}\right) + T_2R_2\hat{n}_2\left(\hat{n}_2 - \frac{t_1r_1}{t_2r_2}\right) \\ &\quad + (T_1T_2 + R_1R_2 - 2t_1r_1t_2r_2)\hat{n}_1\hat{n}_2 \\ &\approx T_1R_1\hat{n}_1(\hat{n}_1 - 1) + T_2R_2\hat{n}_2(\hat{n}_2 - 1) \\ &\quad + (T_1T_2 + R_1R_2 - 2t_1r_1t_2r_2)\hat{n}_1\hat{n}_2,\end{aligned} \tag{4.33, 4.34}$$

where we assume $t_1r_1 \approx t_2r_2$ in the approximation of Eq. (4.33).

It follows that the normalized probability for a simultaneous coincidence event at the detectors is

$$P_N(1_3, 1_4) = \frac{\langle\hat{n}_3\hat{n}_4\rangle}{\langle\hat{n}_3\rangle\,\langle\hat{n}_4\rangle}, \tag{4.35}$$

where the value of $P_N(1_3, 1_4)$ will depend on the initial state at the input ports of the BS. Let us consider the state where the vacuum state is at port 2, and there are at most two photons at port 1, where the probability of a single photon is much great than the probability of a photon pair $P_1 \gg P_2$. The density matrix of

this state is

$$\hat{\rho}_{\text{in}} = P_0 \left|0_1, 0_2\right\rangle\!\left\langle 0_1, 0_2\right| + P_1 \left|1_1, 0_2\right\rangle\!\left\langle 1_1, 0_2\right| + P_2 \left|2_1, 0_2\right\rangle\!\left\langle 2_1, 0_2\right|, \tag{4.36}$$

where $P_0 = 1 - P_1 - P_2$ is the probability of the vacuum state occupation.

The normalized coincidence probability $P_N(1_3, 1_4)$ for $\hat{\rho}_{\text{in}}$ is,

$$P_N(1_3, 1_4) = \frac{\text{Tr}\{\hat{\rho}_{\text{in}}\hat{n}_3\hat{n}_4\}}{\text{Tr}\{\hat{\rho}_{\text{in}}\hat{n}_3\}\,\text{Tr}\{\hat{\rho}_{\text{in}}\hat{n}_4\}} \tag{4.37}$$

$$= \frac{T_1 R_1\,\text{Tr}\{\hat{\rho}_{\text{in}}\hat{n}_1(\hat{n}_1 - 1)\}}{T_1[\text{Tr}\{\hat{\rho}_{\text{in}}\hat{n}_1\}]R_1[\text{Tr}\{\hat{\rho}_{\text{in}}\hat{n}_1\}]} \tag{4.38}$$

$$= \frac{2P_2}{P_1^2}, \tag{4.39}$$

where the only non-zero elements correspond to the operators $\hat{n}_1$ and $\hat{n}_1(\hat{n}_1 - 1)$. Note the equivalence between Eq. (4.38) and (4.25), and Eq. (4.39) and (4.27).

4.4 Indistinguishability

The indistinguishability characterizes the similarity of the spectro-temporal, spatial, and polarization mode between two photons. This characterization can be done for photons from different sources or two subsequent photons from the same source. The indistinguishability is determined by measuring the visibility of the Hong-Ou-Mandel (HOM) interference, which is a quantum phenomenon that is observed for identical particles. If two indistinguishable photons arrive simultaneously, one at each input port of an ideal 50:50 BS, then the photonic fields constructively interfere if they exit the same output port, and destructively interfere when they take opposite paths.

An HOM-interferometer is shown in Figure 4.2 (b), where two incident photons are spatially and temporally overlapped at a 50:50 BS, and there is one detector at each output port. The two-photon interference is characterized by the absence of simultaneous coincidence between the two detectors. If both photons are identical to each other, then the coincidence probability vanishes. In contrast, if the photons are distinguishable, there is a 50% probability of a coincidence that corresponds to the classical limit. The HOM-visibility is obtained by comparing the coincidence probability when the photons are in the same modes, and when they are in orthogonal modes after the beam splitter.

An input state $|1_1, 1_2\rangle$, where the photon at input 1 is identical to the photon at the input 2 of an ideal 50:50 BS, becomes the following output state after HOM-interference

$$|1_1, 1_2\rangle \rightarrow \frac{1}{\sqrt{2}}(|2_3, 0_4\rangle + |0_3, 2_4\rangle) \tag{4.40}$$

where we used Eq. (4.29). In this case, the probability of a coincidence detection is zero and the HOM visibility is one. However, the following factors reduce the visibility from its maximum value [100]:

- one or both photons are not in the same spectro-temporal, spatial and polarization mode,
- there is more than one photon at either BS input port,
- an imperfect 50:50 BS.

Let us analyze the effect of the last two conditions: multi-photon events and imperfect BS. Assuming that the probability of states with more than two photons is negligible and that the probability of a single photon P_1, and the probability of

two photons P_2 are the same at both input ports, the incoming state is represented by the density matrix:

$$\begin{aligned}\hat{\rho}_{\text{in}} = P_0 \left|0_1, 0_2\right\rangle\!\left\langle 0_1, 0_2\right| + P_1 \left|1_1, 0_2\right\rangle\!\left\langle 1_1, 0_2\right| + P_1 \left|0_1, 1_2\right\rangle\!\left\langle 0_1, 1_2\right| \\ + P_1^2 \left|1_1, 1_2\right\rangle\!\left\langle 1_1, 1_2\right| + P_2 \left|2_1, 0_2\right\rangle\!\left\langle 2_1, 0_2\right| + P_2 \left|0_1, 2_2\right\rangle\!\left\langle 0_1, 2_2\right| .\end{aligned} \tag{4.41}$$

Using Eq. (4.33), we find that the coincidence probability $P(1_3, 1_4)$ for $\hat{\rho}_{\text{in}}$ is

$$\begin{aligned}P(1_3, 1_4) &\approx \text{Tr}\{\hat{\rho}_{\text{in}} \hat{n}_3 \hat{n}_4\} \\ &\approx \text{Tr}\{\hat{\rho}_{\text{in}}[T_1 R_1 \hat{n}_1(\hat{n}_1 - 1) + T_2 R_2 \hat{n}_2(\hat{n}_2 - 1) \\ &+ (T_1 T_2 + R_1 R_2 - 2t_1 r_1 t_2 r_2)\hat{n}_1 \hat{n}_2]\} \\ &= (T_1 R_1 + T_2 R_2) 2P_2 + (T_1 T_2 + R_1 R_2 - 2c t_1 r_1 t_2 r_2) P_1^2,\end{aligned} \tag{4.42}$$

where c is the mode overlap in all degrees of freedom of the two incident photons, and it is present in the term where the photons exit the same output port of the BS. Here, the mode overlap is the parameter that describes the indistinguishability obtained from a HOM-interference measurement, and its value can range from zero to one.

Following the assumption that the probability of states with more than two photons is negligible, we use Eq. (4.27), and rewrite the two-photon probability as $P_2 \approx g^{(2)}(0) P_1^2/2$. The coincidence probability becomes:

$$P(1_3, 1_4) \approx \left[T_1 T_2 + R_1 R_2 + (T_1 R_1 + T_2 R_2) g^{(2)}(0) - 2c t_1 r_1 t_2 r_2\right] P_1^2. \tag{4.43}$$

We determine the visibility by comparing the coincidence probability when both photons have the same polarization, and when both photons are in different

polarization states (a convenient way to switch between indistinguishable and fully indistinguishable photons). For the more general case, where the BS coefficients are not the same for the orthogonal polarizations, H, and V, the HOM-visibility $\mathcal{V}$ is

$$\mathcal{V} = \frac{P(1_3, 1_4)_{HV}\big|_{c=0} - P(1_3, 1_4)_{HH}\big|_{c=c}}{P(1_3, 1_4)_{HV}\big|_{c=0}} \tag{4.44}$$

$$\begin{aligned} &= \Big[T_{1_V}T_{2_H} + R_{1_V}R_{2_H} - T_{1_H}T_{2_H} - R_{1_H}R_{2_H} \\ &+ (T_{1_V}R_{1_V} - T_{1_H}R_{1_H})g^{(2)}(0) + 2ct_{1_H}r_{1_H}t_{2_H}r_{2_H}\Big] \\ &\times \Big[T_{1_V}T_{2_H} + R_{1_V}R_{2_H} + (T_{1_V}R_{1_V} + T_{2_H}R_{2_H})g^{(2)}(0)\Big]^{-1}, \end{aligned} \tag{4.45}$$

where we assume that in the case of $P(1_3, 1_4)_{HV}$, the photon at port 1 has H-polarization and the photon at port 2 has V-polarization, similarly for $P(1_3, 1_4)_{HH}$, both incoming photons have $H-$polarization.

In the particular case of a BS with symmetric ports, $T_1 = T_2 = T$ and, $R_1 = R_2 = R$, the visibility reduces to:

$$\mathcal{V} = \frac{2c}{T/R + R/T + 2g^{(2)}(0)}. \tag{4.46}$$

If $T = R = 1/2$ and $g^{(2)}(0) = 0$, then the visibility is equal to the incoming photons mode overlap c.

4.4.1 Time-resolved two-photon quantum interference

So far, we have focused on the probability of coincidence for $\tau = 0$. In this section following the discussion from Ref. [104], we analyze the time dependence

of the joint probability of detecting a photon in port 4 at time $t_0 + \tau$, conditioned on the detection of a photon in port 3 at a time t_0. The field associated with the incoming wave functions of the photons at port 1 and 2 of the BS are defined as,

$$\hat{E}_1(t) = \epsilon_1(t)e^{-i\omega_1 t}\hat{a}_1 \qquad \hat{E}_1^\dagger(t) = \epsilon_2(t)e^{i\omega_1 t}\hat{a}_1^\dagger, \tag{4.47}$$

$$\hat{E}_2(t) = \epsilon_2(t)e^{-i\omega_2 t}\hat{a}_2 \qquad \hat{E}_2^\dagger(t) = \epsilon_2(t)e^{i\omega_2 t}\hat{a}_2^\dagger. \tag{4.48}$$

where we assume that both photons have the same spatial and polarization mode. Using the input-output relations in Eq. (4.29) for an ideal 50:50 BS:

$$\begin{aligned}
\hat{E}_3(t) &= \frac{1}{\sqrt{2}}[\hat{E}_1(t) + i\hat{E}_2(t)] \\
&= \frac{1}{\sqrt{2}}[\zeta_1(t)\hat{a}_1 + i\zeta_2(t)\hat{a}_2] \\
\hat{E}_4(t) &= \frac{1}{\sqrt{2}}[i\hat{E}_1(t) + \hat{E}_2(t)] \\
&= \frac{1}{\sqrt{2}}[i\zeta_1(t)\hat{a}_1 + \zeta_2(t)\hat{a}_2],
\end{aligned} \tag{4.49}$$

here, $\zeta_i = \epsilon_i(t)e^{i\omega_i t}$ are the temporal mode functions. The coincidence probability for the input state $|1_1, 1_2\rangle = \hat{a}_1^\dagger \hat{a}_2^\dagger |0\rangle$ is given by,

$$\begin{aligned}
P_{1_3,1_4}(t_0, \tau) =& \langle 1_1, 1_2|\hat{E}_3^\dagger(t_0)\hat{E}_4^\dagger(t_0+\tau)\hat{E}_4(t_0+\tau)\hat{E}_3(t_0)|1_1, 1_2\rangle \\
&= \frac{1}{4}|\zeta_1(t_0+\tau)\zeta_2(t_0) - \zeta_2(t_0+\tau)\zeta_1(t_0)|^2.
\end{aligned} \tag{4.50}$$

The instantaneous joint probability $P_{1_3,1_4}(t_0, \tau = 0)$ vanishes, no matter how different the temporal mode or the frequency of each photon. By integrating Eq. (4.50)

over all possible values of t_0, we obtain the joint probability as a function of τ:

$$P_{1_3,1_4}(\tau) = \frac{1}{4}\int \mathrm{d}t_0 |\zeta_1(t_0+\tau)\zeta_2(t_0) - \zeta_2(t_0+\tau)\zeta_1(t_0)|^2, \tag{4.51}$$

thus, the width δt_{HOM} of the temporal envelope of $P_{1_3,1_4}(\tau)$ is determined by the convolution of the amplitudes $\epsilon_i(t)$. Moreover, if the photons have different frequencies, quantum beats with frequency $\delta\omega = \omega_2 - \omega_1$ also arise modulating the envelope of $P_{1_3,1_4}(\tau)$. To illustrate this, let us consider a Gaussian amplitude for the photon wave packet as

$$\zeta_i(t) = \frac{1}{(2\pi)^{\frac{1}{4}}\sigma_i} e^{-\frac{(t-t_i)^2}{4\sigma_i^2}} e^{-i\omega_i t}. \tag{4.52}$$

Using Eq. (4.51) and integrating over all possible values of t_1 or t_2, the coincidence probability becomes

$$P_{1_3,1_4}(\tau) = \frac{1}{2}\left(1 - e^{-\frac{1}{8}\left(\frac{1}{\sigma_1^2}+\frac{1}{\sigma_2^2}\right)\tau^2}\cos\delta\omega\tau\right). \tag{4.53}$$

Figure 4.3 shows that $P_{1_3,1_4}(\tau = 0) \to 0$ in Eq. (4.53) for photons with different temporal modes and frequencies.

In practice, detectors have a finite temporal resolution δt_{res}, and measuring $P_{1_3,1_4}(\tau = 0) \to 0$ or quantum beats, require that the detectors resolution is the smallest time scale of the system $\delta t_{\mathrm{HOM}} \gg \delta t_{\mathrm{res}}$, and $1/\delta\omega \gg \delta t_{\mathrm{res}}$. If this condition is satisfied, then both photons are indistinguishable by projecting them in the same spectro-temporal mode for a time-bin δt_{res}. However, these observations become challenging for short pulses or large frequency differences even if the temporal

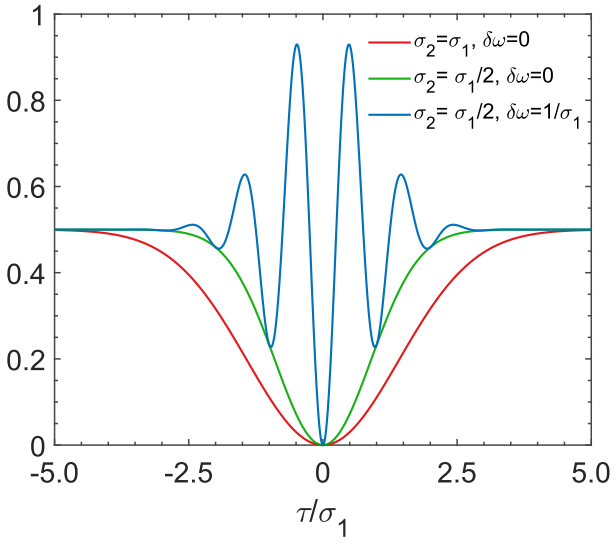

Figure 4.3: **HOM-dip for different photon wave packets.** The HOM-width is determined by σ_1, σ_2 and $\delta\omega$.

resolution of the detector is short enough, since the integration time for a sufficient signal to noise ratio for $P_{1_3,1_4}(\tau)$ is inversely proportional to δt_{res}.

4.5 Fully single-mode efficiency, brightness, and fidelity

Optical quantum information schemes are susceptible to errors if they are not implemented with highly pure and indistinguishable single photons. In addition, scaling up quantum information protocols requires high generation efficiency, since any inefficiency leads to an exponential decrease of the success probability with system size. Finally, the rate of single-photon production provides a limitation on the practicality of any protocol. To that end, we define three metrics that quantify these properties: $\mathcal{F}$, the single-photon fidelity, which is the fraction of emission that consists of a single photon in a single spectral, temporal, polarization, and spatial mode; P_1^{sm}, the probability of generating a single photon in the desired mode; and $\mathcal{R}$, the fully single-mode rate, which is the rate of photon production in the desired mode.

Assuming that the probability of multi-photon events greater than two is negligible, the only outcomes from a source are: single photons in the desired mode with probability P_1^{sm}, single photons in an undesirable mode with probability P_1', two photons in any mode with probability P_2, and null events with probability P_0. Experimentally, the following quantities are measured: the detector-corrected fibered efficiency P; the HOM visibility, $\mathcal{V}$; and the second-order autocorrelation function, $g^{(2)}(0)$. These are given by:

$$P = \frac{1 - P_0}{\eta_{\mathrm{det}}} \approx P_1^{\mathrm{sm}} + P_1' + (2 - \eta_{\mathrm{det}})P_2, \tag{4.54}$$

$$\mathcal{V} = \frac{P_1^{\mathrm{sm}}}{P_1^{\mathrm{sm}} + P_1'}, \tag{4.55}$$

$$g^{(2)}(0) \approx \frac{2P_2}{(P_1^{\mathrm{sm}} + P_1')^2}. \tag{4.56}$$

Here we used Eq. (4.11), where we have assumed that the measurements are taken with standard click/no-click detectors with efficiency η_{det}. In Eq. (4.55) we have assumed that the visibility $\mathcal{V}$ is corrected for multi-photon events (see Eq. (4.45)).

Solving the system of equations for P_1^{sm} to second order in $g^{(2)}(0)$, we get the fully single-mode efficiency:

$$P_1^{\mathrm{sm}} = P\mathcal{V}\left[1 - \frac{Pg^{(2)}(0)}{2}(2 - \eta_{\mathrm{det}})\left(1 - Pg^{(2)}(0)(2 - \eta_{\mathrm{det}})\right)\right]. \tag{4.57}$$

This figure of merit characterizes the efficiency of a fully single-mode single-photon source, including the spectro-temporal coherence measured from the HOM visibility. For many quantum information applications that demand pure indistinguishable single photons, the success probability scales with P_1^{sm} rather than other commonly reported metrics, such as the fibered efficiency, P.

We report the source fully single-mode single-photon rate as $\mathcal{R} = R_{\text{eff}} P_1^{\text{sm}}$, where R_{eff} is the clock rate weighted by the experimental duty cycle. Apart from source rate, the fraction of emission in the desirable mode, quantified by the fidelity $\mathcal{F}$, also matters for applications:

$$\mathcal{F} = 1 - \frac{P_1' + P_2}{P} = \frac{P_1^{\text{sm}}}{P}. \tag{4.58}$$

4.5.1 On-demand single-photon sources performance

Figure 4.4 shows P_1^{sm}, $\mathcal{F}$, and $\mathcal{R}$ for a sample of different single-photon sources[3]. The sources considered are listed in Table 4.2 and in Table 4.3, for solid-state-based sources, and atomic-based sources respectively. In this data collection, we used the quoted η_{det} to determine the detector corrected efficiency P, but assumed $\eta_{\text{det}} = 1$ in Eq. (4.57) to obtain P_1^{sm}. Thus, for sources with a non-negligible $g^{(2)}(0)$, P_1^{sm} is an upper bound. Narrow-bandwidth sources naturally compatible with coherent atomic systems are indicated with filled symbols in Fig. 4.4.

Type	Ref	R (MHz)	P	V	$g^{(2)}(0)$	P_1^{sm}	$\mathcal{R} \times 10^6$ (s^{-1})	$\mathcal{F}$
SPDC	[113]	76	≈0.01	0.91	0.09	0.009	0.69	0.910
SPDC	[114]	80	0.049	0.962	0.03	0.047	3.74	0.961
MUX	[115]	10	≈0.002	0.91	∼0.2	0.002	0.02	0.910
MUX	[116]	0.5	0.667	0.91	0.269	0.562	0.28	0.843
QD	[117]	82	≈0.02	0.996	0.0028	0.020	1.63	0.996
QD	[118]	80	≈ 0.08	0.7	0.013	0.056	4.47	0.699
QD	[119]	76	0.337	0.93	0.027	0.312	23.71	0.926
QD	[120]	76	0.10	0.94	0.006	0.094	7.14	0.940
QD	[121]	76	0.24	0.975	0.025	0.233	17.77	0.972
QD	[122]	81	0.11	0.92	0.05	0.101	8.17	0.918

Table 4.2: **Performance of solid state single-photon sources.** Spontaneous parametric down conversion (SPDC), multiplexed-heralded-single-photon source (MUX) and, quantum dot (QD). Values estimated from available data.

[3]There are much more sources in the literature, but we concentrated on those that reported sufficient measurements to calculate P_1^{sm}, $\mathcal{R}$ and $\mathcal{F}$

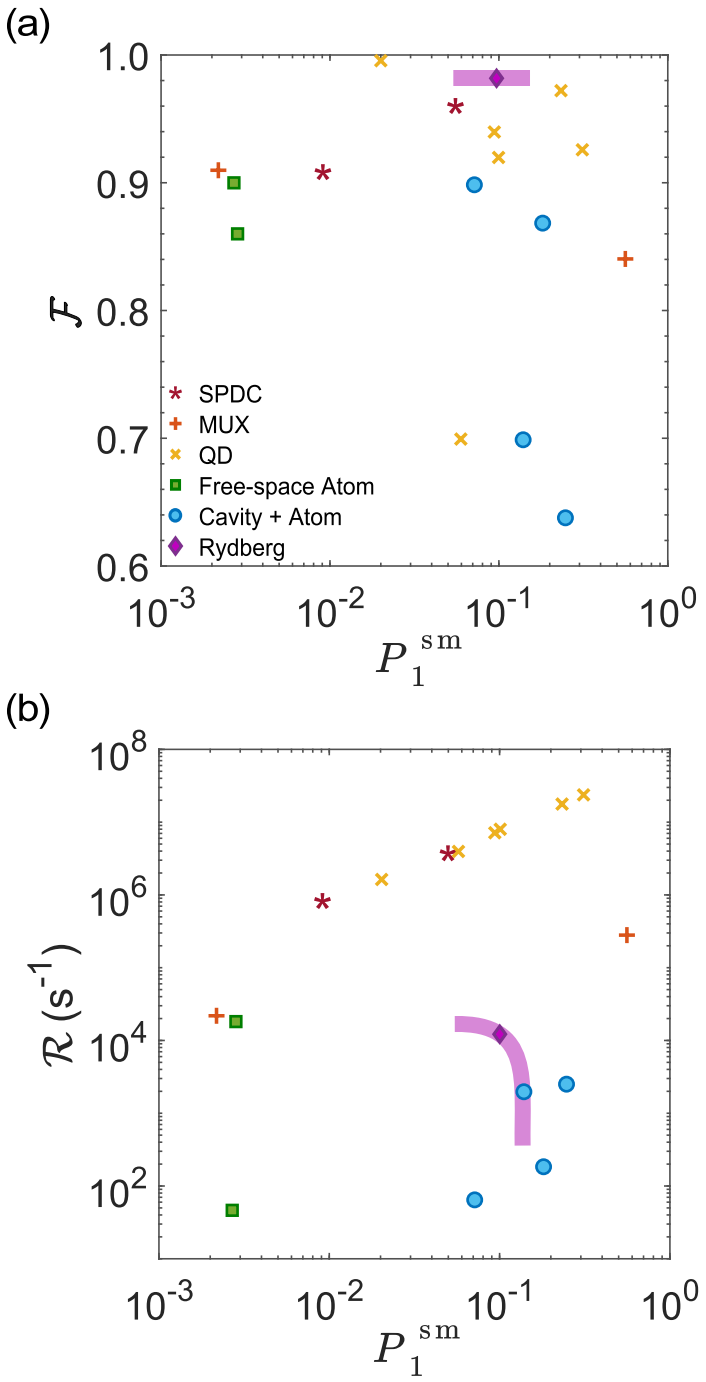

Figure 4.4: **Performance of a sample from different single-photon sources.** Solid-state systems considered are spontaneous parametric down-conversion (SPDC) [113, 114], multiplexed-heralded-single-photon source (MUX-HSPS) [115, 116] and quantum dots (QD) [117–122]. Atomic systems considered are single atoms in free space [15, 123], atoms in cavities [124–127], and Rydberg is the source developed in this thesis work and detailed in Chapter 6. (a) Fidelity $\mathcal{F}$ vs. fully single-mode single-photon efficiency P_1^{sm}. (b) Single-mode single-photon rate $\mathcal{R}$ vs. fully single-mode single-photon efficiency P_1^{sm}.

Type	Ref	Duty Cycle (%)	R (MHz)	P	V	$g^{(2)}(0)$	P_1^{sm}	$\mathcal{R} \times 10^3$ (s^{-1})	$\mathcal{F}$
Yb ion	[123]	80	8	0.003	0.86	$\sim 10^{-3}$	0.003	18.16	0.860
Rb Atom	[15]	33	0.052	0.003	0.9	$\sim 10^{-3}$	0.003	0.05	0.899
Ensemble in cavity	[124]	≈ 1.8	0.05	0.08	0.9	0.05	0.072	0.06	0.898
Atom in cavity	[125]	≈ 2	0.7	0.2	0.7	$\sim 10^{-2}$	0.140	1.96	0.699
Atom in cavity	[126]	0.1	1	0.21	0.87	0.02	0.182	0.18	0.868
Atom in cavity	[127]	100	0.01	0.39	0.64	0.02	0.249	2.49	0.637
Rydberg	*	60	0.2	0.100	0.982	5×10^{-4}	0.098	11.8	0.982
Rydberg	*	60	0.5	0.4	0.99	$\approx 10^{-4}$	≈ 0.4	120	0.99

Table 4.3: **Performance of different atomic single-photon sources.** Here $\mathcal{R}$ is weighted by the duty cycle of operation. Values estimated from available data. *Rydberg source developed in this thesis work see Chapter 6 for details.

As is evident from Fig. 4.4 and Table 4.2- 4.3 that show the wide variety of performance from different sources, an ideal single-photon source is still lacking, there are sources that have developed a high quality in one parameter while compromising in another. This is in general the case for solid-state sources where fidelity can be compromised for efficiency, although quantum dots have increasingly improved over the years to decrease this trade-off [101].

The main limitation for atomic sources is their rate due to their narrow bandwidth. As there is a deeper understanding of dephasing mechanisms hindering fidelity, with better cooling and manipulation techniques and enhanced light-matter coupling, we can also expect improvement for atomic sources.

Chapter 5: Experimental Apparatus

This chapter describes the design and implementation of the experimental apparatus to produce ^{87}Rb cold Rydberg ensembles for the experiments reported in Chapter 6 to Chapter 8. The design was based on previous setups investigating Rydberg interactions in dense cold-atomic mediums [63, 75, 80].

First, we discuss the physical requirements to study Rydberg atoms. The second section describes the vacuum system components, along with the in-vacuum elements to coherently manipulate Rydberg atoms with fine control. The last section outlines the experimental sequence and details of all the different parts and systems to probe Rydberg interactions in a cold atomic medium.

5.1 Experimental requirements

As discussed in Chapter 3, the collective coupling strength scales with $\sqrt{\mathrm{OD}}$, and we require a dense atomic medium where the van der Waals interaction among the Rydberg atoms is the largest energy scale dominating over dephasing mechanisms such as Doppler broadening. These conditions allow us to observe quantum nonlinearities, interacting slow-light polaritons, or collective spin-wave excitations.

High optical densities improve the collective coupling of the probe light with the atoms. The ratio of the resonant absorption length of the medium $l_a = 1/(\rho\sigma_0)$ to the blockade radius measures the interaction strength, parametrized by $\mathrm{OD}_b =$

r_b/l_a. Typically strong Rydberg interactions occur for $\mathrm{OD}_b > 1$.

Dephasing between the ground-state and Rydberg-states and Doppler broadening can reduce the range and coherence of the blockade effect by canceling the energy shift from Rydberg interactions. Low temperatures allow us to diminish dephasing due to motional dynamics, largely neglect the motional degrees of freedom, and coherently manipulate the internal state of the atoms.

Using standard laser cooling and trapping techniques, we produce dense cold ensembles of ^{87}Rb atoms, reaching densities $\rho \sim 10^{12}$ cm^{-3} with mean temperatures of ~ 10 μK in an optical dipole trap. This configuration allows us to investigate the dispersive and dissipative dynamics of Rydberg interactions. Furthermore, we can modify the dipole trap geometry to study different regimes. For example, single-photon generation requires a single Rydberg spin-wave excitation, which is achieved in a fully blockaded ensemble, where the blockade volume is larger than the trapped atom cloud. On the other hand, probing few-body physics involves investigating the interactions of multiple Rydberg excitations inside an elongated atomic medium with longer interaction times.

Throughout this thesis, we study the longitudinal nature of the interactions, reducing the dimensionality of the system by focusing the probe waist much smaller than the blockade radius over the length of the cloud.

5.2 Vacuum system

The main components of our vacuum system are an ion pump, bellows containing a natural Rb source, and various electrical feedthroughs that provide high-voltage and low-voltage for the in-vacuum electrodes. Figure 5.2 shows all these

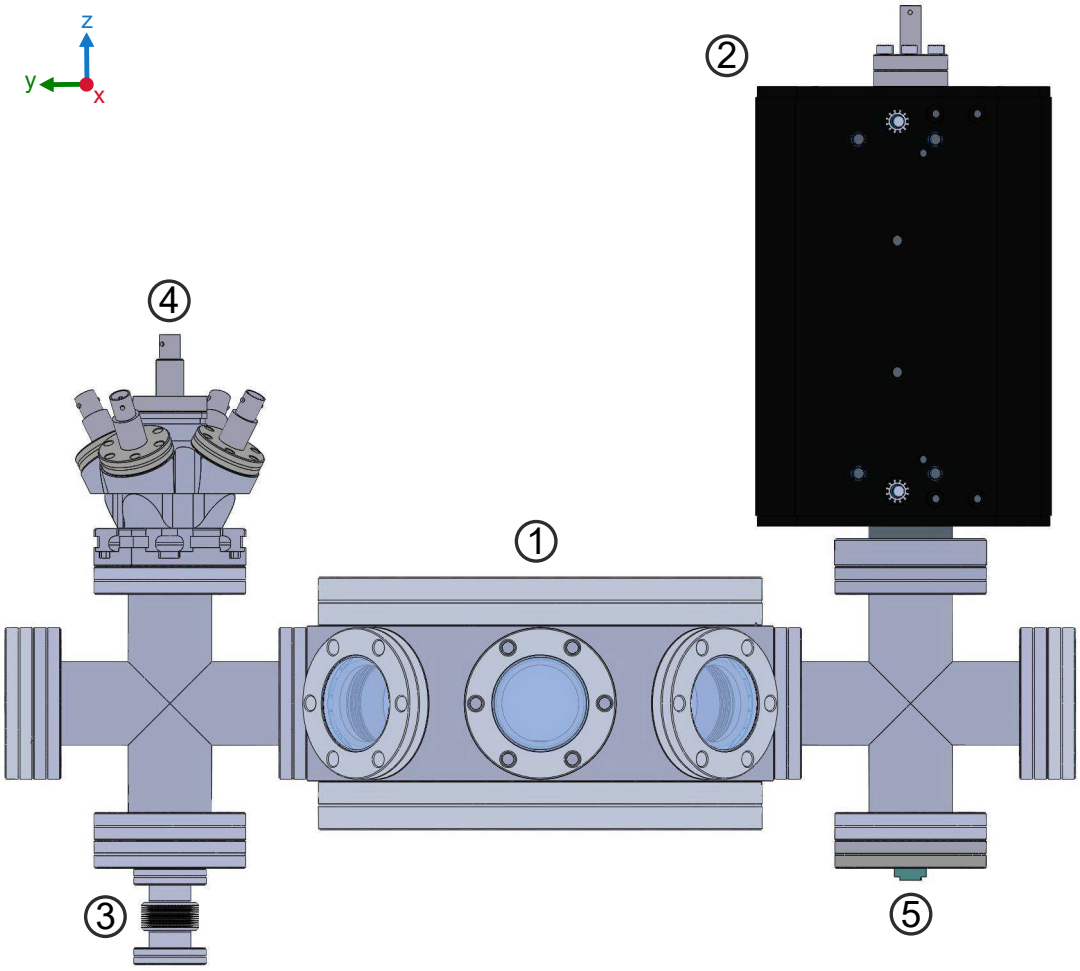

Figure 5.1: **Vacuum system components.** (1) Stainless-steel spherical-octagon chamber. (2) Ion-pump with magnetic shielding. (3) Metallic bellows containing Rb ampule is connected to the cross with a zero-length reducer. (4) HV electrical feedthroughs connected by CF multiplexer. (5) 9 pin D-Sub 2.75" CF feedthrough for low voltage. Viewports with optical access are indicated by light-grey CF flanges.

components are connected through crosses to the main chamber. An all-metal gate valve lies behind the ion pump (not shown), which was used for the initial pumping of the system.

The main chamber is a Kimball Physics spherical octagon compatible with knife-edge conflat CF components for ultra-high vacuum (UHV). It is made of 316L non-magnetic stainless steel (ss) with 8" of inner diameter, 8" CF flanges on top and bottom, and eight 2.75" CF flanges. All of these ports have optical access

to allow for cooling, pumping, trapping, and excitation of the atoms. During the assembly we installed custom made washers under the vacuum bolts of the viewports to mount 60-mm cage systems directly into the octagon (for the design of these washers see Creston Herold thesis [128]).

The Titanium ion pump from Gamma Vacuum (45S-CV-2D-SC-110-N) is magnetically shielded and was placed as far as possible from the atoms to avoid Zeeman shifts due to stray magnetic fields. The pumping speed of 45 L/s keeps the measured background pressure to 6×10^{-10} Torr at the pump when the Rb oven is off. The ion pump is permanently heated to 60 C to avoid Rb deposition.

The bulk Rb source is contained inside the bellows located at the bottom of one of the crosses, and it is attached through a 2.75" to 1.33" zero-length reducer flange. We originally had a custom machined aluminum cylinder to cover the bellows and heated ($\sim$100 C) or cooled ($\sim$14 C) it with a thermoelectric cooler with water-cooling system shared with the quadrupole coils, but this configuration ultimately failed. Currently, the oven is heated with fiberglass heating tape and covered with Al foil. A temperature controller regulates the heating tape voltage with a solid-state relay turning on/off the voltage from a Variac. The temperature is set to 60 C to keep the pressure reading to $\sim 10^{-9}$ Torr at the pump during experimental cycles.

All eight 2.75" CF viewports have fused silica windows with a 304L non-magnetic ss flange. Six of them are along the cooling, imaging, and pumping beam paths and have a broad-band anti-reflection (AR) coating for 550 nm - 1100 nm wavelengths; the other two have a custom AR coating for 470 nm - 490 nm, and 780 nm - 1064 nm for the control, probe, and trapping beams. The 8" CF

viewports have borosilicate windows (they are significantly cheaper but have lower transmission than their fused silica counterpart) with a custom AR coating for 780 nm - 1064 nm.

Finally, there are five Miniature High Voltage (MHV) coaxial feedthroughs attached to a 2.75" to 1.33" CF multiplexer adapter (Kimball Physics). They are connected to the in-vacuum selective ionization components with kapton-coated wire[1]. The 9-pin D-Sub 2.75" CF feedthrough is connected to eight in-vacuum low-voltage electrodes to cancel out stray electric fields.

5.2.1 In-vacuum elements

We installed the following components in-vacuum to achieve fine control over the excitation of the Rydberg states and their interactions:

- A pair of aspheric lenses to tightly focus the probe beam with reduced aberrations, such that the probe beam waist is smaller than the blockade radius along the length of the atomic cloud.

- Eight low-voltage electrodes to compensate DC electric fields in any direction, and avoid shifts on the Rydberg transition due to the high static polarizabilities. These electrodes can also tune Förster resonances by shifting the Rydberg state.

- A selective-state ionization system to identify and detect Rydberg states, and eliminate contaminant states produced by ground-state atoms and Rydberg electron collisions [129]. This system consists of a micro-channel plate

[1]Kapton is a film used as an electrical insulator, it is temperature-stable up to 400 C. It does not out-gas making it compatible with UHV

(MCP) detector, a grid in front of the detector, and an HV electrode. We can also use the latter to do microwave addressing between Rydberg states (and also between the hyperfine manifolds of the ground states).

All these elements are attached to two platforms, which are held in place by a set of groove grabbers (Kimball physics), as shown in Fig. 5.2. The platforms, electrodes, holders, and mounts are made of 316L ss and machined with a ± 50.8 μm tolerance. We also electro-polished these parts to avoid rough surfaces. The four slots along around the center of both platforms to avoid the formation of Eddy currents when changing the magnetic field produced by the surrounding coils.

The lens mounts, platforms, and groove grabbers are all electrically connected to the chamber (the latter is connected to ground through the optical table). At the same time, the elements for fine electric field control and ionization system are isolated from the ground with ceramic (MACOR) hat washers. All the screws used to attach the in-vacuum components are vented, this is to prevent the creation of air pockets between the end of the screw and bottom of the tapped hole that could increase the pressure inside the chamber.

The arrangement of the in-vacuum elements in the platforms allow us to create a magneto-optical trap (MOT) in the 90° optimal configuration with 25 mm diameter beams (see Fig. 5.2(c)).

5.2.1.1 Aspheric lenses

The in-vacuum lenses have multiple purposes: they focus down the probe and control beams to the atoms, collect probe photons, and form a crossed dipole trap, as seen in Fig. 5.2(c). The lenses are A25-40FPX from Asphericon and have

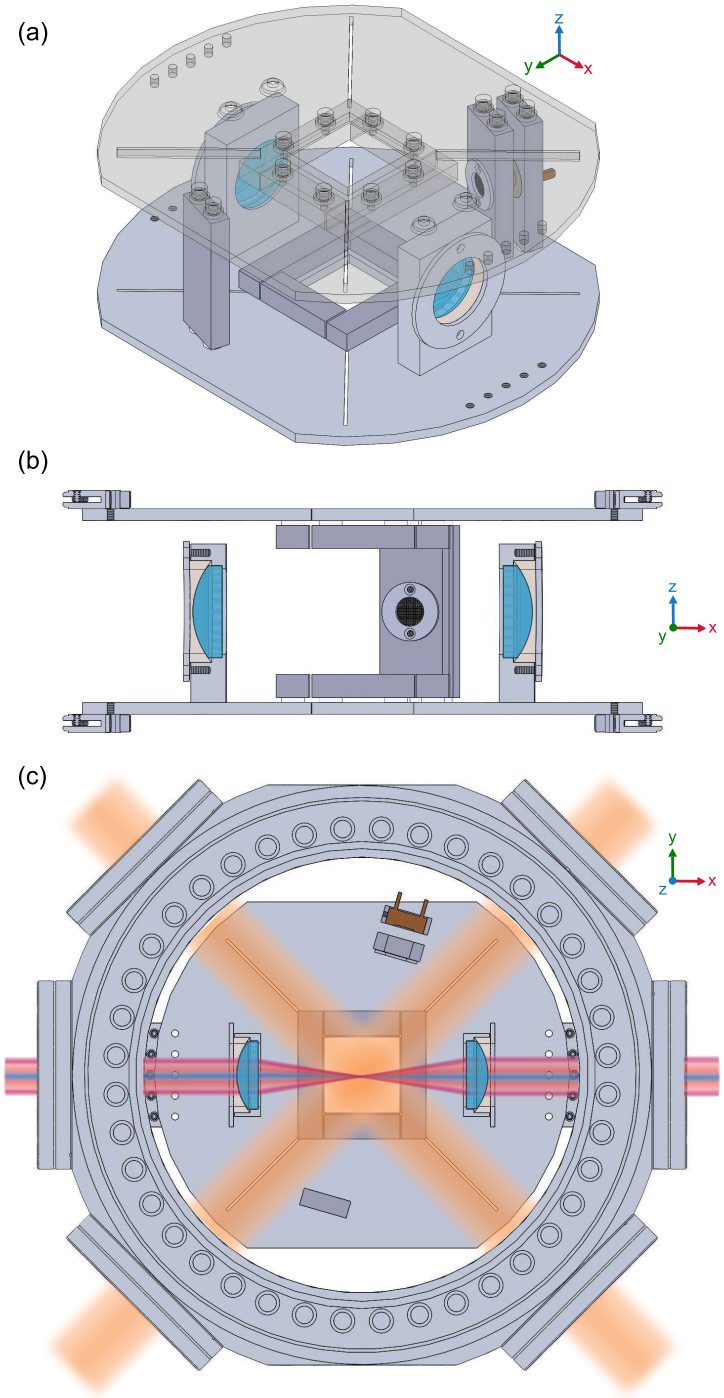

Figure 5.2: **Vacuum system components.** (a) Isometric view of the in-vacuum system. The components at the top consisting of the top platform and low-voltage electrodes are made transparent for clarity. (b) Side cross-section view. Fix mounts hold the aspheric lenses. The parts that are electrically isolated from the ground are depicted with a darker grey. (c) Top view. The in-vacuum configuration allows for cooling with 1" diameter beams (orange) at 90°. The probe (light-red), control (blue), and dipole beams (dark red) go through the aspheric lenses. The crossed dipole beams propagate off-axis from the lenses optical axis and cross at the focal plane.

a custom AR coating for 470 nm - 490 nm and 780 nm - 1064 nm.

The lenses are separated 76.4 cm from each other (which corresponds to twice the focal length[2] for 1012 nm), they are held in place by fixed mounts using a machined PEEK washer[3], and a retaining ring screwed to the mount (see Fig. 5.2(b)).

The maximum NA for this assembly is 0.3., however, to focus the probe beam waist down to $\simeq 3.3$ μm only ≈ 0.1 NA is needed. We achieve a nearly aberration-free Gaussian beam of at the mid-distance of the lenses. The NA for the control and dipole beams is about $\simeq 0.01$. Thus aberrations are negligible, even for the dipole beams propagating off-axis.

During the assembly, we aligned the lenses by using a precisely machined Al block to set the distance between the mounts, and 50 μm shims to adjust the relative height. First, we fix one of the mounts and screw a metal target with a hole concentric with the center of the lens. We aligned a HeNe laser beam to the center of the target, while overlapping the back-reflections of the incoming beam with a flat mirror flushed to the metal target. Once the beam is centered at the target and parallel to the optical axis, we put apertures along the beam path. Then, we carefully move the position of the second mount with a metal target, such that the center of the target is concentric to the beam, while making sure that the beam goes through the far field aperture in the process. We slightly rotated the platform such that there is small angle between the optical axis of the lenses and the center of the chamber ports to avoid interference effects. Since we use a relatively low NA, the alignment does not demand the higher precision

[2]In hindsight, the determination of the 780-nm probe focus, and the relative alignment of the control and dipole beams with respect to the probe, would have been easier if we would have set the distance between the lenses as twice the focal length of the 780-nm light.

[3]PEEK is UHV compatible and has excellent mechanical properties that are maintained at high temperatures, resulting in crack-free lenses after baking the vacuum system at 300 C.

required for other single-atom addressing systems with high NA.

5.2.1.2 Electric field control, Selective ionization system and Microwave addressing

An octopole configuration of electrodes is used to cancel stray electric fields. Figures 5.2(a)-(b) show their arrangement. They consist of two sets of four electrodes with an equal offset from the horizontal plane. Each electrode has a pair of tapped holes and is attached to the platform with 4-40 bolts using ceramic hat-washers on each side of the platform to isolate the electrode electrically. We carefully stripped 14 AWG kapton-wire and wired it around between the washer and the bolt head before tightening, then we used crimp connectors to attach them to the 9-pin D-sub feedthrough.

During the assembly, all electrical connections were intact, but after baking the vacuum system, we realized that one of the bottom electrodes was shorted to ground. However, COMSOL simulations show that we can create a homogeneous or gradient electric field at the atoms with seven working electrodes. Figures 5.3(a)-(c) demonstrate we can finely tune the Rydberg-state resonance by manipulating the electric field in the x-, y- and z- planes, and serves as a calibration of the electric field control.

The selective field ionization system consists of a MCP (MICROTRON MINIATURE APD Photonis) for electron detection, a high-transparency mesh used as a Faraday cage in front of the detector to shield the atoms from the MCP voltage, and a large electrode facing the MCP assembly and equidistant from the atoms. 30 AGW kapton wire and barrel connectors link all these elements to the MHV

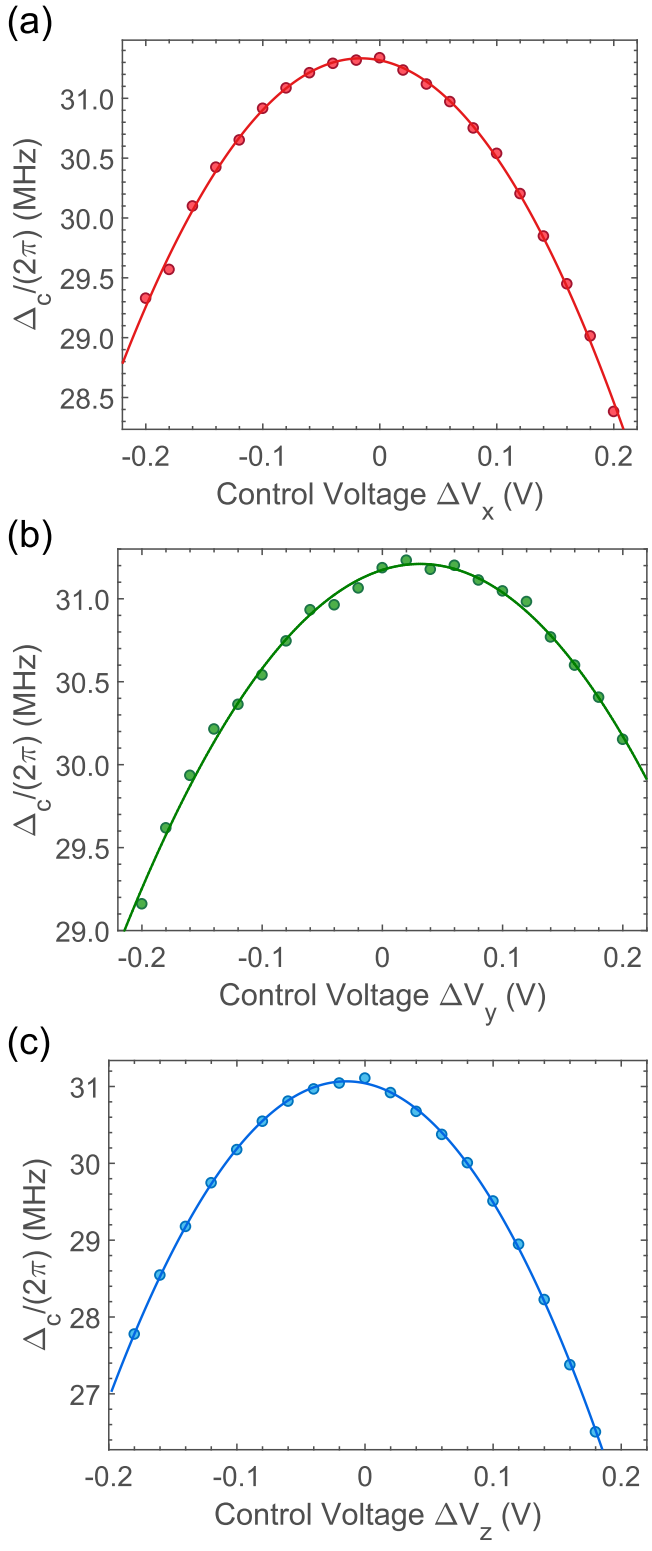

Figure 5.3: **DC electric field control for $99S_{1/2}$ Rydberg state with a detuning Δ_c from resonance.** Measurements (circles) of voltage control and quadratic fits (solid lines) along: (a) the x-plane with electric fields of 103 ± 3 mV/cm per volt applied (b) the y-plane with electric fields of 79 ± 3 mV/cm per volt applied. (c) the z-plane with electric fields of 143 ± 2 mV/cm per volt applied.

coaxial connectors. We measure an electric field of 32±1 mV/cm per volt at the atoms when the MCP and the Faraday cage are grounded and applying a voltage to the large electrode. We can selectively ionize $n > 45$ when applying ±2 kV on both sides.

Since the lenses are not coated with a metallic coating or shielded with a Faraday cage, the dielectric surfaces directly facing the atoms get polarized/charged when the control beam is on and when we charge any of the electrodes with the voltage necessary to field ionize. These surfaces are likely coated with Rb and wavelengths shorter than 548 nm (corresponding to the work function of Rb) can photoionize and generate free electrons, while also ejecting neutral Rb atoms, an effect known as light-induced atom desorption (LIAD) in alkali atoms [130, 131]. The polarization/charging of the stray fields due to the LIAD and high-voltage electrodes slowly changes with a time-scale of minutes, and it is not possible to compensate for the residual electric fields with the control electrodes. This is a problem even for states $n > 100$, which only require an ionizing electric field < 4 V/cm due to their large polarizability > 6 GHz(V/cm)^2, and prevent us from doing selective field ionization with the MCP. Fortunately, we do not charge/polarize the dielectric surfaces for stray electric field compensation, where just apply a few millivolts to the octopole electrodes.

We use the large electrode to address excitations of nearby Rydberg states via microwave fields. For $n \sim 100$ we can obtain more than 100 MHz of Rabi frequency with 2 dBm of power at the MHV connector. Figure 5.4 shows Rabi flopping between $139S_{1/2}$ and $139P_{3/2}$ at a microwave frequency of 1.267 GHz.

Considerably more power is needed, ≈33 dBm to generate Rabi frequencies of

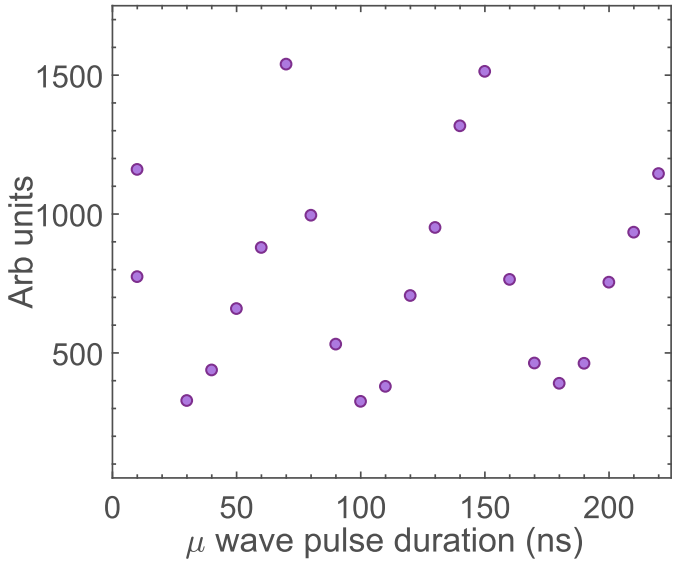

Figure 5.4: **Microwave transition between Rydberg states $S \leftrightarrow P$.** Rabi flopping between $139S_{1/2}$ and $139P_{3/2}$ with a Rabi frequency of $\Omega_\mu/(2\pi) = 13.5 \pm 1.0$ MHz. As determined by photon retrieval from a stored $139S_{1/2}$ spin wave.

$\Omega_\mu/(2\pi) = 1$ kHz at 6.83 GHz between the hyperfine manifolds of the ground-state. We are unable to drive any of the low-voltage electrodes to increase the Rabi frequency at the atoms since the D-sub type connector seems to significantly attenuate fields at microwave frequencies.

5.3 Making cold atomic ensembles

We describe in detail the experimental procedure and components to create Rydberg excitations in cold-atomic ensembles in the next subsections. We start with different stages of cooling the atoms to get high densities $\approx 10^{12}$ cm^{-3} with mean temperatures ≈ 10 μK into the dipole trap. Reaching this regime allows us to coherently excite Rydberg excitations and probe their dynamics for as long as 600 ms before we need to repeat the loading cycle.

5.3.1 Laser Cooling

We start the experiment by loading the atoms from the background rubidium pressure in a MOT. A MOT consists of a magnetic gradient field created by a pair of coils in a quadruple configuration, and a pair of counter-propagating beams with opposite circular polarization in each axis (x, y, z) [132].

Since ^{87}Rb is a multi-level system with two hyperfine manifolds in the ground-state $F = 1$ and $F = 2$. A single cooling beam addressing the closed transition ($|5S_{1/2}, F = 2\rangle \rightarrow |5P_{3/2}, F = 3\rangle$) would eventually off-resonantly pump the atomic cloud into a dark-state in the $F = 1$ manifold. The MOT, therefore, needs two beams: a cooling beam red-detuned from the closed transition resonance, and a repump beam that pumps the atoms out of the dark-state to $F = 2$ to continue the cooling cycle. During the MOT stage, we reach temperatures around 150-200 μK. The MOT loading typically lasts for 250 ms, but we change the loading time to vary the final optical depth in the dipole trap. Figure 5.5 depicts our MOT configuration where we use polarization-maintaining fibers (PMF) to have a well defined transverse and polarization mode for the incoming cooling beams.

Following the first cooling stage, we spatially compressed the MOT (C-MOT) by ramping-up the field magnetic gradient 2.25x. This step increases the density and reduces the sensitivity to stray magnetic field gradients in preparation for molasses. Then, we implement a temporal "dark spot MOT" where we decrease the cooling intensity to $\approx$ 8.5 mW/cm^2, with a dim repump light intensity $\approx$ 0.01 mW/cm^2, while increasing the cooling detuning 5x to reduce the outwards radiation pressure from the scattering of the closed transition [133].

The final cooling phase consists of implementing a Λ-gray molasses, using the

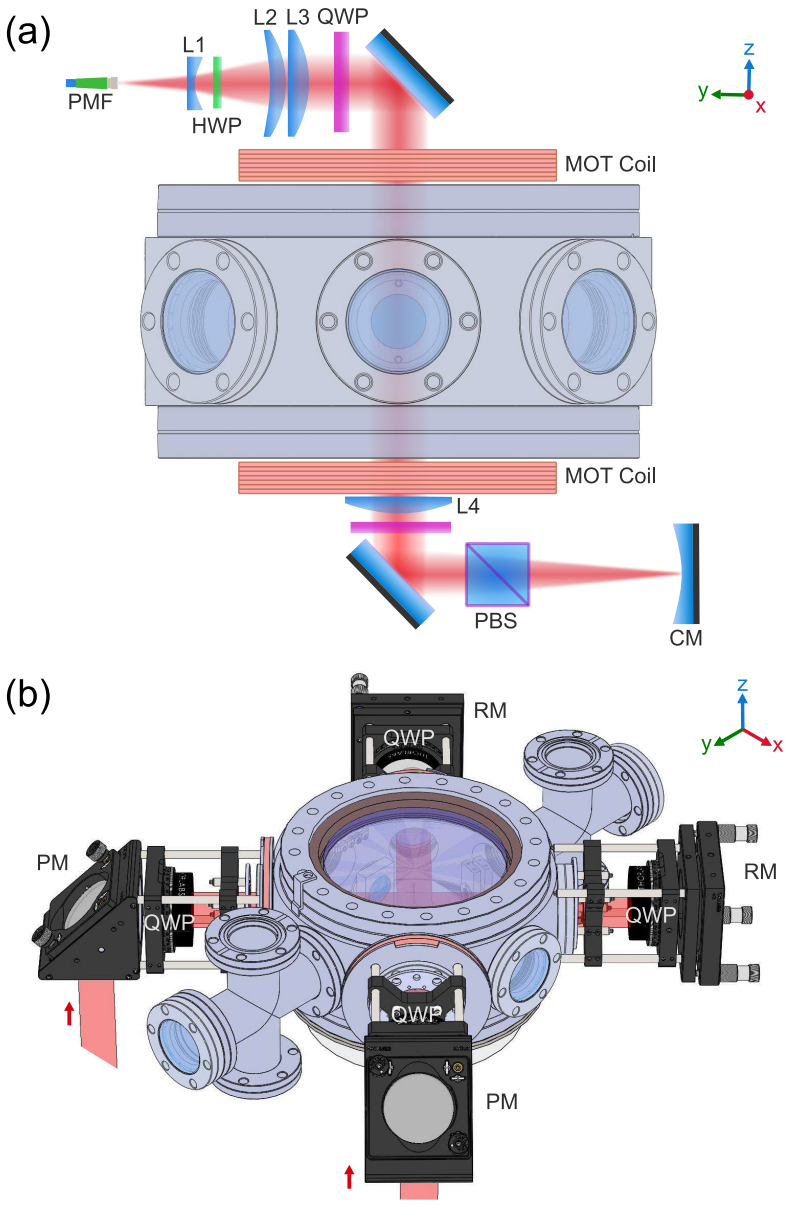

Figure 5.5: **Laser cooling beams configuration.** (a) Beam propagating along the vertical axis. The three lenses L1 (plano-concave f=-30 mm), L2 (meniscus f=150 mm) and L3 (plano-convex f=100 mm) form a compact Galilean telescope to expand and collimate the 2.5 μm beam from the PMF to a 25 mm beam diameter. The half-wave plate ($\lambda/2$) and quarter-wave plates ($\lambda/4$) set the circular polarization. The beam path is shared with the imaging beam, which has opposite polarization and is focused by L4 (f=145 mm); they are separated at the polarizing beam splitter (PBS). The cooling light is retroreflected and re-collimated at the atoms by using a concave mirror (CM f=150 mm). The MOT-coils are in a quadrupole configuration to generate a magnetic field gradient. (b) Cooling beams propagating on the xy-plane. Two sets of periscopes raise the beams to the height of the chamber. The second periscope mirrors (PM), retro-reflecting mirrors (RM) and polarizing optics are held through 2.75" CF to 30 mm Thorlabs cage adapters. The bottom parts of the periscope and MOT coils are not shown.

cooling and repump lasers in a Λ-Raman configuration. Gray molasses works similarly to polarization gradient cooling with far-detuned, dim cooling beams where the magnetic field is zeroed, and there is a polarization lattice along each orthogonal direction [134]. The difference lies in the existence of dark-states. Atoms moving sufficiently slowly remain adiabatically in the dark state created by the lambda-coupling configuration. Instead, fast-moving atoms follow diabatic transitions to the bright states and cool by scattering photons. Blue-detuning the repump and cooling laser from the $|5S_{1/2}, F = 2\rangle \rightarrow |5P_{3/2}, F = 2\rangle$ in a Raman-resonant Λ-configuration creates dark states in a superposition of the ground state $F = 1$ and $F = 2$, dominated by the $F = 1$ sublevel [135]. This process increases the phase-space density by cooling and decreasing the outward radiation pressure. Figure 5.6(a) illustrates the configuration of the Λ-gray molasses in the D2-line, and the narrow enhancement of the peak OD around the Raman resonance is in Figure 5.6(b). We can achieve final temperatures of ≈10 μK with Λ-gray molasses, compared to ≈ 40 μK with molasses alone.

5.3.1.1 Cooling Lasers System

The repump light is produced by a Toptica DL-PRO laser with an external cavity diode laser (ECDL), and it acts as a controller laser. It is locked to the crossover peak of $|5S_{1/2}, F = 1\rangle \rightarrow |5P_{3/2}, F = 0\rangle$ observed in a Doppler-free saturation absorption signal. The probe beam gets equally split in two, where only one beam is overlapped with a counter-propagating pump inside a vapor cell heated at 40 C. The cell is magnetically and thermally isolated. The heating tape is wrapped around the windows of the cell to avoid Rb deposition and additional

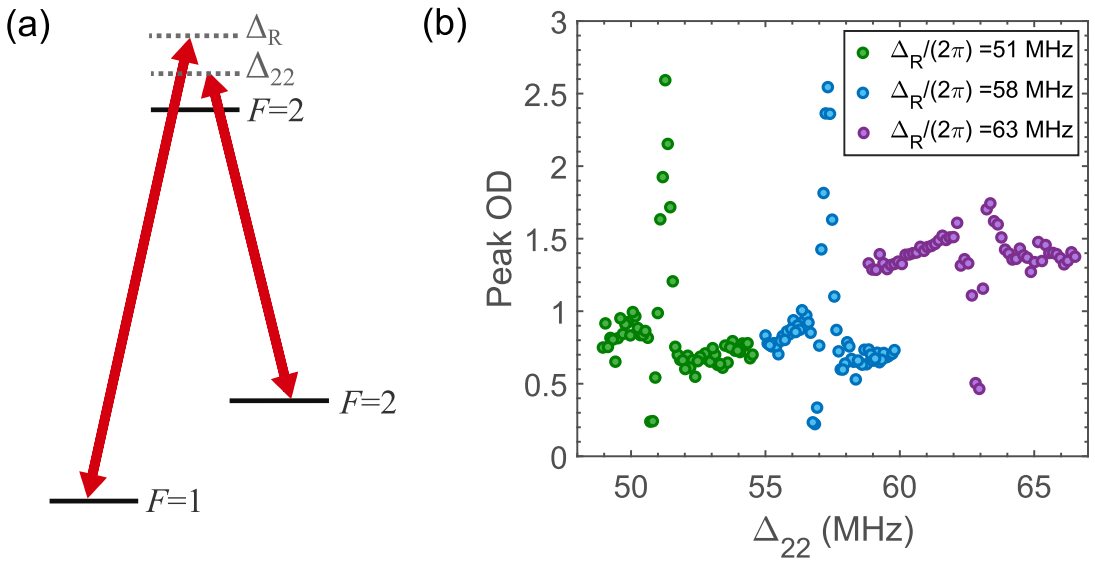

Figure 5.6: **Λ-gray molasses in the D2-line.** (a) Hyperfine levels used in the gray molasses, Δ_{22} is the detuning from the $|5S_{1/2}, F = 2\rangle \rightarrow |5P_{3/2}, F = 2\rangle$ cooling transition, and Δ_R is the detuning from the $|5S_{1/2}, F = 1\rangle \rightarrow |5P_{3/2}, F = 2\rangle$ for the repump light. (b) Measured peak OD after 1.1 ms of releasing the dipole trap and scanning Δ_{22} for a fixed Δ_R. As the detuning Δ_R increases the gray molasses does not work as well due to off-resonant scattering from $|5P_{3/2}, F = 3\rangle$ (see $\Delta_R/(2\pi) = 63$ MHz.

absorption of the probe signal. After interacting with the atoms, each probe is focused on a balanced photodetector (Thorlabs PDB220A2) that subtracts both signals eliminating the Doppler background. A Toptica digital controller (DLC-pro) modulates the laser current at 20 kHz and produces the error signal that is fed back to the laser current. The rest of the repump laser is divided into two fibers, the first one sends the light to a wavemeter and beatnote setup. The other directs the light to a double-pass AOM (acousto-optical modulator)[4] configuration that shifts the laser frequency during the different cooling stages (See Fig. 5.7(a) for repump laser layout).

The cooling laser is derived from a Toptica TA-PRO laser system, consists in an ECDL with a tapered amplifier (TA) delivering up to 3 W of power. It is

[4]All the AOM are used for fast on/off switching of the different laser fields during the experimental cycle and for changing detunings.

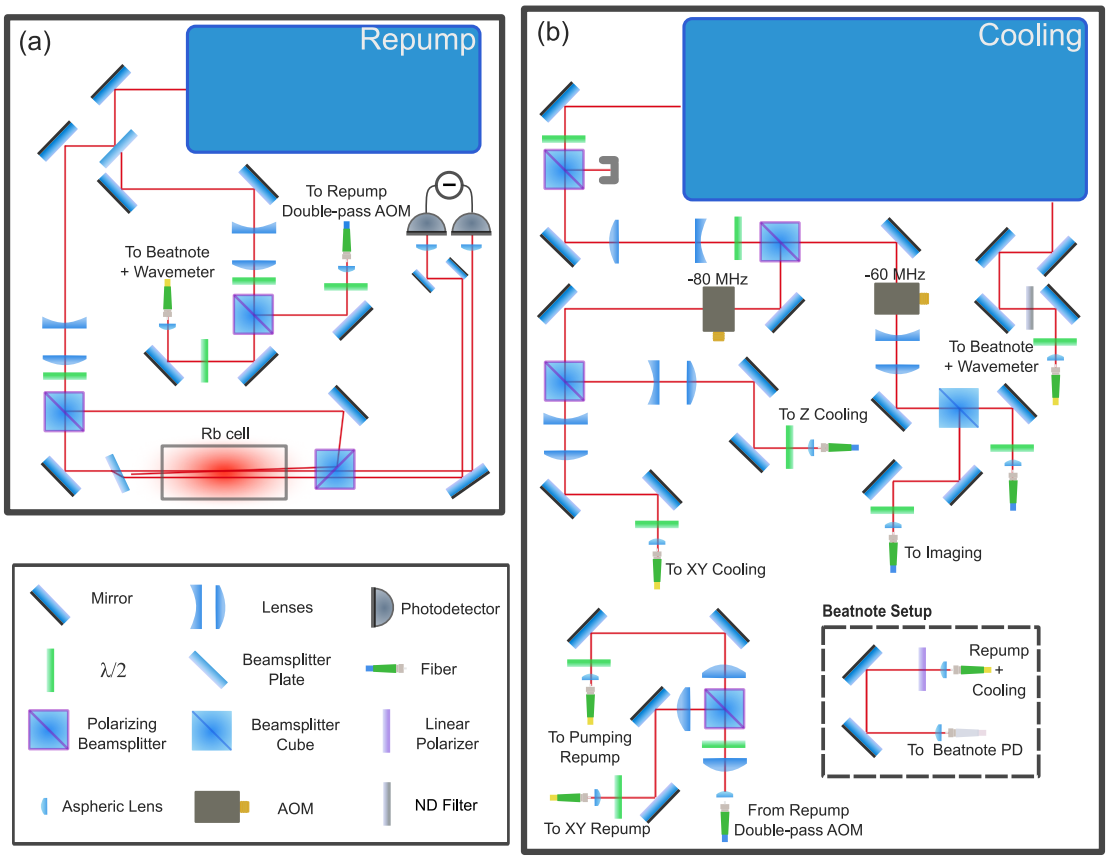

Figure 5.7: **Cooling laser layouts.** (a) Breadboard with Doppler-free sat-abs lock for the repump laser. Double-pass AOM setup to shift the repump frequency is not shown. (b) MOT breadboard with the cooling laser, beatnote setup, and repump fiber launches. All fibers are PM; using a $\lambda/2$ we carefully matched the polarization of the incoming light into one of the axes of the PMF. The first AOM shifts the cooling light by -80 MHz; we control the laser frequency at the various stages by changing the reference frequency of the beatnote lock. Part of the cooling laser light is used for imaging, and the frequency is shifted by -60 MHz with a second AOM. A polarizing 2×1 fiber splitter/combiner combines the z-cooling light and the imaging light. There are three 2×2 50:50 fiber splitter/combiner indicated by the yellow fibers. The first one combines the cooling and repump light for the beatnote lock and wavemeter ((High Finesse ANGSTROM WS/U-2). The second fiber splitter sends cooling and repump light to the two periscope launches (see Fig. 5.5(b)). We only use one arm of the last 2×2 fiber splitter to send optical pumping light and repump light to the chamber see Fig. 5.9(b) .

frequency stabilized by locking the current and the piezo to a beatnote lock, where the cooling laser (minion) interferes with the repump laser (controller) in a fibered fast photodetector (Vescent D2-160). The beatnote signal is sent to a phase-locked loop (PLL) circuit, which is referenced to a frequency from a Novatech and

multiplied by 48 (see Table 5.1 and Fig. 5.15). The reference frequency changes to set the cooling frequency for the MOT, dark, gray-molasses, and imaging. The error signal is directly fed back to the laser current from the beatnote circuit, another output from the beatnote circuit goes to the DLC-pro that produces an error signal to stabilize the piezo. Figure 5.7(b) depicts the "MOT breadboard" that contains the layout for the cooling light and repump light that is sent to the atoms, the beatnote lock, and imaging light.

5.3.2 Magnetic Field Control

Four pairs of coils control the magnetic field at every stage of cooling, pumping, and excitation of the atoms. Fig. 5.8 shows the coil geometry. Each pair is connected to a bipolar 20 A current supply (Kepco BOP20-20M).

The MOT coils are arranged in a quadrupole configuration to produce magnetic field gradients during the MOT loading and compression. Their inner diameter is 14.2 cm with seven turns and seven layers, which allows the generation of gradients of ≈2 G/cm/A. They are made of square profile kapton-coated copper tubing and have plumbing fittings for water cooling.

The other three pairs of coils, the Bias coils, move the center of the MOT-gradient field, compensate for stray magnetic fields during molasses, and set the quantization axis during pumping and probing of the atoms. The Z-Bias coils are parallel to the MOT-Coils, they consist of five turns and two layers of 22 AWG copper wire with an inner diameter of 21.6 cm, and together they generate fields of ≈ 1 G/A along the z-axis. The two other pairs (XY-Bias coils) central axis is at $\pm 45^\circ$ angle with respect to the x-axis (See Fig. 5.8). They have four

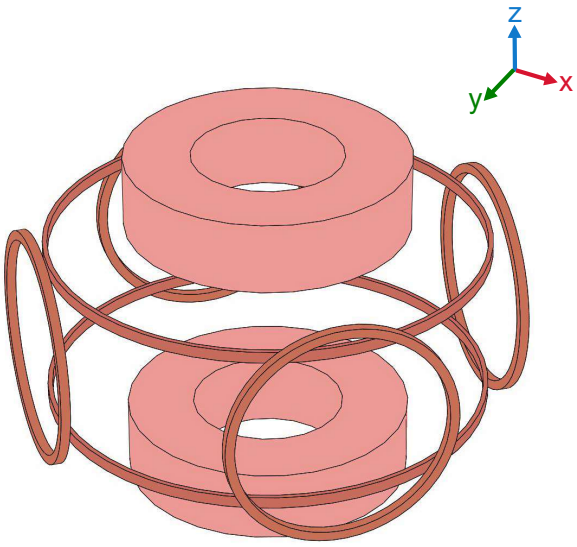

Figure 5.8: **Coil geometry to control the magnetic field.** The magnetic quadrupole is generated by the MOT coils, indicated by the light-copper color. Three pairs of dipole coils (Bias coils) shifts the zero-magnetic field gradient, cancel stray fields and produce homogeneous magnetic fields in any direction; they are indicated by the dark-copper color.

turns and four layers with 12 cm of inner diameter, each pair produces fields up to ≈0.3 G/A. However, measurements with atoms show that the actual field produced is about half ≈0.15 G/A. The current hypothesis is that there is some leftover magnetization in the vacuum components due to machined in-vacuum components (despite being made of 316L non-magnetic ss). This magnetization reduces the field magnitude by about half for the XY-Bias coils, but it does not seem to affect the field along the vertical z-direction, comparing with measurements done with the coils outside the chamber.

During the MOT, C-MOT and dark time stage, the Bias Coils move the center of the MOT to the dipole trap location to maximize loading into the trap. For gray molasses the quadrupole is off, and we change the current of the bias coils to zero the magnetic field. Then, we define a quantization axis for optical pumping along the y-azis, by ramping the current of the bias coils. We perform this ramp

over 25 ms to ensure adiabatic following. After pumping, we slowly ramp the current one more time to define a quantization axis along the probe propagation direction (x-axis).

5.3.3 Optical Pumping

After cooling, the atomic population is distributed over all m_F states of both hyperfine manifolds. However, for the main experiments presented in this thesis we need to prepare the atoms into the $|5S_{1/2}, F = 2, m_F = 2\rangle$ state to address the stretched state $|5P_{3/2}, F = 3, m_F = 3\rangle$, and then excite to the $|nS_{1/2}, J = 1/2, m_j = 1/2\rangle$ state. This two-photon excitation has several advantages: it is magnetically insensitive, it only allows one excitation pathway to a single m_J-state in the $nS_{1/2}$ Rydberg level which simplifies our scheme. Finally, it has the largest Clebsh-Gordan coefficients of all the hyperfine transitions, so we measure higher probe absorption (higher optical depths), and we obtain higher Rabi frequencies for the control field.

To optically pump the m_F levels we use dark-state optical pumping on the D1-line with a hyperfine repump laser in the D2-line. Both lasers are σ^+-polarized where the bias field (3 G) defines the quantization axis along the y-axis as shown in Fig. 5.9. In contrast to dark-state pumping using the D2 line $|5S_{1/2}, F = 2\rangle \rightarrow |5P_{3/2}, F = 2\rangle$ where there can be off-resonant scattering from $|5P_{3/2}, F = 3, m_F = 3\rangle$ that heats the atoms, the D1 pumping is completely dark for pure σ^+-polarization since there are only two hyperfine levels separated by 816 MHz in the excited state.

We optimize the polarization of the incoming beams by rotating the quanti-

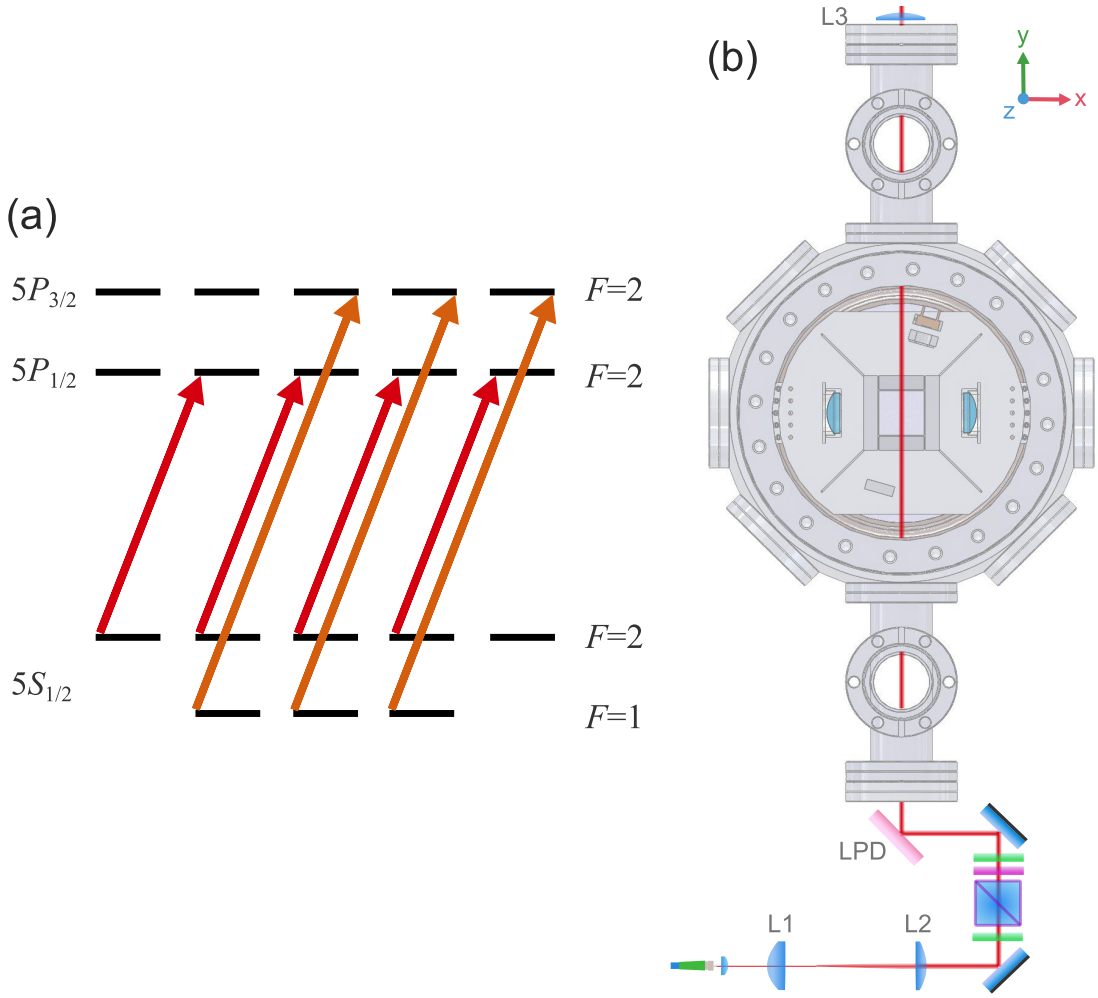

Figure 5.9: **Dark-state pumping schematic.** (a) Atomic levels for pumping in the D1-line with the repump in the D2-line. (b) The pumping and repump beams propagate along the quantization axis defined by the B-field of 3 G parallel to the y-axis. Both the pump and repump come from the same fiber, where a 4x magnifying telescope (L1 and L2) increases the beam waist to ≈ 4 mm. The PBS filters the polarization, and the wave-plates are adjusted, so the pumping beam is σ^+-polarized. A long-pass dichroic mirror (LPD Thorlabs DMLP900L) directs the beam to the atoms with an intensity of ≈ 1.6 mW/cm^2 for the pump and ≈ 0.02 mW/cm^2 for the repump. L3 is a plano-convex lens with $f = 250$ mm used for imaging.

zation axis along the x-axis, and measuring the transmission of a σ^+-polarized probe. We tune the probe frequency to the $F = 2 \rightarrow F = 2$ of the D2-line, after pumping for about 100 ms. If the atoms are prepared in the $|F = 2, m_F = 2\rangle$ state by setting the right pumping polarization, then the probe transmission should be nearly 100%.

5.3.4 Dipole Trap

After the MOT loading, we turn-on the dipole trap during the C-MOT stage by adibatically increasing the power of the dipole beams using a gaussian ramp. At the end of grey-molasses and optical pumping, the cloud has densities up to 7×10^{11} cm^{-3} with $\sim 2 \times 10^5$ atoms and temperatures of ~ 10 μK. Figure 5.10(b) shows the trap geometry consisting of three beams intersecting at the probe beam focus. The crossed trap is formed by two orthogonally polarized nearly counter-propagating beams with waist $\omega_d \approx 30$ μm at an angle of $\approx 22°$. After going through the chamber, the linearly-polarized incoming beam of the crossed trap passes through a PBS, a telescope, a waveplate that rotates the polarization by 90°, then is reflected and focused back at the atoms (due to optical losses, the reflected beam has about $\approx 77\%$ of the incoming dipole beam power). The third beam or "dimple" beam has an elliptical beam shape with focused waists $\omega_x \approx 56$ μm and $\omega_z \approx 28$ μm, it propagates along the y-axis intersecting the center of the crossed dipole trap. The dimple beam is detuned by +10 MHz with respect to the crossed dipole beams to avoid creating a static lattice. By adjusting the relative optical power between the different beams, we can modify the dipole trap geometry.

The crossed beams are produced by a 2 W Moglabs TA seeded by a Toptica TA pro laser system with a tunable ECDL from 1002 nm-1020 nm with up to 2 W output power. By adjusting the detuning of the laser from the transition $|nS_{1/2}\rangle \rightarrow |6P_{1/2}\rangle$ ($\approx$1004 nm) or $|nS_{1/2}\rangle \rightarrow |6P_{3/2}\rangle$ ($\approx$1012 nm) at a "magic wavelength", it is possible to generate a trapping potential for both ground-state and Rydberg atoms, since the dynamic scalar polarizability of both states can become nearly equal [91, 138, 139]. This allows reducing motional dephasing and

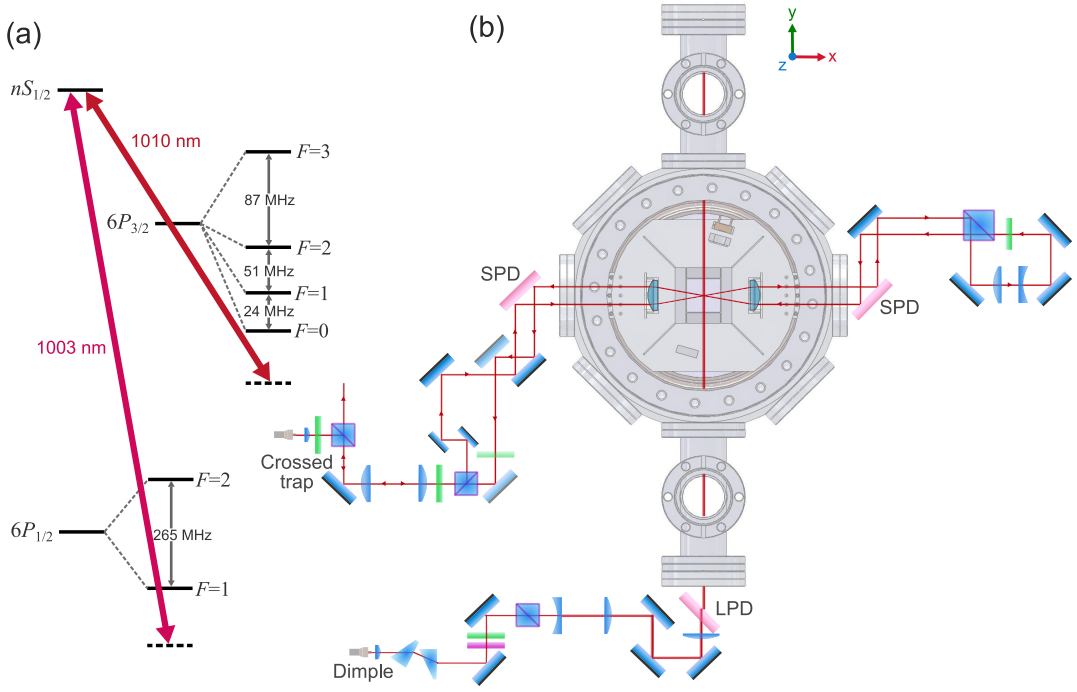

Figure 5.10: **Dipole trap schematic.** (a) Levels $6P_{1/2}$ and $6P_{3/2}$ for state-insensitive trapping. The hyperfine structure is in Refs. [136, 137]. (b) Dipole trap geometry of crossed trap + dimple. The dipole light for the crossed trap is delivered by a 15-μm mode-field diameter photonic crystal fiber (NKT Photonics LMA-PM-15). The incoming and reflected beams propagate off-axis from the in-vacuum lenses optical axis and get focused to form a crossed trap, the crossing angle can be modified by changing the distance from the in-vacuum lenses optical axis. The telescope for the incoming beam consists of two achromatic lenses of $f = 45$ mm and $f = 45$ mm, for the reflected beam the telescope has a plano-convex lens of $f = 60$ mm and a plano-concave lens with $f = -50$ mm. The dimple light also comes from a photonic crystal fiber (LMA-PM-15) is shaped with an elliptical beam profile by 2:1 anamorphic prisms, and is ≈3x magnified by two lenses with $f = -30$ mm and $f = 100$ mm. A 300 mm lens focuses the beam at the crossed dipole trap, the mirror prior to a lens is mounted in a pico motor mount for fine adjustment. The short-pass dichroic mirrors (SPD Chroma T 800 DCSPXR) combine the dipole light with 780-nm probe light. The long-pass dichroic mirror (Thorlabs DMLP900L) in the dimple path combines the trapping light and the optical pumping light.

position-dependent differential-Stark shifts, which are usually of opposite sign for Rydberg atoms compared to ground-state atoms, where the dipole trap has to be turned off during the Rydberg excitation.

The crossed dipole trap consists of nearly counter-propagating beams with opposite linear polarization at a frequency blue-detuned from the transition $|nS_{1/2}, J = 1/2\rangle \rightarrow$

$|6P_{1/2}, F = 1\rangle$. In this configuration and with the quantization field pointing along the trap direction, there is a polarization lattice that results in position-dependent vector-light shifts, so that $\sigma^{\pm}$-polarized light acts as a fictitious magnetic field for the Zeeman sub-levels. The dimple beam has π polarization and it is detuned from the crossed beams, so in principle, it only adds a scalar light shift to both states. In general, the detuning that cancels-out differential vector light-shifts does not compensate for differential scalar light shifts (See Fig. 5.11). We operate with a detuning where the differential vector light-shift is nearly cancelled or has a magnitude of a few kHz. Here, the scalar polarizability is close to the free-electron polarizability. We empirically determined that operating in this regime, resulted in lower Rydberg linewidths, rather than operating where the scalar differential light shift vanishes. Despite the different light shifts, we can continuously excite the Rydberg level for 100 ms up to 600 ms with moderate total trap powers of 0.75 up to 1.5 W, limited by the lifetime of the dipole trap (about 1.1 s).

We lowered the power of the incoming beam in the crossed trap to 130 mW, such that the overall optical power is about 230 mW. The dimple power is kept at its maximum of 550 mW to set the root mean square (RMS) axial width of the dipole trap to 27 μm for the experiments generating single-photons (See Chapter 6). Using $n = 139$, we can blockade the full atomic cloud in this configuration to create a single Rydberg spin-wave excitation. Lowering the power also reduces the ground-Rydberg differential light shifts. By measuring the retrieval photon probability as a function of the storage time of the Rydberg spin wave, we extract a coherence time of $\tau_s = 1.9 \pm 0.2$ μs.

The Rydberg EIT experiments presented in Chapter 8 are performed with

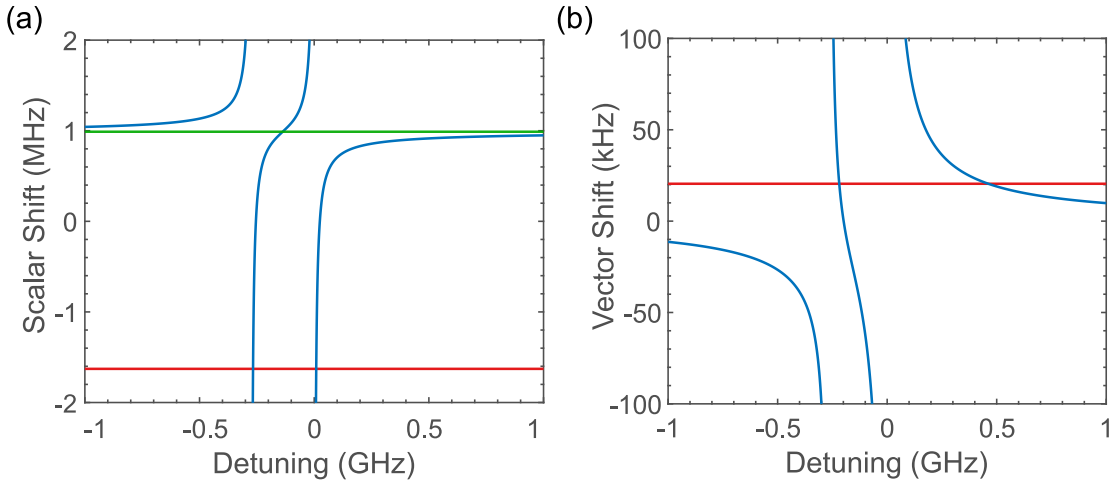

Figure 5.11: **Calculated light shifts for the ground state and the $139S_{1/2}$ Rydberg state in a crossed + dimple configuration.** The power of the incoming crossed trap beam is ≈ 130 mW (about 100 mW in the reflected beam), and the power of the dimple beam is ≈ 550 mW. The Toptica EDCL is blue detuned by 450 MHz from $|139S_{1/2}, J = 1/2\rangle \rightarrow |6P_{1/2}, F = 1\rangle$ transition (indicated at the origin of the x-axis). (a) Scalar light shift due to the crossed + dimple dipole trap for the ground state (red) and Rydberg state (blue). The green line indicates the light shift due to the free-electron polarizability. The differential scalar light shift vanishes around 8 MHz. The polarizability of the Rydberg state is close to the free-electron polarizability for typical operating detunings. (b) Vector light shift due to the crossed trap for the ground state (red) and Rydberg state (blue). The differential vector light shift is ≈800 kHz for a detuning of 8 MHz where the differential scalar light shift vanishes.

the crossed dipole trap beams blue detuned by 1 GHz from $|82S_{1/2}, J = 1/2\rangle \rightarrow |6P_{1/2}, F = 1\rangle$. At full optical power of ≈ 1.5 W, we observe that the $n = 82$ ground-Rydberg dephasing rate corresponds to $\gamma/(2\pi) = 0.4 \pm 0.1$ MHz from EIT spectra fits.

Other dephasing mechanisms, such as atomic motion and collisions and laser phase noise [140] from the control beam, also contribute to the decoherence of the ground-Rydberg spin wave and γ besides the light-shifts due to the dipole trap. We are currently investigating implementing a ground-state blue-detuned "anti-trap" where there would not be problems with light shifts since the atoms lie in the dark region. Another option is implementing a lattice, but even in that configuration,

there is a residual non-lattice potential that contributes to dephasing and increases for $n > 50$ [139].

5.3.5 Two-Photon Excitation

We use a two-photon transition to excite the $nS_{1/2}$ Rydberg level, as discussed in section 5.3.3. This excitation scheme allows us to create and study Rydberg-dark polaritons through EIT, as well as retrieving single-photons from a collective atomic excitation in a write-storage-retrieval sequence. Figure 5.12(a) shows the relevant atomic levels and laser fields, where the probe light addresses the transition of the ground state to the intermediate state $|5S_{1/2}, F = 2, m_F = 2\rangle \rightarrow |5P_{3/2}, F = 3, m_F = 3\rangle$, and the control field couples the intermediate state with the Rydberg state $|5P_{3/2}, F = 3, m_F = 3\rangle \rightarrow |nS_{1/2}, J = 1/2, m_j = 1/2\rangle$. Figure 5.12(b) depicts the probe and control field paths through the experimental setup.

The probe light is collimated from a PMF using a triplet lens collimator package (Thorlabs TC25FC-780), resulting in a beam waist of 2.7 mm. After going through a Galilean telescope, the beam waist is focused to ≈ 3.3 μm at the atoms by the in-vacuum lens as measured by an imaging setup using the second in-vacuum lens. The PBS, HWP, and QWP are as close to the chamber to avoid polarization deviations due to thermal drifts over the surface of the 2" mirrors, that we employ to align the probe prior to the chamber. These mirrors are mounted in picomotor mounts (Newport 8822) with 0.7 μrad of angular precision for fine alignment to the in-vacuum lenses. For more details on the probe alignment see Appendix A.

Choosing the right dichroic mirrors along to combine all the different wave-

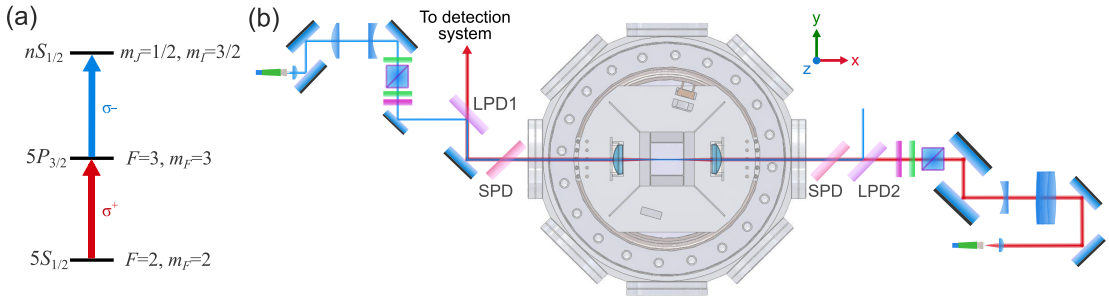

Figure 5.12: **Two-photon excitation schematic.** (a) Atomic levels for the Rydberg excitation through the stretch state transitions. (b) Probe and control beam paths. The beams are overlapped by two long-pass dichroic mirrors, LPD1 (Chroma T540lpxr) and LPD2 (Semrock FF757-D101). The probe telescope is formed by an aplanat lens $f = 145$ mm (CVI LAI-145.0-40.0) and a plano-concave lens $f = -125$ mm, in this configuration the curvatures of the lenses reduce spherical aberrations. The picomotor mounts are located between the telescope and polarization optics. We also use dichroic mirrors that transmit 780-nm light (for combining the probe with both control and dipole beams) to avoid other optical aberrations such as astigmatism in the focused probe beam. The quantization axis is defined along the x-axis during probing.

lengths is crucial to avoid aberrations in the focused beams. Since the probe beam has the smallest waist at the atoms, all the dichrocic transmit 780-nm light, we have observed that widely available dichroics (e.g. from Thorlabs) that reflect 780-nm produced astigmatism in the focused probe beam. To avoid aberrations in the focused control beam we use a high-quality long-pass mirror (Chroma T540lpxr) with surface roughness of $< \lambda/4$ (see Fig. 5.12(b)). The second dichroic mirror (Semrock FF757-D101) sends the blue beam into a fiber launch for monitoring the laser power and alignment, and therefore this dichroic mirror does not have a high quility surface.

A PMF (Schäfter and Kirchhoff) with a cut-off wavelength of 460 nm and a mode field diameter of 3.0 ± 0.5 μm delivers the control field to the chamber. It is collimated with an aspheric lens f=7.5 mm (A375TM-A); a de-magnifying telescope ($f = 175$ mm and $f = -75$ mm) and the in-vacuum lens focus the beam to ≈ 19 μm as estimated from Rabi frequencies extracted from EIT fits. The

larger beam waist for the control beam has two main motivations: the first is to have a homogeneous field along the probe area, and the second is to reduce the loss of ground-state atoms due to its the anti-trap effect.

The control field is counter-propagating to the probe beam, and it is overlapped by two different LPD mirrors and an ultra-broadband high reflecting mirror (Newport 10Q20BB.3). The coarse alignment is done by overlapping the beams as far as possible from the chamber. The fine alignment is done by maximizing the EIT transmission on resonance using a picomotor mount (the closest mirror to the chamber in Fig. 5.12(b)).

After passing through the chamber, the probe is coupled to a multi-mode fiber to take EIT spectra as diagnostics. There is a 1-nm bandwidth filter (Alluxa 780-1 OD6), and a broader 12.5-nm bandwidth filter (Semrock LL01-780-12.5) to reduce 780-nm broadband light[5] and dipole laser leakage. The final probe collection arrangement depends on the specific measurements we perform; see Figures 6.1, 7.1 and 8.2. Finally, we use single-photon avalanche detectors (SPADs Excelitas SPCM-780-13, see Table 5.2 for specifications) to detect light at the single-photon level and a time tagger (Roithner Lasertechnik TTM8000) to record the detection events with time stamps.

5.3.5.1 Probe and Control Laser Systems

An ECDL Toptica DL-pro laser produces the probe light. It is locked via the Pound Drever Hall (PDH) technique to a high-finesse ultra-low expansion (ULE)

[5]It appears that the control laser causes broadband fluorescence from the chamber windows, the exact mechanism is unknown and it is potentially related to LIAD. While the 1-narrow band interference filter reduces most of the broadband fluorescence, we have found that volume Bragg-gratings extinguishes this fluorescence. However, it has a lower transmission than the interference filter (≈75% vs. >98%)

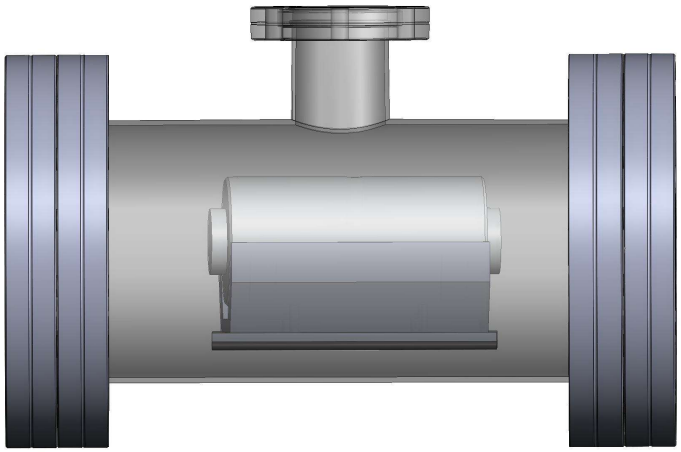

Figure 5.13: **ULE cavity setup.** The cavity is isolated from the environment by a CF reducing tee of 6" to 2.74". A 1 l/s ion pumpm (Modion) keeps the pressure down to 4×10^{-8} Torr. There are four contact points between the ULE cavity and the mount through viton pads (not shown). The mount is attached to a flat platform that is held by viton barrels (in black). This configuration was specially designed for passive mechanical stability and high-frequency vibration damping [141].

cavity. Using this scheme, we achieve laser linewidths on the order or below the kHz level [142, 143]. Having narrow-linewidth lasers that couple the ground and Rydberg states is crucial for the coherent addressing and control of Rydberg atoms, given their small natural linewidth. It also significantly reduces long-term drifts on laser detunings while exciting to the Rydberg state.

The ULE cavity (ATFilms) has custom mirror coatings to be highly reflective at 780 nm and 958 nm, which results in a finesse of more than 150,000 for both wavelengths. The mirrors form a modified hemispherical cavity (with curvatures $R_1 = 50$ cm, and $R_2 = \infty$), they are fixed in place by cylindrical ULE glass spacer with a length of 10 cm. To avoid fluctuations from the air refractive index and to thermally isolate it from the environment, the cavity is kept inside a small vacuum chamber with a pressure of 4×10^{-8} Torr as shown in Fig. 5.13. The chamber is thermally stabilized at 33 C where the thermal expansion coefficient derivative of the ULE glass is zero. For passive mechanical stability and high-frequency

vibration damping, we use a specialized mount design compatible with our cavity geometry (For details on PDH stabilization and the mechanical stability design see Neal Pisenti's thesis [141]). This mount also places the optical axis of the cavity at a 4° angle with respect to the windows of the main chamber in order to avoid etaloning effects.

The PDH technique uses the interference between a carrier and its phase-modulated sidebands that are reflected from an optical resonator to discriminate and stabilize the laser frequency. Since it responds to a phase change, the stabilization system bandwidth is not limited by the response time of the cavity and can be used to narrow the laser linewidth to less than 100 Hz (as implemented originally) [142,143]. The PDH lock is the most suitable locking technique, since the coherent and fine control of Rydberg states requires that the combined laser linewidth of the two-photon transition is narrower than the Rydberg state linewidth.

Figure 5.14(a) shows the PDH lock schematic for the probe laser. A fiber electro-optical modulator (EOM iXBlue NIR-MPX800-LN-0.1[6]) does the phase modulation of the probe at a frequency of Ω =18 MHz. A fast-photodiode (Newport 1801-FS) detects the beatnote signal from the reflected carrier and sidebands, and a low-pass filter removes the beating between the two sidebands at 2Ω. The filtered beatnote signal is then combined with the modulation frequency in a mixer to produce the demodulated PDH error signal. Finally, to feedback the error signal to the ECDL current, we use a laser servo (Vescent D2-125) with a double integrator loop filter PI^2D and adjustable gain. The piezo is also locked using a

[6]This modulator does not show any measuarable residual amplitude modulation after testing different models.

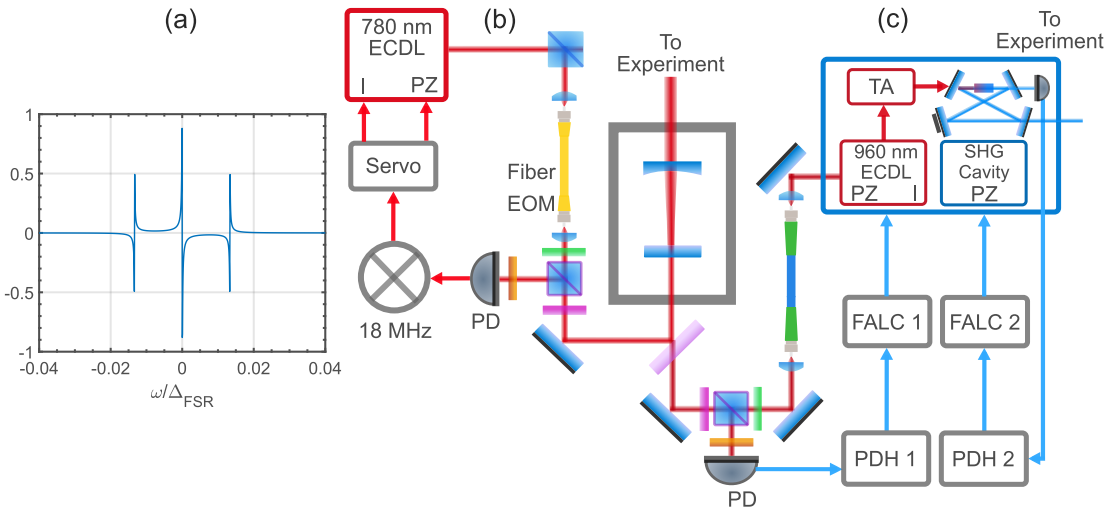

Figure 5.14: **Probe and control locking schematic.** (a) Pound-Drever Hall error signal as a function of detuning from the cavity resonance. Here the finesse corresponds to 150×10^3, free-spectra range (FSR) of 1.5 GHz and frequency modulation of 20 MHz. (b) Probe and (c) control laser PDH locking setup using the ULE cavity. The interference filters before each photodetector (PD) avoid cross-talk between the 780-nm light and 960-nm light. See the text for more details.

lower bandwidth loop to compensate for long-term drifts. In principle, the optimal modulation RF power of the EOM for a maximal loop-bandwidth is when the sidebands have 50% of the carrier power [143]; however, that decreases the power of the transmitted mode, so we do not operate in this higher bandwidth regime (therefore the P-value of the lock also decreases).

The PDH lock suppresses laser noise at frequencies below the filter loop bandwidth. However, laser phase noise will be highest around the loop bandwidth frequency. It has been observed that this high-frequency noise reduces the coherence of the Rydberg excitation [140, 144], so to resolve this problem, we use the transmitted light from the ULE cavity to interrogate the atoms. The transmitted light has no high-frequency noise since an optical resonator acts as a frequency filter. We estimate that the linewidth of the transmitted probe is about 8 kHz (corresponding to the Lorentzian linewidth of the cavity). We measure higher

transmissions on EIT resonance (≈1.4x) when probing the atoms with the light from the cavity, which is a signature that the Rydberg linewidth is narrower.

Finally, we use a high-bandwidth AOM (Brimrose) with modulation carrier frequencies up to 1 GHz to tune the probe frequency from the cavity resonance to the atomic resonance. We lock the laser to the cavity mode at 384.229145 THz, and take the first negative diffracted order of the AOM at 1.21 GHz. We couple this order to a fiber, and send the light to a double-pass AOM setup with driving frequencies centered around 90 MHz to quickly scan the probe frequency from -50 MHz to 50 MHz away from resonance.

The control light is derived from a Toptica SHG (second harmonic generation) laser assembly, where an ECDL tuned around 958 nm is amplified by a TA up to $\approx$ 1.9 W, and then it is frequency-doubled to 479 nm by a non-linear crystal in a ring cavity. We also lock the 958 nm seed laser to the ULE cavity via a PDH lock (see Fig. 5.14(b)). We use a high-bandwidth Brimrose AOM to shift the 960-nm laser frequency to the cavity resonance, such that the 480-nm light is also resonant to a target Rydberg level. The current of the seed laser is frequency modulated at Ω =20 MHz by a Toptica PDH module. Here, the beatnote signal from the fast photodiode is demodulated, and the gain and phase are adjusted to produce an error signal. The lock loop filter is optimized using a Toptica fast laser locking (FALC) module, where the error signal is fed back to the laser current. We do not use the light transmitted from the ULE cavity to do an injection locking for the seed ECDL, so the control laser exhibits high-frequency phase noise.

A second PDH module generates an error signal from the photodiode detecting leakage blue-light from the doubling (SHG) cavity. The error signal is then fedback

to the piezo on one of the mirrors of the SHG cavity through another FALC module (see Fig. 5.14(c)).

The frequency of the doubled 960-nm light coming from the SHG cavity is either shifted by a single-pass AOM, or a double-pass AOM with driving frequencies centered around 80 MHz. For the experiment in Chapter 8, where we need as much power as possible and the laser frequency can be fixed, we use the single-pass AOM. For generating on-demand single photons as described in Chapter 6, we need a double-pass AOM configuration to change the control detuning for writing a spin wave and then change the frequency for the subsequent retrieval.

5.3.6 Experimental Sequence

Here we summarize the experimental sequence for making cold atomic ensembles. Figure 5.15 shows the detunings for the cooling and repump light during the loading and cooling of the atoms. The values of laser intensities, magnetic field gradients, and variations in the different stages of the experimental sequence are in Fig. 5.16.

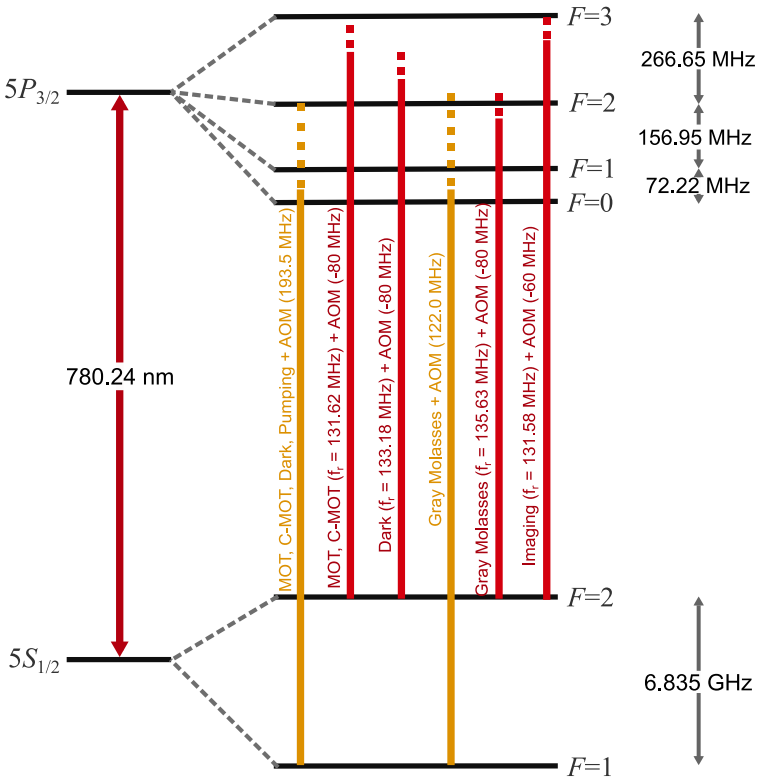

Figure 5.15: **Repump and cooling detunings used during the different cooling steps.** The cooling light (red) is locked to the repump (orange) using a beatnote lock. The reference frequency (f_r) is multiplied by 48 in the beatnote lock and adjusted to change the detuning of the cooling laser at each cooling stage. A fixed -80 MHz offset from an AOM sets the final frequency to address the atoms. For the repump light, the locking frequency is fixed to the $F = 1 \rightarrow F = 0$ crossover, and a double-pass AOM for the repump shifts the laser frequency as needed. Solid lines indicate locking frequencies, and dotted lines indicate AOM offsets. Hyperfine splittings of the D2-line is taken from Ref. [145].

5.3.7 Diagnostic tools

Here, we briefly describe the imaging systems and methods to characterize and optimize the experimental parameters.

5.3.7.1 Imaging

We employ absorption imaging to characterize the dimensions of the dipole trap, atom number, mean temperature via time of flight measurements, and to overlap the dipole trap beams to the focus of the probe beam.

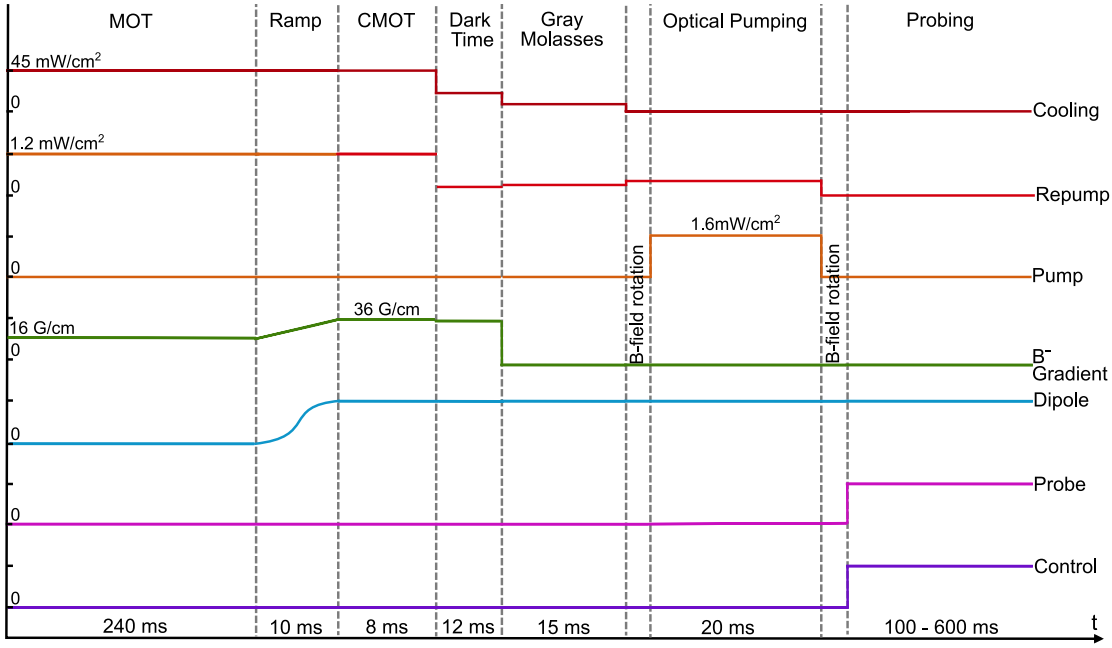

Figure 5.16: **Schematic of the experimental sequence.** The cooling, repump, and optical pumping total intensity, as well as the values for the magnetic field gradient. The magnetic field gradient on the xy-plane is half than in the z-axis(shown in the diagram). There is a 10 μs-time between the dark time and the molasses to ramp the MOT-Coil current to zero. The first B-field rotation, ramps the current in the XY Bias coils (see Fig. 5.8) from zeroing the field to set the quantization axis along the y-axis with 3 G for optical pumping, it lasts for 25 ms to achieve adiabatic following. The field is rotated a second time for 25 ms to set the quantization axis along the x-axis with 5 G for probing. The probe and control time-dependence is subject to the type of experiment we are performing, as well as the dipole trap intensity. For example, for single photon-generation we pulse both the probe and control beams (see Fig. 6.1) with a lower dipole trap power. For polariton experiments, the probe and control are continuously on with maximum dipole power.

The first imaging system shares its path with the cooling beam propagating along the z-direction, but the imaging light has opposite polarization. It is reflected at the post-chamber PBS as shown in Fig. 5.5. An aplanat lens (CVI LAI-145.0-40.0) with focal length $f = 145$ mm and a diameter of 40 mm collects the light from the chamber. An identical aplanat focuses the beam into a CCD camera (see Table 5.1 for more camera details). The maximum NA is ≈ 0.14 with a measured resolution of ≈ 6 μm, and magnification M =1 in the xy-plane. We also have a second imaging system for the xz-plane, and we use it mostly to

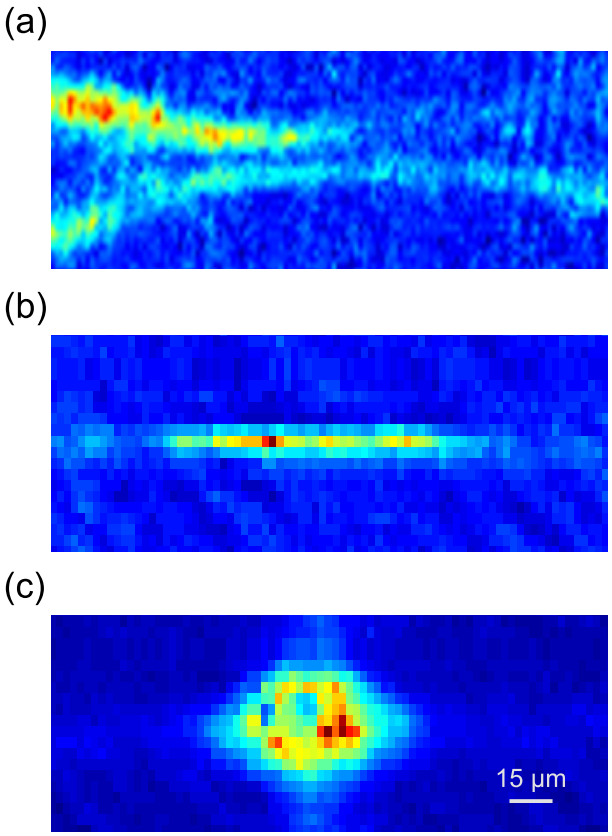

Figure 5.17: **Probe and dipole trap relative alignment in the xy-plane.** (a) Crossed dipole trap bifurcated by the probe with an intensity higher than the saturation intensity and tuned close to resonance. (b) Probe trap, the intensity has to be carefully set; otherwise, the radiation pressure can push the atoms away from the probe focus. (c) Crossed dipole trap + dimple overlapped with the probe beam and centered at the probe focus.

monitor the fluorescence of the MOT. A plano-convex 250 mm lens with 25 mm of diameter collects the light, and the second lens that focuses on the CCD camera has a focal length of 500 mm and magnification M =2. This system has a low NA ≈ 0.05 with a resolution ≈ 19 μm. Figure 5.9(b) shows the same fiber delivers the imaging light as the optical pumping beams for absorption imaging.

A challenge of experiments with Rydberg atoms in cold ensembles is to align a dipole trapped atomic cloud with dimensions of a few tens of microns to the tightly focused probe with waist of a few microns. Our first attempts consisted of bifurcating the dipole trap by blowing a "hole" with the probe beam across the

center, here the probe light frequency is tuned close to resonance and with a few nanowatts of power, see Fig. 5.17(a). However, we have found that using the probe beam as an optical trap has proven to be more straightforward for determining the position of the probe beam focus. We set the detuning to -100 GHz from resonance to make a probe trap with $\sim$ 100 μW of power. Despite the finite resolution of both imaging systems, we can resolve the probe trap after the MOT loading. We identify the pixels of the probe trap location, and by walking the dipole beams to the same area for both imaging planes, we can overlap all beams in the transverse and vertical position. Figure 5.17(b)-(c) depicts the view of the probe trap and dipole trap when they are overlapped.

5.3.7.2 Spectroscopy

We can characterize the coherent optical excitation to the Rydberg state and quantify important parameters such as optical densities, Rabi frequencies and the Rydberg-state linewidth by performing spectroscopy of the probe after propagating through the trapped atoms. For spectroscopic measurements, we scan the frequency of the probe light and measure its transmission with a SPAD, while the probe is interrogating the atoms under different circumstances.

For example, to measure the broadening due to the presence of the intense dipole trap and the control beams, we lock the control laser 1.5 GHz away from resonance and scan the probe detuning by a few MHz around the resonance transition $|5S_{1/2}, F = 2, m_F = 2\rangle \rightarrow |5P_{3/2}, F = 3, m_F = 3\rangle$ with an OD$\approx$ 3. We fit the spectra assuming we have a two-level system, setting OD and Γ as free parameters. The transmitted photon flux reaches a saturation point due to the optical-

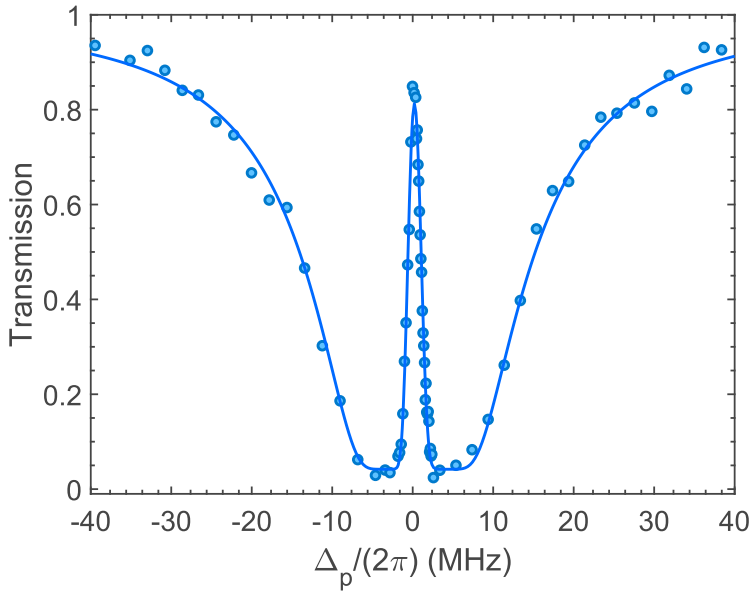

Figure 5.18: **Measured EIT spectrum and fit..** Measured EIT transmission with a multi-mode fiber (blue circles) and fit (dark-blue line). The fitted parameters indicate optical depth OD=12.7±0.6, control Rabi frequency $\Omega_c/(2\pi) = 7.4 \pm 0.1$ MHz, and Rydberg dephasing rate $\gamma/(2\pi) = 140 \pm 20$ kHz.

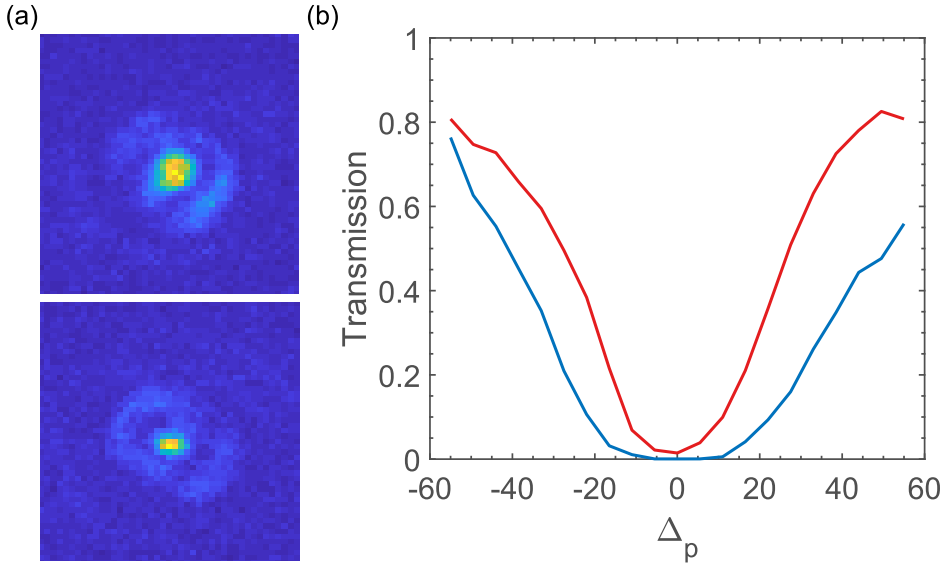

Figure 5.19: **Refractive effects due to the propagation of the probe through a dense atomic medium.** (a) Absorption image of the probe beam transversal profile for -10 MHz (top) and +10 MHz (bottom) detuning. The images were taken with an Andor EMCCD camera and using the second in-vacuum lens as the collection lens. (b) Transmission spectra taken with MMF (red) with a fitted OD= 50 ± 3, and a SMF (blue) with a fitted OD= 116 ± 8. After propagating through the cloud, the distorted beam does not couple as well to the SMF resulting in an apparent higher OD. The two-level spectrum also looks asymmetric due to the frequency dependence of refractive effects, as illustrated in (a).

nonlinearity of the system during two-photon excitation for EIT-spectra [44, 146]. The saturation level depends on the principal quantum number n and the control Rabi frequency. The photon flux should be below this level to obtain a good estimate of the control Rabi frequency and the Rydberg linewidth when fitting to an EIT spectrum (see Fig. 5.18). We therefore typically excite the atoms with a low photon flux $\sim 10^5$ s^{-1}. The OD is unaffected by this saturation when used as a free parameter in the fit.

We have noticed (as other groups as well [147]), that measuring the OD with a single-mode fiber (SMF) results in a higher value, compared to measuring with a multi-mode fiber (MMF). The difference is due to the dispersion of the probe beam while propagating through the medium, and is more significant for larger ODs. When the probe is off resonance, the refractive index can focus, defocus or refract the beam [148]. Figure 5.19 illustrates the refraction of the off-resonance probe beam as well as the apparent increase of OD when using a SMF, due to the mode-mismatch when the transversal mode gets distorted after interacting with the atoms. For EIT diagnostic scans and correlation measurements, where we are only interested in the time evolution, we couple the light into MMFs. For experiments that require to project the outgoing mode of the probe into a single-transverse mode we couple the light into SMFs.

5.3.8 Computer control and data acquisition

We use a programmable TTL pulse generator (SpinCore PulseBlasterUSB) as a controller device to control the timing of other minion devices during the experimental sequence, such as shutters, AOMs, cameras, digital to analog con-

verters (DAC) cards, etc. (See Table 5.1 for relevant devices). We program the PulseBlaster and minion devices through Setlist, a Labview-based software control interface. Setlist allows us to define a time table of the digital (TTL signals) and analog values for each device with a minimum of 10-ns resolution.

Device	Type	Characteristics
PB24-100-4k-PCIe (C)	TTL	24 output with 100 MHz clock frequency
Novatech409 (M)	DDS	4 channels with +4 dBm output and up to 171 MHz
NI PCI-6733 (M)	AO	Eight 16-bit DAC with a max output of ± 10 V
NI USB-6363 (M)	I/O	Multifunction with digital and analog I/O channels
TTM8000 (M)	Time-tagger	8 channel output with a resolution of 82.3 ps
FL3-GE-28S4M-C (M)	Camera	2.8 MP with 3.69 μm pixel size $\approx$ 25% QE @ 780 nm
Agilent E4426B (M)	SG	Single-channel output 250 kHz-4 GHz up to 7 dBm
ADF 4351 (M)	DDS	Dual-channel output 35 MHz-4.4 GHz up to 4 dBm

Table 5.1: **Relevant controller (C) and minion (M) devices.** The acronyms definition are the following, DDS: Direct Digital Synthesizer; AO: Analog Output; I/O: Input/Output; SG: Signal Generator; QE: Quantum Efficiency.

The majority of our data consists of single-photon detection events from our SPADs (SPAD see Table 5.2). The events are recorded by the time-tagging device (Roithner Lasertechnik TTM8000) as time tags relative to an absolute relative time set by a trigger. Software written in C++ [7] sorts the time tags in vectors for a specified number of windows (three windows for absorption spectra and one for correlations between detections of two or more detectors) and saves them in an HDF5 file. Finally, a LabView virtual instrument (VI) appends the experimental sequence and variable values to the HDF5 file and moves it to the specified folder.

Property	Value*
QE @ 780-nm	67%
Resolution	350 ps
Dead time	25 ns
Dark count	60 cps
Linearity	up to 200 kc/s

Table 5.2: **Properties and values for our SPADs Excelitas SPCM-780-13.** *Values are approximate.

[7] See A. Craddock repository for details `https://github.com/acraddoc91/timeTaggerODMeasurement`

We take absorption images to measure the geometry of the cloud and its temperature, as well as for alignment purposes. We trigger the camera three times for absorption imaging (one with atoms, one without atoms, and one of the background) and save the images to a single HDF5 file. A LabView VI toggles between the cameras of the two different imaging systems (for vertical and side imaging), processes the data and allows for defining regions of interest.

Chapter 6: Single-photon source based on a Rydberg Ensemble

Engineering single-photon sources with high efficiency, purity, and indistinguishability is a long-standing goal for applications such as linear optical quantum computation [149], boson sampling [150], quantum networks [151] and quantum metrology [152]. Atomic systems have shown significant progress towards quantum light-matter interfaces, including efficient quantum memories [33], quantum networks [37], high-fidelity light-matter entanglement [153], atomic gates [16], and quantum simulators [154]. Atomic platforms require spectrally matched single photons that can coherently couple with atomic processors, provided with high-efficiency generation, purity, and indistinguishability.

Strongly interacting Rydberg atoms provide a particularly promising system. They have proven to be versatile for engineering strong interactions between photons, exhibiting nonlinearities at the single-photon level [44, 46, 86, 155]. Recent experiments using Rydberg interactions have demonstrated on-demand single-photon generation [45, 156], as well as photon transistors [48–50], photonic and atomic phase gates [52–54, 144, 157, 158], high-visibility quantum interference in hybrid systems [59], and quantum simulators [159–162].

This Chapter describes an efficient single-photon source based on collective excitation and de-excitation of a cold, trapped ensemble of atoms through a highly excited Rydberg state [45,62,156]. During two-photon excitation from the ground

to the Rydberg state via an intermediate state, long-range van der Waals interactions suppress multiple Rydberg excitations within a blockade radius, r_b [40]. The resulting single, collective atomic excitation is coherently shared among N ground-state atoms g as a spin wave [62].

$$|S\rangle = \frac{1}{\sqrt{N}} \sum_{j=1}^{N} e^{i\mathbf{k}_s \cdot \mathbf{x}_j} |g_1, g_2 \dots g_{j-1}, r_j, g_{j+1} \dots g_{N-1}, g_N\rangle , \tag{6.1}$$

where $\mathbf{k}_s$ is the spin wave k-vector equal to the difference of the excitation lasers wavevectors, and r_j is j-th atom excited to the Rydberg state at position $\mathbf{x}_j$. Due to the collective nature of the excitation, if the initial phase coherence $\mathbf{k}_s \cdot \mathbf{x}_j$ of the spin wave is maintained, the subsequent coupling of the Rydberg state to the intermediate state can efficiently map the excitation onto a single photon in the forward-propagating mode [31].

Our system produces single photons with repetition rates up to 400 kHz, a generation probability up to 0.40(4), $g^{(2)}(0) = 5.0(1.6) \times 10^{-4}$, and indistinguishability of 0.980(7). Operating at 60% duty cycle with repetition rate of 200 kHz, we observe a fully single-mode efficiency $P_1^{\mathrm{sm}} = 0.098(2)$, a single-mode rate of $\mathcal{R} = 1.18(2) \times 10^4\ s^{-1}$, and single-mode fidelity $\mathcal{F} = 0.980(7)$. We model the write and retrieval process, including the measured spin-wave dephasing rate. We identify long-lived contaminant Rydberg states [163] as a limiting factor on the source efficiency for increasing production rates.

This Chapter is organized as follows: First, we describe the experimental sequence to generate single-photons in a Rydberg super atom. Next, we present the multi-photon emission and HOM-visibility of the source. Then, we discuss the effect of the creation of nearby-Rydberg states on the single-photon produc-

tion and present a theoretical model to estimate the generation efficiency of the source. Finally, we briefly describe some steps we followed to optimize the source performance.

6.1 Single-photon generation procedure

We start the experiment by cooling, loading and optically pumping the atoms to the ground-state $|g = |5S_{1/2}, F = 2, m_F = 2\rangle$ in a 1003-nm crossed dipole trap (for more details on this procedure, see Chapter 5). The relative powers of the dipole-trap-creating beams are adjusted so that the RMS dimesion of the trapped atomic clouds are $\sigma_r = 20$ μm in the radial direction and $\sigma_z = 27$ μm along the direction of the beam propagation. For most experiments presented in this chapter, the initial loading time lasts 250 ms and results in $\sim 10^4$ atoms in the dipole trap giving an OD of 13; if we need to adjust the atomic density, we change the loading time, from 50 ms to 1500 ms (with OD up to $\approx$16).

We use a two-photon excitation scheme to write the spin wave. We couple the ground state, $|g\rangle$ to the Rydberg state $|r\rangle = |139S_{1/2}, m_J = 1/2\rangle$ via the intermediate state $|e\rangle = |5P_{3/2}, F = 3, m_F = 3\rangle$ with an intermediate detuning $\Delta_p/(2\pi) =$ 50 MHz, as shown in Figure 6.1(a). The probe beam coupling $|g\rangle$ to $|e\rangle$ is focused into the atom cloud with a waist of $\approx$ 3.3 μm, and a Rabi frequency $\Omega_p/(2\pi) \approx 1$ MHz. The counter-propagating control beam coupling $|e\rangle$ to $|r\rangle$ has a larger, $\approx$ 19 μm waist and peak Rabi frequency $\Omega_c/(2\pi) \approx 7$ MHz. The larger beam waist provides an approximately uniform control field across the probe area.

The van der Waals coefficient of the Rydberg state $139S_{1/2}$ is $C_6/(2\pi) \approx -2.3\times$

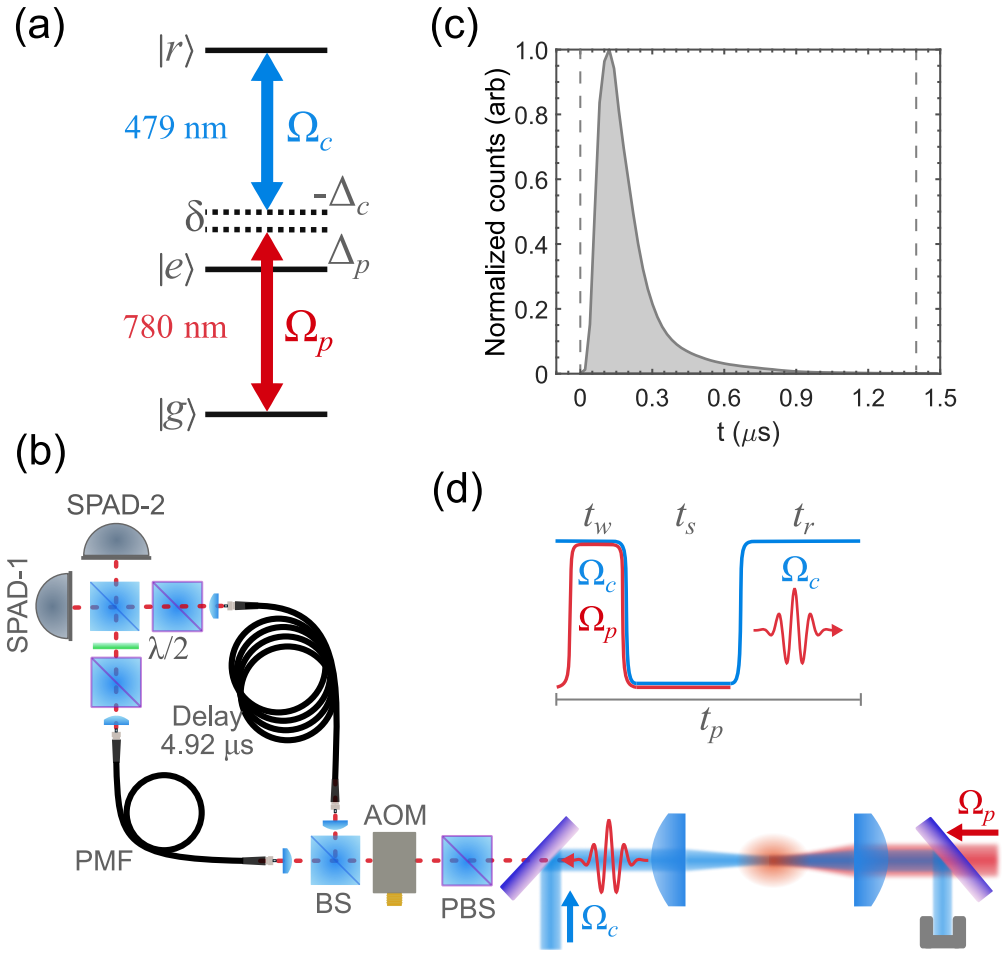

Figure 6.1: **Schematic of the experiment.** (a) Relevant atomic levels for single-photon generation. During the spin-wave writing stage we set the single-photon detuning $\Delta_p/(2\pi) \approx 50$ MHz, and the two-photon detuning $\delta = \Delta_p + \Delta_c$ to Raman resonance, $\delta/(2\pi) \approx -2$ MHz. For retrieval, $\Delta_c/(2\pi) \approx 7$ MHz. (b) Experimental schematic. A polarization beamsplitter projects the photons into a single polarization mode, followed by an AOM that shutters the incoming photons during the write pulse. All the light is directed to the PMF to realize a $g^{(2)}(0)$ measurement. For the indistinguishability characterization, we split the light such that the rate is roughly the same at both ports of the second BS. By rotating the HWP, we can control the relative polarization of the photons coming from the PMF port and the long-delay port. After each port of the final 50:50 BS, the photons are coupled to a single-mode fiber (not shown) connected to a SPAD. (c) Photon temporal envelope. Gray dashed lines indicate the gate window containing more than 99.9% of the pulse. (d) Timing sequence for the generation of successive single photons, the writing π-pulse lasts for $t_w \approx 370$ ns. We use a minimum storage time $t_s \approx 350$ ns to maximize the retrieval and vary t_r to change the repetition rate, $R = 1/t_p$.

10^6 GHz μm^6, which results in a calculated blockade radius $r_b \approx 60$ μm (using Eqs. 3.56 and 3.59, see Chapter 3) during the spin-wave writing. Since r_b is larger

than the probe beam waist and the atomic cloud extension in the propagation direction, $\sigma_z \approx 27$ μm, the entire excitation volume is blockaded, suppressing the writing or storing of more than a single spin-wave excitation in the medium. This is in contrast to other Rydberg-based approaches, where pair-spin-wave dephasing purifies a single-photon excitation [45, 156, 164]. Furthermore, the effective two-photon Rabi frequency, $\Omega_{2\text{ph}} = \frac{\Omega_p \Omega_c}{2\Delta_p}$ is enhanced by a factor $\sqrt{N} \approx 20$ from the N atoms participating in the collective excitation [62, 165].

Following the writing stage, we turn off the excitation lasers, and hold (store) the spin wave in the medium for $\approx$ 350 ns; this is the minimum time required to switch the control AOM frequency. We turn on the control field blue-detuned from the intermediate state by $\Delta_c/(2\pi) \approx 7$ MHz, which is the detuning that we empirically determined maximizes the retrieval efficiency of the spin wave into a single photon. We can vary the repetition rate of the write-retrieval pulse sequence up to 400 kHz, with interrogation times up to 600 ms (0.6 duty cycle) before we need to reload the optical dipole trap.

After exiting the chamber, the probe light passes through a PBS, and a set of bandpass filters centered at 780 nm, a narrow 1-nm bandwidth filter (Alluxa 780-1 OD6), and a broader 12.5-nm bandwidth filter (Semrock LL01-780-12.5) before being coupled into a single-mode polarization-maintaining fiber (PMF). Prior to the PMF, an AOM shutters the write pulse to avoid saturating the photon-counting detectors. The light is then sent to a HOM interferometer, which has another set of broad filters in front of single-mode fibers (SMF). In the end, the photons are detected by two SPADs (Excelitas SPCM-780-13) with a quantum efficiency of $\approx 70\%$, and dark counts (plus background ambient light) of ≈ 90 s^{-1}. The arrival

of every event is recorded with an externally triggered time-tagging device (Roithner TTM8000), which allows the defining of gating windows around the photon pulses and calculation of correlation functions off-line after data collection.

Table 6.1 shows the measurements of the optical losses along the path of the probe light to characterize the generation efficiency. The propagation efficiency includes all the optical elements, such as filters, dichroics, mirrors, polarizing beamsplitters, and lenses. With realistic improvements on higher transmission coatings and using an electro-optical modulator instead of an AOM to shutter the write pulse, we estimate that we could get an efficiency up to 0.65 after the PMF, from the current 0.44.

Element	Efficiency
Optics transmission	0.75(2)
AOM diffraction	0.79(2)
PMF coupling	0.75(2)
HOM interferometer	0.38(1)
SPAD	0.67(1)

Table 6.1: List of the efficiencies along the probe path.

6.2 Purity and Indistinguishability

We use Hanbury Brown-Twiss and Hong-Ou-Mandel interferometers to characterize the purity and indistinguishability of our single photons (see Fig. 6.1(b)). The purity of our single-photon source is defined as $1 - g^{(2)}(0)$, where $g^{(2)}(\tau)$ is the second-order autocorrelation function. We apply a 1.4 μs-long gate window starting just before the photon rising edge, as indicated in Figure 6.1(c). Coincidences at zero time delay are substantially suppressed, as shown in Figure 6.2(a), with strong antibunching $g^{(2)}_{\mathrm{raw}}(0) = 0.0145(2)$, integrating the area around

$\tau = 0$ and without background subtraction. The background coincidence rate is dominated by coincidences involving photon events with background counts unrelated to the single-photon generation, coming from detector dark counts and room light leakage. The independently measured background rate, photon shape, and photon rate are constant throughout each experimental run, from which we determine that the accidental coincidences contribute to $g^{(2)}_{\text{back}}(0) = 0.0140$. The gray curve in Figure 6.2(b) shows the background coincidence profile within the gate window. After background subtraction (for details see Appendix B), our single-photon source has $g^{(2)}(0) = 5.0(1.6) \times 10^{-4}$.

We use a Hong-Ou-Mandel interferometer to measure the photon indistinguishability. We implement a fiber-based 4.92-μs delay in one arm to overlap adjacently produced photons temporally. Additionally, there is a PBS at the output of each fiber to clean up for any prior polarization rotation. At the exit of the short arm, there is a half-wave plate (HWP) to rotate the polarization and control the degree of distinguishability of the photons. Figure 6.2(c) shows the normalized coincidences for orthogonal and parallel polarizations. Integrating the number of coincidences in a window around $\tau = 0$ for the two cases, we measure a raw HOM interference visibility $\mathcal{V}_{\text{raw}} = 1 - C_{\parallel}/C_{\perp} = 0.892(6)$. Accounting for the accidental coincidences with background events the visibility is $\mathcal{V}_{\text{raw}} = 0.964(6)$, and accounting for the slight differences in the transmission and reflection coefficients of our combining beamsplitter shown in Table 6.2, the mode overlap becomes 0.980(7) (see Eq. (4.45)).

We note that to do the normalization for both purity and indistinguishability, we integrate the counts of 80 gated and background-subtracted pulses for $|\tau| >$

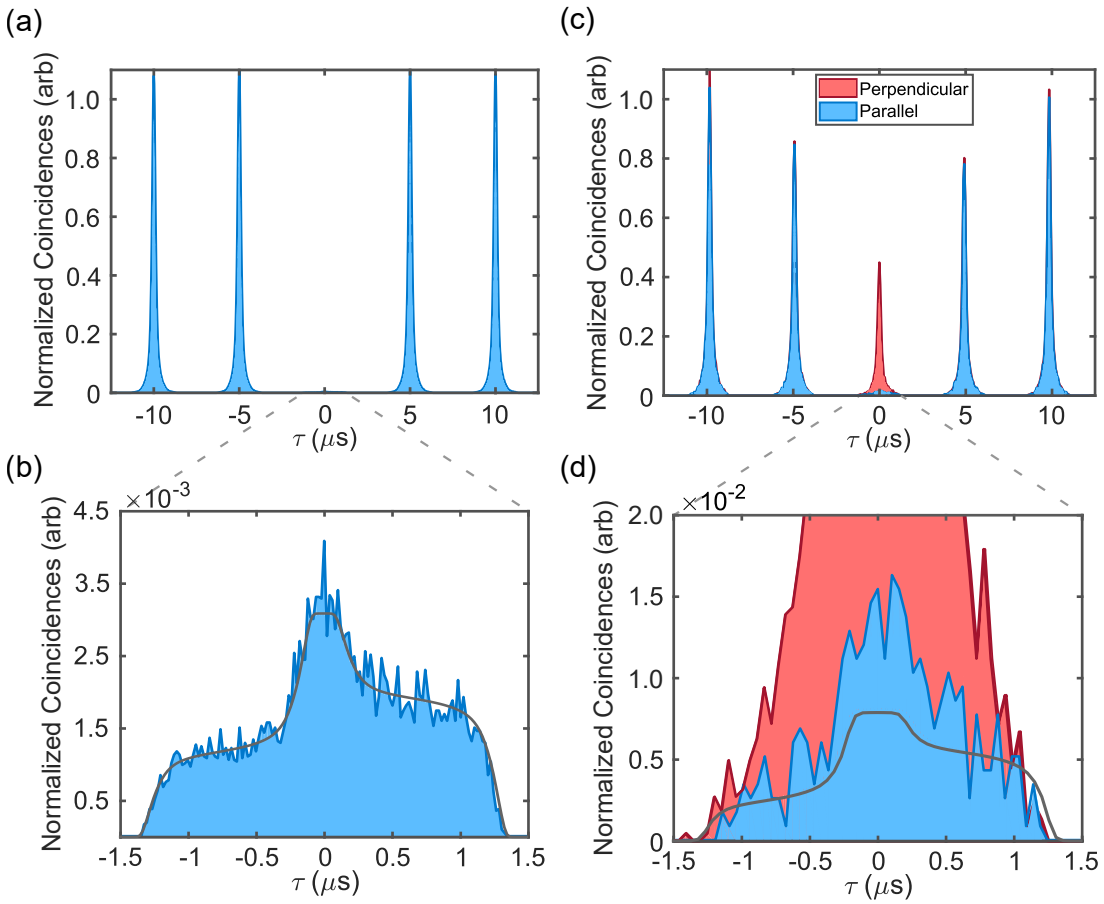

Figure 6.2: **Measured normalized coincidences for purity and indistinguishability characterization.** (a) Normalized coincidences for $g^{(2)}(\tau)$ with 5 μs cycle. (b) Normalized coincidences for $g^{(2)}(\tau)$ around $\tau = 0$, grey line represents the background coincidences with 20-ns bins. The shape of this profile arises from the convolution of the photon pulse shape with a constant background within the gate window, and the pedestal asymmetry is because the background rate is not the same for each channel. All $\sim 2.4 \times 10^9$ pulse cycles for the data shown were taken with 60% duty cycle. (c) Normalized coincidences for HOM characterization with 4.92-μs cycle. Indistinguishable polarization states are indicated in blue, and distinguishable polarization states are in red. (d) Normalized coincidences for HOM around $\tau = 0$, the grey line represents the background coincidences with 52-ns bins. All $\sim 3 \times 10^8$ pulse cycles for the data shown were taken with 60% duty cycle.

200 μs, and averaged them together to have better statistics[1].

[1]The main source of statistical uncertainty comes from the integrated counts around $\tau = 0$, since the uncertainty $\propto 1/\sqrt{N}$.

Port/Polarization	T	R
Port 1 H	0.502(5)	0.421(3)
Port 1 V	0.484(5)	0.428(3)
Port 2 H	0.511(9)	0.426(5)

Table 6.2: Transmission and reflection coefficients for the BS used in the HOM interferometer.

6.3 Source Efficiency

We measure a peak fibered efficiency of 0.18(2) after polarization filtering and averaged for a 20% duty cycle. Accounting for optical losses and assuming that the single photon has the same spatial mode as the 780-nm write beam, we estimate a generation probability of 0.40(4) immediately after the atomic ensemble. The average fibered and generation efficiencies reduce to 0.14(1) and 0.31(2) respectively, for a 60% duty cycle.

We observed that the average photon production efficiency decreased at higher repetition rates, as shown in Figure 6.3(a). Here the photon probability is determined immediately after the atom cloud by accounting for independently measured optical losses. The initial pulse in a series had higher efficiency; however, the efficiency of subsequent pulses decreased exponentially to the steady-state value on a ≈ 60 μs time scale (see Figure 6.3(b)).

These observations are consistent with the creation of contaminant atoms in other long-lived Rydberg states due to collisions with ground-state atoms surrounding the Rydberg electron [129]. Since the pollutants are in other Rydberg states they can not be removed by the retrieval field. These states interact strongly with the target Rydberg state, affecting subsequent writing events. Similar contaminant states have been observed in previous experiments [163, 166, 167], and

have been analyzed extensively [129, 168–171]. Once a contaminant is present, it disables the writing of a spin wave until it decays. The generation probability is significantly reduced for pulses with periods much shorter than the lifetime of the pollutant.

6.3.1 Pollutant States

We use a simple model to capture the effect of contaminants on photon production. We assume that on a given pulse, there is a probability P_c that a stored spin wave is converted to a contaminant. If the contaminant state has a lifetime τ_c, then the probability P_n of having a contaminant in the n-th pulse of a pulse series with period t_p is

$$P_n = P_{n-1}e^{-t_p/\tau_c} + (1 - P_{n-1})P_c, \tag{6.2}$$

here, the first term is the probability that a pollutant created in the previous pulse did not decay, and the second term is the probability of creating a contaminant P_c given that no pollutant existed in the previous pulse. If we set the initial condition to be $P_1 = P_c$, and use the identity $(1 - x)\sum_{j=0}^{n-1} x^j = 1 - x^n$, we get that the probability P_n takes the form,

$$P_n = P_c \frac{1 - (e^{-t_p/\tau_c} - P_c)^n}{1 - e^{-t_p/\tau_c} + P_c}. \tag{6.3}$$

For $\tau_c \gg t_p$, the average contaminant probability as $n \to \infty$ can be significant, even if P_c is small.

The probability of successfully generating a photon on the n-th pulse $P_g(n)$, in

the presence of a contaminant (either created previously or in the current attempt) is decreased by,

$$\begin{aligned} P_g(n) &= P_{max}(1 - P_n) \\ &= P_{max}\left(1 - P_c \frac{1 - (e^{-t_p/\tau_c} - P_c)^n}{1 - e^{-t_p/\tau_c} + P_c}\right), \end{aligned} \tag{6.4}$$

where P_{max} is the maximum probability of generating a photon in the absence of pollutants. For $n \to \infty$, the steady state probability P_s,

$$P_s \approx P_{max}\left(1 - \frac{P_c}{1 - e^{-t_p/\tau_c} + P_c}\right). \tag{6.5}$$

Fitting Eq. (6.5) to the pulse sequence data as shown in Fig. 6.3(b), we determine $P_c = 1.9(3) \times 10^{-2}$, and $\tau_c = 65(8)$ μs, which is in good agreement with the data in Fig. 6.3(a). Fixing a single decay time is an approximation, since there may be different contaminant states with different τ_c.

We find that P_c increases linearly with atomic density ρ (see Fig. 6.3(c)), which suggests that the source of contaminants is ground-Rydberg interactions. For high principal quantum number, n, collisionally produced contaminants were identified in Ref. [129] to be Rydberg states with principal quantum number $n - 4$ and quantum angular momentum $l > 2$. Furthermore, we find that P_c increases with storage time t_s at a rate $\approx 3 \times 10^{-2}$ μs^{-1}, which gives a contaminant generation time scale of ≈ 33 μs for a density $\approx 4 \times 10^{11}$ cm^{-3}. Contaminants are not a fundamental limitation since strong electric field pulses between writing pulses could be used to remove them. We were unable to implement this removal procedure in our current apparatus due to technical limitations associated with charging effects

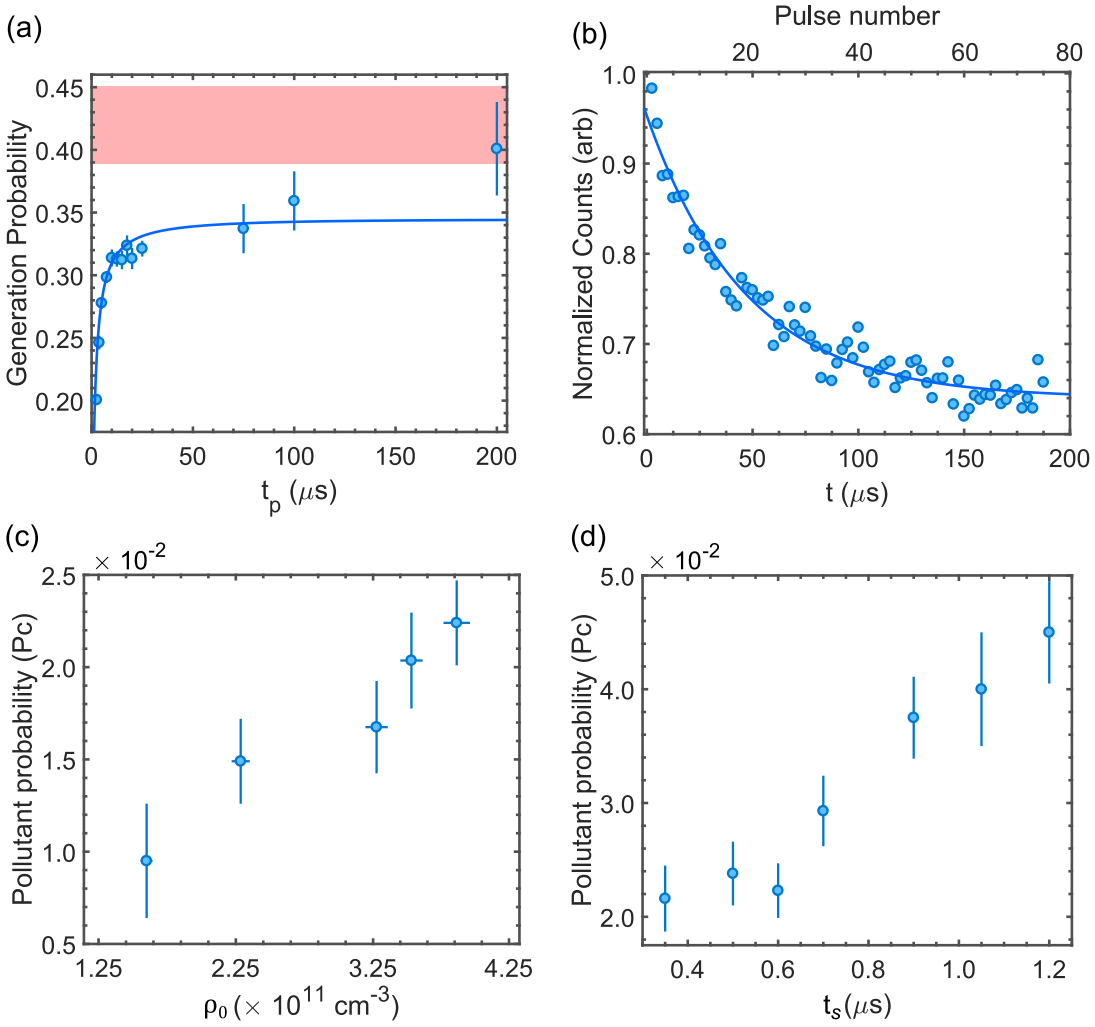

Figure 6.3: **Effect of contaminants on single-photon generation.** (a) Photon generation probability as function of pulse period t_p. Dark blue line is fitted using Eq. (6.5) in steady state for $n \to \infty$ using the values for $P_c = 1.9 \times 10^{-2}$ and $\tau_c = 65$ μs, we obtain $P_{max} = 0.35(2)$. Red band shows the generation probability predicted by the theoretical model. (b) Normalized summed counts per pulse for a pulse train with 2.5-μs pulse period. Dark-blue line is fitted with Eq. (6.3). (c) P_c vs. peak atomic density ρ_0 with a fixed storage $t_s = 350$ ns. (d) P_c vs. storage time t_s with a fix density $\rho_0 \approx 4 \times 10^{11}$ cm^{-3}.

of nearby dielectric surfaces (See Chapter 5).

Atom loss becomes more significant for interrogation times longer than 100 ms, due to effects such as heating and atom depolarization from rescattering. For short t_p, where this problem is most prominent, the average probability of generating a photon during 600 ms is $\approx$ 75% of the generation probability during the first 100 ms. However, these effects can be mitigated by detuning farther from the

intermediate state.

We also note that there was no statistical difference in $g^{(2)}(0)$ as a function of the pulse cycle t_p (to the level of $g^{(2)} \sim 10^{-3}$ for a smaller set of measurements), supporting our hypothesis that contaminants only prevent the spin-wave writing but do not affect the purity. Under the same argument, the indistinguishability should not change with the repetition rate, but we were not able to measure it for different delay times due to a fixed fiber delay available[2].

Despite the fact that the contaminants do not affect the purity of the photons, they do have an effect on $g^{(2)}(\tau \neq 0)$. We model how the correlation function, $g^{(2)}(m\ t_p)$ for integer $m \neq 0$, is modified due to contaminants:

$$\begin{aligned} g^{(2)}(mt_p) &= \frac{\langle P_s P_g(m) \rangle}{\langle P_s^2 \rangle} \\ &= 1 + P_c \frac{(e^{-t_p/\tau_c} - P_c)^{|m|}}{1 - e^{-t_p/\tau_c}}. \end{aligned} \tag{6.6}$$

This manifests as a bunching feature around $\tau = 0$ as shown in Fig. 6.4.

6.3.2 Theoretical estimation of photon generation

We calculate $P_{\text{th}} = \eta_w \eta_s \eta_r$ as a product of the writing, η_w, storage, η_s, and retrieval, η_r, efficiencies to estimate the theoretical probability of generating a photon. Using independently measured experimental values as input parameters, we obtain a theoretical prediction of $P_{\text{th}} \approx 0.42(3)$. This value is consistent with the measured generation probability for the longest pulsing periods, t_p.

Since our system closely behaves as a super-atom due to the blockade effect, the

[2]There are two challenges for measuring HOM-visibility at lower rates, first the time that it takes to accumulate coincidences goes as the square of the rate, and second the long delay lines needed of more than a kilometer would yield to a substantial loss at 780 nm where typical attentions are on the order of 4.0 dB/km, see spec sheet.

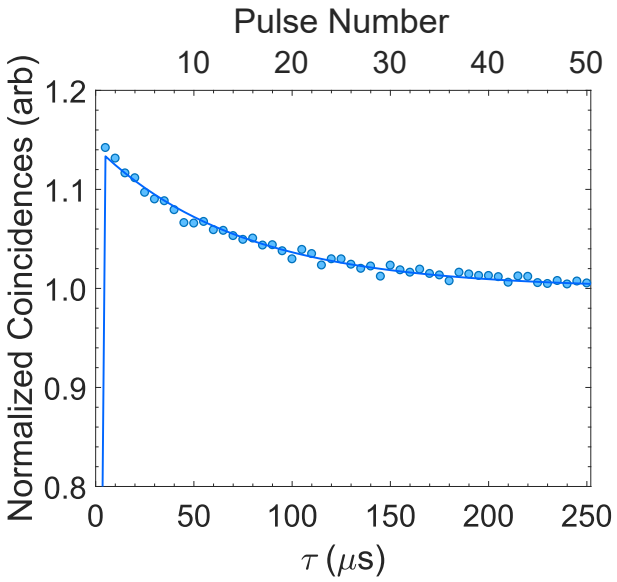

Figure 6.4: **Effect of contaminants on $g^{(2)}(\tau)$.** Pulse period corresponds to 5 μs.

write-store process is well described by the simple model using a master equation for a single-multi-level atom with an enhanced Rabi frequency. Figure 6.5 shows the energy levels and decay rates of the super-atom.

We simulate the writing stage as driving the super-atom from the ground to the Rydberg state, with a $\sqrt{N}$-enhanced Rabi frequency. During the writing time, t_w, the Rabi frequencies, $\Omega_p/(2\pi) = 1.0(2)$ MHz and $\Omega_c/(2\pi) = 6.8(3)$ MHz are kept constant. For the storage time, t_s, these driving frequencies are set to zero.

Not including the motional energy, the Hamiltonian describing the system depicted in Fig. 6.5 is given by:

$$H(t) = \frac{\hbar}{2}\begin{pmatrix} 0 & \sqrt{N}\Omega_p(t) & 0 & 0 \\ \sqrt{N}\Omega_p(t) & -2\Delta_p & \Omega_c(t) & 0 \\ 0 & \Omega_c(t) & -2\delta & 0 \\ 0 & 0 & 0 & 0 \end{pmatrix}, \tag{6.7}$$

in the basis of $|g\rangle$, $|e\rangle$, $|r\rangle$, $|c\rangle$, for the ground, intermediate, Rydberg and con-

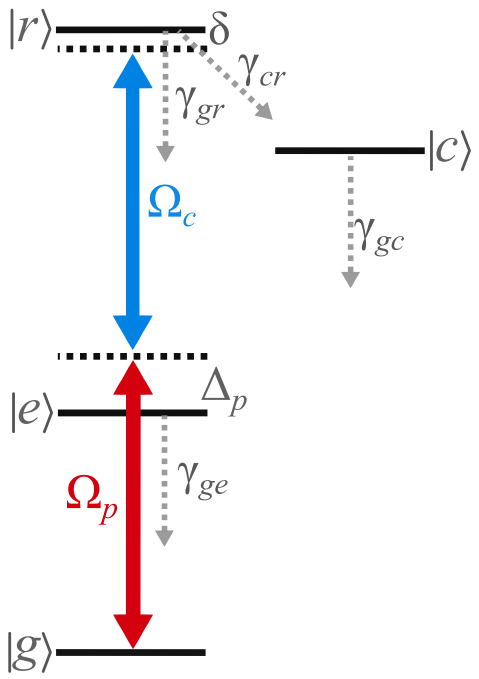

Figure 6.5: **Super-atom levels and decay rates.** Here we show the ground-state, as $|g\rangle = |5S_{1/2}\rangle$, the intermediate state $|e\rangle = |5P_{3/2}\rangle$, Rydberg state $|r\rangle = |139S_{1/2}\rangle$, and the contaminants states as $|c\rangle$.

taminant state, respectively.

Using the Python package QuTip [172], we calculated the non-unitary dynamics of this first stage using the master equation for the four-level density matrix ρ:

$$\dot{\rho} = -\frac{i}{\hbar}[H, \rho] + \sum_n \left(C_n \rho C_n^\dagger - \frac{1}{2}\{\rho, C_n^\dagger C_n\} \right), \tag{6.8}$$

where $C_1 = \sqrt{\gamma_{ge}}\,|g\rangle\langle e|$, $C_2 = \sqrt{\gamma_{gr}}\,|g\rangle\langle r|$, $C_3 = \sqrt{\gamma_{rc}}\,|r\rangle\langle c|$, and $C_4 = \sqrt{\gamma_{gc}}\,|g\rangle\langle c|$ are the jump operators for the dephasing and decay channels. In our experiment the scalar differential light shift from the trapping light is the main contribution to γ_{gr}, followed by other dephasing mechanisms due to the finite temperature of the atoms, such as Doppler broadening, or transit broadening.

Given the decay rates of the different states are: $\gamma_{ge}/(2\pi) = 6.9(6)$ MHz, $\gamma_{ge}/(2\pi) = 88(6)$ kHz, $\gamma_{rc}/(2\pi) = 5(1)$ kHz, and $\gamma_{gc}/(2\pi) = 2.5(3)$ kHz, we

estimate that the writing and storage efficiency are $\eta_w = 0.82(1)$, $\eta_s = 0.82(1)$, respectively.

We calculate the retrieval efficiency using the optical Maxwell-Bloch equations derived in Chapter 3 by following the formalism in Ref. [95]. Changing to the co-moving frame of the field, and defining the re-scaled coordinate $\tilde{z} = z/L$, where L is the length of the atomic medium, and the dimensionless time $\tilde{t} = t/\gamma_{ge}$, the equations of motion (3.33)-(3.35) become

$$\partial_{\tilde{z}}\mathcal{E} = i\sqrt{d}P, \tag{6.9}$$

$$\partial_{\tilde{t}}P = -(1 - i\tilde{\Delta})P + \sqrt{d}\mathcal{E} + i\tilde{\Omega}S, \tag{6.10}$$

$$\partial_{\tilde{t}}S = -\tilde{\gamma}_s + i\tilde{\Omega}P, \tag{6.11}$$

here, the equations are in terms of the dimensionless parameters: $\tilde{\gamma}_s = (\gamma_{gr} + \gamma_{cr})/\gamma_{ge}$, $\tilde{\Delta} = 2\Delta_p/\gamma_{ge}$, $\tilde{\Omega}(t) = \Omega_c(t)/\gamma_{ge}$, with $\mathcal{E} \to \mathcal{E}\sqrt{c/(L\gamma_{ge})}$, and the optical depth d=OD/2.

In the re-scaled unit-less coordinates, $\tilde{z} = 0$ and $\tilde{z} = 1$ represent the front and the end of the atomic cloud, respectively. Supposing a perfect spin wave in the beginning of the retrieval stage at time $\tilde{t} = 0$, the shape of the spin wave is given by $S(\tilde{z}, \tilde{t} = 0) = 1$ for $\tilde{z} \in [0, 1]$ and $S(\tilde{z}, \tilde{t} = 0) = 0$ for $\tilde{z}$ elsewhere. The retrieval efficiency can be expressed in terms of the photon field $\mathcal{E}(\tilde{z}, \tilde{t})$ emitted by the stored spin wave at the end of the atomic cloud:

$$\eta_r = \int_0^\infty d\tilde{t}|\mathcal{E}(\tilde{z} = 1, \tilde{t})|^2. \tag{6.12}$$

Calculating $\mathcal{E}(1,\tilde{t})$ requires solving:

$$\begin{aligned}\mathcal{E}(1,\tilde{t}) = -\sqrt{d}\tilde{\Omega}(\tilde{t})\exp\left(-\tilde{\gamma}_s\tilde{t}\right)\int_0^1 d\tilde{z}\frac{\exp\left(-\frac{h(0,\tilde{t})+d\tilde{z}}{1+i\tilde{\Delta}}\right)}{1+i\tilde{\Delta}} \\ \times I_0\left(2\frac{\sqrt{h(0,\tilde{t})d\tilde{z}}}{1+i\tilde{\Delta}}\right)S(1-\tilde{z}),\end{aligned} \tag{6.13}$$

where $h(\tilde{t},\tilde{t}') = \int_{\tilde{t}}^{\tilde{t}'}|\tilde{\Omega}(\tilde{t}'')|^2 d\tilde{t}''$, and I_0 is the $0th$-order modified Bessel function of the first kind. When the control field Ω_c is constant in time, we define the dimensionless parameter $x_s = 2\tilde{\gamma}_s/|\tilde{\Omega}_c|^2$ which characterizes the strength of the decay rate compared to the control field. Eq. (6.12) can be evaluated as

$$\eta_r = \int_0^1 d\bar{z}\int_0^1 d\bar{z}' K_r S(1-\bar{z})S^*(1-\bar{z}'), \tag{6.14}$$

where K_r is given by

$$\begin{aligned}K_r = &\frac{df(x_s)}{2} \\ &\times\exp\left[-\frac{df(x_s)}{2}\left((1+x_s(1-i\tilde{\Delta}))\bar{z}+(1+x_s(1+i\tilde{\Delta}))\bar{z}'\right)\right] \\ &\times I_0(d\sqrt{\bar{z}\bar{z}'}f(x_s)),\end{aligned} \tag{6.15}$$

and $f(x_s) = \frac{2}{2+x_s(1+\tilde{\Delta}^2)}$.

Numerically integrating Eq. (6.14), we obtain the retrieval efficiency $\eta_r = 0.63(2)$. With these results, we estimate that the photon generation probability at the end of the cloud is $P_{\text{th}} = 0.42(3)$.

With feasible experimental improvements, such as implementing a Rydberg-ground-state blue-detuned dipole trap and decreasing the mean atomic temperature to 5 μK (from the current 10 μK), the spin-wave dephasing rate could

decrease by at least a factor of two. By increasing the following parameters as well, $\Omega_c/(2\pi) = 10$ MHz, $\Delta_p/(2\pi) = 100$ MHz and OD=20, we estimate that the generation efficiency could be up to $\eta = 0.62$, with $\eta_w\eta_s = 0.86$ and $\eta_r = 0.72$, while maintaining a relatively low contaminant probability $P_c \approx 3 \times 10^{-2}$.

The main limiting factor to increasing the efficiency, according to the theoretical model, is the retrieval process. In principle, the retrieval efficiency increases with higher OD; however, the contaminant production also grows with OD. A Rydberg ensemble with low OD coupled to a cavity [173, 174] could further increase light-matter interactions, and increase the overall photon production probability, making it a promising platform for scalable quantum information applications.

Despite this model predicting a photon generation efficiency within the experimental error bars, we also note that it is based on many simplifications. For instance, it fails to reproduce some experimental observations accurately (see Fig. 6.6), it does not take into account Rydberg blockade effect during the writing stage, neglects the interactions from contaminants, or does not considers other collective effects such as the decay to other bright states [175].

6.3.3 Source optimization

One limitation of a Rydberg-based photon source is the finite coherence time of the ground-Rydberg spin wave. As we discussed in Chapter 5, a major source of decoherence is the differential light shifts from our dipole trap. We lowered the overall power in our crossed dipole trap to decrease the ground-Rydberg differential light shifts, but kept the dimple beam at full power. In this configuration, the dimple reduces the axial length of the medium, so that we can produce a single

spin-wave excitation during writing (given the blockade radius) and retrieve it as a highly pure photon as demonstrated in Fig. 6.2(a)-(b). Furthermore, the collective constructive interference from the N atom spin wave allows the directed emission of photons into a well defined single-mode, making them highly indistinguishable (see Fig. 6.2(c)-(d)).

The success of spin-wave forward retrieval with a finite coherence time reaches a maximum as a function of OD, for a coherence time of ≈ 2 μs the retrieval probability peaks around OD=25 as predicted from Eqs. (6.14) and (6.15). We work with an OD=13, where there are different factors limiting the maximum density we can achieve to increase the success of retrieval. First, lowering the dipole trap power to reduce decoherence, also reduces the atomic density. Second, we load the MOT for only for 250 ms to increase the duty cycle of the experiment and optimize the flux of retrieved photons per second. Lastly, as discussed in Section 6.3.1 the long-lived contaminant creation grows with atomic density. For example, the pollutant probability per pulse is $\approx 3.5\%$ for an OD=25 when extrapolating the data from Fig. 6.3(c). Using Eq. (6.5) the average retrieval probability is $0.67P_{\max}$, with an estimate of $P_{\max} \approx 0.38$ then $P_s = 0.25$, for a repetition rate of 5 μs and a contaminant lifetime of $\tau_s = 68$ μs. Comparing with the current OD=13, where the average probability is[3] $P_s = 0.8$ and $P_{\max} = 0.28$; it is an example of how pollutants are detrimental when operating at high repetition rates, despite an improvement of $P_{\max}$ by increasing OD.

We also noticed that the retrieval efficiency is maximum at a control detuning $\Delta_c/(2\pi)$ =7 MHz from the transition $\left|139S_{1/2}\right\rangle \rightarrow \left|5P_{3/2}\right\rangle$ resonance frequency.

[3]Estimated generation probability for 100 ms of interrogation time where we neglect the atomic loss due to scattering events from the writing pulses.

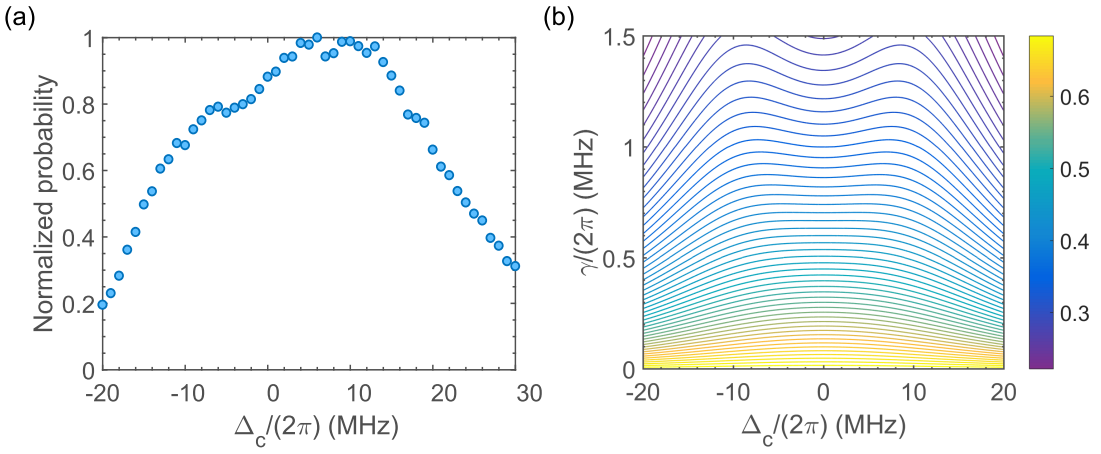

Figure 6.6: **Retreival probability as a function of Δ_c.** (a) Measured normalized retrieval probability, at $\Delta_c = 0$ the probability is reduced by 12% from the peak probability. (b) Contour plot of the numerical integration of Eq. (6.14) as a function of γ and Δ_c for OD=13.

The efficiency is also asymmetric as illustrated in Fig. 6.6(a). This behavior is very peculiar, since we would expect the probability would peak on resonance and that it would be symmetric around $\Delta_c = 0$. From measurements, we determine that the optimum retrieval detuning is independent of OD, repetition rate, or the initial writing conditions. It seems that there might be some dependence on Rabi frequency, Rydberg level n, and or the dephasing rate, although these observations are inconclusive. Eqs. (6.14) and (6.15) predict that the retrieval could be optimal for $\Delta_c \neq 0$ for a given spin-wave dephasing rate (see Fig. 6.6(b)). However, using our parameters to observe a peak probability around $\Delta_c/(2\pi)$ =7 MHz, the predicted dephasing rate would be $\gamma_s/(2\pi) \approx 0.9$, which is about an order of magnitude larger than the measured one. Furthermore, the theoretical model fails to reproduce the asymmetry with Δ_c. Without additional measurements on the origin of this behavior, it is difficult to formulate a more accurate model.

6.4 Results and Outlook

By using the quantum nonlinearities of strongly-interacting Rydberg states in a cold atomic ensemble, we demonstrated a single-photon source, operating with a 60% duty cycle, single-mode efficiency $P_1^{\mathrm{sm}} = 0.098(2)$, a single-mode rate of $\mathcal{R} = 1.18(2) \times 10^4\ s^{-1}$, and single-mode fidelity $\mathcal{F} = 0.980(7)$. This fidelity is the highest reported to our knowledge for an atomic-based source. For a comparison with other single-photon sources see Figure 4.4. Furthermore, we investigated the limitations of our current setup arising from nearby long-lived contaminant states.

Implementing feasible experimental upgrades, we estimate that we can achieve up to $P_1^{\mathrm{sm}} \approx 0.4$. Moreover, ionizing pulses after each write-retrieval pulse to remove atoms in pollutant states may increase the rate up to $\mathcal{R} \approx 1.2 \times 10^5\ s^{-1}$ without decreasing the duty cycle or the fidelity. The efficiency could be improved if the ensemble were coupled to a cavity. Given their high efficiency, rate, and fidelity, we have shown that single-photon sources based on Rydberg-atomic ensembles provide a promising platform for scalable quantum photonics, for example, boson-sampling, and quantum networking. Furthermore, they are inherently compatible with narrow-bandwidth atomic platforms that have shown significant progress towards quantum information applications. As we show in the next chapter, we observe a high-visibility HOM-interference between our high-fidelity photons and single-photons emitted from a remote single-trapped ion. This demonstration is a crucial step towards building hybrid-atomic quantum networks.

Chapter 7: Two-photon interference between Photons from an Atomic Ensemble and a Remote Single Ion

Breakthroughs in distributed quantum entanglement for quantum networks will likely require heterogeneous quantum nodes that take advantage of the complementary strengths and functions of different quantum platforms [176–178]. However, spectrally matching photons from disparate systems has been the main limitation to generate remote entanglement in hybrid networks [31, 178, 179]. In this chapter, we describe the demonstration of time-resolved two-photon quantum interference between high fidelity photons generated from our Rydberg-ensemble and photons produced by a remote trapped Barium ion.

We achieve high HOM-visibility by closely matching the frequency of the photons using difference frequency conversion (DFG) and linking both systems through a 150-m fiber. This work is the outcome of a joint collaboration with the group of Q. Quraishi at the Army Research Lab (ARL). They built the Barium ion apparatus, optimized the ion-produced photon generation, and assembled the DFG setup.

This result, published in [59], is a significant step towards remote entanglement for hybrid quantum networks, between two of the most promising platforms in quantum information: Rydberg atoms [45,46,48–50,89–92], and trapped ions [153, 179–186].

7.1 Experimental setup

Figure 7.1(a) shows a schematic of our experiment spanning two buildings. Building A contains a single trapped $^{138}Ba^{+}$ ion as well as two DFG setups. Building B contains our ^{87}Rb atomic ensemble and a HOM interferometer to measure two-photon interference. An externally-triggered time-tagging device records detection events for two SPADs, 1 and 2 from the HOM interferometer. Each building contains a Hanbury Brown-Twiss setup (not pictured in Fig. 7.1) for the measurement of the second-order intensity auto-correlation functions.

The ARL trapped ion experiment as well as the frequency conversion setup are detailed in Refs. [187, 188]. The ion emits single photons near 493 nm via spontaneous emission from the $6P_{1/2}$ excited state to the $6S_{1/2}$ ground state. A lens collects these photons with $\approx 4\%$ efficiency, and couples them with $\approx 30\%$ efficiency into a SMF, which is connected to DFG-1, (for more details of the setup see Ref. [188]). We spatially overlap these photons with a strong 1343-nm pump and couple both into a periodically poled lithium niobate waveguide. Here, the DFG converts the 493-nm photons to 780 nm, while preserving their quantum statistics [188, 189].In addition to converted single photons, the pump light produces noise at longer wavelengths than the pump due to effects such as spontaneous down-conversion, Raman scattering, and noise near 780 nm due mainly to anti-stokes Raman scattering. After filtering out this pump induced noise [187] to a rate negligible compared to the dark count rate of the SPADs (typically $\approx$100 s^{-1}), the converted photons are sent to the HOM interferometer in Building B via a 150-m PMF.

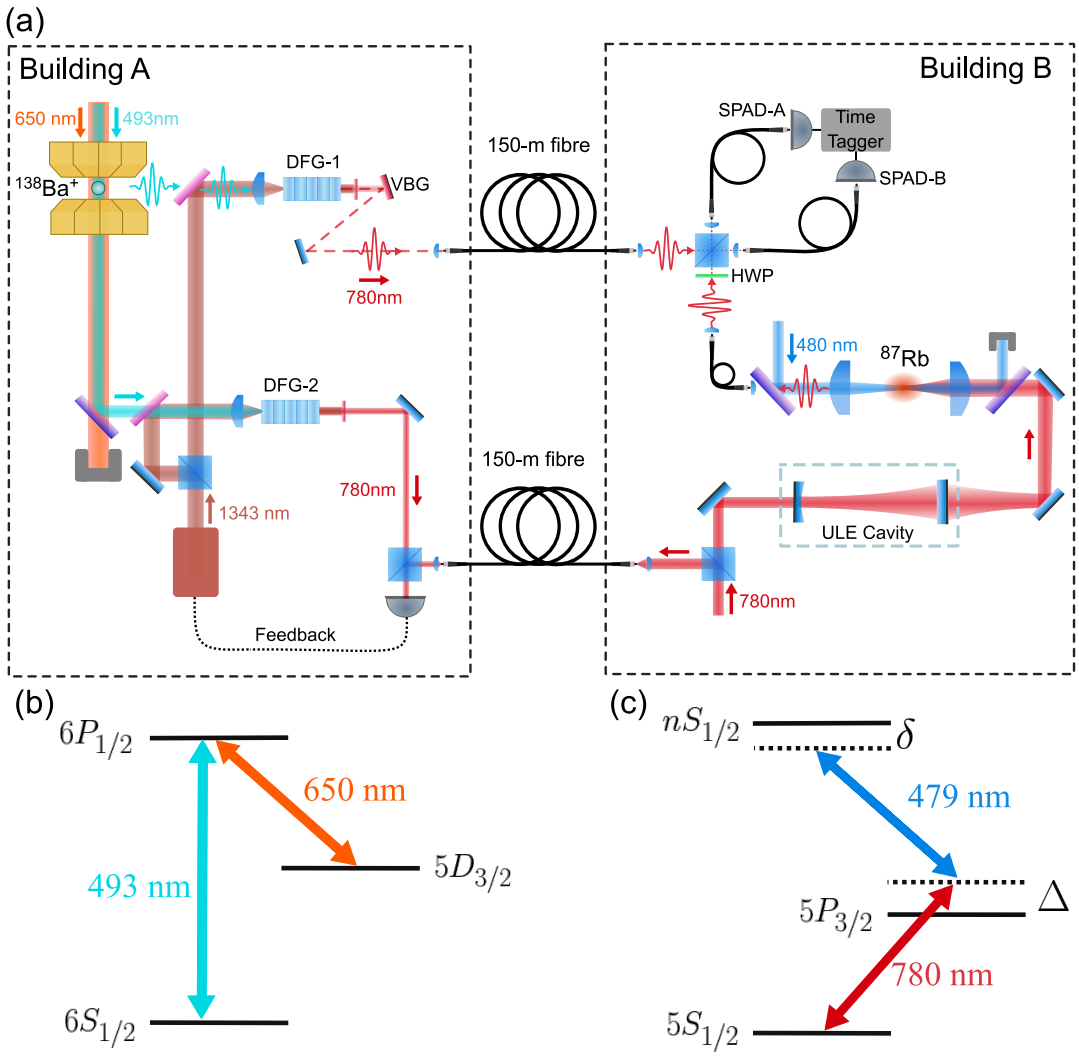

Figure 7.1: **Experimental layout and energy level diagrams for the two sources.** (a) Building A contains a $^{138}Ba^{+}$ ion which emits photons at 493 nm, and Building B contains a ^{87}Rb atomic ensemble producing 780-nm photons. Ion-emitted photons are converted to 780 nm using DFG-1 and sent to Building B via PMF. DFG-2 produces 780-nm light used to frequency stabilize the output of DFG-1 by optical beat note locking with reference light sent from Building B. Light from the ion and ensemble source is sent to the HOM interferometer for two-photon interference measurements. A HWP in one input path allows for control of the relative polarization of the photons. The photons interfere at a nearly 50:50 beamsplitter before being coupled into two SMF, which are connected to SPADs linked to a time-tagging device triggered by an external electronic reference. Here VBG stands for a volume Bragg grating and ULEC for ultra-low expansion cavity. (b) Level scheme for $^{138}Ba^{+}$. (c) Level scheme for ^{87}Rb.

A second frequency conversion setup DFG-2 ensures the converted ion-produced photons are at a similar frequency as our photons. Continuous-wave (CW) laser light at 493-nm, with a ± 10 MHz detuning from the photons emitted by the ion, is

combined with the same pump light used in DFG-1 to produce CW 780-nm light from DFG-2. The output frequencies of DFG-1 and DFG-2 can both be controlled by changing the pump frequency. We send a small fraction of 780-nm laser-light (locked to our high finesse cavity) to Building A by a 150-m optical fiber, this stabilized light interferes with the 780-nm light from DFG-2 at a fast photodetector (PD) producing a beat note signal. By using the output beat note to generate an error signal feeding back to the pump laser, we stabilize and set the frequency of the output 780-nm light from both DFG setups. There are non-negligible uncertainties in the center frequency of the converted 780-nm single photons, which affect the two-photon interference. This is a consequence of the uncertainties from the ion spectroscopy and drifts in the 493-nm and 650-nm laser wavemeter locks.

The ion in is prepared in the $5D_{3/2}$ manifold via optical pumping using 493-nm light to produce on-demand single photons. A pulse of 650-nm light then excites to the $6P_{1/2}$ manifold, from which decay to the $6S_{1/2}$ ground manifold produces a single 493-nm photon [190], with measured $g^{(2)}_{\text{ion}}(0) = 0(1) \times 10^{-2}$ after background subtraction. Due to the magnetic bias field (≈ 5 G) splitting the Zeeman states in the $6S_{1/2}$ and $5D_{3/2}$ levels, combined with technical limitations resulting in a near-equal population distribution in the $5D_{3/2}$ manifold after pumping, the average photon spectrum consists of several peaks with a center frequency determined by the detuning of the 650-nm laser used to excite the ion from the $5D_{3/2}$-$6P_{1/2}$ transition.

The ion-produced photon detection probability is $\approx 2 \times 10^{-5}$ per attempt at the output of the HOM interferometer. The ion-photon pulse exhibits a nearly exponential decaying temporal profile, with a decay constant (≈ 50 ns) set by the

effective Rabi frequency of the 650-nm retrieval pulse. In comparison, our photon had a per-attempt detection probability of $\approx 3 \times 10^{-2}$ at the output of the HOM interferometer, and the pulse temporal profile is well approximated to a decaying exponential with a decay constant of ≈ 120 ns.

Instead of using the polarization degree of freedom to make the photons distinguishable for the HOM indistinguishability measurement, we used the arrival time or temporal mode to discriminate the photons as distinguishable or indistinguishable. We doubled the repetition rate of the ion-produced photons (400 kHz) with respect to the repetition rate of our photons (200 kHz), so we alternate the simultaneous arrival time of the ion-produced photons and our photons (where both have the same temporal mode at the BS), with instances when their arrival times are not overlapped, depicted in Fig. 7.2(a). To synchronize the arrival of the photons, we operate in a controller-minion configuration, our experiment in Building B is the controller, and the ion lab in building A is the minion. We generate 1064-nm optical pulses using an AOM, which are sent over a fiber to the ion lab (the 1064-nm laser and fiber are not shown in Fig. 7.1). Then, the optical pulse is converted to a TTL signal, using a high bandwidth PD (ThorLabs PDA05CF2), which triggers the ion photon production. Due to drifts in the 1064-nm optical pulse power, we observe small drifts ($\leq$20 ns over several hours) in the ion-produced photon arrival time relative to an electronic reference that defines an absolute time within the 5-μs cycle. To ensure the photon profiles overlap, even with these drifts, we offset the average arrival time of the ion-produced photon$\approx$+40 ns relative to the peak of our photon pulse. Calculations indicate that this offset and small temporal drifts have a negligible effect on the two-photon

interference. We observed no measurable drift between the temporally overlapped and non-overlapped photons produced by the ion, with a temporal separation of 2.5 μs. There was no measurable drift between the arrival time of our photon and the electronic reference.

This procedure allows us to measure the visibility in a single experimental run. Furthermore, using coincidences across several shifted pulse periods (corresponding to coincidences due to distinguishable modes) reduces the statistical noise for calculating the visibility [59]. We operate at an experimental duty cycle of 0.6, with the non-data-taking time required to reload our atomic ensemble.

7.2 Results and Outlook

We apply a 120-ns gate window (containing $\approx 80\%$ of the ion-produced photon pulse) in SPAD 1 during the data post-processing, to mitigate noise counts, predominantly due to detector dark counts and ambient photons. Figure 7.2(b) and (c) show the resulting data for 5-ns bins after counting coincidences events between SPAD 1 and 2, and subtracting background coincidences, all within the gate window[1]. Comparing the temporally overlapped and non-overlapped coincidences respectively at $\tau = 0$ within a 5-ns bin, we calculate a visibility of 1.1(2). Despite the photons having different spectral properties, we obtain high-visibility by projecting both photons into the same spectro-temporal mode in a 5-ns time bin. We are able to resolve this feature because the time-resolution is much smaller than any other characteristic time-scale of the photons. The observed width of

[1] In a similar way that we did the background subtraction within a gate window to characterize $g^{(2)}(0)$ and indistinguishability of our photons detailed in Appendix B. The difference here is that the gating is applied to a single time coordinate t_1 rather than both time coordinates.

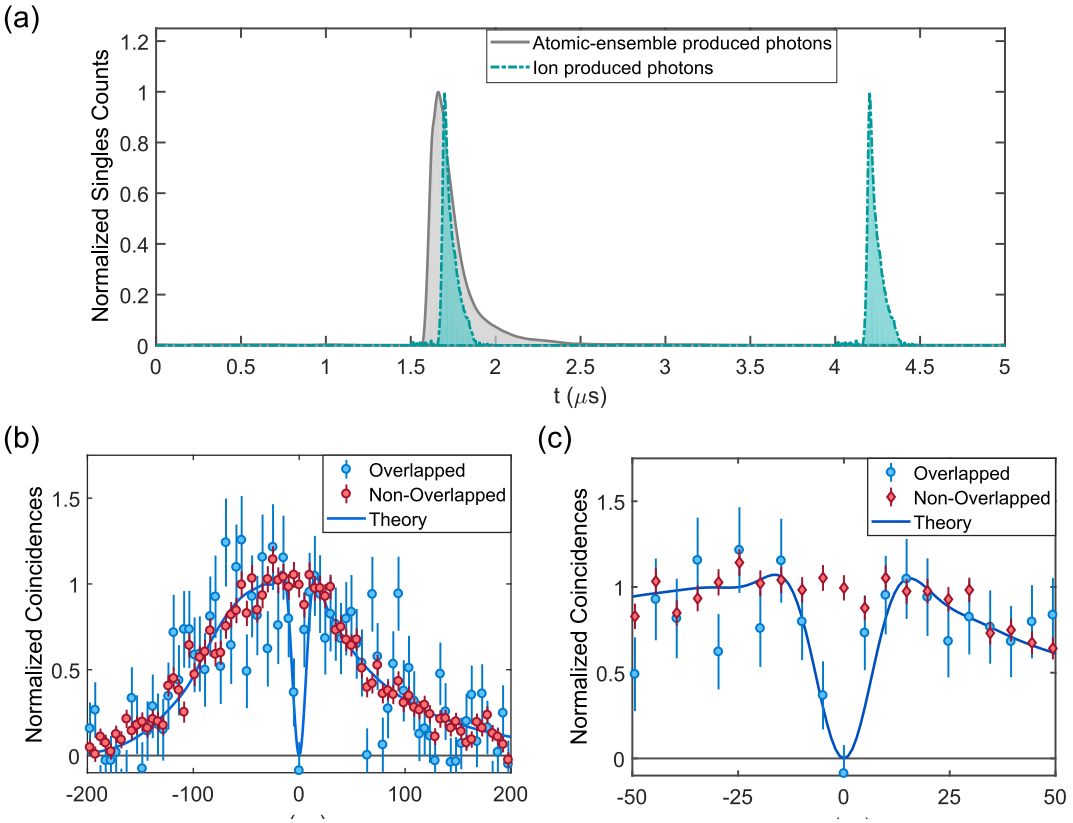

Figure 7.2: **On-demand pulse sequence and interference.** (a) Schematic of pulse sequence for one period. The atomic-ensemble produced photon profile, and ion-produced photon profile at $t \approx 4.25\ \mu s$, are measured directly. The ion-produced photon profile at $t \approx 1.75\ \mu s$ is a time-shifted copy of that at $t \approx 4.25\ \mu s$ to allow for easy comparison of the photon temporal shapes from the two sources. We offset the ion-produced photon peak +40 ns from our photon pulse to lessen the effects of small drifts in the relative arrival times. (b), and (c), Normalized coincidences when the photons from the two sources are temporally overlapped (non-overlapped) shown in blue (red). Both curves represent the data after gating, background subtraction, and using 5 ns bins. Dashed lines in **b** indicate the range shown in (c). The theory curve is obtained by taking into account the non-transform limited nature, probabilistic spectrum of the ion-produced photon, and plausible estimates of the relative drift ($2\pi \times 10$ MHz) and offset ($2\pi \times 20$ MHz) between the center frequencies of the photons from the two sources. Data presented accumulated over ≈ 22 hours. In all cases, the error bars denote statistical uncertainties.

the interference dip is narrower than expected if we only consider the temporal profile of the photons[2]. However, accounting for the multiple peaks in the ion-produced photon spectra, plausible laser-frequency drifts, and average center-frequency differences of the two photons (for details see [59]), we obtain good

[2]See discussion in Chapter 4, for a more in-depth analysis see Ref. [104]

agreement between theory and experiment, as seen in Fig. 7.2(b) and (c).

Having observed interference between photons generated from two fundamentally different quantum sources, we now examine our results in the context of hybrid quantum networking. We consider the entanglement generation scheme in [179, 186], as a natural extension of our setup to create a Bell-state analyzer, enabling the heralded generation of maximally entangled matter qubits. With this scheme, the resulting state fidelity, assuming perfect photon-matter entanglement and polarization discrimination, can be related to the visibility of the two-photon interference as $F = (1 + \mathcal{V})/2$. For the 5-ns bins in Fig. 7.2(c), we project $F \approx 1$. With the measured ≈ 40 bunching events and ≈ 22 hours experimental run time, we infer an entanglement rate of ≈ 2 hour^{-1}. These calculations assume negligible detector dark counts, achievable with commercially-available detectors, and through improved shielding of the detectors from ambient leakage light.

We can increase the entanglement rate compromising the achievable entanglement fidelity by using a larger time bin [191]. For example, with 10-ns bins, we estimate an entanglement rate of ≈ 4 hour^{-1} with $F \approx 0.9$, still well above the classical limit. Such entanglement rates would be comparable with the first experiments using similar schemes with homogeneous matter qubits [17, 192]. Additionally, we note that with reasonable improvements to the ion photon collection and detection, entanglement generation rates on the order of several events per minute, with $F > 0.9$ are achievable.

In conclusion, we have demonstrated high-visibility quantum interference between photons produced by an ion and atomic-ensemble. With the current configuration, we project that entanglement rates of ≈ 2 hour^{-1} are achievable. With

modest practical experimental upgrades, which predominantly improve the ion-produced photon collection, DFG conversion efficiency, and reducing optical losses through various elements, the entanglement rate could increase to several events per minute, making the realization of a hybrid ion-atomic ensemble quantum network practical.

Chapter 8: Tunable three-body interactions between Rydberg Polaritons

As discussed in Chapter 3, it is possible to engineer interactions between single photons by coupling them to strongly interacting Rydberg atoms and form Rydberg polaritons [43, 193]. The control over the degrees of freedom of this system, allow us to manipulate the coherent or dissipative character of the Rydberg polariton interactions, which are inherently multi-body [43, 97–99, 194–196]. The study of few-body systems with long-range interactions can help us engineer more complex many-body quantum systems and understand their properties and potential limitations due to loss, decoherence, or recombination. Realizing precise and reliable control of three-body effects can lead to the observation of rich phenomena, such as the universality of Efimov states [197], the purification of a quantum gas [198], and the emergence of strongly-correlated photonic states [56, 57].

Three-body effects between Rydberg polaritons can be strong [56, 57, 97, 99, 195], which distinguishes them from the usually weak three-body forces[1] observed with ultracold atoms and molecules near their ground state [200–203]. The three-body Rydberg polariton system has been analyzed in single-mode cavities [195, 204], as well as in three-dimensions in free-space [97]. Experimental works have explored three body-effects in elongated clouds in the dispersive regime [56], as well

[1]For a recent proposal showing how to enhance three-body interactions between atoms in optical potentials see Ref. [199].

for atomic mediums shorter than the range of the interactions [57] However, the study of dissipative three-body interactions for long atomic clouds is still lacking.

This chapter reports the investigation of tunable three-body loss of Rydberg polaritons. First, we describe the Rydberg-polariton system and show how energy and momentum conservation allows for three dark-state polaritons to scatter into lossy channels. Next, we outline the experimental procedure and present the measurements of two- and three-photon correlation functions as a way to probe two- and three-polariton interactions. We compare our measurements with numerical simulations of the Schrödinger equation (the numerical code was written by Michael Gullans). For completeness, we show the calculation of the rate of three-body scattering using Fermi's Golden Rule, this calculation was developed by Przemyslaw Bienias and Michael Gullans. Finally, we discuss the limitations of our system and some potential directions for the study of few- and many-body physics with Rydberg polaritons in our system.

8.1 Three-body scattering in Rydberg-EIT

Figure 8.1(a) depicts the atomic-level configuration for Rydberg-EIT that dresses the incoming photon. The ground state $|G\rangle$ of an ensemble of atoms is coupled to an intermediate state $|P\rangle$ by a weak quantum probe field with a collective coupling strength g. A strong classical field with Rabi frequency Ω_c couples $|P\rangle$ to an atomic Rydberg state $|S\rangle$. The Hamiltonian describing the propagation of a single excitation is given by [94, 98]

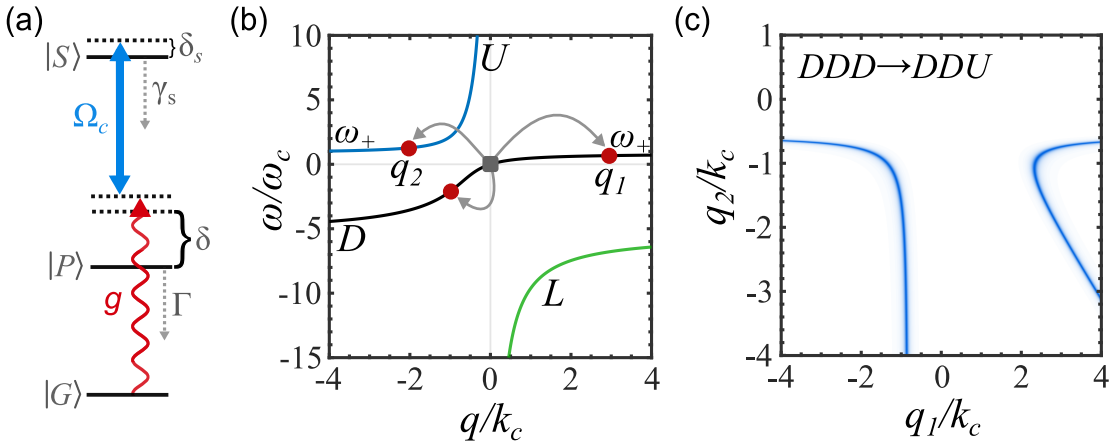

Figure 8.1: **Rydberg polariton system.** (a) Atomic structure: A weak coherent probe, with collectively enhanced single-photon coupling g, and a strong classical field, with Rabi frequency Ω_c, couples the ground state, $|G\rangle$, to the Rydberg state $|S\rangle$ via an intermediate state $|P\rangle$. (b) Dispertion relation of the three polariton branches for $\delta/(2\pi) = 25$ MHz, $\delta_s/(2\pi) = 0$, $\Omega_c/(2\pi) = 23.5$ MHz, assuming an homogeneous cloud of OD=37. The black curve is the dark-state branch (D), while the blue and green curves are the bright states (U and L). The diagram depicts the allowed three-body scattering for three polaritons initially near the EIT resonance at $\omega_j = q_j = 0$ ($j = 1, 2, 3$ labels the three initial DSPs). ω_+ corresponds to the energy where the dispersion curve for ω_D and ω_U become approximately flat (c) Allowed final momentum states for the three-body loss near the EIT resonance. Only the process depicted in (b) is relevant for small $\delta_s \approx 0$. There is no two-body loss process allowed because there are no final states with $q_1 = 0$ or $q_2 = 0$.

$$H = \begin{pmatrix} cq & g & 0 \\ g & -\Delta - \delta_s & \Omega_c/2 \\ 0 & \Omega_c/2 & -\Delta_s \end{pmatrix}, \tag{8.1}$$

here, c is the speed of light and $\hbar = 1$. This Hamiltonian is defined in the basis of $\{\mathcal{E}, P, S\}$, where $\mathcal{E}$ is the wavefunction of the photonic component, P and S are the wavefunctions of the intermediate- and Rydberg-state collective spin excitations, respectively [94]. The complex detunings $\Delta = \delta + i\Gamma/2$ and $\Delta_s = \delta_s + i\gamma_s/2$ take into account the decay rates of the excited states, and cq corresponds to the kinetic energy of the photon in the rotating frame.

After solving the Hamiltonian in Eq. (8.1), we obtain three new eigenstates,

corresponding to the dark, D, bright lower, L, and bright upper, U, polaritons. Figure 8.1(b) shows the dispersion relation of the polariton branches depicted by $\omega_D(q)$, $\omega_L(q)$, and $\omega_U(q)$. The convention is chosen so that the incoming probe photons have energy $\omega(q) = 0$, and momentum $q \approx 0$. For small δ_s, the dark-state polariton (DSP), which is a coherent superposition of $\mathcal{E}$ and $\mathcal{S}$, propagates with little loss through the medium[2] [205]. In contrast, the lower- and upper-bright polaritons are lossy since they have a significant component of the P-state.

The energy scale of the system is set by $\omega_c \equiv \Omega_c^2/4|\Delta|$, with characteristic momentum $k_c = \omega_c/v_g$, where $v_g \approx \frac{\Omega_c^2}{g^2}c$ is the group velocity. For a single or two incoming low-energy DSP with $|\delta_s| \ll \omega_c$, the scattering process from dark to the lossy bright polaritons is strongly suppressed [98], see Fig. 8.1(c). Intuitively, this suppression arises from energy and momentum conservation where DSPs with $q = 0$ are not allowed to scatter to any of the bright channels. However, for three polaritons, the scattering from the dark branch to the lossy channels is allowed by conservation laws, which results in tunable three-body losses. Furthermore, the character of the interactions and the dispersion relation can lead to resonant enhancement of three-body loss by adjusting the system parameters: OD, Ω_c, δ, and δ_s. In the following sections, we detail the observation of this scattering process by changing the detunings δ, and δ_s, with the largest attainable OD and Rabi frequency Ω_c.

[2]For large values $|q|$ of momenta this branch becomes lossy.

8.2 Experimental setup

We load and cool ^{87}Rb atoms in a crossed optical dipole trap (as described in Chapter 5). The atomic cloud has RMS dimensions $\sigma_r = 20 \pm 2$ μm ($\sigma_z = 40 \pm 4$ μm) in the radial (axial) direction with $\simeq 10^5$ atoms, wich corresponds to an OD=37$\pm$4 with mean temperature of 10 μK.

After preparing the atoms in the $|G\rangle = |5S_{1/2}, F = 2, m_F = 2\rangle$ ground state, we generate Rydberg polaritons using the three level configuration (see Fig. 8.1(a)). A weak coherent probe couples the ground-state to the intermediate state $|P\rangle = |5P_{3/2}, F = 3, m_F = 3\rangle$, with a collective coupling strength $g \simeq 10^3$ MHz and a beam waist of 3.3 μm. The control field couples the intermediate state to the Rydberg state $|S\rangle = |82S_{1/2}, m_J = 1/2\rangle$ with a Rabi frequency of $\Omega_c/(2\pi) = 23.5 \pm 1.5$ MHz and a waist of 19 μm. We vary the single-photon detuning δ and the two-photon detuning δ_s to change the interactions among polaritons, while keeping the photon flux, Rabi frequency and optical density fixed.

The average incoming photon rate is $R_{in} \simeq 3\,\mu\text{s}^{-1}$, so that there are at most a few photons in the cloud at a time propagating as polaritons with a velocity $v_g \approx 5\times10^3$ m/s. Here we make the approximation that the atomic medium with a Gaussian density profile has an homogeneous profile with a length $L = 4.2\times\sigma_z$ [55].

The van der Waals coefficient for the Rydberg state $82S_{1/2}$ is $C_6/(2\pi) = -5.4\times 10^3$ GHz μm^2, which results in a blockade radius r_b ranging from 7 μm to 10 μm (depending on δ and δ_s). Since the blockade radius is much larger than the probe waist, the system can be effectively reduced to a single dimension corresponding to the probe propagation axis.

We continuously interrogate the atoms for 100 ms (≈0.13 duty cycle), during this time we lose less than 10% of the atoms from the initial density. We choose this time to maintain the atomic density as high as possible and measure the effect of the interactions at their peak strength, which is parametrized by the optical depth per blockade radius $\mathrm{OD}_b = r_b \mathrm{OD}/(\sqrt{2\pi}\sigma_z)$. This continuous interrogation allows for higher data collection per experimental cycle (compared to free fall or modulating the dipole light during the two-photon excitation). However, we measure linewidths broadening of $\Gamma/(2\pi) = 7 \pm 1$ MHz and $\gamma_s/(2\pi) = 0.4 \pm 0.1$ MHz, for the intermediate and Rydberg state, respectively, due to the presence of the dipole beams.

8.3 Photon correlation functions

The n-photon correlation function can be used to extract information about the impact of n-polariton interactions. Initially, the incoming photons are uncorrelated, when they enter to the medium and propagate as polaritons, the dynamics of the interactions between the polaritons can be mapped to the n-photonic wavefunction, which are manifested as correlations. After exiting the medium, the outgoing wavefunction maintains its acquired correlations which can be probed by measuring the n-th order correlation function. In particular for two- and three-photons:

$$g^{(2)}(\tau) = \frac{|\mathcal{E}\mathcal{E}(L, c\tau)|^2}{|\mathcal{E}(L)|^4}, \tag{8.2}$$

$$g^{(3)}(\tau_1, \tau_2) = \frac{|\mathcal{E}\mathcal{E}\mathcal{E}(L, c\tau_1, c\tau_2)|^2}{|\mathcal{E}(L)|^6}. \tag{8.3}$$

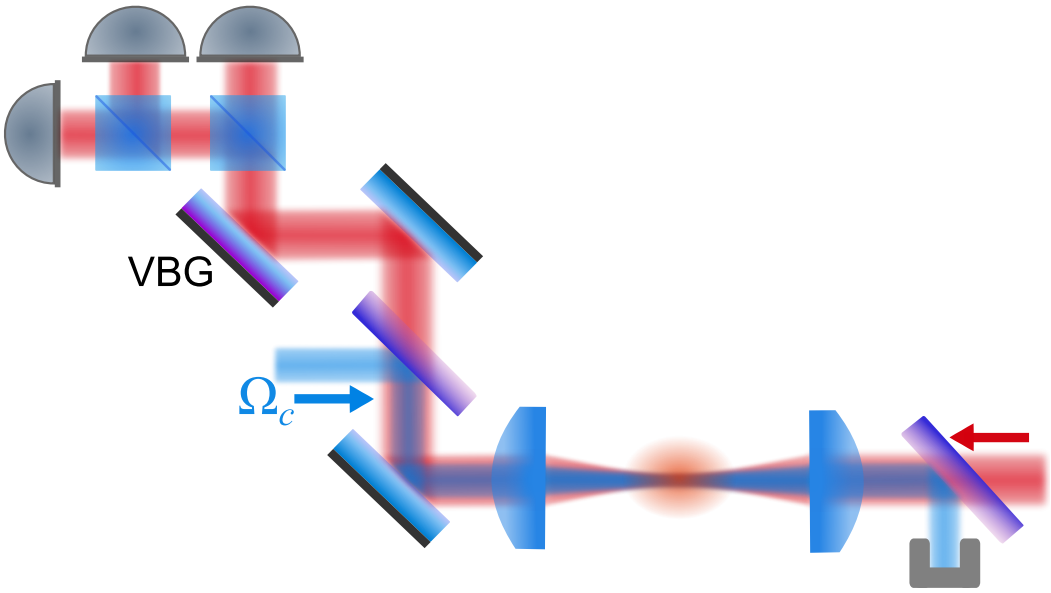

Figure 8.2: **Setup for photon-correlation measurements.** The probe beam and the control beam are overlapped along the propagation axis and counter-propagating from each other. The interactions among photons are probed via the correlation functions of the probe light that exits the medium. It is split equally onto three paths and coupled into three multi-mode fibers (not shown) and send into avalanche photodetectors. The volume Bragg grating (VBG Optigrate) filters the transmitted probe light from unwanted scattered laser light.

where $\mathcal{E}(z_1)$, $\mathcal{EE}(z_1, z_2)$, and $\mathcal{EEE}(z_1, z_2, z_3)$ are the single-, two- and three-photon wavefunction, and $c\tau_i = z_i - z_j$ is the relative time between the photons i and j. After exiting the medium for $z \geq L$, $\mathcal{E}(z) = \mathcal{E}(L)$. The two-photon wavefunction can be composed of scattering and bound states (dimers). The three-photon wavefuntion may have contributions from scattering states of three photons, all the permutations of one dimer and a free photon, or a three-body bound state. Since $g^{(3)}(\tau_1, \tau_2)$ includes two-body interactions, it cannot be considered as a measure of pure three-body interactions. To illustrate the presence of two-body effects in $g^{(3)}(\tau_1, \tau_2)$, see Fig. 8.3. Note that for long relative times when one particle separates from the other two, or for $\tau_1 = \tau_2$ when two photons are on top of each other, $g^{(3)}$ approaches $g^{(2)}(0)$. Hence, to characterize the impact of three-body loss relative to two-body effects at low photon rates, we use the connected

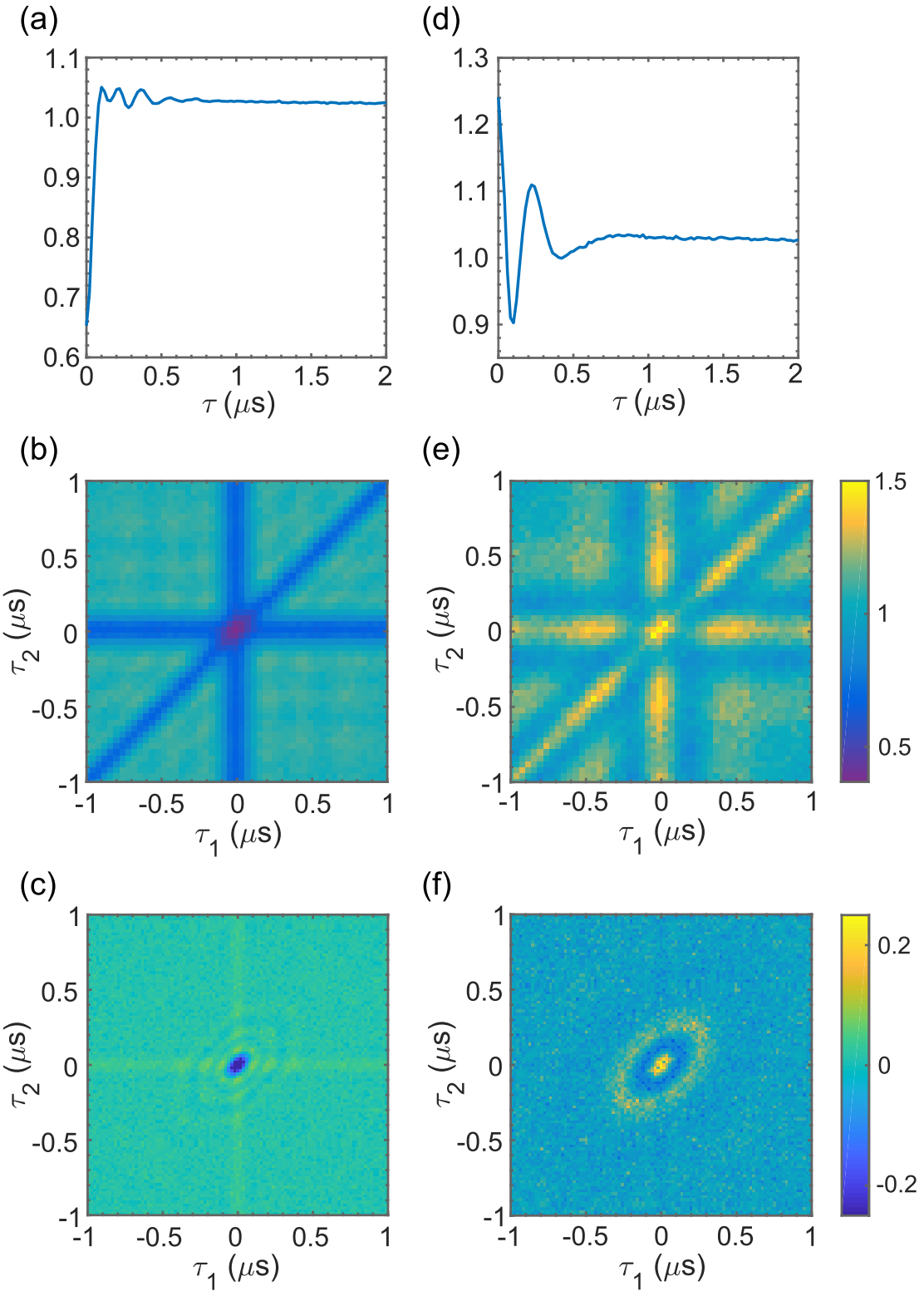

Figure 8.3: **Measured correlation functions with $\eta_3(0,0) < 0$ and $\eta_3(0,0) > 0$.** (a) $g^{(2)}(\tau)$ (b) $g^{(3)}(\tau_1, \tau_2)$ and (c) $\eta_3(\tau_1, \tau_2)$ for $\delta/(2\pi) = 15$ MHz and $\delta_s/(2\pi) = -2$ MHz, where we observe $\eta_3(\tau_1, \tau_2) < 0$. (d) $g^{(2)}(\tau)$ (e) $g^{(3)}(\tau_1, \tau_2)$ and (f) $\eta_3(\tau_1, \tau_2)$ for $\delta/(2\pi) = 22.5$ MHz and $\delta_s/(2\pi) = 2$ MHz, with $\eta_3(\tau_1, \tau_2) > 0$.

correlation [57, 195], defined as,

$$\eta_3(\tau_1, \tau_2) = g^{(2)}(\tau_1) + g^{(2)}(\tau_2) + g^{(2)}(\tau_2 - \tau_1) - g^{(3)}(\tau_1, \tau_2) - 2. \tag{8.4}$$

For example, in the case of dominant two-body loss, there is a high probability of absorbing at least one out of two or three incoming photons, so that $g^{(2)}(0) \to 0$ and $g^{(3)}(0,0) \to 0$, resulting in $\eta_3(0,0) < 0$ (strong two-body repulsion [206] has a similar effect). On the other hand, if two-body loss and dispersive two-body interactions are both weak ($g^{(2)}(0) \sim 1$), while three-body loss is strong ($g^{(3)}(0,0) \to 0$), results in $\eta_3(0,0) > 0$.

We obtain $g^{(2)}(\tau)$ and $g^{(3)}(\tau_1, \tau_2)$ by measuring the relative temporal delay of transmitted photons detected in three single-photon counting detectors arranged in a generalized Hanbury Brown and Twiss setup, as depicted in Fig. 8.2. The detection events are recorded as time-stamps by our time-tagger device and post-processed to construct the second- and third- order correlation functions. The measurements in Fig. 8.3 and Fig. 8.4 are averaged over 1500 experimental cycles and binned in 20-ns time bins.

Figure 8.3 shows the measured second- and third-order correlation and their respective connected correlation function for the case when $\eta_3(0,0) < 0$, and $\eta_3(0,0) > 0$. Note that for the connected correlation in Fig. 8.3(c) and (f), there is almost no structure along the diagonal $\tau_1 = \tau_2$, and for $\tau_i = 0$. As we would intuitively expect for $g^{(2)}(0) \to 0$ and $g^{(3)}(0,0) \to 0$ results in $\eta_3(0,0) < 0$. For weak attractive two-body interactions with $g^{(2)}(0) > 1$, and dominant three-body loss results in $\eta_3(0,0) > 0$. Here, three-body loss is not strong enough to make $g^{(3)}(0,0) \to 0$.

8.4 Experimental results and comparison with theory

Figure 8.4(a-b) shows the measured correlation functions at zero time delay, $g^{(2)}(0)$ and $g^{(3)}(0,0)$, as a function of δ and δ_s, at fixed Ω_c and OD. Both $g^{(2)}(0)$ and $g^{(3)}(0,0)$ display an antibunching to bunching trend as δ increases and δ_s becomes positive. Figure 8.4(c) shows the measured connected correlation $\eta_3(0,0)$. The region where $\eta_3(0,0) > 0$ (indicative of dominant three-body loss) occurs in a roughly linear band in δ-δ_s space with a negative slope.

Figure 8.4(d-f) shows the correlation functions at zero-time delay obtained by numerically solving the Schrodinger equation for the two- and three-polariton wavefunctions propagating through the Rydberg-EIT medium. The details and code for this numerical simulation are in Michael Gullans thesis in Ref. [207]. Here, the van der Waals potential is approximated as a hard-sphere potential for the two-and tree-body interaction as:

$$\begin{aligned} V_{\text{2-body}}(z) &= V_0\theta(r_b - |z_1 - z_2|), \\ V_{\text{3-body}}(z) &= V_0 \sum_{i\neq j} \theta(r_b - |z_i - z_j|), \end{aligned} \tag{8.5}$$

where $\theta(z)$ is the Heaviside step function and V_0 is the effective interaction strength defined by the van der Waals coefficient C_6 and $\bar{\chi}(0)$ (see Eq. (8.7) for the definition of this function).

Using parameters that are within the experimental uncertainties, we reproduce the antibunching to bunching behavior in $g^{(2)}(0)$ and $g^{(3)}(0,0)$, as well as the resonant-like feature in $\eta_3(0,0)$ observed in the experimental data, which we attribute to three-body loss. We also note that limitations from our numeri-

cal description (possibly contributing to the discrepancy in amplitudes between experimental and numerical results) might arise from using the hard-sphere approximation for the interaction potential $V(z)$ to reduce the computation time.

Another source of discrepancy could arise from the presence of contaminant states which affect the behavior of the correlation functions, in the regime of continuous photon flux [171]. However, including a microscopic description of the contaminants greatly increases the complexity of the model [170]. Since there is a good qualitative agreement on the resonant feature in Fig. 8.4(c) and (f), we considered that adding a more complex model would not contribute to understanding the cause of the dominant three-body loss.

8.5 Fermi's Golden Rule

We first discuss the form of two-body interactions, then describe the three-body scattering process within a Fermi's Golden Rule approximation to understand the source of the resonant-like enhancement of $\eta_3(0,0)$. Finally, we compare the results with the experimental and numerical observations of the resonant three-body loss feature (See Fig. 8.4(f)).

The bare atoms in Rydberg states interact via van der Waals potential $V(r) = C_6/r^6$. This potential between individual atoms is renormalized into an effective potential between the DSPs [98]

$$V_e(\omega, r) = \frac{V(r)}{1 - \bar{\chi}(\omega)V(r)}. \tag{8.6}$$

Here, $\bar{\chi}$ characterizes the saturation of the effective potential at distances less than

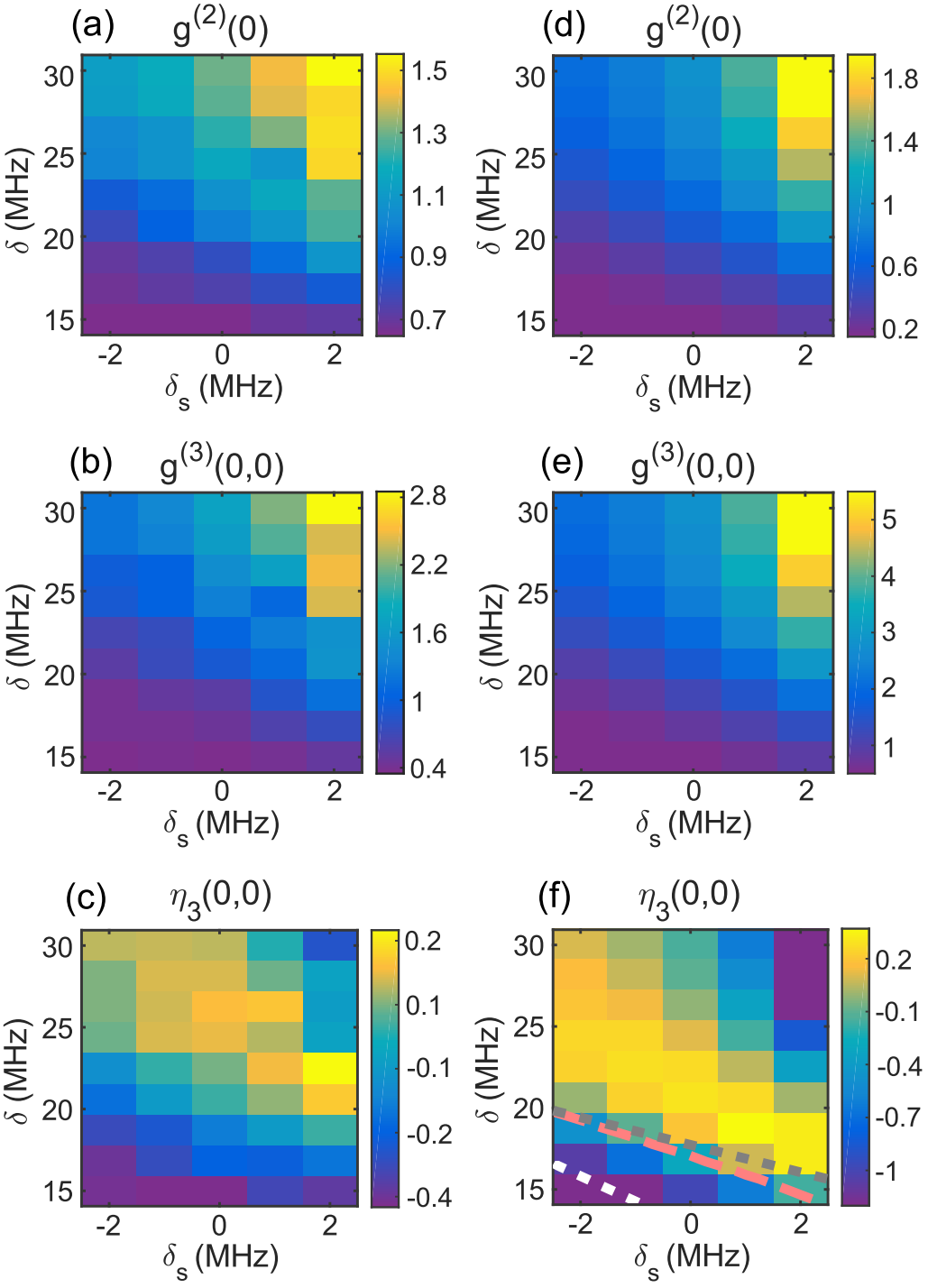

Figure 8.4: **Measurements and theoretical predictions.** (a)-(c) Experimental data of the second-order, $g^{(2)}(0)$, third-order, $g^{(3)}(0,0)$, and connected third order, $\eta_3(0,0)$, correlation functions with $\Omega_c/(2\pi) = 23.5 \pm 1.5$ MHz, for a cloud with OD=37±4 and $\sigma_z = 42 \pm 4$ μm. (d)-(f) Numerical simulations for the same correlation functions. Parameters used for the simulations are: OD = 37, $\Omega_c/(2\pi) = 25$ MHz, $\gamma_s/(2\pi) = 0.3$ MHz and $\sigma_z = 40\mu$m. Regions with $\eta_3(0,0) > 0$ indicate excess of three-body loss with respect to two-body loss. The dashed lines indicate the enhanced three-body loss predicted by the Fermi's Golden Rule calculation (see section 8.5).

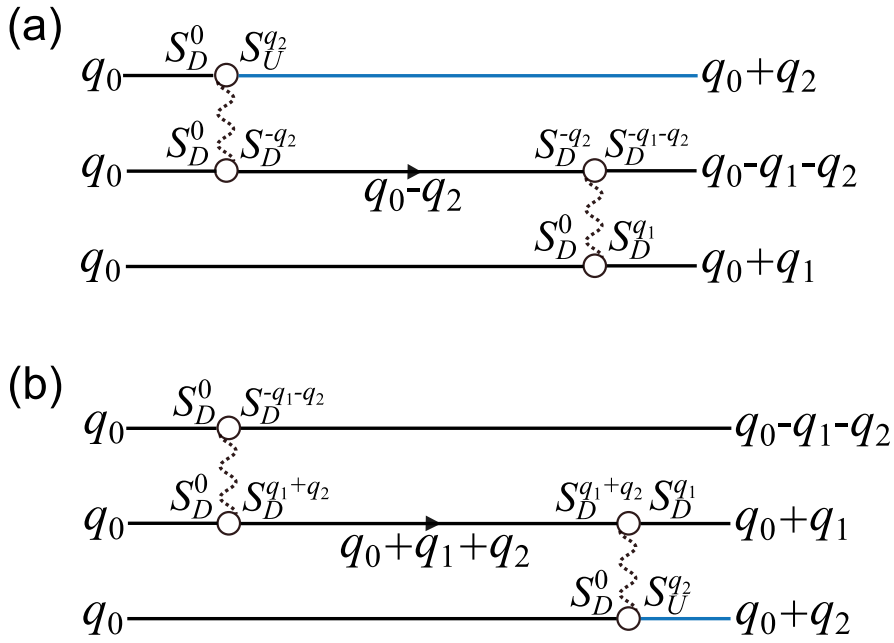

Figure 8.5: **Lowest order diagrams that contribute to three-body loss.** In these diagrams, the straight lines are the input/output states (black is for the DSP and blue is for the upper-bright polariton), the vertex (circle) is the overlap between the $\nu-$branch polariton and the bare Rydberg state at momentum q is given by S_ν^q. The wavy dotted line represents the effective interaction $\tilde{V}_q[\omega]$, which is symmetric in q. The arrowed line is the single body propagator defined in Eq. (8.9). In addition to this diagram, there are five similar diagrams (total of six) for both (a-b) obtained by permuting the input and output states.

the blockade radius $r_b = (|C_6\bar{\chi}|)^{1/6}$ [98] and is given by

$$\bar{\chi}(\nu) = \frac{4\Delta^2 + 6\Delta\nu + 2\nu^2 - \Omega_c^2}{2(\Delta+\nu)\left(\nu(2\Delta+\nu) - \Omega_c^2\right)}, \tag{8.7}$$

with $\nu = \omega + 2\Delta_s$.

Using V_{eff}, we can use a Fermi's Golden Ruleargument to obtain the three-body scattering rate β, for incoming dark Rydberg polaritons near the EIT resonance due to processes like the one indicated in Fig. 8.1(b).

The lowest-order diagrams contributing to the scattering rate β are second-order in V_{eff}. As stated earlier, the conservation of energy and momentum restricts the available scattering channels. In Fig. 8.5(a-b), we show the leading contribu-

tions to β, which involve scattering from DDD to DDU, with D gaining large q and becoming lossy. Other allowed processes, such as scattering to DUU, are not relevant due to their small overlap amplitude with the Rydberg state, resulting in weaker effective interactions involving these bright polaritons.

The incoming polaritons have $\omega_D(q_0) = 0$. In general, $q_0 \neq 0$ for $\delta_s \neq 0$, but, for brevity of presentation, we show the expressions for $\delta_s = 0$ and $q_0 = 0$. Using Fermi's Golden Rule based on the diagrams in Fig. 8.5(a-b), β is given by

$$\begin{aligned}\beta = \frac{18}{\pi} \int \mathrm{d}q_1 \mathrm{d}q_2 |S_D^0|^6 |S_D^{q_1}|^2 |S_D^{-q_1-q_2}|^2 |S_U^{q_2}|^2 \\ \times \Big| \tilde{V}_{q_2}[0] G_{ss}[-q_2, -\omega_U(q_2)] \tilde{V}_{q_1}[-\omega_U(q_2)] \\ + \tilde{V}_{q_1+q_2}[0] G_{ss}[q_1+q_2, -\omega_D(-q_1-q_2)] \tilde{V}_{q_2}[-\omega_D(-q_1-q_2)] \Big|^2 \\ \times \delta\left(\omega_U(q_2) + \omega_D(q_1) + \omega_D(-q_1-q_2)\right). \end{aligned} \tag{8.8}$$

Here, $\tilde{V}_q[\omega]$ is the Fourier transform of $V_{\text{eff}}(\omega, r)$, $\omega_\nu(q)$ is the dispersion of the ν-branch, S_ν^q is the overlap amplitude of the Rydberg state with a polariton at momentum q on branch $\nu \in \{D, L, U\}$, and $G_{ss}[q, \omega]$ is the single-body propagator

$$G_{ss}[q, \omega] = \frac{(\omega - cq)(\Delta + \Delta_s + \omega) - g^2}{(\Delta_s + \omega)((\omega - cq)(\Delta + \Delta_s + \omega) - g^2) + \frac{\Omega_c^2}{4}(cq - \omega)}, \tag{8.9}$$

which includes the projection of the Rydberg state onto the dark-state polariton with momentum q, $G_{ss}[q, \omega] \equiv G(q, \omega)|S_D^q|^2$.

The behavior of Eq. (8.8) depends on the interaction strength, which can be quantified by $\varphi = |r_b/\sqrt{\bar{\chi}/m}|$, where $m \approx -2g^4/\Delta\Omega^2c^2$ is the effective mass. In our experiment, $\mathrm{OD}_b < 4$, and for the detunings considered here, $\varphi < 0.32$.

In the moderately interacting regime of $\varphi < 1$, which applies to our experi-

mental parameters, we can simplify the evaluation of Eq. (8.8) by noting that the dispersions for ω_D and ω_U, become approximately flat and saturate to ω_+ in the relevant range of the momentum transfer $\sim 1/r_b$, which is about 3.5× to 5× larger than the characteristic threshold momentum k_c (see Fig. 8.1(b-c)). Here, ω_+ is defined as,

$$\omega_+ = \frac{1}{2}\left(-\Delta + \Delta_s + \sqrt{(\Delta + \Delta_s)^2 + \Omega_c^2}\right). \tag{8.10}$$

Taking into account these considerations, the second term in Eq. (8.8) vanishes because $\tilde{V}_{q_2}[-\omega_D(-q_1 - q_2)] \approx \tilde{V}_{q_2}[2\omega_+] \to 0$, so β can be simplified[3] to

$$\beta \approx \frac{18}{\pi}\int \frac{\mathrm{d}q}{v_g(-2\omega_+)}\left|\tilde{V}_q[0]G_{ss}[q_2 \to \infty, -\omega_+]\tilde{V}_q[-\omega_+]\right|^2, \tag{8.11}$$

which has a complicated dependence on the microscopic parameters. We concentrate on qualitative features of Eq. (8.11) to understand the behavior of β. In the regime where $\Omega_c \ll |\delta|$, the scattering rate is

$$\beta \approx \frac{A\pi^4\Omega^2}{9\delta}\varphi r_b^2 \tag{8.12}$$

where $A \approx 1$ is a numerical constant. Here, β increases with increasing interactions, but does not feature any resonances as a function of δ.

In contrast, for $\Omega_c \sim \delta$, the scattering rate given by Eq. (8.11) could have resonant behavior for two reasons. First, the density of outgoing states, given by[4], diverges. Second, the interaction vertices $\tilde{V}_q[0]$ or $\tilde{V}_q[-\omega_+]$, which are inversely proportional to $\bar{\chi}(0)$ and $\bar{\chi}(-\omega_+)$, can have a resonance due to the vanishing

[3]In the relevant regime $|S_\nu^q| \sim 1$ and do not change the position of the resonances.

[4]For the full expression of v_g see Eq. (3.52) $1/v_g(-2\omega_+)$, note that in this chapter $g \to g/2$ compared to the definition of g in Chapter 3

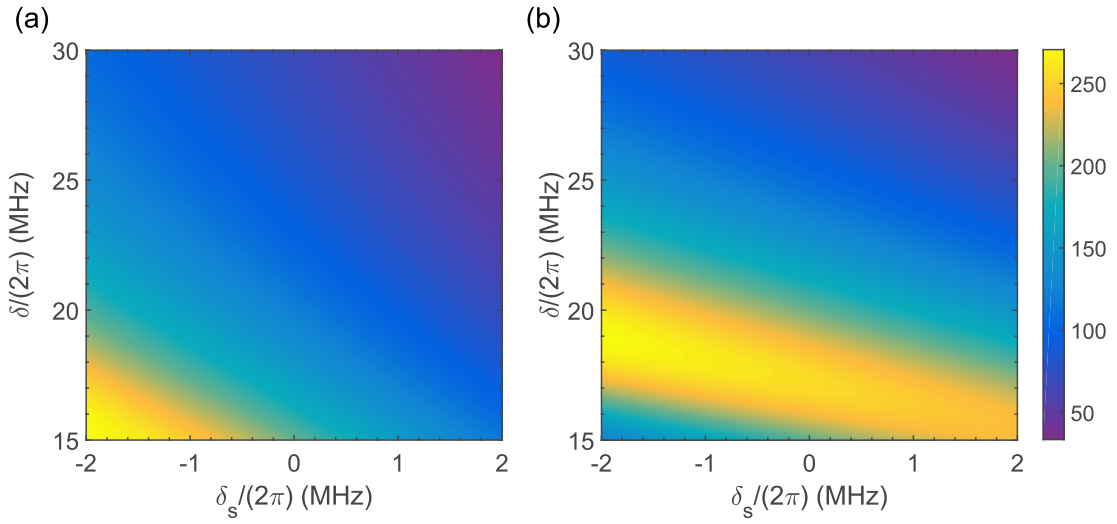

Figure 8.6: **Divergences of the integrand in Eq. (8.11) to calculate β as a function of δ and δ_s.** (a) Divergence for DSPs with energy $\omega = 0$, corresponding to the white dashed line in Fig. 8.4(f). (b) Divergence for scattered DSPs to branches with energy $\omega = \omega_+$, corresponding to the grey dotted line in Fig. 8.4(f). The resonances are smoothed due to the finite Γ and γ_s, which results in a single effective resonance in β, indicated by the pink dashed line in Fig. 8.4(f).

value of $\bar{\chi}$ at these energies. This divergence in the interaction vertices will be smoothed out in our regime of finite Γ, γ_s, but will still have a significant impact on β. We find that the divergence in the density of states is nearly canceled by the simultaneous vanishing of $\tilde{V}_q[-\omega_+]$, resulting in the density of states divergence not contributing to the resonant behavior.

The interaction vertices $\tilde{V}_q[0]$ and $\tilde{V}_q[-\omega_+]$ diverge for δ approaching specific detunings δ_- and δ_+ where $\bar{\chi}(0)$ and $\bar{\chi}(-\omega_+)$ vanish. These divergences are shown in Fig 8.6 as a function of δ and δ_s. In the experimentally relevant limit of $\delta_s \ll \Omega_c, \Delta$, the expressions for $\delta_\pm$ simplify to

$$\delta_- = \frac{1}{2}\Omega_c - \frac{3}{2}\delta_s, \qquad \delta_+ \approx 0.7\Omega_c - 0.8\delta_s. \tag{8.13}$$

Here δ_- corresponds to $\omega = 0$, and δ_+ indicates the divergence for $\omega = \omega_+$. These dependencies are shown in Fig. 8.4(f): the gray dotted line depicts δ_+, whereas the

white dotted line depicts δ_-. In our system, the decay Γ leads to such significant broadening of the two resonances that two peaks are no longer distinguishable, leading to a single, effective resonant feature for β. In Fig. 8.4(f), the pink dashed curve depicts the value of δ for which $|\beta|$ given by Eq. (8.11) is maximal for a fixed δ_s. The maximal curve is closer to the δ_+ line because, for our parameters, this resonance is stronger than the δ_- resonance. The resulting overall resonance is a three-body effect because it predominantly comes from the δ_+ resonance, which is not present for the two-body scattering. Our full Schrödinger equation numerics indicate that the resonance slope position in $\delta - \delta_s$ space also shows a dependence on the control Rabi frequency (rather than other parameters) in agreement with our Fermi's Golden Rule results.

The interaction strength could become significant and negative in the vicinity of the divergent $\bar{\chi}$, leading to the emergence of a second bound state, which would happen for $\varphi \approx 3$ [98]. This non-perturbative effect could hinder the applicability of the Fermi's Golden Rule. However, since in our system $\varphi < 0.3$, we can neglect the second bound state.

8.6 Discussion and Outlook

Summarizing, we demonstrate the ability to tune Rydberg-polariton interactions leading to dominant three-body losses over two-body losses. These interactions are experimentally probed using the few-photon auto-correlation functions of the outgoing light field. Our numerical simulations reproduce the experimentally observed features with good qualitative agreement. Likewise, the scattering process of three DSPs to two lossy DSPs (accompanied with a large momentum

transfer) and a bright-state polariton, described by Fermi's Golden Rule, is consistent with our observations. It should be possible to observe a sharper and stronger three-body loss resonance by detuning farther from single-photon resonance with a larger δ which would decrease the contribution from the intermediate state dissipation. However, since $\Omega_c \sim \delta$, the optical power needed to achieve strong enough Rabi frequencies becomes experimentally challenging.

Having a local oscillator interfering with the output light from the cloud would provide phase information, which we could use to reconstruct the few-photon wave function (besides the correlations which are based on the intensity, see Chapter 4) and could help to understand better the nature of the interactions [55, 56, 206].

Our work is a demonstration of yet another degree of tunability offered by Rydberg systems, showing promising directions in the study and control of few and many-body physics of strongly-interacting photons. For example, by increasing the strength of the interactions and the optical density, we could have the ability to tune the scattering length and observe another bound-state associated with a photon-photon scattering resonance [98], or making photonic clusters via Lennard-Jones potentials [208]. Extending the system to three dimensions and altering the polariton effective mass and interactions, along the transverse and axial directions could result in the formation of photonic Efimov trimers [97].

Chapter 9: Conclusions and Outlook

This thesis presented a series of experiments where we generate effective interactions among photons by means of strongly-interacting Rydberg states in cold atomic ensembles. We used this interacting photon system to generate highly pure and indistinguishable single photons, and demonstrated two photon quantum interference between our single photons and photons produced from a single ion. We also report the observation of tunable three-body interactions in the dissipative regime. These results reinforce the fact that Rydberg systems are attractive platforms towards quantum information applications, as well as the study of few and many-body phenomena.

Many of these research directions use additional states beyond the Rydberg state. The current experimental efforts are focused on addressing another ground-state in the $F = 1$ hyperfine manifold. Adding a new ground state to the system would allow shelving Rydberg collective excitations in different states. This scheme can be used for example, to generate arbitrary superposition of photon Fock-states [84, 209].

We are exploring the generation of dual-rail single-photon qubits that can be entangled with the quantum state of the atomic ensemble y addressing two hyperfine ground states and two different Rydberg states [92]. After successful creation of photon-spinwave entanglement, we can use these atom-photon qubits to gener-

ate hybrid entanglement with ion-photon qubits by means of two-photon quantum interference [179], and realize a simple hybrid ion-atomic ensemble quantum network. We could also achieve entanglement by storing the ion qubit in different ground states of the atomic ensemble. We expect that with experimental upgrades in the ion-collection optics and frequency conversion, high-fidelity entanglement should be achievable with a few entanglement events per minute [59].

One of the main limitations of our system is the Rydberg spin-wave finite coherence time. Increasing the coherence time would increase the success and fidelity of arbitrary Fock-states and atom-photon entangled qubits. There are multiple contributions to the spin-wave decoherence, including, but not limited to: Doppler broadening, collisional dephasing, and differential light shifts arising from the optical dipole trap. We are in the process of assessing mitigating these mechanisms. An option to lower the temperature of the atoms is adding another cooling stage like Raman-sideband cooling [210]. Using an optical barrier or "box" potential, where differential light shifts vanish since the atoms are trapped in the dark, we estimate that the Rydberg spin-wave coherence time would increase by at least a factor of two. Another possible configuration to decrease differential Stark shifts is to use a combination of a lattice and a box potential. On the one hand, the optical lattice provides long coherence times between ground and Rydberg spin wave [139], as well as spin waves between two different ground states [211], where we can store a Rydberg excitation in the second shelving ground state. On the other hand, a box potential can be used to modify the shape and size of the lattice.

It could also be interesting to use an optical diffractive element to shape the

anti-trapping light into arbitrary potentials would offer the flexibility to create two or more adjacent ensembles. We could use different atomic ensembles as independent atomic qubits [39], explore the angular dependence of interactions between higher angular momentum Rydberg states, or study correlations in a subsequent array of superatoms [57].

So far, most of the study of Rydberg interactions in atomic ensembles have been done along a single spatial dimension. Using diffractive elements in the probe beam can add another degree of freedom to engineer the transversal and longitudinal propagation mode. This extra knob could be used to study in a controlled way, the regime of Rydberg interactions in two- and three dimensions, where we could see the formation of photonic Efimov states [97]. It could also be used to shape collective spin waves and potentially increase their retrieval as photons [93].

Creating collective Rydberg spin waves with P-excitations also open other research directions, from the study of strongly correlated states of light [208, 212], to the implementation of conditional phase gates [158, 213].

The field of Rydberg physics is an exciting field of research, which is rapidly evolving with a growing number of proposals and demonstrations, for both the development of quantum technologies and the study of fundamental physics.

Appendix A: Probe alignment

This Appendix describes how to align the probe laser to the in-vacuum lenses. This step is crucial for the experiments since proper alignment minimizes aberrations. Aberrations along the probe propagation inside the atomic cloud could hinder the blockade fidelity. Moreover, the probe focus constraints all the other beam paths for trapping and exciting the atoms.

A.1 Alignment procedure

The in-vacuum optics are AR coated for 780-nm light, so we use back reflections from the in-vacuum lenses of a HeNe laser with 632-nm wavelength to do a coarse alignment. Overlapping the back reflections with the incoming beam would guarantee that the laser light propagates along the optical axis. Figure A.1 shows Zemax simulations of the expected back reflections from each surface for a beam with ≈ 0.5 mm waist. Additionally, there is another back reflection from the window that does not diverge, and it is straightforward to distinguish it from the others. Since the normal of the window is at a different angle from the lenses optical axis, we do not overlap this back reflection with the others coming from the lenses.

Because the lenses are concentric to each other, it is sufficient to overlap two of the back reflections at two different spatial points (the further these points are

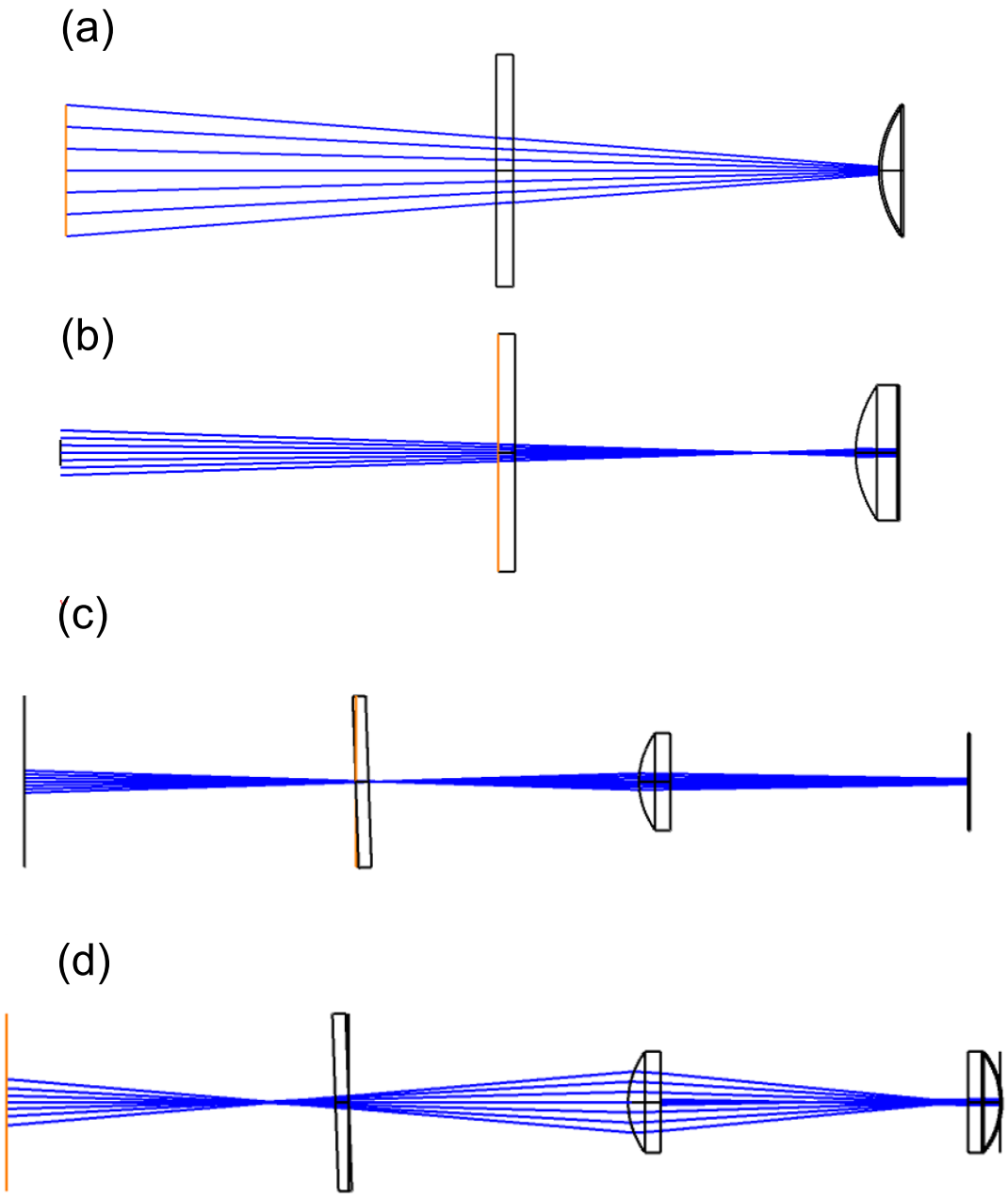

Figure A.1: **Back reflections from each surface of the in-vacuum lenses 2 cm away from the first window.** (a) Back reflection from the curved surface of the first lens. (b) Back reflection from the flat surface of the first lens. (c) Back reflection from the flat surface of the second lens. (d) Back reflection from the curved surface of the second lens.

from each other, the better). Close to the first chamber window along the probe path ($\approx$ 2 cm) is easy to identify each one of them (see Fig. A.1). However, at larger distances some of the back reflections diverge more and are harder to view. The back reflections from the flat surfaces of the first Fig. A.1(b) and second

Fig. A.1(c) lens show the least divergence for alignment far from the window.

Once the back reflections are overlapped with each other and the incoming beam, we overlap the probe light to the HeNe. To do the fine alignment of the probe beam, we image the focused probe into a CCD camera, using the second in-vacuum lens as an imaging lens, and a 400-mm focal length lens outside the vacuum chamber as a focusing lens. We walk the picomotor mirrors (see Fig. 5.12(b) for the probe optical layout) in both vertical and horizontal directions until we see that the probe transverse profile shows azimuthal symmetry on focus and off focus. We check this symmetry by translating the image plane at the CCD with the second focusing lens. Some examples of the imaged pron on the CCD are illustrated in Figure A.2.

Fig. A.2(a) shows the probe off focus with astigmatism, this aberration was produced from the reflection of a dichroic mirror (this mirror was subsequently replaced by a short-pass dichroic that transmits 780-nm light). Figure A.2(b) shows the probe off focus with some aspherical aberrations but approximately symmetric azimuthally. Finally, Fig. A.2(c) shows the probe on-focus at the CCD camera image plane. Identifying aberrations and symmetries in imaging systems has been used before to align optical systems for cold atoms experiments [214].

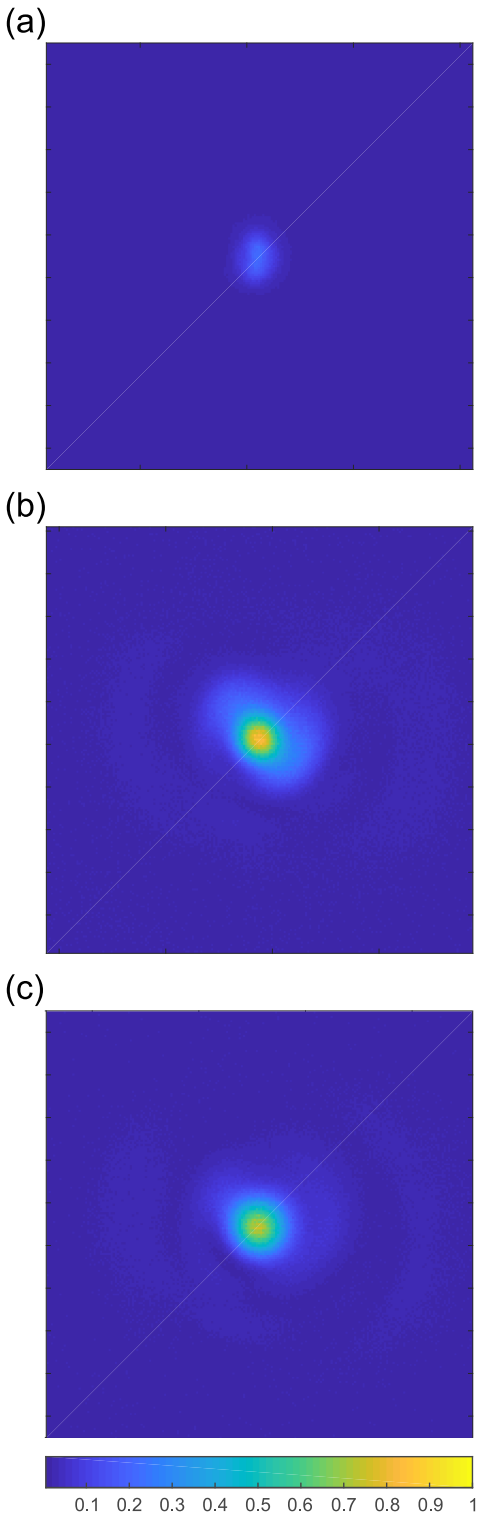

Figure A.2: **Imaging of probe focus.** (a) Probe with astigmatism. (b) Off-focus probe at image plane. (c) On-focus probe at image plane. Images are normalized to the maximum intensity of the probe on the focused image plane.

Appendix B: Background subtraction and Gating

Subtracting background noise from the detection system or light sources independent from the single-photon source to study, allows us to have a more accurate estimate of its efficiency, $g^{(2)}(0)$, and indistinguishability. For example, the additional background counts would lead to an overestimation of the source efficiency, especially if the signal to noise ratio $S/N \sim 1$. Since the joint detector coincidence probability quantifies $g^{(2)}$ and the HOM-visibility, accidental coincidences from photon-background and background-background coincidences would lead to a higher value for $g^{(2)}(0)$ and a decreased visibility. Background subtraction requires a careful characterization of the background-count rate for each detector.

It is also convenient to define a "gate window" around the photon pulse for on-demand sources. Gating can improve the signal to noise ratio, remove unwanted coincidences, and lessen the effects of fluctuations. This can be done in "hardware" by electronically gating the detectors, or equivalently, in "software" during the post-processing of the data. The software gate is done by setting the registered single counts from each detector outside the gating window to zero. One advantage, of software gating, is that it provides all the detected counts for a full generation cycle as opposed to the hardware gate, if the pulse duration is shorter than the cycle-generation period, we can extract the background count-rate for each detector, and then subtract the background contribution to the efficiency,

$g^{(2)}(0)$ and HOM-visibility measurements.

This appendix outlines the procedure to define a gate window containing most of the photon pulse, identifying the background noise, and then subtracting off the accidental coincidences within that gate. Finally, we analyze that the temporal profile of background coincidences is not constant when applying a gate, as it arises from the convolution of the gated photon pulse shape and a square pulse which height corresponds to the noise level.

B.1 Temporal profile of background coincidences in a gate window

We use two SPADs for all our single-photon measurements, with average background rates of ≈ 80 s^{-1} and ≈ 100 s^{-1}. This count rate is due to detector dark counts (≈ 60 s^{-1}) and leakage of ambient light.

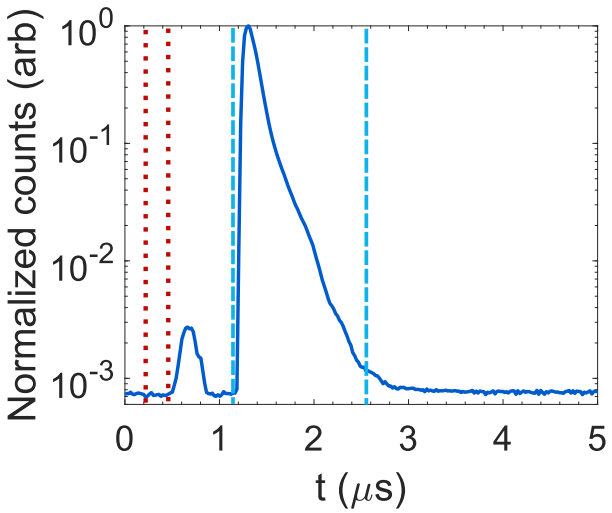

Figure B.1: **Dark-blue solid line shows the counts recorded by SPAD 1 for a full cycle of 5 μs.** The red-dotted lines show the window where we extract the mean background probability per unit time $B_1(B_2)$ when the shutter AOM is off. The light-blue dashed lines indicate the gating window to obtain the photon signal probability per unit time $P_1(t_1)$, $P_1(t_2)$ for SPAD 1, SPAD 2. The smaller peak at the left of the photon signal are leakage counts from the write pulse.

Figure B.1 shows the detected SPAD counts as a function of time during a

pulse period t_p=5 μs, plotted on a logarithmic scale. A small amount of leakage of the write pulse through the AOM shutter is evident in addition to the photon pulse. Since the photons arrive at the detectors at a known time, we apply a software gate corresponding to a 1.4 μs time window (indicated by the blue-dashed lines), which contains more than 99.9% of the pulse. The gate is implemented during the post-processing of the data and is equivalent to hardware gating the detectors. We determine the mean detector background singles count rate by measuring the counts during a time window (indicated by the red dashed lines) in which the shutter AOM is off. The background count rate when the AOM is on, increases by $\simeq$ 4% (not easily visible in Fig. B.1), indicating a small amount of additional background produced by the apparatus. We do not include this additional background in the subtraction described below.

First, we determine the background-photon and background-background coincidences profile within the gate window, from the measured background noise level for each detector and the single-photon profile. Then, we proceed to subtract this calculated background profile from the total measured coincidence count rate.

The probability of a background coincidence, c_{back}, is the sum of the products of single event rates:

$$c_{\text{back}}(t_1, t_2) = P_1(t_1)B_2(t_2) + B_1(t_1)P_2(t_2) + B_1(t_1)B_2(t_2), \tag{B.1}$$

where t_1 and t_2 are absolute times relative to a clock, for SPAD 1 and 2 respectively. $P_i(t_i)$, is the probability per unit time of a photon detection event at detector i, and $B_i(t_i)$ is the probability per unit time of a background count. Changing the

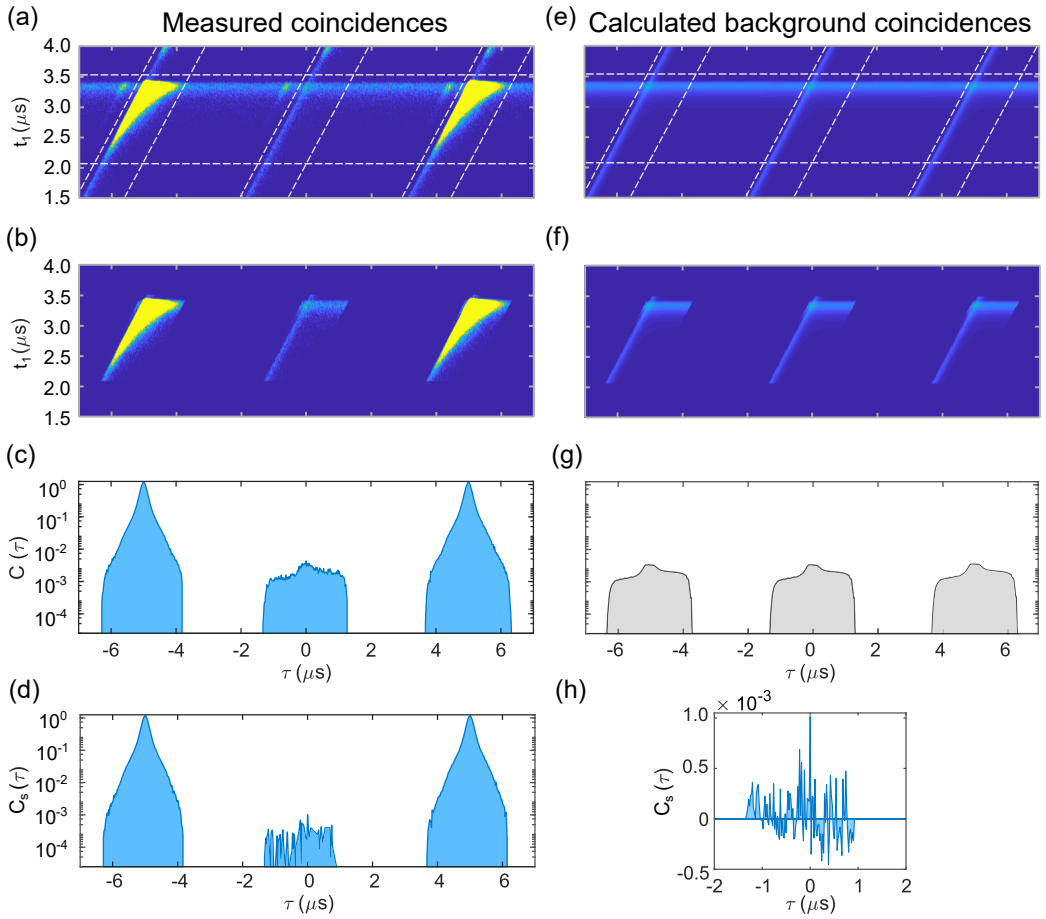

Figure B.2: **Reconstruction of coincidences given the background and photon rate measured at each detector.** (a) Raw data coincidences as a function of absolute time t_1, for SPAD 1 and τ, the relative time between both SPADs. White dashed lines indicate the position of the gating window for each repetition cycle. (b) Data with gate applied. (c) Total coincidence rate after applying the gate as a function of τ. (d) Photon-photon coincidence rate after subtracting the background from the data. (e) Calculated background coincidence $c_{\text{back}}(t_1, \tau)$, based on the measured single-event rates $P_i(t)$ and B_i. (f) Calculated background coincidences after the gate. (g) Gated-background coincidence rate $C_{\text{back}}(\tau)$. (h) Zoom around $\tau = 0$ of background-subtracted data in linear scale. The software to process the correlation data from the time-tagger is in A. Craddock repository `https://github.com/acraddoc91/RbRy_Correlations`.

relative time coordinate, $\tau = t_1 - t_2$, the background coincidence probability is

$$c_{\text{back}}(t_1, \tau) = P_1(t_1)B_2(\tau + t_1) + B_1(t_1)P_2(\tau + t_1) + B_1(t_1)B_2(\tau + t_1). \tag{B.2}$$

We integrate t_1 over a time window $t_{\text{end}} - t_{\text{start}}$ to obtain the total background

coincidence rate as a function of the relative time, τ:

$$C_{\text{back}}(\tau) = \int_{t_{\text{start}}}^{t_{\text{end}}} dt_1 \big[P_1(t_1)B_2(\tau + t_1) + B_1(t_1)P_2(\tau + t_1) + B_1(t_1)B_2(\tau + t_1) \big], \tag{B.3}$$

where, t_{start}, is synchronized to the photon arrival. In the presence of the gate, the background, and pulse probability have the following time dependence:

$$B_1(t_1), P_1(t_1) = \begin{cases} B_1, P_1(t_1) & t_{\text{start}} \leq t_1 \leq t_{\text{end}} \\ 0 & \text{otherwise} \end{cases} \tag{B.4}$$

$$B_2(\tau + t_1), P_2(\tau + t_1) = \begin{cases} B_2, P_2(\tau + t_1) & t_1 - t_{\text{end}} \leq \tau \leq t_1 - t_{\text{start}} \\ 0 & \text{otherwise} \end{cases} \tag{B.5}$$

The process in Eq. B.3 is shown graphically in Figure B.2, where C_{back} are the total accidental-coincidences rate from photon-background and background-background around $\tau = 0$. Finally, Figure B.2(h) shows the background subtracted coincidences rate, $C_s(\tau)$, within the gate window.

In the case for the results in Chapter 7, only the gating defined in Eq. (B.4) is applied, in order to increase the signal to noise ratio of the HOM-interference, due to the low ion-produced photon rate.

Bibliography

[1] M. D. Eisaman, J. Fan, A. Migdall, and S. V. Polyakov. Invited Review Article: Single-photon sources and detectors. *Review of Scientific Instruments*, 82(7):071101, 2011.
(Cited on pages 1, 60, 61, and 67.)

[2] Darrick E. Chang, Vladan Vuletić, and Mikhail D. Lukin. Quantum nonlinear optics — photon by photon. *Nature Photonics*, 8(9):685–694, Sep 2014.
(Cited on pages 1, 3, and 4.)

[3] Emanuel Knill, Raymond Laflamme, and Gerald J Milburn. A scheme for efficient quantum computation with linear optics. *Nature*, 409(6816):46–52, 2001.
(Cited on page 1.)

[4] Scott Aaronson and Alex Arkhipov. The Computational Complexity of Linear Optics. In *Proceedings of the Forty-Third Annual ACM Symposium on Theory of Computing*, STOC '11, page 333–342, New York, NY, USA, 2011. Association for Computing Machinery.
(Cited on page 1.)

[5] H. J. Kimble. The quantum internet. *Nature*, 453(7198):1023–1030, Jun 2008.
(Cited on page 1.)

[6] Vittorio Giovannetti, Seth Lloyd, and Lorenzo Maccone. Advances in quantum metrology. *Nature photonics*, 5(4):222, 2011.
(Cited on page 1.)

[7] Michael J Hartmann. Quantum simulation with interacting photons. *Journal of Optics*, 18(10):104005, sep 2016.
(Cited on page 1.)

[8] Changsuk Noh and Dimitris G Angelakis. Quantum simulations and many-body physics with light. *Reports on Progress in Physics*, 80(1):016401, nov 2016.
(Cited on page 1.)

[9] R.W. Boyd. *Nonlinear Optics*. Elsevier Science, 2020.
(Cited on page 2.)

[10] Isaac L. Chuang and Yoshihisa Yamamoto. Simple quantum computer. *Phys. Rev. A*, 52:3489–3496, Nov 1995.
(Cited on page 2.)

[11] Jeffrey H. Shapiro. Single-photon Kerr nonlinearities do not help quantum computation. *Phys. Rev. A*, 73:062305, Jun 2006.
(Cited on page 2.)

[12] Michael Fleischhauer, Atac Imamoglu, and Jonathan P. Marangos. Electromagnetically induced transparency: Optics in coherent media. *Rev. Mod. Phys.*, 77:633–673, Jul 2005.
(Cited on pages 2, 35, and 37.)

[13] Hau, Lene and Harris, S. and Dutton, Zachary and Behroozi, Cyrus. Light speed reduction to 17 m per second in an ultracold atomic gas. *Nature*, 397:594–598, Feb 1999.
(Cited on page 2.)

[14] C. Crocker, M. Lichtman, K. Sosnova, A. Carter, S. Scarano, and C. Monroe. High purity single photons entangled with an atomic qubit. *Opt. Express*, 27(20):28143–28149, Sep 2019.
(Cited on page 3.)

[15] Wenjamin Rosenfeld, Daniel Burchardt, Robert Garthoff, Kai Redeker, Norbert Ortegel, Markus Rau, and Harald Weinfurter. Event-Ready Bell Test Using Entangled Atoms Simultaneously Closing Detection and Locality Loopholes. *Phys. Rev. Lett.*, 119:010402, Jul 2017.
(Cited on pages 3, 84, and 85.)

[16] C. J. Ballance, T. P. Harty, N. M. Linke, M. A. Sepiol, and D. M. Lucas. High-Fidelity Quantum Logic Gates Using Trapped-Ion Hyperfine Qubits. *Phys. Rev. Lett.*, 117:060504, Aug 2016.
(Cited on pages 3 and 127.)

[17] D. L. Moehring, P. Maunz, S. Olmschenk, K. C. Younge, D. N. Matsukevich, L.-M. Duan, and C. Monroe. Entanglement of single-atom quantum bits at a distance. *Nature*, 449(7158):68–71, Sep 2007.
(Cited on pages 3 and 155.)

[18] L. J. Stephenson, D. P. Nadlinger, B. C. Nichol, S. An, P. Drmota, T. G. Ballance, K. Thirumalai, J. F. Goodwin, D. M. Lucas, and C. J. Ballance. High-Rate, High-Fidelity Entanglement of Qubits Across an Elementary Quantum Network. *Phys. Rev. Lett.*, 124:110501, Mar 2020.
(Cited on page 3.)

[19] K. M. Birnbaum, A. Boca, R. Miller, A. D. Boozer, T. E. Northup, and H. J. Kimble. Photon blockade in an optical cavity with one trapped atom. *Nature*, 436(7047):87–90, Jul 2005.
(Cited on page 4.)

[20] H G Barros, A Stute, T E Northup, C Russo, P O Schmidt, and R Blatt. Deterministic single-photon source from a single ion. *New Journal of Physics*, 11(10):103004, oct 2009.
(Cited on page 5.)

[21] Andreas Reiserer, Norbert Kalb, Gerhard Rempe, and Stephan Ritter. A quantum gate between a flying optical photon and a single trapped atom. *Nature*, 508(7495):237–240, Apr 2014.
(Cited on page 5.)

[22] Stephan Ritter, Christian Nölleke, Carolin Hahn, Andreas Reiserer, Andreas Neuzner, Manuel Uphoff, Martin Mücke, Eden Figueroa, Joerg Bochmann, and Gerhard Rempe. An elementary quantum network of single atoms in optical cavities. *Nature*, 484(7393):195–200, Apr 2012.
(Cited on page 5.)

[23] Nathan Schine, Albert Ryou, Andrey Gromov, Ariel Sommer, and Jonathan Simon. Synthetic Landau levels for photons. *Nature*, 534(7609):671–675, Jun 2016.
(Cited on page 5.)

[24] Julian Léonard, Andrea Morales, Philip Zupancic, Tilman Esslinger, and Tobias Donner. Supersolid formation in a quantum gas breaking a continuous translational symmetry. *Nature*, 543(7643):87–90, Mar 2017.
(Cited on page 5.)

[25] Jonathan D. Hood. *Atom-light interactions in a photonic crystal waveguide.* PhD thesis, Caltech, September 2017.
(Cited on page 5.)

[26] E. Vetsch, D. Reitz, G. Sagué, R. Schmidt, S. T. Dawkins, and A. Rauschenbeutel. Optical Interface Created by Laser-Cooled Atoms Trapped in the Evanescent Field Surrounding an Optical Nanofiber. *Phys. Rev. Lett.*, 104:203603, May 2010.
(Cited on page 5.)

[27] Pablo Solano, Jeffrey A. Grover, Jonathan E. Hoffman, Sylvain Ravets, Fredrik K. Fatemi, Luis A. Orozco, and Steven L. Rolston. Chapter Seven - Optical Nanofibers: A New Platform for Quantum Optics. volume 66 of *Advances In Atomic, Molecular, and Optical Physics*, pages 439 – 505. Academic Press, 2017.
(Cited on page 5.)

[28] A. Goban, C.-L. Hung, S.-P. Yu, J. D. Hood, J. A. Muniz, J. H. Lee, A. C. Martin, M. J.and McClung, K. S. Choi, D. E. Chang, O. Painter, and H. J. Kimble. Atom–light interactions in photonic crystals. *Nature Communications*, 5(1):3808, May 2014.
(Cited on page 5.)

[29] Jonathan D. Hood, Akihisa Goban, Ana Asenjo-Garcia, Mingwu Lu, Su-Peng Yu, Darrick E. Chang, and H. J. Kimble. Atom–atom interactions

around the band edge of a photonic crystal waveguide. *Proceedings of the National Academy of Sciences*, 113(38):10507–10512, 2016.
(Cited on page 5.)

[30] L.-M. Duan, M. D. Lukin, J. I. Cirac, and P. Zoller. Long-distance quantum communication with atomic ensembles and linear optics. *Nature*, 414(6862):413–418, Nov 2001.
(Cited on page 6.)

[31] Nicolas Sangouard, Christoph Simon, Hugues de Riedmatten, and Nicolas Gisin. Quantum repeaters based on atomic ensembles and linear optics. *Rev. Mod. Phys.*, 83:33–80, Mar 2011.
(Cited on pages 7, 128, and 148.)

[32] D. N. Matsukevich and A. Kuzmich. Quantum State Transfer Between Matter and Light. *Science*, 306(5696):663–666, 2004.
(Cited on page 7.)

[33] Yunfei Wang, Jianfeng Li, Shanchao Zhang, Keyu Su, Yiru Zhou, Kaiyu Liao, Shengwang Du, Hui Yan, and Shi-Liang Zhu. Efficient quantum memory for single-photon polarization qubits. *Nature Photon*, 13(5):346–351, 2019.
(Cited on pages 7 and 127.)

[34] Mahdi Hosseini, Ben M. Sparkes, Gabriel Hétet, Jevon J. Longdell, Ping Koy Lam, and Ben C. Buchler. Coherent optical pulse sequencer for quantum applications. *Nature*, 461(7261):241–245, Sep 2009.
(Cited on page 7.)

[35] Haruka Tanji-Suzuki, Wenlan Chen, Renate Landig, Jonathan Simon, and Vladan Vuletić. Vacuum-Induced Transparency. *Science*, 333(6047):1266–1269, 2011.
(Cited on page 7.)

[36] Wenlan Chen, Kristin M. Beck, Robert Bücker, Michael Gullans, Mikhail D. Lukin, Haruka Tanji-Suzuki, and Vladan Vuletić. All-Optical Switch and Transistor Gated by One Stored Photon. *Science*, 341(6147):768–770, 2013.
(Cited on page 7.)

[37] Yong Yu, Fei Ma, Xi-Yu Luo, Bo Jing, Peng-Fei Sun, Ren-Zhou Fang, Chao-Wei Yang, Hui Liu, Ming-Yang Zheng, Xiu-Ping Xie, Wei-Jun Zhang, Li-Xing You, Zhen Wang, Teng-Yun Chen, Qiang Zhang, Xiao-Hui Bao, and Jian-Wei Pan. Entanglement of two quantum memories via fibres over dozens of kilometres. *Nature*, 578(7794):240–245, Feb 2020.
(Cited on pages 7 and 127.)

[38] Thomas F. Gallagher. *Rydberg Atoms*. Cambridge University Press, 1994. Cambridge Books Online.
(Cited on pages 7, 13, 16, and 23.)

[39] M. Saffman, T. G. Walker, and K. Mølmer. Quantum information with Rydberg atoms. *Rev. Mod. Phys.*, 82:2313–2363, Aug 2010.
(Cited on pages 7, 8, and 177.)

[40] M. D. Lukin, M. Fleischhauer, R. Cote, L. M. Duan, D. Jaksch, J. I. Cirac, and P. Zoller. Dipole Blockade and Quantum Information Processing in Mesoscopic Atomic Ensembles. *Phys. Rev. Lett.*, 87:037901, Jun 2001.
(Cited on pages 8, 13, 30, and 128.)

[41] Inbal Friedler, David Petrosyan, Michael Fleischhauer, and Gershon Kurizki. Long-range interactions and entanglement of slow single-photon pulses. *Phys. Rev. A*, 72:043803, Oct 2005.
(Cited on page 8.)

[42] A. K. Mohapatra, T. R. Jackson, and C. S. Adams. Coherent Optical Detection of Highly Excited Rydberg States Using Electromagnetically Induced Transparency. *Phys. Rev. Lett.*, 98:113003, Mar 2007.
(Cited on page 9.)

[43] Alexey V. Gorshkov, Johannes Otterbach, Michael Fleischhauer, Thomas Pohl, and Mikhail D. Lukin. Photon-Photon Interactions via Rydberg Blockade. *Phys. Rev. Lett.*, 107:133602, Sep 2011.
(Cited on pages 9, 14, and 157.)

[44] Thibault Peyronel, Ofer Firstenberg, Qi-Yu Liang, Sebastian Hofferberth, Alexey V Gorshkov, Thomas Pohl, Mikhail D Lukin, and Vladan Vuletić. Quantum nonlinear optics with single photons enabled by strongly interacting atoms. *Nature*, 488(7409):57–60, 2012.
(Cited on pages 9, 14, 31, 124, and 127.)

[45] Y. O. Dudin and A. Kuzmich. Strongly Interacting Rydberg Excitations of a Cold Atomic Gas. *Science*, 336(6083):887–889, 2012.
(Cited on pages 9, 31, 32, 127, 131, and 148.)

[46] D. Maxwell, D. J. Szwer, D. Paredes-Barato, H. Busche, J. D. Pritchard, A. Gauguet, K. J. Weatherill, M. P. A. Jones, and C. S. Adams. Storage and Control of Optical Photons Using Rydberg Polaritons. *Phys. Rev. Lett.*, 110:103001, Mar 2013.
(Cited on pages 9, 31, 127, and 148.)

[47] Simon Baur, Daniel Tiarks, Gerhard Rempe, and Stephan Dürr. Single-Photon Switch Based on Rydberg Blockade. *Phys. Rev. Lett.*, 112:073901, Feb 2014.
(Cited on page 9.)

[48] H. Gorniaczyk, C. Tresp, J. Schmidt, H. Fedder, and S. Hofferberth. Single-Photon Transistor Mediated by Interstate Rydberg Interactions. *Phys. Rev. Lett.*, 113:053601, Jul 2014.
(Cited on pages 9, 32, 127, and 148.)

[49] Daniel Tiarks, Simon Baur, Katharina Schneider, Stephan Dürr, and Gerhard Rempe. Single-Photon Transistor Using a Förster Resonance. *Phys. Rev. Lett.*, 113:053602, Jul 2014.
(Cited on pages 9, 32, 127, and 148.)

[50] Hannes Gorniaczyk, Christoph Tresp, Przemek Bienias, Asaf Paris Mandoki, Weibin Li, Ivan Mirgorodskiy, H. Büchler, Igor Lesanovsky, and S. Hofferberth. Enhancement of Rydberg-mediated single-photon nonlinearities by electrically tuned Förster resonances. *Nature Communications*, 7:12480, 07 2016.
(Cited on pages 9, 32, 127, and 148.)

[51] L. Isenhower, E. Urban, X. L. Zhang, A. T. Gill, T. Henage, T. A. Johnson, T. G. Walker, and M. Saffman. Demonstration of a Neutral Atom Controlled-NOT Quantum Gate. *Phys. Rev. Lett.*, 104:010503, Jan 2010.
(Cited on pages 9 and 32.)

[52] K. M. Maller, M. T. Lichtman, T. Xia, Y. Sun, M. J. Piotrowicz, A. W. Carr, L. Isenhower, and M. Saffman. Rydberg-blockade controlled-not gate and entanglement in a two-dimensional array of neutral-atom qubits. *Phys. Rev. A*, 92:022336, Aug 2015.
(Cited on pages 9 and 127.)

[53] Yong Zeng, Peng Xu, Xiaodong He, Yangyang Liu, Min Liu, Jin Wang, D. J. Papoular, G. V. Shlyapnikov, and Mingsheng Zhan. Entangling Two Individual Atoms of Different Isotopes via Rydberg Blockade. *Phys. Rev. Lett.*, 119:160502, Oct 2017.
(Cited on pages 9 and 127.)

[54] Daniel Tiarks, Steffen Schmidt-Eberle, Thomas Stolz, Gerhard Rempe, and Stephan Dürr. A photon–photon quantum gate based on Rydberg interactions. *Nature Physics*, 15(2):124–126, 2019.
(Cited on pages 9 and 127.)

[55] Ofer Firstenberg, Thibault Peyronel, Qi-Yu Liang, Alexey V Gorshkov, Mikhail D Lukin, and Vladan Vuletić. Attractive photons in a quantum nonlinear medium. *Nature*, 502(7469):71–75, 2013.
(Cited on pages 9, 161, and 174.)

[56] Qi-Yu Liang, Aditya V. Venkatramani, Sergio H. Cantu, Travis L. Nicholson, Michael J. Gullans, Alexey V. Gorshkov, Jeff D. Thompson, Cheng Chin, Mikhail D. Lukin, and Vladan Vuletić. Observation of three-photon bound states in a quantum nonlinear medium. *Science*, 359(6377):783–786, 2018.
(Cited on pages 9, 157, and 174.)

[57] Nina Stiesdal, Jan Kumlin, Kevin Kleinbeck, Philipp Lunt, Christoph Braun, Asaf Paris-Mandoki, Christoph Tresp, Hans Peter Büchler, and Sebastian Hofferberth. Observation of Three-Body Correlations for Photons Coupled to a Rydberg Superatom. *Phys. Rev. Lett.*, 121:103601, Sep 2018.
(Cited on pages 9, 157, 158, 165, and 177.)

[58] D. P. Ornelas-Huerta, A. N. Craddock, E. A. Goldschmidt, A. J. Hachtel, Y. Wang, P. Bienias, A. V. Gorshkov, S. L. Rolston, and J. V. Porto. On-demand indistinguishable single photons from an efficient and pure source based on a Rydberg ensemble. *Optica*, 7(7):813–819, Jul 2020.
(Cited on pages 10 and 32.)

[59] A. N. Craddock, J. Hannegan, D. P. Ornelas-Huerta, J. D. Siverns, A. J. Hachtel, E. A. Goldschmidt, J. V. Porto, Q. Quraishi, and S. L. Rolston. Quantum Interference between Photons from an Atomic Ensemble and a Remote Atomic Ion. *Phys. Rev. Lett.*, 123:213601, Nov 2019.
(Cited on pages 10, 32, 127, 148, 153, 154, and 176.)

[60] A. Radzig and A. Smirnov. *Reference Data on Atoms, Molecules, and Ions*, volume 25. Springer, 08 1986.
(Cited on page 13.)

[61] D. Jaksch, J. I. Cirac, P. Zoller, S. L. Rolston, R. Côté, and M. D. Lukin. Fast Quantum Gates for Neutral Atoms. *Phys. Rev. Lett.*, 85:2208–2211, Sep 2000.
(Cited on pages 13 and 30.)

[62] M. Saffman and T. G. Walker. Creating single-atom and single-photon sources from entangled atomic ensembles. *Phys. Rev. A*, 66:065403, Dec 2002.
(Cited on pages 14, 31, 32, 127, 128, and 131.)

[63] Jonathan D. Pritchard. *Cooperative Optical Non-linearity in a Blockaded Rydberg Ensemble*. PhD thesis, Durham University, June 2011.
(Cited on pages 15, 19, 29, and 86.)

[64] Wenhui Li, I. Mourachko, M. W. Noel, and T. F. Gallagher. Millimeter-wave spectroscopy of cold Rb Rydberg atoms in a magneto-optical trap: Quantum defects of the ns , np , and nd series. *Phys. Rev. A*, 67:052502, May 2003.
(Cited on pages 16 and 17.)

[65] Jianing Han, Yasir Jamil, D. V. L. Norum, Paul J. Tanner, and T. F. Gallagher. Rb nf quantum defects from millimeter-wave spectroscopy of cold ^{85}Rb Rydberg atoms. *Phys. Rev. A*, 74:054502, Nov 2006.
(Cited on pages 16 and 17.)

[66] Markus Mack, Florian Karlewski, Helge Hattermann, Simone Höckh, Florian Jessen, Daniel Cano, and József Fortágh. Measurement of absolute transition frequencies of ^{87}Rb to nS and nD Rydberg states by means of electromagnetically induced transparency. *Phys. Rev. A*, 83:052515, May 2011.
(Cited on page 16.)

[67] Ali Sanayei, Nils Schopohl, Jens Grimmel, Markus Mack, Florian Karlewski, and József Fortágh. Quasiclassical quantum defect theory and the spectrum of highly excited rubidium atoms. *Phys. Rev. A*, 91:032509, Mar 2015.
(Cited on pages 16 and 18.)

[68] M. Pawlak, N. Moiseyev, and H. R. Sadeghpour. Highly excited Rydberg states of a rubidium atom: Theory versus experiments. *Phys. Rev. A*, 89:042506, Apr 2014.
(Cited on page 16.)

[69] M. Marinescu, H. R. Sadeghpour, and A. Dalgarno. Dispersion coefficients for alkali-metal dimers. *Phys. Rev. A*, 49:982–988, Feb 1994.
(Cited on page 18.)

[70] Constantine E. Theodosiou. Lifetimes of alkali-metal¯atom Rydberg states. *Phys. Rev. A*, 30:2881–2909, Dec 1984.
(Cited on page 18.)

[71] A. Kramida, Yu. Ralchenko, J. Reader, and and NIST ASD Team. NIST Atomic Spectra Database (ver. 5.3), [Online]. Available: `http://physics.nist.gov/asd` [2016, January 27]. National Institute of Standards and Technology, Gaithersburg, MD., 2015.
(Cited on page 19.)

[72] Myron L. Zimmerman, Michael G. Littman, Michael M. Kash, and Daniel Kleppner. Stark structure of the Rydberg states of alkali-metal atoms. *Phys. Rev. A*, 20:2251–2275, Dec 1979.
(Cited on page 19.)

[73] S. A. Bhatti, C. L. Cromer, and W. E. Cooke. Analysis of the Rydberg character of the $5d7d\,^1D_2$ state of barium. *Phys. Rev. A*, 24:161–165, Jul 1981.
(Cited on page 19.)

[74] B. E. King. Angular Momentum Coupling and Rabi Frequencies for Simple Atomic Transitions, 2008.
(Cited on pages 21, 22, and 23.)

[75] Robert Löw, Hendrik Weimer, Johannes Nipper, Jonathan B Balewski, Björn Butscher, Hans Peter Büchler, and Tilman Pfau. An experimental and theoretical guide to strongly interacting Rydberg gases. *Journal of Physics B: Atomic, Molecular and Optical Physics*, 45(11):113001, 2012.
(Cited on pages 26, 27, 29, and 86.)

[76] M. S. O'Sullivan and B. P. Stoicheff. Scalar polarizabilities and avoided crossings of high Rydberg states in Rb. *Phys. Rev. A*, 31:2718–2720, Apr 1985.
(Cited on page 26.)

[77] A. W. Glaetzle, M. Dalmonte, R. Nath, I. Rousochatzakis, R. Moessner, and P. Zoller. Quantum Spin-Ice and Dimer Models with Rydberg Atoms. *Phys. Rev. X*, 4:041037, Nov 2014.
(Cited on page 28.)

[78] Raul Celistrino Teixeira. *Effets mécaniques de l'interaction dipolaire des atomes de Rydberg sondés par spectroscopie microonde. Agrégats*

Moléculaires et Atomiques. PhD thesis, Université Pierre et Marie Curie, March 2015.
(Cited on page 29.)

[79] N. Thaicharoen, A. Schwarzkopf, and G. Raithel. Measurement of the van der Waals interaction by atom trajectory imaging. *Phys. Rev. A*, 92:040701, Oct 2015.
(Cited on page 29.)

[80] Thibault Peyronel. *Quantum Nonlinear Optics Using Cold Atomic Ensembles*. PhD thesis, Massachusetts Institute of Technology, September 2013.
(Cited on pages 29 and 86.)

[81] Alpha Gaëtan, Yevhen Miroshnychenko, Tatjana Wilk, Amodsen Chotia, Matthieu Viteau, Daniel Comparat, Pierre Pillet, Antoine Browaeys, and Philippe Grangier. Observation of collective excitation of two individual atoms in the Rydberg blockade regime. *Nature Physics*, 5(2):115–118, 2009.
(Cited on page 31.)

[82] E. Urban, T.A. Johnson, T. Henage, L. Isenhower, T.G. Walker, and M. Saffman. Observation of Rydberg Blockade between Two Atoms. *Nature Physics*, 5, 05 2008.
(Cited on page 31.)

[83] L. Béguin, A. Vernier, R. Chicireanu, T. Lahaye, and A. Browaeys. Direct Measurement of the van der Waals Interaction between Two Rydberg Atoms. *Phys. Rev. Lett.*, 110:263201, Jun 2013.
(Cited on page 31.)

[84] Matthew Ebert, Alexander Gill, Michael Gibbons, Xianli Zhang, Mark Saffman, and Thad G. Walker. Atomic Fock State Preparation Using Rydberg Blockade. *Phys. Rev. Lett.*, 112:043602, Jan 2014.
(Cited on pages 31 and 175.)

[85] Johannes Zeiher, Peter Schauß, Sebastian Hild, Tommaso Macrì, Immanuel Bloch, and Christian Gross. Microscopic Characterization of Scalable Coherent Rydberg Superatoms. *Phys. Rev. X*, 5:031015, Aug 2015.
(Cited on page 31.)

[86] Asaf Paris-Mandoki, Christoph Braun, Jan Kumlin, Christoph Tresp, Ivan Mirgorodskiy, Florian Christaller, Hans Peter Büchler, and Sebastian Hofferberth. Free-Space Quantum Electrodynamics with a Single Rydberg Superatom. *Phys. Rev. X*, 7:041010, Oct 2017.
(Cited on pages 31 and 127.)

[87] E. Brion, L. H. Pedersen, M. Saffman, and K. Mølmer. Error Correction in Ensemble Registers for Quantum Repeaters and Quantum Computers. *Phys. Rev. Lett.*, 100:110506, Mar 2008.
(Cited on page 32.)

[88] M. Ebert, M. Kwon, T. G. Walker, and M. Saffman. Coherence and Rydberg Blockade of Atomic Ensemble Qubits. *Phys. Rev. Lett.*, 115:093601, Aug 2015.
(Cited on page 32.)

[89] Bo Zhao, Markus Müller, Klemens Hammerer, and Peter Zoller. Efficient quantum repeater based on deterministic Rydberg gates. *Phys. Rev. A*, 81:052329, May 2010.
(Cited on pages 32 and 148.)

[90] Yang Han, Bing He, Khabat Heshami, Cheng-Zu Li, and Christoph Simon. Quantum repeaters based on Rydberg-blockade-coupled atomic ensembles. *Phys. Rev. A*, 81:052311, May 2010.
(Cited on pages 32 and 148.)

[91] L Li, Y.O. Dudin, and A. Kuzmich. Entanglement between light and an optical atomic excitation. *Nature*, 498(7455):466–469, 2013.
(Cited on pages 32, 107, and 148.)

[92] Neal Solmeyer, Xiao Li, and Qudsia Quraishi. High teleportation rates using cold-atom-ensemble-based quantum repeaters with Rydberg blockade. *Phys. Rev. A*, 93:042301, Apr 2016.
(Cited on pages 32, 148, and 175.)

[93] Alexey V. Gorshkov, Axel André, Michael Fleischhauer, Anders S. Sørensen, and Mikhail D. Lukin. Universal Approach to Optimal Photon Storage in Atomic Media. *Phys. Rev. Lett.*, 98:123601, Mar 2007.
(Cited on pages 34 and 177.)

[94] M. Fleischhauer and M. D. Lukin. Dark-State Polaritons in Electromagnetically Induced Transparency. *Phys. Rev. Lett.*, 84:5094–5097, May 2000.
(Cited on pages 35, 43, 47, 49, 158, and 159.)

[95] Alexey V. Gorshkov, Axel André, Mikhail D. Lukin, and Anders S. Sørensen. Photon storage in Λ-type optically dense atomic media. II. Free-space model. *Phys. Rev. A*, 76:033805, Sep 2007.
(Cited on pages 35, 43, and 142.)

[96] Przemyslaw Bienias. Few-body quantum physics with strongly interacting Rydberg polaritons. *The European Physical Journal Special Topics*, 225(15):2957–2976, 2016.
(Cited on pages 36, 43, 51, 52, and 57.)

[97] M. J. Gullans, S. Diehl, S. T. Rittenhouse, B. P. Ruzic, J. P. D'Incao, P. Julienne, A. V. Gorshkov, and J. M. Taylor. Efimov States of Strongly Interacting Photons. *Phys. Rev. Lett.*, 119:233601, Dec 2017.
(Cited on pages 56, 59, 157, 174, and 177.)

[98] P. Bienias, S. Choi, O. Firstenberg, M. F. Maghrebi, M. Gullans, M. D. Lukin, A. V. Gorshkov, and H. P. Büchler. Scattering resonances and bound states for strongly interacting Rydberg polaritons. *Phys. Rev. A*, 90:053804,

Nov 2014.
(Cited on pages 57, 59, 157, 158, 160, 167, 169, 173, and 174.)

[99] M. J. Gullans, J. D. Thompson, Y. Wang, Q.-Y. Liang, V. Vuletić, M. D. Lukin, and A. V. Gorshkov. Effective Field Theory for Rydberg Polaritons. *Phys. Rev. Lett.*, 117:113601, Sep 2016.
(Cited on pages 59 and 157.)

[100] Martin J. Stevens. Chapter 2 - Photon Statistics, Measurements, and Measurements Tools. In Alan Migdall, Sergey V. Polyakov, Jingyun Fan, and Joshua C. Bienfang, editors, *Single-Photon Generation and Detection*, volume 45 of *Experimental Methods in the Physical Sciences*, pages 25–68. Academic Press, 2013.
(Cited on pages 61, 62, 63, 64, 65, and 76.)

[101] Pascale Senellart, Glenn Solomon, and Andrew White. High-performance semiconductor quantum-dot single-photon sources. *Nature Nanotechnology*, 12(11):1026–1039, Nov 2017.
(Cited on pages 61 and 85.)

[102] A. I. Lvovsky, H. Hansen, T. Aichele, O. Benson, J. Mlynek, and S. Schiller. Quantum State Reconstruction of the Single-Photon Fock State. *Phys. Rev. Lett.*, 87:050402, Jul 2001.
(Cited on page 61.)

[103] Tim Thomay, Sergey V. Polyakov, Olivier Gazzano, Elizabeth Goldschmidt, Zachary D. Eldredge, Tobias Huber, Vivien Loo, and Glenn S. Solomon. Simultaneous, Full Characterization of a Single-Photon State. *Phys. Rev. X*, 7:041036, Nov 2017.
(Cited on page 61.)

[104] T. Legero, T. Wilk, A. Kuhn, and G. Rempe. Time-resolved two-photon quantum interference. *Applied Physics B*, 77(8):797–802, Dec 2003.
(Cited on pages 61, 78, and 154.)

[105] Raphaël Proux, Maria Maragkou, Emmanuel Baudin, Christophe Voisin, Philippe Roussignol, and Carole Diederichs. Measuring the Photon Coalescence Time Window in the Continuous-Wave Regime for Resonantly Driven Semiconductor Quantum Dots. *Phys. Rev. Lett.*, 114:067401, Feb 2015.
(Cited on page 61.)

[106] Rodney Loudon. *The Quantum Theory of Light*, volume 42. OUP Oxford, 01 2000.
(Cited on pages 62 and 71.)

[107] Hans-A Bachor and Timothy Ralph. *A Guide to Experiments in Quantum Optics*. Wiley Online Library, 09 2019.
(Cited on pages 62 and 69.)

[108] Elizabeth A. Goldschmidt. *Quantum Nonlinear Optics Using Cold Atomic Ensembles*. PhD thesis, University of Maryland, September 2013.
(Cited on pages 62, 66, and 68.)

[109] Pieter Kok, W. J. Munro, Kae Nemoto, T. C. Ralph, Jonathan P. Dowling, and G. J. Milburn. Linear optical quantum computing with photonic qubits. *Rev. Mod. Phys.*, 79:135–174, Jan 2007.
(Cited on page 65.)

[110] E. Wolf. Optics in terms of observable quantities. *Il Nuovo Cimento (1943-1954)*, 12(6):884–888, Dec 1954.
(Cited on page 65.)

[111] Roy J. Glauber. The Quantum Theory of Optical Coherence. *Phys. Rev.*, 130:2529–2539, Jun 1963.
(Cited on page 65.)

[112] Ravitej Uppu, Tom A. W. Wolterink, Tristan B. H. Tentrup, and Pepijn W. H. Pinkse. Quantum optics of lossy asymmetric beam splitters. *Opt. Express*, 24(15):16440–16449, Jul 2016.
(Cited on pages 72 and 73.)

[113] Xi-Lin Wang, Luo-Kan Chen, W. Li, H.-L. Huang, C. Liu, C. Chen, Y.-H. Luo, Z.-E. Su, D. Wu, Z.-D. Li, H. Lu, Y. Hu, X. Jiang, C.-Z. Peng, L. Li, N.-L. Liu, Yu-Ao Chen, Chao-Yang Lu, and Jian-Wei Pan. . *Phys. Rev. Lett.*, 117:210502, Nov 2016.
(Cited on pages 83 and 84.)

[114] Han-Sen Zhong, Yuan Li, Wei Li, Li-Chao Peng, Zu-En Su, Yi Hu, Yu-Ming He, Xing Ding, Weijun Zhang, Hao Li, Lu Zhang, Zhen Wang, Lixing You, Xi-Lin Wang, Xiao Jiang, Li Li, Yu-Ao Chen, Nai-Le Liu, Chao-Yang Lu, and Jian-Wei Pan. 12-Photon Entanglement and Scalable Scattershot Boson Sampling with Optimal Entangled-Photon Pairs from Parametric Down-Conversion. *Phys. Rev. Lett.*, 121:250505, Dec 2018.
(Cited on pages 83 and 84.)

[115] C. Xiong, X. Zhang, Z. Liu, M. J. Collins, A. Mahendra, L. G. Helt, M. J. Steel, D.-Y. Choi, C. J. Chae, P. H. W. Leong, and B. J. Eggleton. Active temporal multiplexing of indistinguishable heralded single photons. *Nature Communications*, 7(1):10853, Mar 2016.
(Cited on pages 83 and 84.)

[116] F. Kaneda and P. G. Kwiat. High-efficiency single-photon generation via large-scale active time multiplexing. *Science Advances*, 5(10):eaaw8586, 2019.
(Cited on pages 83 and 84.)

[117] N. Somaschi, V. Giesz, L. De Santis, J. C. Loredo, M. P. Almeida, G. Hornecker, S. L. Portalupi, T. Grange, C. Antón, J. Demory, C. Gómez, I. Sagnes, N. D. Lanzillotti-Kimura, A. Lemaítre, A. Auffeves, A. G. White, L. Lanco, and P. Senellart. Near-optimal single-photon sources in the solid state. *Nature Photon*, 10(5):340–345, Mar 2016.
(Cited on pages 83 and 84.)

[118] Juan C. Loredo, Nor A. Zakaria, Niccolo Somaschi, Carlos Anton, Lorenzo de Santis, Valerian Giesz, Thomas Grange, Matthew A. Broome, Olivier Gazzano, Guillaume Coppola, Isabelle Sagnes, Aristide Lemaitre, Alexia Auffeves, Pascale Senellart, Marcelo P. Almeida, and Andrew G. White. Scalable performance in solid-state single-photon sources. *Optica*, 3(4):433–440, Apr 2016.
(Cited on pages 83 and 84.)

[119] Hui Wang, Yu He, Yu-Huai Li, Zu-En Su, Bo Li, He-Liang Huang, Xing Ding, Ming-Cheng Chen, Chang Liu, Jian Qin, Jin-Peng Li, Yu-Ming He, Christian Schneider, Martin Kamp, Cheng-Zhi Peng, Sven Höfling, Chao-Yang Lu, and Jian-Wei Pan. High-efficiency multiphoton boson sampling. *Nature Photon*, 11(6):361–365, Apr 2017.
(Cited on pages 83 and 84.)

[120] Gabija Kiršanskė, Henri Thyrrestrup, Raphaël S. Daveau, Chris L. Dreeßen, Tommaso Pregnolato, Leonardo Midolo, Petru Tighineanu, Alisa Javadi, Søren Stobbe, Rüdiger Schott, Arne Ludwig, Andreas D. Wieck, Suk In Park, Jin D. Song, Andreas V. Kuhlmann, Immo Söllner, Matthias C. Löbl, Richard J. Warburton, and Peter Lodahl. Indistinguishable and efficient single photons from a quantum dot in a planar nanobeam waveguide. *Phys. Rev. B*, 96:165306, Oct 2017.
(Cited on pages 83 and 84.)

[121] Hui Wang, Yu-Ming He, T.-H. Chung, Hai Hu, Ying Yu, Si Chen, Xing Ding, M.-C. Chen, Jian Qin, Xiaoxia Yang, Run-Ze Liu, Z.-C. Duan, J.-P. Li, S. Gerhardt, K. Winkler, J. Jurkat, Lin-Jun Wang, Niels Gregersen, Yong-Heng Huo, Qing Dai, Siyuan Yu, Sven Höfling, Chao-Yang Lu, and Jian-Wei Pan. Towards optimal single-photon sources from polarized microcavities. *Nature Photonics*, 13(11):770–775, Nov 2019.
(Cited on pages 83 and 84.)

[122] Hélène Ollivier, Ilse Maillette de Buy Wenniger, Sarah Thomas, Stephen Wein, Abdelmounaim Harouri, Guillaume Coppola, Paul Hilaire, Clément Millet, Aristide Lemaitre, Isabelle Sagnes, Olivier Krebs, Loic Lanco, J. Loredo, Carlos Anton-Solanas, Niccolo Somaschi, and Pascale Senellart. Reproducibility of High-Performance Quantum Dot Single-Photon Sources. *ACS Photonics*, 7:1050, 03 2020.
(Cited on pages 83 and 84.)

[123] Peter Maunz, DL Moehring, S Olmschenk, KC Younge, DN Matsukevich, and C Monroe. Quantum interference of photon pairs from two remote trapped atomic ions. *Nature Phys*, 3(8):538–541, 2007.
(Cited on pages 84 and 85.)

[124] Thompson, James K. and Simon, Jonathan and Loh, Huanqian and Vuletić, Vladan. A high-brightness source of narrowband, identical-photon pairs. *Science*, 313(5783):74–77, 2006.
(Cited on pages 84 and 85.)

[125] T. Wilk, S. C. Webster, H. P. Specht, G. Rempe, and A. Kuhn. Polarization-Controlled Single Photons. *Phys. Rev. Lett.*, 98:063601, Feb 2007.
(Cited on pages 84 and 85.)

[126] Peter B R Nisbet-Jones, Jerome Dilley, Daniel Ljunggren, and Axel Kuhn. Highly efficient source for indistinguishable single photons of controlled shape. *New Journal of Physics*, 13(10):103036, Oct 2011.
(Cited on pages 84 and 85.)

[127] Martin Mücke, Joerg Bochmann, Carolin Hahn, Andreas Neuzner, Christian Nölleke, Andreas Reiserer, Gerhard Rempe, and Stephan Ritter. Generation of single photons from an atom-cavity system. *Phys. Rev. A*, 87:063805, Jun 2013.
(Cited on pages 84 and 85.)

[128] Creston D. Herold. *Ultracold Mixtures of Rubidium and Ytterbium for open quantum system engineering.* PhD thesis, University of Maryland College Park, June 2014.
(Cited on page 89.)

[129] Michael Schlagmüller, Tara Cubel Liebisch, Felix Engel, Kathrin S. Kleinbach, Fabian Böttcher, Udo Hermann, Karl M. Westphal, Anita Gaj, Robert Löw, Sebastian Hofferberth, Tilman Pfau, Jesús Pérez-Ríos, and Chris H. Greene. Ultracold Chemical Reactions of a Single Rydberg Atom in a Dense Gas. *Phys. Rev. X*, 6:031020, Aug 2016.
(Cited on pages 90, 135, 136, and 137.)

[130] A. Gozzini, F. Mango, J. H. Xu, G. Alzetta, F. Maccarrone, and R. A. Bernheim. Light-induced ejection of alkali atoms in polysiloxane coated cells. *Il Nuovo Cimento D*, 15(5):709–722, May 1993.
(Cited on page 96.)

[131] C. Klempt, T. van Zoest, T. Henninger, O. Topic, E. Rasel, W. Ertmer, and J. Arlt. Ultraviolet light-induced atom desorption for large rubidium and potassium magneto-optical traps. *Phys. Rev. A*, 73:013410, Jan 2006.
(Cited on page 96.)

[132] H.J. Metcalf and P. van der Straten. *Laser Cooling and Trapping.* Graduate Texts in Contemporary Physics. Springer New York, 2001.
(Cited on page 98.)

[133] Wolfgang Ketterle, Kendall B. Davis, Michael A. Joffe, Alex Martin, and David E. Pritchard. High densities of cold atoms in a dark spontaneous-force optical trap. *Phys. Rev. Lett.*, 70:2253–2256, Apr 1993.
(Cited on page 98.)

[134] William D. Phillips. Nobel Lecture: Laser cooling and trapping of neutral atoms. *Rev. Mod. Phys.*, 70:721–741, Jul 1998.
(Cited on page 100.)

[135] Sara Rosi, Alessia Burchianti, Stefano Conclave, Devang S. Naik, Giacomo Roati, Chiara Fort, and Francesco Minardi. Λ-enhanced grey molasses on the D2 transition of Rubidium-87 atoms. *Scientific Reports*, 8(1):1301, Jan 2018.
(Cited on page 100.)

[136] A. D. Shiner, A. A. Madej, P. Dubé, and J. E. Bernard. Absolute optical frequency measurement of saturated absorption lines in Rb near 422 nm. *Applied Physics B*, 89(4):595–601, Dec 2007.
(Cited on page 108.)

[137] JE Navarro-Navarrete, A Díaz-Calderón, LM Hoyos-Campo, F Ponciano-Ojeda, J Flores-Mijangos, F Ramírez-Martínez, and J Jiménez-Mier. Doppler-free saturation of the cascade fluorescence that follows excitation of the $5s \rightarrow 6p$ transition in atomic rubidium. *arXiv preprint arXiv:1906.07114*, 2019.
(Cited on page 108.)

[138] E. A. Goldschmidt, D. G. Norris, S. B. Koller, R. Wyllie, R. C. Brown, J. V. Porto, U. I. Safronova, and M. S. Safronova. Magic wavelengths for the $5s$–$18s$ transition in rubidium. *Phys. Rev. A*, 91:032518, Mar 2015.
(Cited on page 107.)

[139] J. Lampen, H. Nguyen, L. Li, P. R. Berman, and A. Kuzmich. Long-lived coherence between ground and Rydberg levels in a magic-wavelength lattice. *Phys. Rev. A*, 98:033411, Sep 2018.
(Cited on pages 107, 111, and 176.)

[140] Sylvain de Léséleuc, Daniel Barredo, Vincent Lienhard, Antoine Browaeys, and Thierry Lahaye. Analysis of imperfections in the coherent optical excitation of single atoms to Rydberg states. *Phys. Rev. A*, 97:053803, May 2018.
(Cited on pages 110 and 116.)

[141] Neal C. Pisenti. *Isotope Shift Spectroscopy of Ultracold Strontium*. PhD thesis, University of Maryland College Park, January 2019.
(Cited on pages 114 and 115.)

[142] R. W. P. Drever, J. L. Hall, F. V. Kowalski, J. Hough, G. M. Ford, A. J. Munley, and H. Ward. Laser phase and frequency stabilization using an optical resonator. *Applied Physics B*, 31(2):97–105, Jun 1983.
(Cited on pages 114 and 115.)

[143] Eric D. Black. An introduction to Pound–Drever–Hall laser frequency stabilization. *American Journal of Physics*, 69(1):79–87, 2001.
(Cited on pages 114, 115, and 116.)

[144] Harry Levine, Alexander Keesling, Ahmed Omran, Hannes Bernien, Sylvain Schwartz, Alexander S. Zibrov, Manuel Endres, Markus Greiner, Vladan Vuletić, and Mikhail D. Lukin. High-Fidelity Control and Entanglement of Rydberg-Atom Qubits. *Phys. Rev. Lett.*, 121:123603, Sep 2018.
(Cited on pages 116 and 127.)

[145] Daniel Steck. Rubidium 87 D Line Data. September 2001.
(Cited on page 119.)

[146] J. D. Pritchard, D. Maxwell, A. Gauguet, K. J. Weatherill, M. P. A. Jones, and C. S. Adams. Cooperative Atom-Light Interaction in a Blockaded Rydberg Ensemble. *Phys. Rev. Lett.*, 105:193603, Nov 2010.
(Not cited.)

[147] Qiyu Liang. *Strongly interacting photons via Rydberg-Rydberg interactions*. PhD thesis, Massachusetts Institute of Technology, 1 2017.
(Cited on page 124.)

[148] Stetson Roof, Kasie Kemp, Mark Havey, I. M. Sokolov, and D. V. Kupriyanov. Microscopic lensing by a dense, cold atomic sample. *Opt. Lett.*, 40(7):1137–1140, Apr 2015.
(Cited on page 124.)

[149] Jacques Carolan, Christopher Harrold, Chris Sparrow, Enrique Martín-López, Nicholas J. Russell, Joshua W. Silverstone, Peter J. Shadbolt, Nobuyuki Matsuda, Manabu Oguma, Mikitaka Itoh, Graham D. Marshall, Mark G. Thompson, Jonathan C. F. Matthews, Toshikazu Hashimoto, Jeremy L. O'Brien, and Anthony Laing. Universal linear optics. *Science*, 349(6249):711–716, 2015.
(Cited on page 127.)

[150] Hui Wang, Jian Qin, Xing Ding, Ming-Cheng Chen, Si Chen, Xiang You, Yu-Ming He, Xiao Jiang, L. You, Z. Wang, C. Schneider, Jelmer J. Renema, Sven Höfling, Chao-Yang Lu, and Jian-Wei Pan. Boson Sampling with 20 Input Photons and a 60-Mode Interferometer in a 10^{14}-Dimensional Hilbert Space. *Phys. Rev. Lett.*, 123:250503, Dec 2019.
(Cited on page 127.)

[151] Juan Yin, Yuan Cao, Yu-Huai Li, Sheng-Kai Liao, Liang Zhang, Ji-Gang Ren, Wen-Qi Cai, Wei-Yue Liu, Bo Li, Hui Dai, Guang-Bing Li, Qi-Ming Lu, Yun-Hong Gong, Yu Xu, Shuang-Lin Li, Feng-Zhi Li, Ya-Yun Yin, Zi-Qing Jiang, Ming Li, Jian-Jun Jia, Ge Ren, Dong He, Yi-Lin Zhou, Xiao-Xiang Zhang, Na Wang, Xiang Chang, Zhen-Cai Zhu, Nai-Le Liu, Yu-Ao Chen, Chao-Yang Lu, Rong Shu, Cheng-Zhi Peng, Jian-Yu Wang, and Jian-Wei Pan. Satellite-based entanglement distribution over 1200 kilometers. *Science*, 356(6343):1140–1144, 2017.
(Cited on page 127.)

[152] Sergei Slussarenko, Morgan M Weston, Helen M Chrzanowski, Lynden K Shalm, Varun B Verma, Sae Woo Nam, and Geoff J Pryde. Unconditional violation of the shot-noise limit in photonic quantum metrology. *Nature Photon*, 11(11):700–703, 2017.
(Cited on page 127.)

[153] Matthiasa Bock, Pascal Eich, Stephan Kucera, Matthias Kreis, Andreas Lenhard, Christoph Becher, and Jürgen Eschner. High-fidelity entanglement between a trapped ion and a telecom photon via quantum frequency

conversion. *Nature Communications*, 9(1):1998, May 2018.
(Cited on pages 127 and 148.)

[154] Christian Gross and Immanuel Bloch. Quantum simulations with ultracold atoms in optical lattices. *Science*, 357(6355):995–1001, 2017.
(Cited on page 127.)

[155] Lin Li and A. Kuzmich. Quantum memory with strong and controllable Rydberg-level interactions. *Nature Communications*, 7(1):13618, Nov 2016.
(Cited on page 127.)

[156] Fabian Ripka, Harald Kübler, Robert Löw, and Tilman Pfau. A room-temperature single-photon source based on strongly interacting Rydberg atoms. *Science*, 362:446–449, 10 2018.
(Cited on pages 127 and 131.)

[157] Daniel Tiarks, Steffen Schmidt, Gerhard Rempe, and Stephan Dürr. Optical π phase shift created with a single-photon pulse. *Science Advances*, 2(4), 2016.
(Cited on page 127.)

[158] Jeff D. Thompson, Travis L. Nicholson, Qi-Yu Liang, Sergio H. Cantu, Aditya V. Venkatramani, Soonwon Choi, Ilya A. Fedorov, Daniel Viscor, Thomas Pohl, Mikhail D. Lukin, and Vladan Vuletić. Symmetry-protected collisions between strongly interacting photons. *Nature*, 542(7640):206–209, Feb 2017.
(Cited on pages 127 and 177.)

[159] Peter Schauß, Marc Cheneau, Manuel Endres, Takeshi Fukuhara, Sebastian Hild, Ahmed Omran, Thomas Pohl, Christian Gross, Stefan Kuhr, and Immanuel Bloch. Observation of spatially ordered structures in a two-dimensional Rydberg gas. *Nature*, 491(7422):87–91, Nov 2012.
(Cited on page 127.)

[160] Johannes Zeiher, Jae-yoon Choi, Antonio Rubio-Abadal, Thomas Pohl, Rick van Bijnen, Immanuel Bloch, and Christian Gross. Coherent Many-Body Spin Dynamics in a Long-Range Interacting Ising Chain. *Phys. Rev. X*, 7:041063, Dec 2017.
(Cited on page 127.)

[161] Vincent Lienhard, Sylvain de Léséleuc, Daniel Barredo, Thierry Lahaye, Antoine Browaeys, Michael Schuler, Louis-Paul Henry, and Andreas M. Läuchli. Observing the Space- and Time-Dependent Growth of Correlations in Dynamically Tuned Synthetic Ising Models with Antiferromagnetic Interactions. *Phys. Rev. X*, 8:021070, Jun 2018.
(Cited on page 127.)

[162] Hyosub Kim, YeJe Park, Kyungtae Kim, H.-S. Sim, and Jaewook Ahn. Detailed Balance of Thermalization Dynamics in Rydberg-Atom Quantum Simulators. *Phys. Rev. Lett.*, 120:180502, May 2018.
(Cited on page 127.)

[163] E. A. Goldschmidt, T. Boulier, R. C. Brown, S. B. Koller, J. T. Young, A. V. Gorshkov, S. L. Rolston, and J. V. Porto. Anomalous Broadening in Driven Dissipative Rydberg Systems. *Phys. Rev. Lett.*, 116:113001, Mar 2016.
(Cited on pages 128 and 135.)

[164] F. Bariani, Paul M. Goldbart, and T. A. B. Kennedy. Dephasing dynamics of Rydberg atom spin waves. *Phys. Rev. A*, 86:041802, Oct 2012.
(Cited on page 131.)

[165] Y.O. Dudin, L. Li, F. Bariani, and A. Kuzmich. Observation of coherent many-body Rabi oscillations. *Nature Physics*, 8(11):790–794, 2012.
(Cited on page 131.)

[166] B. J. DeSalvo, J. A. Aman, C. Gaul, T. Pohl, S. Yoshida, J. Burgdörfer, K. R. A. Hazzard, F. B. Dunning, and T. C. Killian. Rydberg-blockade effects in Autler-Townes spectra of ultracold strontium. *Phys. Rev. A*, 93:022709, Feb 2016.
(Cited on page 135.)

[167] D. P. Sadler, E. M. Bridge, D. Boddy, A. D. Bounds, N. C. Keegan, G. Lochead, M. P. A. Jones, and B. Olmos. Radiation trapping in a dense cold Rydberg gas. *Phys. Rev. A*, 95:013839, Jan 2017.
(Cited on page 135.)

[168] J. A. Aman, B. J. DeSalvo, F. B. Dunning, T. C. Killian, S. Yoshida, and J. Burgdörfer. Trap losses induced by near-resonant Rydberg dressing of cold atomic gases. *Phys. Rev. A*, 93:043425, Apr 2016.
(Cited on page 136.)

[169] T. Boulier, E. Magnan, C. Bracamontes, J. Maslek, E. A. Goldschmidt, J. T. Young, A. V. Gorshkov, S. L. Rolston, and J. V. Porto. Spontaneous avalanche dephasing in large Rydberg ensembles. *Phys. Rev. A*, 96:053409, Nov 2017.
(Cited on page 136.)

[170] Jeremy T. Young, Thomas Boulier, Eric Magnan, Elizabeth A. Goldschmidt, Ryan M. Wilson, Steven L. Rolston, James V. Porto, and Alexey V. Gorshkov. Dissipation-induced dipole blockade and antiblockade in driven Rydberg systems. *Phys. Rev. A*, 97:023424, Feb 2018.
(Cited on pages 136 and 167.)

[171] Przemyslaw Bienias, James Douglas, Asaf Paris-Mandoki, Paraj Titum, Ivan Mirgorodskiy, Christoph Tresp, Emil Zeuthen, Michael J. Gullans, Marco Manzoni, Sebastian Hofferberth, Darrick Chang, and Alexey V. Gorshkov. Photon propagation through dissipative Rydberg media at large input rates. *Phys. Rev. Research*, 2:033049, Jul 2020.
(Cited on pages 136 and 167.)

[172] J Robert Johansson, Paul D Nation, and Franco Nori. QuTiP 2: A Python framework for the dynamics of open quantum systems. *Computer Physics Communications*, 184(4):1234–1240, 2013.
(Cited on page 141.)

[173] Valentina Parigi, Erwan Bimbard, Jovica Stanojevic, Andrew J. Hilliard, Florence Nogrette, Rosa Tualle-Brouri, Alexei Ourjoumtsev, and Philippe Grangier. Observation and Measurement of Interaction-Induced Dispersive Optical Nonlinearities in an Ensemble of Cold Rydberg Atoms. *Phys. Rev. Lett.*, 109:233602, Dec 2012.
(Cited on page 144.)

[174] Jia Ningyuan, Alexandros Georgakopoulos, Albert Ryou, Nathan Schine, Ariel Sommer, and Jonathan Simon. Observation and characterization of cavity Rydberg polaritons. *Phys. Rev. A*, 93:041802, Apr 2016.
(Cited on page 144.)

[175] Nina Stiesdal, Hannes Busche, Jan Kumlin, Kevin Kleinbeck, Hans Büchler, and Sebastian Hofferberth. Observation of collective decay dynamics of a single Rydberg superatom. *arXiv preprint arXiv:2005.05089*, 05 2020.
(Cited on page 144.)

[176] M. Lettner, M. Mücke, S. Riedl, C. Vo, C. Hahn, S. Baur, J. Bochmann, S. Ritter, S. Dürr, and G. Rempe. Remote Entanglement between a Single Atom and a Bose-Einstein Condensate. *Phys. Rev. Lett.*, 106:210503, May 2011.
(Cited on page 148.)

[177] H. M. Meyer, R. Stockill, M. Steiner, C. Le Gall, C. Matthiesen, E. Clarke, A. Ludwig, J. Reichel, M. Atatüre, and M. Köhl. Direct Photonic Coupling of a Semiconductor Quantum Dot and a Trapped Ion. *Phys. Rev. Lett.*, 114:123001, Mar 2015.
(Cited on page 148.)

[178] Nicolas Maring, Pau Farrera, Kutlu Kutluer, Margherita Mazzera, Georg Heinze, and Hugues de Riedmatten. Photonic quantum state transfer between a cold atomic gas and a crystal. *Nature*, 551(7681):485–488, Nov 2017.
(Cited on page 148.)

[179] Christoph Simon and William T. M. Irvine. Robust Long-Distance Entanglement and a Loophole-Free Bell Test with Ions and Photons. *Phys. Rev. Lett.*, 91:110405, Sep 2003.
(Cited on pages 148, 155, and 176.)

[180] C. Figgatt, D. Maslov, K. A. Landsman, N. M. Linke, S. Debnath, and C. Monroe. Complete 3-Qubit Grover search on a programmable quantum computer. *Nature Communications*, 8(1):1918, Dec 2017.
(Cited on page 148.)

[181] Hartmut Häffner, Christian F Roos, and Rainer Blatt. Quantum computing with trapped ions. *Physics reports*, 469(4):155–203, 2008.
(Cited on page 148.)

[182] R. Blatt and C. F. Roos. Quantum simulations with trapped ions. *Nature Physics*, 8(4):277–284, Apr 2012.
(Cited on page 148.)

[183] J. Zhang, G. Pagano, P. W. Hess, A. Kyprianidis, P. Becker, H. Kaplan, A. V. Gorshkov, Z.-X. Gong, and C. Monroe. Observation of a many-body dynamical phase transition with a 53-qubit quantum simulator. *Nature*, 551(7682):601–604, Nov 2017.
(Cited on page 148.)

[184] C. Langer, R. Ozeri, J. D. Jost, J. Chiaverini, B. DeMarco, A. Ben-Kish, R. B. Blakestad, J. Britton, D. B. Hume, W. M. Itano, D. Leibfried, R. Reichle, T. Rosenband, T. Schaetz, P. O. Schmidt, and D. J. Wineland. Long-Lived Qubit Memory Using Atomic Ions. *Phys. Rev. Lett.*, 95:060502, Aug 2005.
(Cited on page 148.)

[185] T. P. Harty, D. T. C. Allcock, C. J. Ballance, L. Guidoni, H. A. Janacek, N. M. Linke, D. N. Stacey, and D. M. Lucas. High-Fidelity Preparation, Gates, Memory, and Readout of a Trapped-Ion Quantum Bit. *Phys. Rev. Lett.*, 113:220501, Nov 2014.
(Cited on page 148.)

[186] D. Hucul, I. V. Inlek, G. Vittorini, C. Crocker, S. Debnath, S. M. Clark, and C. Monroe. Modular entanglement of atomic qubits using photons and phonons. *Nature Physics*, 11(1):37–42, Jan 2015.
(Cited on pages 148 and 155.)

[187] J. D. Siverns, J. Hannegan, and Q. Quraishi. Demonstration of slow light in rubidium vapor using single photons from a trapped ion. *Science Advances*, 5(10), 2019.
(Cited on page 149.)

[188] James D. Siverns, John Hannegan, and Qudsia Quraishi. Neutral-Atom Wavelength-Compatible 780 nm Single Photons from a Trapped Ion via Quantum Frequency Conversion. *Phys. Rev. Applied*, 11:014044, Jan 2019.
(Cited on page 149.)

[189] Prem Kumar. Quantum frequency conversion. *Opt. Lett.*, 15(24):1476–1478, Dec 1990.
(Cited on page 149.)

[190] James D. Siverns and Qudsia Quraishi. Ion trap architectures and new directions. *Quantum Information Processing*, 16(12):314, Nov 2017.
(Cited on page 151.)

[191] S. Olmschenk, D. Hayes, D. N. Matsukevich, P. Maunz, D. L. Moehring, and C. Monroe. Quantum Logic Between Distant Trapped Ions. *International Journal of Quantum Information.*
(Cited on page 155.)

[192] D. N. Matsukevich, P. Maunz, D. L. Moehring, S. Olmschenk, and C. Monroe. Bell Inequality Violation with Two Remote Atomic Qubits. *Phys. Rev. Lett.*, 100:150404, Apr 2008.
(Cited on page 155.)

[193] David Petrosyan, Johannes Otterbach, and Michael Fleischhauer. Electromagnetically Induced Transparency with Rydberg Atoms. *Phys. Rev. Lett.*, 107:213601, Nov 2011.
(Cited on page 157.)

[194] Matthias Moos, Michael Höning, Razmik Unanyan, and Michael Fleischhauer. Many-body physics of Rydberg dark-state polaritons in the strongly interacting regime. *Phys. Rev. A*, 92:053846, Nov 2015.
(Cited on page 157.)

[195] Krzysztof Jachymski, Przemysław Bienias, and Hans Peter Büchler. Three-Body Interaction of Rydberg Slow-Light Polaritons. *Phys. Rev. Lett.*, 117:053601, Jul 2016.
(Cited on pages 157 and 165.)

[196] Filippo Maria Gambetta, Chi Zhang, Markus Hennrich, Igor Lesanovsky, and Weibin Li. Long-range multi-body interactions and three-body anti-blockade in a trapped Rydberg ion chain, 2020.
(Cited on page 157.)

[197] V. Efimov. Energy levels arising from resonant two-body forces in a three-body system. *Physics Letters B*, 33(8):563 – 564, 1970.
(Cited on page 157.)

[198] Lena H. Dogra, Jake A. P. Glidden, Timon A. Hilker, Christoph Eigen, Eric A. Cornell, Robert P. Smith, and Zoran Hadzibabic. Can Three-Body Recombination Purify a Quantum Gas? *Phys. Rev. Lett.*, 123:020405, Jul 2019.
(Cited on page 157.)

[199] F. M. Gambetta, W. Li, F. Schmidt-Kaler, and I. Lesanovsky. Engineering NonBinary Rydberg Interactions via Phonons in an Optical Lattice. *Phys. Rev. Lett.*, 124:043402, Jan 2020.
(Cited on page 157.)

[200] H. P. Büchler, E. Demler, M. Lukin, A. Micheli, N. Prokof'ev, G. Pupillo, and P. Zoller. Strongly Correlated 2D Quantum Phases with Cold Polar Molecules: Controlling the Shape of the Interaction Potential. *Phys. Rev. Lett.*, 98:060404, Feb 2007.
(Cited on page 157.)

[201] A. J. Daley, J. M. Taylor, S. Diehl, M. Baranov, and P. Zoller. Atomic Three-Body Loss as a Dynamical Three-Body Interaction. *Phys. Rev. Lett.*, 102:040402, Jan 2009.
(Cited on page 157.)

[202] P R Johnson, E Tiesinga, J V Porto, and C J Williams. Effective three-body interactions of neutral bosons in optical lattices. *New Journal of Physics*, 11(9):093022, Sep 2009.
(Cited on page 157.)

[203] L. Mazza, M. Rizzi, M. Lewenstein, and J. I. Cirac. Emerging bosons with three-body interactions from spin-1 atoms in optical lattices. *Phys. Rev. A*, 82:043629, Oct 2010.
(Cited on page 157.)

[204] Marcin Kalinowski, Yidan Wang, Przemysław Bienias, Michael J. Gullans, Dalia Ornelas-Huerta, A. N. Craddock, Steven Rolston, Porto James V., Hans Peter Buechler, and Gorshkov Alexey V. Enhancement and tunability of three-body loss between strongly interacting photons, 2020.
(Cited on page 157.)

[205] M. Fleischhauer and M. D. Lukin. Quantum memory for photons: Dark-state polaritons. *Phys. Rev. A*, 65:022314, Jan 2002.
(Cited on page 160.)

[206] Sergio H. Cantu, Aditya V. Venkatramani, Wenchao Xu, Leo Zhou, Brana Jelenković, Mikhail D. Lukin, and Vladan Vuletić. Repulsive photons in a quantum nonlinear medium. *Nature Physics*, Jun 2020.
(Cited on pages 165 and 174.)

[207] Michael J Gullans. *Controlling atomic, solid-state and hybrid systems for quantum information processing*. PhD thesis, Harvard University, April 2013.
(Cited on page 166.)

[208] Przemyslaw Bienias, Michael J Gullans, Marcin Kalinowski, Alexander N Craddock, Dalia P Ornelas-Huerta, Steve L Rolston, J V Porto, and Alexey V Gorshkov. Exotic photonic molecules via Lennard-Jones-like potentials. *arXiv preprint arXiv:2003.07864*, 2020.
(Cited on pages 174 and 177.)

[209] C. K. Law and J. H. Eberly. Arbitrary Control of a Quantum Electromagnetic Field. *Phys. Rev. Lett.*, 76:1055–1058, Feb 1996.
(Cited on page 175.)

[210] Jiazhong Hu, Alban Urvoy, Zachary Vendeiro, Valentin Crépel, Wenlan Chen, and Vladan Vuletić. Creation of a Bose-condensed gas of 87Rb by laser cooling. *Science*, 358(6366):1078–1080, 2017.
(Cited on page 176.)

[211] R. Zhao, Y. O. Dudin, S. D. Jenkins, C. J. Campbell, D. N. Matsukevich, T. A. B. Kennedy, and A. Kuzmich. Long-lived quantum memory. *Nature Physics*, 5(2):100–104, Feb 2009.
(Cited on page 176.)

[212] J. Ruseckas, I. A. Yu, and G. Juzeliūnas. Creation of two-photon states via interactions between Rydberg atoms during light storage. *Phys. Rev. A*, 95:023807, Feb 2017.
(Cited on page 177.)

[213] Przemyslaw Bienias and Hans Peter Büchler. Two photon conditional phase gate based on Rydberg slow light polaritons. *Journal of Physics B: Atomic, Molecular and Optical Physics*, 53(5):054003, feb 2020.
(Cited on page 177.)

[214] J. D. Wong-Campos, K. G. Johnson, B. Neyenhuis, J. Mizrahi, and C. Monroe. High-resolution adaptive imaging of a single atom. *Nature Photonics*, 10(9):606–610, Sep 2016.
(Cited on page 180.)